REVIEW

ADVANCED ENERGY MATERIALS

www.advenergymat.de

Single-Atom Catalysts for Hydrogen Generation: Rational Design, Recent Advances, and Perspectives

Chenyu Zhang, Hou Wang, Hanbo Yu, Kaixin Yi, Wei Zhang, Xingzhong Yuan, Jinhui Huang, Yaocheng Deng,* and Guangming Zeng**

Hydrogen is widely believed to be a promising fuel to solve the global energy crisis and environmental issues. The catalytic system represented by metal-supported catalysts is an important process of upgrading the hydrogen source in industry. Single-atom catalysts (SACs), which inherit the advantages of homogeneous and heterogeneous catalysts, provide a broad prospect for low-cost H_2 production technology. This review focuses on the potential mechanisms in the rational design of SACs, including active sites, coordination configuration, mass loading, heteroatom-doping, and metal–support interaction. The design strategies of single metal atoms on different supports are reviewed to give a proposal on how to immobilize the atomic active sites and modulate the geometric/electronic structures of SACs. Subsequently, the synergistic effect in SACs and the dynamic evolution of the atomically dispersed heterometal catalysts are introduced, aiming to provide further guidelines for H_2 evolution SACs. H_2 generation from the water–gas shift reaction and electro-/photocatalytic water splitting are the main research directions at present. The latest progress of SACs employed in these applications is thoroughly reviewed. At the end of this review, personal perspectives on the prospects and challenges of H_2 evolution SACs are put forward, hoping to promote the rapid development of SACs toward superior H_2 evolution performance.

1. Introduction

Global energy development is facing the issues such as resource shortage, environmental pollution, and climate change. Promoting the global energy transformation and achieving green development has become the common cause of human society. The ideal fuels of the future need to be able to solve the increasingly serious energy crisis, environmental challenges with clean and sustainable energy conversion. Hydrogen (H_2) has attracted great attention because of its cleanliness and extremely high weight energy density (122 kJ g^{-1}).[1] As we all know, the final product from H_2 energy is water no matter how it is used, which can truly achieve zero-emission and zero-pollution. Therefore, H_2 energy is considered to be one of the most ideal energy sources in the future.[2] Traditional H_2 production technologies are mainly formed by steam reforming of fossil fuels, such as natural gas and petroleum ($CH_4 + H_2O \rightarrow CO + 3H_2$, $CO + H_2O \rightarrow CO_2 + H_2$).[3] The key point that must be paid attention to is to reduce pollution and improve the efficiency of H_2 evolution from fossil fuels. In the future, H_2 production industrially should present the coexistence form of diversified development in which the advantages of the fossil raw material route and the renewable raw material route complement each other.

Water electrolysis and photocatalytic water splitting have been promising techniques for sustainable H_2 production, and they are important supplements to the H_2 generation from fossil fuels. However, there are still plenty of technical problems industrially, which hinder their wide application in practice. On the one hand, with the continuous increase in the global energy demand, noble metal-based catalysts dominated by platinum group metal (PGM) have severely restricted the further development of the energy industry owing to their high cost, natural scarcity, and poor anti-poisoning. On the other hand, the catalytic efficiency of earth-abundant transition-metal-based nanocatalysts employed as an alternative to PGM-based catalysts is far from the criterion of industrial applications.[4] It can be seen that improving the utilization of noble metal active centers and developing efficient noble metal-free catalysts are available solutions. This is still a hugely challenging task, for which we should first survey the reasonable development of the catalytic system.

The evaluation indexes of the catalytic reaction include selectivity and conversion. The key points that need to be studied are: i) active center and adsorption site; ii) the size-dependent effects of catalysts; iii) interactions between active species and the support, surface effect, and interfacial effect. The

C. Zhang, H. Wang, H. Yu, K. Yi, W. Zhang, X. Yuan, J. Huang, G. Zeng
College of Environmental Science and Engineering
Hunan University
Changsha 410082, P. R. China
E-mail: huangjinhui@hnu.edu.cn; zgming@hnu.edu.cn

Y. Deng
College of Resources and Environment
Hunan Agricultural University
Changsha 410082, P. R. China
E-mail: dengyaocheng@hunau.edu.cn

The ORCID identification number(s) for the author(s) of this article can be found under https://doi.org/10.1002/aenm.202200875.

DOI: 10.1002/aenm.202200875

© 2022 Wiley-VCH GmbH

understanding of catalytic active sites is an unfading topic in the field of catalysis. Early studies showed that certain catalytic reactions depend on isolated atoms rather than the aggregation of atoms.[5] Rooney and co-workers referred to the idea of metal atoms forming active sites as the "π-bonding theory of catalysis", which was often used to explain the hydrocarbon reactions, including the exchange of paraffins, olefins, and aromatics with deuterium, as well as hydrogenation, dehydrogenation, and isomerization reactions.[5a,6] Some studies after this confirmed that single metal atoms could play the role of active sites in a variety of catalytic reactions.[7] The breakthrough results were reported by the Flytzani-Stephanopoulos' group and Xu et al. They found that Au or Pt species with nonmetallic nature were the real active sites, while metal nanoparticles were not involved in the reaction.[8] However, the immature experimental conditions and techniques lead to no direct characterization evidence to support this result. Hence, the active sites may not be isolated and dispersed, but small clusters that have been retained.

With the development of nanocatalysis and advanced characterization technologies, some reports involved directly observing isolated metal atoms and measuring the dispersion of active sites began to appear.[9] It has been found that the coordinatively unsaturated metal atoms on the surface are usually active sites of catalysis.[10] The catalytic performance can be improved by controlling the size and morphology of metal-based nanomaterials and adjusting the distribution of the atoms on the catalyst surface.[11] The energy level and electronic structure will change fundamentally when the size of nanocatalysts is reduced to atomic clusters or even single atoms (SAs).[12] Examples include larger surface area, quantum size effect, and metal–support interactions (MSIs) (**Figure 1**). Although there are hundreds or even thousands of metal atom aggregates in heterogeneous catalysts, only a few of them are in contact with the reactants. The heterogeneity of these aggregates leads to a small number of coordinately unsaturated metal centers, thereby reducing the metal utilization efficiency. One feasible way to balance the enhancement of catalytic activity with the decrease of manufacturing costs is to reduce the size of precious metals from nanoparticles to clusters or even SAs, to maximize the utilization.

In short, the key to improving the performance of the catalytic systems is how to increase the density and intrinsic activity of active centers.[13] The size of these nanocatalysts is already small, but not enough. For certain catalytic reactions, nanoclusters with multiple active centers are not always ideal.[14] Fortunately, metal active sites in the state of atomic distribution may be the best solution to maximize the efficiency of supported catalysts, namely "single-atom catalysts (SACs)". Compared to nanoclusters, nanoparticles, and bulk materials, SACs have shown remarkable advantages, such as unsaturated coordination environment, unique electronic structure, maximum atom utilization, and well-defined catalytic sites. The concept of SACs was proposed by Zhang and co-workers in 2011. They successfully synthesized a Pt SAC with FeO_x as support and proved its high CO oxidation activity.[15] It is reported that the electronic structure of the Pt atom can be altered during the process of electron transfer to FeO_x, thus ensuring the high stability and activity of the dispersed single Pt atoms. Thereafter, SACs with unique features have received increasing attention worldwide.[16] These SACs are not only diverse in material synthesis, but also show excellent performance in different catalytic systems.

Before starting the discussion on the rational design of SACs, we should clearly understand the conceptual framework of SACs. It is worth noting that the following two aspects are easy to be misunderstood and confused. First of all, the valance of isolated single metal atoms in SACs is not in fact zero. Strictly speaking, the active sites of SACs cannot be called an atom. Single metal atoms (M-SAs) need to be stabilized by covalent coordination or ionic interaction with adjacent surface atoms or ligands on the support.[17] Such a MSI makes M-SAs partially charged. Another issue that can be easily confused is the three terms used to describe other similar metal-supported catalysts, that is, "single-site heterogeneous catalysts (SSHCs)", "site-isolated heterogeneous catalysts (SIHCs)" and "atomically

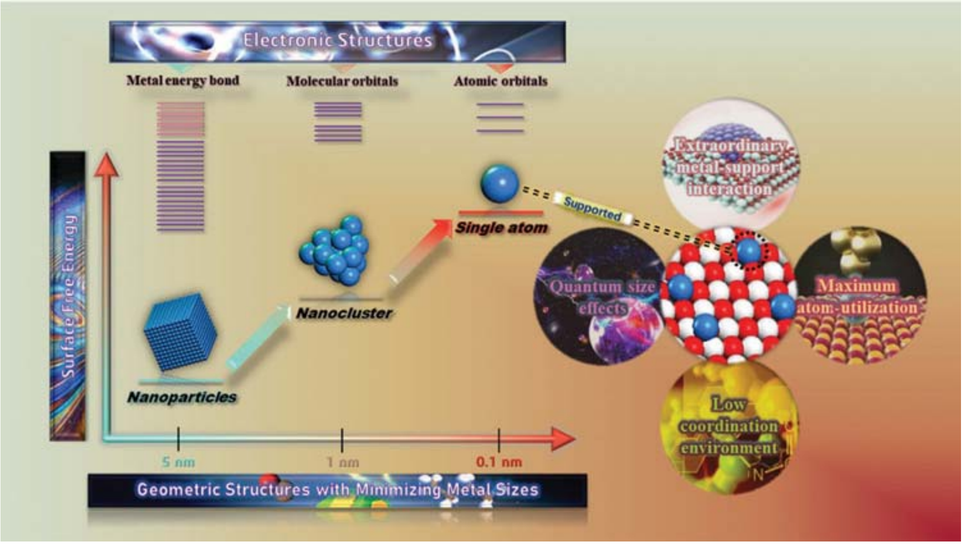

Figure 1. Geometric and electronic structures of nanoparticle, nanocluster, and SA with unique features.

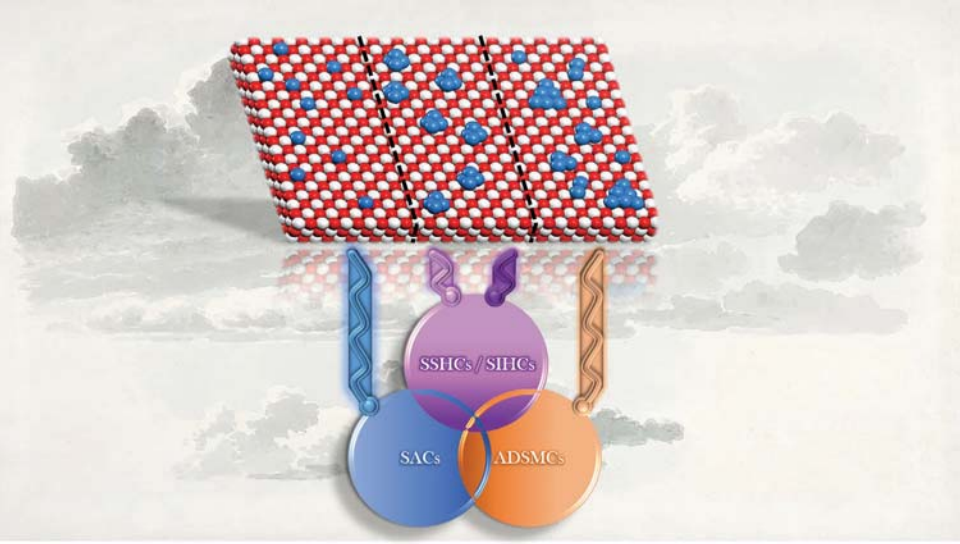

Figure 2. Schematic comparison of SACs (left), SSHCs (middle) and ADSMCs (right).

dispersed supported metal catalysts (ADSMCs)", as manifested in **Figure 2**i) SSHCs is a concept introduced by Thomas in 2005. It should be pointed out that SACs are not equivalent to SSHCs with multinuclear active sites.[14] According to the strict definition of SSHCs, the energy of the interaction between each catalytic active site and the reactant should be the same, that is to say, the catalytic behavior of all active sites is consistent. Unfortunately, such an idealized state is harsh for heterogeneous catalysts. Owing to the heterogeneity in the surface structures of the supports, the active sites of SACs are not necessarily uniform. In other words, the interaction between metal species and the support will lead to different catalytic behaviors. Therefore, SACs with the same definition as SSHCs may appear only when the loading of active species is extremely low. In addition, the "single-site" in SSHCs can be composed of isolated ions, atoms, molecular complexes, and clusters as long as they exhibit good structural characteristics like single-sites in the homogeneous catalysts.[18] ii) To tackle the problem that various metal species formed between metal and support affect the catalytic activity, McKittrick et al. introduced and designed SIHCs with uniformly isolated sites and an easy-to-characterized structure.[19] SIHCs are defined as heterogeneous catalysts composed of isolated metal-organic complexes with well-defined structures. The typical feature of SIHCs is that the active sites are protected by ligands, and the catalytic behavior of all active sites is consistent. More importantly, the active sites in SIHCs may not be uniformly dispersed metal atoms. Hence, SIHCs with only one type of active site can be considered as SSHCs. iii) There are two main views on the description of ADSMCs. Partial point of view is that single metal atoms are the active sites in ADSMCs, which is the same as SACs.[20] The other is that ADSMCs are metal-supported catalysts with completely dispersed active species.[17,21] The latter has the most extensive concept. If the active sites are uniformly distributed, the catalytic metal centers can be SAs, ions, complexes, or in the form of clusters, trimers, dimers, monomers, or even 2D bamboo structures. Gates et al. proposed that ADSMCs should also include single-site metal catalysts, site-isolated metal catalysts, and molecular/atomically dispersed metal catalysts.[21] SACs are, to some extent, a subset of ADSMCs, but the structure and active sites of SACs are sharper and more specific than those of ADSMCs. This is not in contradiction with the fact that SACs are supported by heterogeneous catalysts. SACs emphasize that active sites are isolated atoms (metal or nonmetal atoms) dispersed on the support surface and can be anchored via interaction with the support. SACs can be clearly defined and understood compared with other supported catalysts.

At present, electrocatalytic hydrogen evolution reaction (HER) is still the main focus in hydrogen evolution SACs. Taking SACs in HER as an example, M-SAs will transfer electrons to the support owing to the difference in electronegativity between M-SAs and their coordination atoms, resulting in emptier *d*-orbitals on metal atoms. Then the 1*s* orbitals of hydrogen preferentially combine with these unoccupied metal *d*-orbitals, thereby optimizing hydrogen adsorption binding energy.[22] Compared with traditional catalysts, SACs are still a rising star in the field of H_2 generation. How to further crack the codes of SACs in catalytic reaction to finding the key for a new era of hydrogen production must receive the attention and efforts of utilizing a multidisciplinary research community. In recent years, there have been some excellent reviews about SACs toward H_2 evolution.[22,23] Apart from electrochemical HER, these papers hardly follow with interest the application of SACs in other H_2 generation techniques, for instance, photocatalytic hydrogen evolution (PHE), and water–gas shift reaction (WGSR). Given that the currently industrialized H_2 production technology is not systematic, recent research should be devoted to the direction of coexistence, commonality, and sharing of various technologies toward H_2 production. In particular, photocatalytic technology can directly obtain H_2 from water, or indirectly provide electrical energy for electrocatalytic H_2 evolution. SACs, which inherit the advantages of homogeneous and heterogeneous catalysts, have shown great potential in energy-related catalysis (Figure 1), and are expected to reduce the loading of noble metals and maximize the catalytic performance of non-noble metal active centers. What we want

© 2022 Wiley-VCH GmbH

to emphasize is that it is not enough to summarize the preparation strategies and characterization technologies of SACs for H_2 generation from the technical level. The importance of exploring the rational design and catalytic mechanism of SACs from the atomic scale cannot be ignored.

Based on the above discussion, this review aims to provide a comprehensive overview of SACs toward H_2 production. We begin this review by highlighting the design rules for improving the H_2 evolution performance of SACs. Different from other articles that merely focus on the fabrication methods for stabilizing SAs, we believe that in-depth revealing the active sites, coordination configuration, mass loading, heteroatom doping, and MSI are the necessary and sufficient conditions to stimulate the catalytic potential of SACs. Likewise, we specifically emphasize the importance of rational construction of metal–support interfaces, since the coordination geometry and electronic properties of M-SAs are closely related to their surrounding environment. To promote the rapid development of SACs with high H_2 evolution activity, the subsequent section is devoted to describing the interaction between atomically dispersed metal species and various support materials. Moreover, we will explicitly reveal the metal–metal interaction in SACs, including the synergistic effects between homometallic atoms and the coordination chemistry of heterometallic catalysts. In the following sections, we will summarize the recent advances of SACs used in main catalytic H_2 generation reactions, to grasp the future development and application prospect of SACs as a whole. In the end, we put forward some prospects for the major challenges and opportunities that H_2 evolution SACs still face in the future.

2. Rational Guidelines of SACs toward Efficient Hydrogen Evolution

A large number of research examples show that SACs are expected to build a platform for elucidating the structure–reaction relationship of catalysts and the mechanism of catalytic reactions at the atomic level. In turn, this breakthrough can be used to further enhance the H_2 evolution activity of SACs. For example, during the alkaline HER process, an ideal catalyst with high activity can respond to the formation of adsorbed H atoms (E-H*, E refers to the active site) intermediate on the active sites at relatively low voltage. According to reports, single iodide atoms can accelerate H_2O dissociation and H adsorption through the formation of I-H* intermediates, thereby boosting HER kinetics.[24] In acidic media, the atomically dispersed $Pt{-}O_{Pt}$ dual-site interface constructed by Yao et al. greatly improved HER performance.[25] Such well-structured dual $Pt{-}O_{Pt}$ sites promoted the synergetic H_{ads}-coupling, thereby accelerating the Volmer–Tafel kinetics which dominated the whole H_2 evolution process.

In the past few years, SACs with breakthrough H_2 production performance have been reported in large numbers,[26] which adequately demonstrates their broad prospects. The selection of the ideal supports and the development of reasonable design strategies are the main problems to be solved urgently prior to practical industrial production. The possible issues in the SACs system, such as geometric effect, electronic effect, or ensemble effect, will affect the consistency of the active sites and the nanointerface. Therefore, it is of great significance to in-depth exploration of the coordination environment and electronic properties at the interface sites of SACs in catalytic reactions for the design of high-performance SACs. Up to now, more relevant works have been focused on the SACs used for WGSR, electro/photo-chemical water splitting toward H_2 generation. To help develop SACs with tunable active centers, high selectivity, and H_2 evolution efficiency, we will discuss the potential mechanisms that should be considered in the design from the following aspects (**Figure 3**): i) the construction of homogeneous active sites, which is helpful to comprehensively understand the catalytic mechanism and significantly increase the activity/selectivity; ii) the modulation the coordination configuration and the oxidation state of the catalytic centers; iii) precisely controlling the loading mass of SACs, and developing strategies that can high loading rate with uniformly dispersed active sites; iv) regulating the local coordination environment in SACs via heteroatom doping; v) the rational construction of the metal–support interface via strong metal–support interaction (SMSI) as well as electronic metal–support interaction (EMSI). The above-mentioned rules determine whether the hydrogen generation efficiency of SACs can make a major breakthrough.

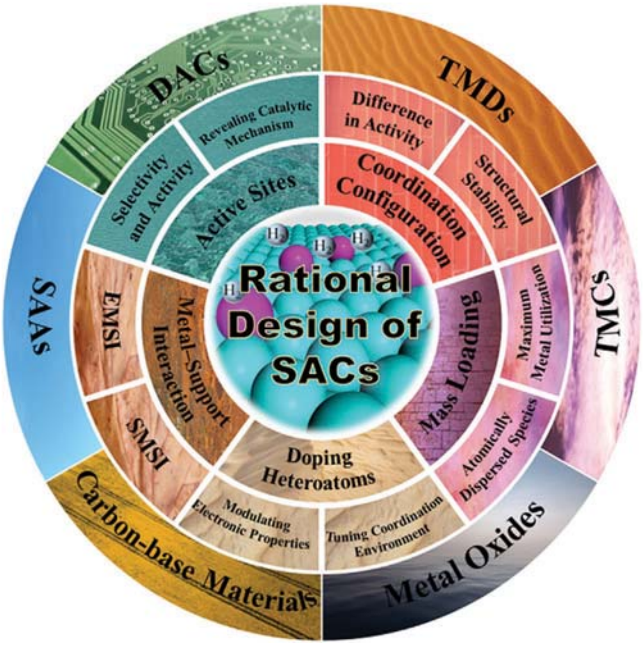

Figure 3. Rational design guidelines of SACs for high-performance hydrogen evolution.

2.1. Identifying and Constructing Homogeneous Active Sites

Different operating conditions in catalytic reactions, such as reaction temperature, potential, pH value, and adsorption capacity, lead to catalyst reconstruction, which makes it difficult to reveal the catalytic mechanism.[27] Considering that the dynamics of HER in alkaline environments are more complex and slower than that in acidic environments, there is a higher

© 2022 Wiley-VCH GmbH

demand for the identification of active species. The construction of a catalytic model that can uniformly support single-atom centers (similar to homogeneous active centers) guides surveying the structure and intermediate transition states of true active sites in a practical catalytic reaction environment. The structure of the active site in SACs is not uniform. This is not a contradiction. As described above, the synergistic effect between supported metal atoms and surrounding coordination atoms is the main reason for the high performance of SACs. Thus, the inherent inhomogeneity of the supports, as well as the uncontrollability of the fabrication approaches, lead to the presence of dispersed atoms in different forms. Zhang and co-workers noted that even though Fe in Fe-N-C SAC was present as dispersed SAs, four different FeN_x species would form (including FeN_4, High-spin $X{-}Fe^{III}N_4{-}Y$, Low-spin $N{-}Fe^{III}N_4{-}N$, and Medium-spin $N{-}Fe^{III}N_4$).[28]

By combining modern characterization techniques with theoretical modeling, researchers can systematically understand the positions of atoms, the bonding between isolated atoms and supports, and the reaction mechanism. Characterization techniques commonly employed to analyze the structure of SACs include, but are not limited to, X-ray diffraction (XRD), transmission electron microscopy (TEM), X-ray photoelectron spectroscopy (XPS), Fourier transform infrared spectroscopy (FTIR), Raman spectroscopy, and nuclear magnetic resonance (NMR).[29] In particular, aberration-corrected electron microscopy can be used to directly observe the spatial distributions of SAs on the supports and the defect-induced modes.[30] X-ray absorption fine structure (XAFS) spectra, also known as X-ray absorption spectroscopy (XAS), is a powerful tool for studying the internal structures, electronic properties, and catalytic activity of SACs at the atomic scale.[31] XAFS spectrum is divided into two regions: X-ray absorption near-edge spectroscopy (XANES) and extended X-ray absorption fine structure spectroscopy (EXAFS). First, XANES can accurately determine the electronic properties of SAs sites (such as oxidation state, coordination chemistry, and electron transfer between catalytic centers and supports). Second, EXAFS can determine information such as coordination number and bond length. Naturally, it is not enough to study SACs through both high-resolution imaging and spectroscopy tools. The reliable model of the active sites calculated by density function theory (DFT) calculation allows us to further explore the relationship between the structure and the catalytic activity of SACs.

A major challenge in the synthesis of SACs is how to controllably construct active sites with uniform structures. Nevertheless, we mean to emphasize that the identification of the active site is equally important. The results of accurate identification, on the one hand, can help us clarify the real sites that promote the reaction, and provide guidance for the synthesis of SACs. On the other hand, the dynamic evolution of the coordination environment during the reaction can be clearly understood.

XAFS spectroscopy is a useful tool for identifying the atomic dispersion of active metal species. In particular, operando XAFS analysis can be employed to investigate the dynamic electronic structure and local coordination environment of the catalysts during the reaction process.[32] For the first time, Wei and co-workers used extended operando XAFS and theoretical calculations to precisely identify the structure of the real active sites of atomically dispersed cobalt-based catalysts in alkaline HER.[33] The single and homogeneous active site structure with excellent catalytic activity offered an ideal model system for comprehending the intrinsic active sites as well as the reaction mechanism. Aberration corrected high-angle annular dark-field scanning transmission electron microscopy (HAADF-STEM) was employed to directly identify the distribution of single Co species (**Figure 4**a). The subsequent XAFS spectroscopy further demonstrated the presence of Co in the obtained catalyst as dispersed atoms. As shown in Figure 4b, Co K-edge XANES analysis confirmed the Co average valence state of approximately +2.02 (close to +2.0). Under the reaction conditions, as illustrated in Figure 4c, the Co—N/O coordination peaks in the first shell shifted to the low-R (1.63 to 1.56 Å), indicating that the coordination environment had altered significantly. Next, DFT calculations and EXAFS determined the most stable coordination configuration (i.e., $OH{-}Co_1{-}N_2$) which could immobilize the single Co site and favor the preferential adsorption of H_2O molecule on Co, forming the $H_2O{-}(HO{-}Co_1{-}N_2)$ intermediate (Figure 4d). These results revealed that the coordinatively unsaturated Co sites were sensitive to the environment. Similar to the work of Sargent and co-workers,[34] the constructed high-valence $HO{-}Co_1{-}N_2$ site exhibited a high reactivity towards water adsorption.

It is, however, inescapable that high surface energy typically usually leads to bulk or particle morphologies in conventional catalysts using typical synthesis routes.[35] Both the electronic and geometric interactions between M-SAs and supports markedly affect the catalytic activity of SACs. M-SAs, which exhibit a high valence state similar to cations, are adverse to the electrochemical reduction reaction owing to scarce d-electrons involved in the reaction. The construction of active centers with freeatoms-like electronic structures is an effective means to overcome this issue.[36] The nearly uniform local coordination environment is obtained via anchoring single Pt atoms to specific positions of the N-doped carbon framework.[37] XAFS revealed that Pt-SAs as efficient active sites presented a near-free state. In particular, at + 0.5 V potential, only capacitive charging occurred on the electrode surface without any redox reaction, so + 0.5 V is generally considered to be located in the double-layer region.[38] This can explain the reason why the white-line intensities of the catalyst remained unchanged at ex situ, open circuit, and +0.5 V (Figure 4e), and proved Pt-SAs sites are structurally stable.[37] Additionally, the evolution of the coordination configuration of Pt-SAs was further determined by the change of the applied potential. The ligand stabilization or precursor stabilization has been proved a reliable method to fabricate SACs with stable and dispersed active sites. For example, the direct H_2 reduction approach protected via ligands can inhibit the aggregation of Rh atoms on MFI-type zeolites during the reduction process.[39] STEM and EXAFS showed that the sinusoidal 5-membered rings stabilized by the zeolite framework oxygens were the anchor sites of Rh-SAs. In the study of Pt-doped MoS_2 nanosheets, the active sites in HER were derived from S atoms in Pt-MoS_2 sample instead of Pt atoms.[40] Also, Jiang et al. claimed that introducing a Pt-SAs into Al-TCPP (an aluminum-based porphyrinic metal–organic framework) could significantly improve H_2 generation activity through spectral characterization and DFT calculations.[41] In

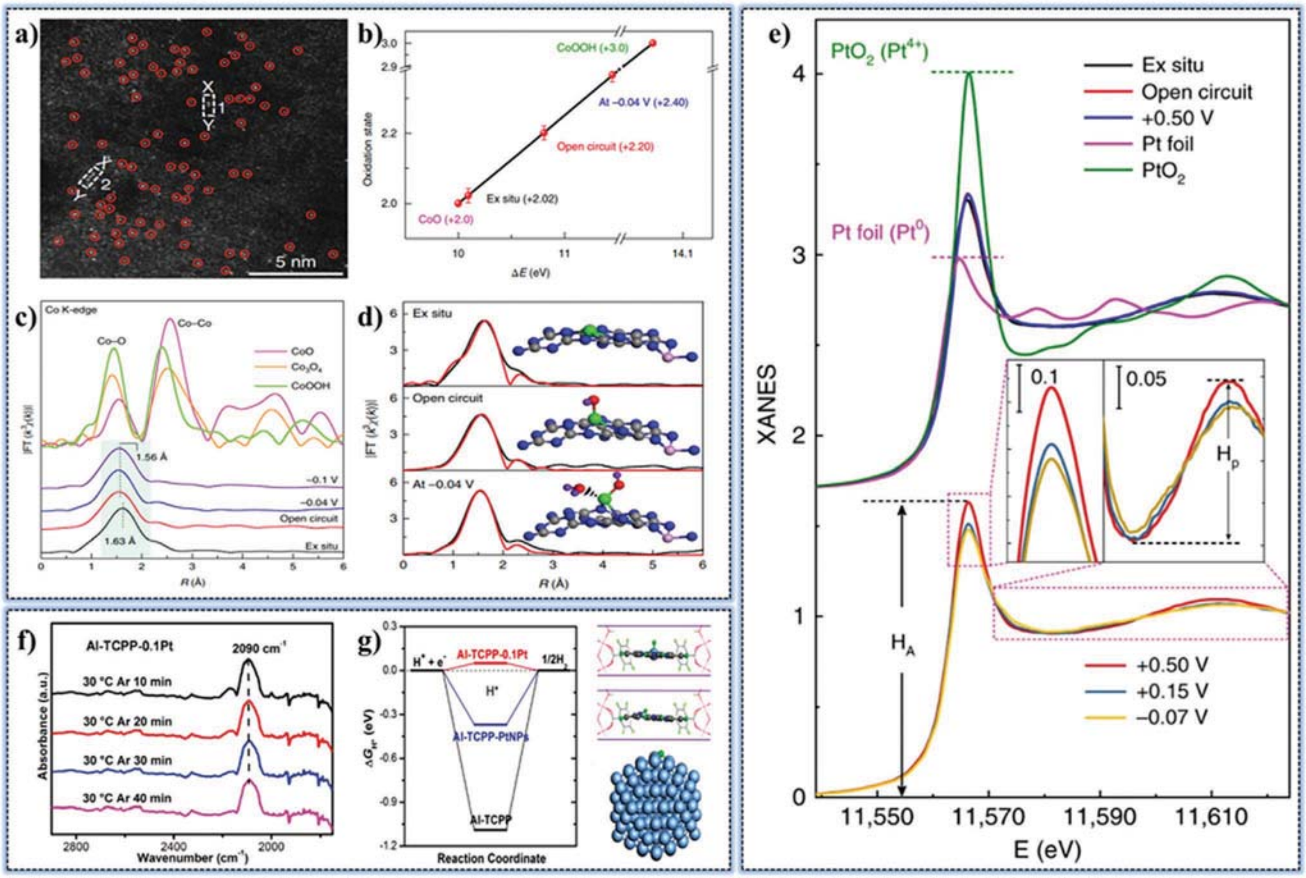

Figure 4. a) Atomic-resolution HAADF–STEM image of Co_1/PCN. b) The fitted average oxidation states of Co from XANES spectra. c) Corresponding k^3-weighted Fourier transform (FT) spectra. d) First-shell fitting of EXAFS spectra. Insets: corresponding coordination configurations. H: purple; C: grey; N: blue; O: green; P: pink; Co: red. Reproduced with permission.[33] Copyright 2019, Nature Publishing Group. e) Selected XANES spectra under different applied voltages from open-circuit condition to −0.07 v during HER, as well as the XANES data of each reference standard. Reproduced with permission.[37] Copyright 2020, Nature Publishing Group. f) DRIFT spectra of CO adsorbed on Al-TCPP-0.1Pt after being purged with Ar gas for different time lengths and g) calculated free energy diagram for photocatalytic H_2 production. Reproduced with permission.[41] Copyright 2018, John Wiley and Sons.

that work, they achieved the stability of Pt-SAs by using the strong interaction of pyrrole N atoms in Al-TCPP. The symmetry of the peak shows the uniform structure of Pt-SAs (Figure 4f). Meanwhile, as shown in Figure 4g, the introduction of Pt-SAs into metal–organic frameworks (MOFs) increased the binding energy of hydrogen, thereby significantly enhancing the PHE activity. Notably, the modification of suitable organic pillars or functionalized bridging linkers enriches coordination sites employed to capture M-SAs in MOFs.[42]

The homogeneous active sites are helpful to probe where the catalytic reaction occurs. There is no metal–metal bond in the active sites of SACs, meanwhile the SA does not form metal–oxygen bonds with an oxygen atom (or other atom) in the support, thus the chemical environment of all active sites is uniform.[43] Such a special feature makes the establishment of the theoretical model and the investigation of dynamic evolution clearer as well as more concise, which greatly promotes the comprehensive understanding of the catalytic mechanism. More importantly, since only atomically dispersed active sites are available, SACs may exhibit different catalytic mechanisms from the catalytic pathway with multiatom involving nanocatalysts. The advantages of a single active site can be realized only when M-SAs active sites have the same (or higher) catalytic activity as the metal atoms on the nanoparticle surface.[44]

2.2. Engineering Coordination Configuration

In addition to the uniformity of active sites, the unique electronic and steric effects created by the coordination configuration of the catalytic centers also play a decisive role in the properties of the catalyst. Coordinatively unsaturated or ligand-exchangeable catalytic centers are beneficial for substrates to interact, as well as take part in the catalytic cycle.[45] Hence, modulating the coordination configuration and the oxidation state of the catalytic centers is believed to be another critical measure to optimize the catalytic properties of SACs. By replacing the metal sites in the metal oxide support, the atomically dispersed metal species as active centers in SACs are highly coordinated and unsaturated.[28,46] Generally speaking, the reactants are easily adsorbed on the surface because of the characteristic that the *d*-electron orbitals of noble metals are not filled completely, which favors the formation of active intermediates for the reaction. Accordingly, noble metal catalysts have better catalytic activity.

In heterogeneous catalysis, structure–performance relationship has been a longstanding challenge for a majority of reactions. Since the stability of the M-SAs depends on covalent and ionic bonding with the support, the local coordination chemistry should mainly determine the geometric and electronic properties of SAs.[45,47] Based on this, the coordination number of SAs may be a reasonable descriptor to help us understand the structure–performance relationship. In a report on Pt_1/def-TiO_2 materials, as shown in **Figure 5**a, the first shell coordination number of Pt and O atoms was about 5, and the corresponding bond length was about 1.98 Å.[48] This result suggested that each active site had five Pt—O bonds. Furthermore, Pt SAs anchored on the surface steps of CdS with unsaturated coordination geometry could be formed abundant Pt—S bonds with the unsaturated sulfur atoms.[49] EXAFS demonstrated that Pt centers were the four-coordinated tetrahedron configuration, and the coordination number of the nearest S atoms around a single Pt atom is 4.0 with a distance of 2.32 Å, as illustrated in Figure 5b. The above researches elucidate the fact that the surface defects of unsaturated coordination provide an ideal electronic environment for the stability of SAs. Simultaneously, the unsaturated coordination of the active site atoms can increase the possibility of contact with the substrate molecules, enhancing the catalytic activity.[50] For example, the Co—N coordination bonds in Co SAs/N-C were broken owing to the increase of the pyrolysis temperature (coordination number decreased from 4 to 2), which made Co-SAs exhibit higher activity toward oxygen reduction activity.[51] Another example is Ni_{SA}-N_x-C SAC synthesized via using polypyrrole (PPy) as a nitrogen source to stabilize isolated Ni atoms. The two-coordinated Ni-N structure (Ni_{SA}-N_2-C) obtained by also controlling the pyrolysis temperature showed more efficient electrocatalytic CO_2 reduction than the three- or four-coordinated Ni—N shell. Theoretical calculations revealed the reason for its excellent activity: the low coordination number of Ni-SA sites was conducive to the formation of COOH* intermediate.[52] Zhang's group achieved fine-tuning of Pt-SAs coordination environment via adjusting rapid thermal treatment (RTT) temperature in the inert atmosphere.[46a] They found that, the coordination number of Pt—O in Pt_1/Fe_2O_3 decreased from 3.8 to 1.8 as the RTT temperature was increased from 500 to 600 °C. Hydrogen chemisorption experiment and DFT calculations demonstrated that the coordination structure with the lowest coordination number was easier to activate H_2 molecules, thereby promoting the hydrogenation reactions.[46a] It should be pointed out that the great majority of these studies on coordination structure–performance were devoted to thermocatalytic and electrocatalytic systems. In addition, these studies usually determined the change of coordination number by controlling the pyrolysis temperature of the precursor in an inert atmosphere.

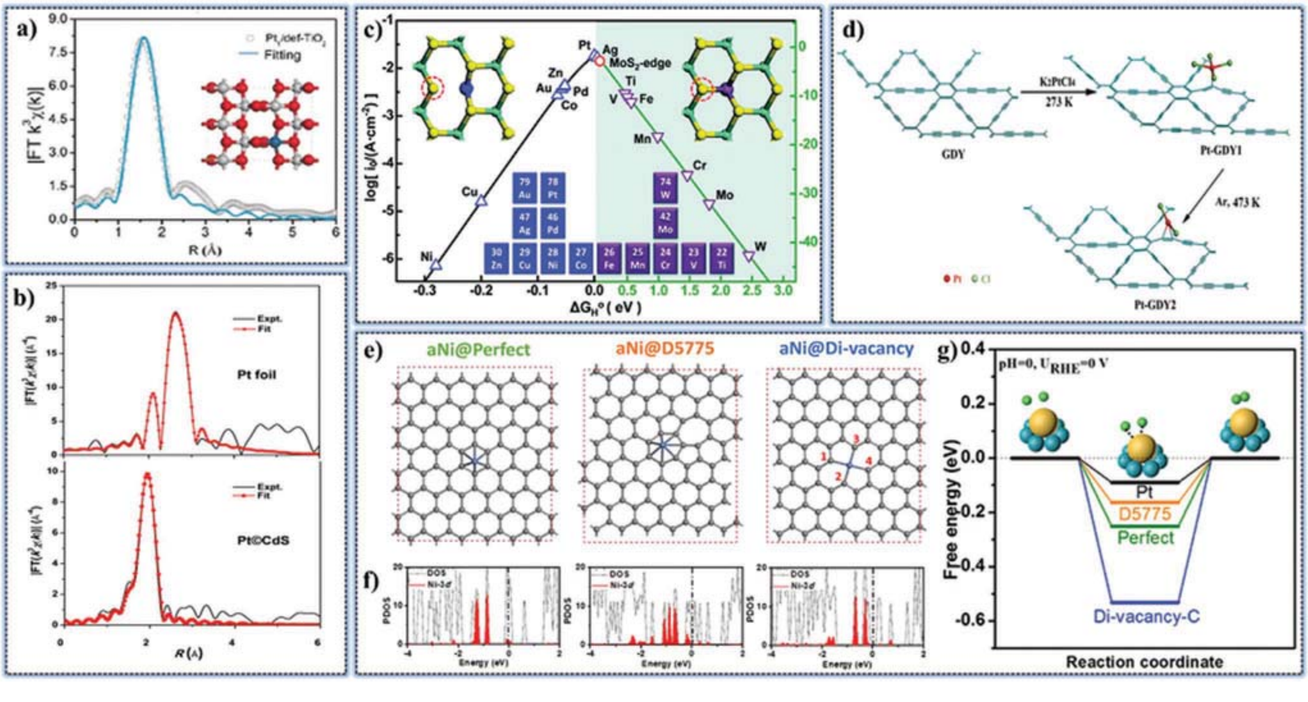

Figure 5. a) EXAFS R space fitting curve and the experimental data of the Pt_1/def-TiO_2 catalyst. Reproduced with permission.[48] Copyright 2020, Wiley-VCH. b) Fourier-transformed magnitudes of Pt L_3-edge EXAFS spectra in R space for Pt foil and Pt/CdS. Reproduced with permission.[49] Copyright 2018, Elsevier Inc. c) Volcano curve presents the relation between currents ($\log(i_0)$) and $\Delta G_H°$ shows. The figure shows the different configurations of different metal-doped MoS_2 coordinated with 4 (left) and 6 (right) S atoms. The red dashed circles, green balls, yellow balls, blue balls, and purple balls present the adsorption positions of H, Mo, S, M_L, and M_R, respectively. Reproduced with permission.[40] Copyright 2015, Royal Society of Chemistry. d) Illustration for the synthesis and the calculated adsorption energy (ΔE_{ads}) of Pt-GDY_1 and Pt-GDY_2. Reproduced with permission.[46b] Copyright 2018, John Wiley and Sons. e) Three different types of active sites and f) three configurations of PDOS corresponding to an Ni SAs supported on perfect hexagons (left), D5775 (middle), and Di-vacancy (right). g) Energy profiles of the three configurations for HER. Reproduced with permission.[56] Copyright 2018, Elsevier Inc.

From the perspective of coordination chemistry, compared to the coordination number of the surface atoms in supported nano-catalysts, SACs have a lower coordination number of the active site atoms, which is more propitious to boost the chemical reaction activity.[53] For example, cobalt-based materials, such as Co—Pi, CoP, and CoOOH, have been considered suitable catalysts for the photolysis of water to produce hydrogen.[54] The common feature of these catalysts is the coordination of unsaturated configuration, which can expose the cobalt-containing groups to the greatest extent, thereby improving the performance of H_2 production.[55] The coordination number of the active centers in SACs is usually less than six. The lower coordination number not only creates more opportunities for the adsorption of catalytic substrates, but also affects the reaction process in certain catalytic systems. Predictably, the difference in the coordination structure formed by the doping with different single metal atoms will be able to produce different catalytic activities. Taking single-atom metal-doped MoS_2 as an example, some metal atoms (denoted as M_R) tend to bond with six S atoms when substituted Mo atoms, while other metal atoms (denoted as M_L) only bonded with only four S atoms to form the coordinatively unsaturated state of S atoms.[40] Compared with M_L-doped, the binding ability of M_R-doped MoS_2 with H was almost all weaker, resulting in lower HER activity. Different coordination structures significantly altered the adsorption behavior of H atoms, thus affecting the activity of H atoms, which was proved by DFT calculations as well (Figure 5c). It cannot be ignored that the overly strong adsorption of H* by unsaturated S atoms neighboring the dopants can inhibit the HER activity of MoS_2. Two kinds of Pt-SACs with different coordination environments were synthesized on the same graphdiyne (GDY) support via different treatments, which also proved the above point. The Pt-SAs supported catalyst formed by the reaction of GDY with K_2PtCl_4 aqueous solution were marked as Pt-GDY_1, and the catalyst formed after Pt-GDY_1 was annealed in Ar atmosphere was marked as Pt-GDY_2.[46b] HAADF-STEM and XAFS spectroscopy combined with DFT calculations showed that the atomic Pt species were stabilized firmly on the surface of the support through the coordination with the alkynyl C atoms in GDY, and Pt atoms had different coordination environments in Pt-GDY_1 and Pt-GDY_2 (Figure 5d). The HER catalytic activity of Pt-GDY_2 with four-coordinated Pt atoms of C_2-Pt-Cl_2 is much higher than that of Pt-GDY_1 with five-coordinated C—Pt—Cl_4. The reason is that the Pt-GDY_2 with C_2—Pt—Cl_2 species possessed higher unoccupied 5d densities of states of Pt atoms and near zero Gibbs free energy of H* adsorption (ΔG_{H*}), thereby facilitating the transmission of electrons and the HER progress.[46b] It was also reported that the difference in Ni—C coordination conditions in aNi@DG had a significant impact on the activity of HER and oxygen evolution reaction (OER). Interestingly enough, this phenomenon is different from the catalytic mechanism of traditional metal—N—C catalysts.[56] The linear combination fitting (LCF) analysis of the XANES curve allowed to provide three reasonable typical configurations of aNi@DG (Figure 4e) and projected densities of state (PDOS) (Figure 4f). Obviously, the ideal hexagonal sites or D5775 had a stronger interaction between the substrate and the adsorbate. As shown in Figure 5g, DFT calculations demonstrated that aNi@D5775 possessed the highest HER activity, and its desorption energy was close to Pt.

On the basis of these observations, it can be concluded that XPS, XAFS, and DFT calculations have become indispensable research tools for constructing and optimizing the coordination configuration of SACs. Specifically, XPS analysis is employed to gain insight into the valence states and possible local electronic structure of SACs, while the unraveling of local coordination chemistry by XAFS spectroscopy is in favor of detecting the bonds in SACs and verifying the XPS results. When DFT calculation results are highly consistent with the EXAFS fitting date, the most possible real configuration can be obtained. At the same time, by comparing the XPS results and EXAFS fitting, other coordination configurations can also be excluded.

2.3. Optimizing Mass Loading

As mentioned in the previous sections, the atoms merely exposed on the surface can get involved in the practical catalytic reaction. Notably, excessive loading will cause serious aggregation of single metal atoms. Consequently, the influence of metal loading on the catalytic system must be considered in the design of SACs as heterogeneous catalysts. For example, with the increase of Pt loading, the H_2 evolution activity of Pt/CdS presented an interesting trend: it enhanced significantly first, then decreased rapidly, and subsequently enhanced slowly again.[49] Consequently, the precise control of active metal species loading in SACs is crucial to the catalytic activity as well as stability. In a previous report, Yang's group compared the PHE efficiency of Pt/TiO_2 SAC with different Pt loadings (0.2, 0.5, and 2 wt.%) and TiO_2-PD (pure TiO_2 photodeposited 1 wt.% Pt-NPs).[57] The results showed that the photocatalytic activity was the highest when Pt loading was 0.2 wt.%, and the H_2 production rate can reach 169.6 μmol $h^{-1}g^{-1}$ (**Figure 6**a). Another example is the formation of Pt-NPs when the Pt loading was increased from 1.15 to 1.54 wt.% (Figure 6b), resulting in an obvious decrease in the PHE rate.[58] It is worth noting that the enhancement of metal atoms on HER activity can be proved by calculating the trend of Tafel slope changing with the metal atoms content in SACs.[59] One of the routes for obtaining SACs with different loadings is by controlling the annealing temperature in Ar/H_2 atmosphere, since the heat treatment can substantially influence the defect distribution.[60]

Compared to the particles in the nano-catalysts, the atoms dispersed in SACs provide higher energy and are easier to act as the active centers for enhancing reactivity.[61] However, highly dispersed M-SAs preferred to aggregate into clusters/nanoparticles at high temperatures because of the high surface energy as well as thermodynamic instability. It is still challenging to maximize both the activity and durability of heterogeneous metals.[62] Inspired by the concerns above, Song et al. successfully fabricated Ru/Ni_5P_4 SAC with a Ru loading of 3.83 wt.% via the strong interaction between Ni defect sites and Ru^{3+}.[63] Wan and co-workers reported a cascade anchoring strategy for the synthesis of SACs. First, a chelating agent (glucose) was employed to isolate the metal ions, and then the generated chelated metal complexes were pyrolyzed to protect the metal atoms.[64] Moreover, Uzun et al. anchored Ir-SAs by oxygen-containing groups on reduced graphene aerogel (rGA), obtaining a SAC with ultrahigh Ir loading amount of 14.8 wt.%.[65] The

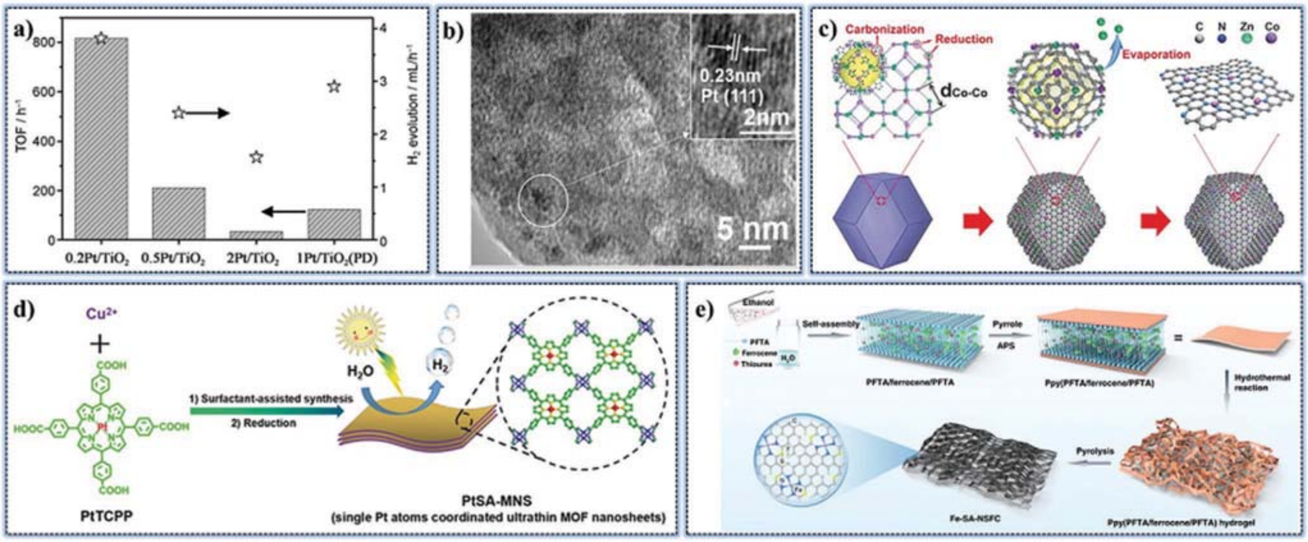

Figure 6. a) Comparison of the H_2 evolution activity and TOFs of different loadings of Pt/TiO_2 under UV/Vis light irradiation. Reproduced with permission.[57] Copyright 2014, Wiley-VCH. b) HRTEM image of Pt nanoparticles with a diameter of ≈4 nm. Reproduced with permission.[58] Copyright 2019, Elsevier Inc. c) Illustration of the preparation approach for the PtSA-MNSs. Reproduced with permission.[70] Copyright 2019, John Wiley and Sons. d) The formation of Co SAs/N-C. Reproduced with permission.[51] Copyright 2016, John Wiley and Sons. e) Illustration of the synthetic route toward the Fe–SA–NSFC. Reproduced with permission.[75] Copyright 2020, Nature Publishing Group.

highlight of this brilliant synthesis strategy was that Ir-SAC was fabricated via the reaction of precursor $Ir(CO)_2(acac)$ with the rGA support, in which $Ir(CO)_2$ species were grafted onto rGA. First, rGA support. Specifically, rGA contained abundant surface oxygen atoms and provided a high surface area (1000 m^2 g^{-1}). These surface oxygen atoms can react with $Ir(CO)_2(acac)$, which was similar to the clean reaction on metal oxides. Very recently, a facile hydrothermal method has been employed to fabricate a Ru SAC containing a high amount of atomic Ru species (7.2 wt.%).[66] In this study, N, S-codoped graphene oxide was prepared as support. The strong coordination interactions between atomic Ru species and support with enriched functional groups induced good sorption and chelation capacities. Furthermore, the migration and aggregation of Ru atoms were well avoided in a mild hydrothermal environment. In another work, a Pt SAC supported on the chemically exfoliated MoS_2 (Pt-SAs/MoS_2, containing 5.1 wt.% Pt) was obtained by the underpotential deposition (UPD) approach.[67] It has been revealed that the interaction between metals and the support is more energetically favorable than metal–metal interaction in the metal bulk during the UPD process. As a result, the growth of Pt-SAs would be automatically controlled to terminate. Such a self-termination offers a promising strategy to rapidly and controllably prepare high-performance SACs with high metal loading.

From the perspective of chemical reaction collision theory, one of the strategies to improve the activity of catalysts is to prepare high-loading SACs, that is, to increase the amount of metal in exchange for high catalytic activity. The difficulty of this strategy is that high concentrations SACs (>2 wt.%) are still prone to serious agglomeration even on strongly polar metal oxide supports.[68] Therefore, it is very important to optimize the design strategies of SACs. The typical methods usually implemented the anchoring of SAs through the post-modification strategy on the synthesized supports, which greatly limited the loading of M-SAs.[69] In this regard, Zhou et al. coordinated the Pt SAs with the porphyrin precursor group, and subsequently assembled them into ultrathin (2.4 ± 0.9 nm) 2D metal–organic framework (MOFs) nanosheets to obtain PtSA-MNSs with ultrahigh Pt loading up to 12 wt.%, as illustrated in Figure 6c.[70] This strategy of introducing M-SAs first and then constructing the support provides a new idea for the preparation of 2D SACs. Besides, zirconium–porphyrinic MOF hollow nanotubes (HNTM) synthesized through a competitive coordination strategy can satisfactorily support a variety of precious metals, including Ir (1.41 wt.%), Pt (2.74 wt.%), Ru (1.92 wt.%), Au (1.18 wt.%), and Pd (3.68 wt.%).[71] Another remarkable preparation approach is to pyrolyze the pre-designed bimetallic Zn/CO MOFs (Figure 6d). After selectively evaporating Zn at a high temperature above 800 °C, the loading of Co-SAs on Ndoped porous carbon can be as high as more than 4 wt.%.[51] Intriguingly, the addition of Zn^{2+} was substituted for a certain proportion of Co^{2+} sites, thereby acting as a fence to extend the distance between adjacent Co atoms.

It is unneglected that the appropriate supports are the key to the fabrication of high-loading SACs as well. MOFs materials have become the ideal choice results from their flexible geometry, size, and function.[72] However, the use of a large number of metal precursors as well as high-temperature pyrolysis still does not strictly prevent metal aggregation, especially when an acid etching process is required to remove nonmetallic species.[73] The greater challenge is how to controllably and uniformly create single active sites on the supports to improve reproducibility.[74] To this end, Feng's group reported a multilayer stabilization strategy to construct ultrahigh loading (up to 16 wt.%) M-SACs (M = Fe, Co, Ru, Ir, and Pt) in N, S, and F codoped graphitized carbon (NSFC).[75] As illustrated in Figure 6e, the authors first restricted the organometallic precursors (OMs) to

© 2022 Wiley-VCH GmbH

perfluorotetradecanoic acid (PFTA) bilayers, and then the final pyrolysis process was conducted after further coating with PPy layers. The migration of OMs during the pyrolysis process was effectively prevented by the confinement of PFTA and PPy, which promoted the coordination of isolated metal atoms with the N atoms in the porous graphitized carbon. Another issue is that the numbers of defects and anchoring ligands usually limit the metal mass loading in the common preparation strategies of SACs. In this regard, substitutionally doping M-SAs into MoS_2 via a spontaneous reduction method is an effective means of avoiding this limitation, obtaining a Ru/np-MoS_2 SAC with high Ru loading amount of approximately 8.0 at %.[76]

According to the above discussion, briefly, the strategies for fabricating SACs with high mass loading and uniformly dispersed active sites are mainly divided into two parties: i) optimizing preparation strategies, for instance, using precursors, hightemperature pyrolysis, and changing the order of SAs introduction; ii) selection of suitable supports, such as with high surface area as well as defects. To be sure, from the point of view of industrialization, "low loading–high reactivity" is certainly one of the main hard indicators for the practical application of SACs due to cost–effectiveness. Nevertheless, it cannot be ignored that "higher loading–higher reactivity" means that the density of catalytic sites will increase by orders of magnitude, which is a key criterion for practical catalytic applications as well. More importantly, SACs with high mass loading are difficult to design, for which researchers need to be considerate enough during synthesis. In the long run, the structure–performance relationship in SACs and the universality of synthetic strategies will surely be greatly developed as a result.

2.4. Doping Heteroatoms into Supports

The catalytic performance and selectivity of SACs are also affected by the coordination environment surrounding active metal sites. Heteroatom doping is a very effective strategy, which can well regulate the coordination chemical environment in SACs to adapt to different catalytic systems. As for HER, heteroatom doping can optimize the thermodynamic hydrogen adsorption/desorption on the catalyst surface via adjusting the electronic configuration of SACs. Typically, in addition to M-SAs participating in the catalytic reaction, the neighboring coordination atoms also play a critical role in catalytic reactions. As shown in **Figure 7**a, the electronic structure of metal sites in SACs can alter with the difference of the binding sites in the first coordination shell around it, which leads to the altering of catalytic performance. This property is similar to the important

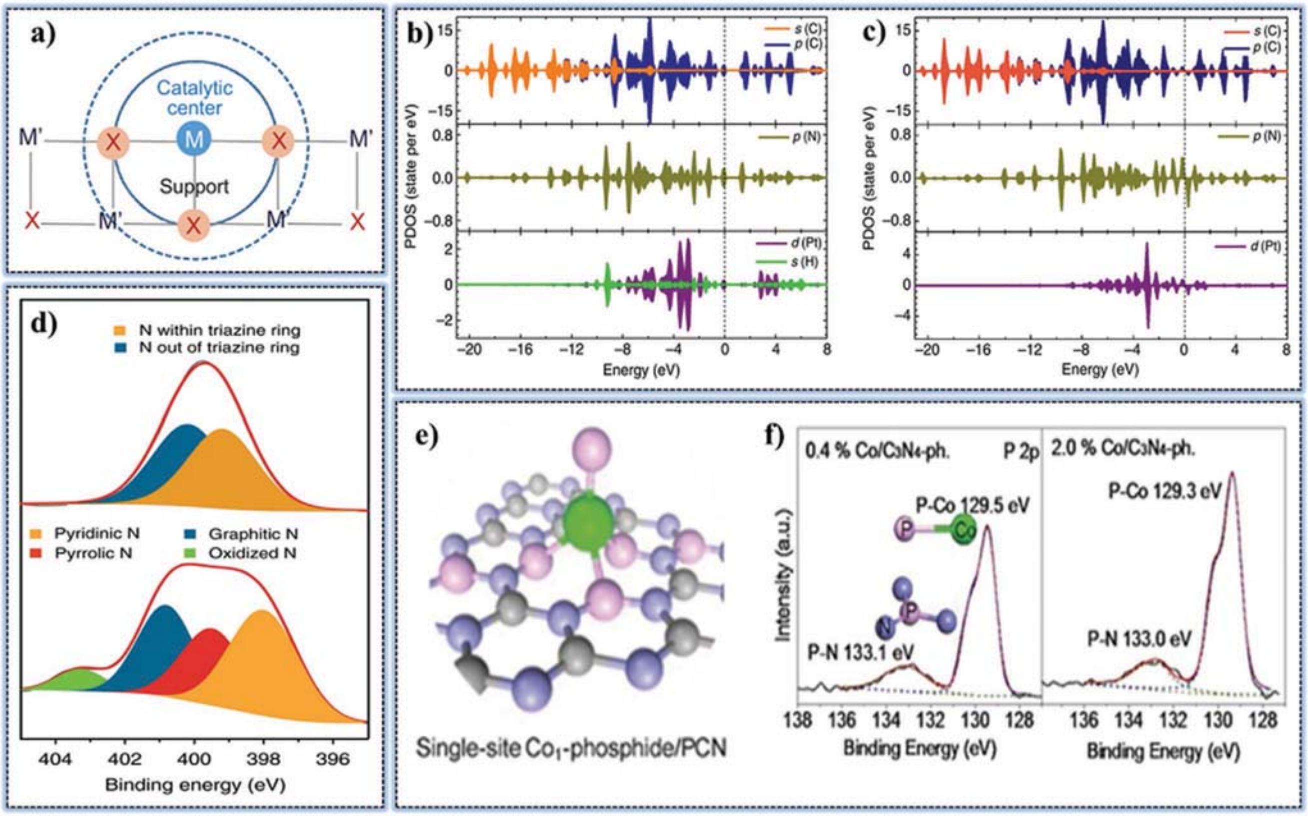

Figure 7. a) Illustration of the first and second coordination shells of atomically dispersed catalysts. Reproduced with permission.[47] Copyright 2018, National Science Review. b,c) pDOS of (b) hydrogen-free and (c) two hydrogen atoms adsorbed on Pt catalysts supported by NGNs with Fermi level shifted to zero. pDOS of graphene, N atom and *d*-orbitals of Pt are shown in the upper, middle, and lower parts of the panel, respectively. Reproduced with permission.[85] Copyright 2016, Nature Publishing Group. d) N 1s spectra of Ru- formaldehyde (top) and Ru-NC-700 (bottom). Reproduced with permission.[86c] Copyright 2019, Nature Publishing Group. e) P_{2p} XPS spectra of Co_1-phosphorus/PCN samples. f) Schematic diagram of the structure of Co_1-phosphorus/PCN. Reproduced with permission.[55b] Copyright 2017, John Wiley and Sons.

role of ligands in homogeneous catalysts. In addition, the metal cations on the support can easily become the second coordination shell and get involved in the catalytic reaction together with the primary catalytic metal atoms.[47] The modulation of the local coordination environment around M-SAs is of great significance to the enhancement of the catalytic performance and stability toward H_2 evolution.

Currently, catalysts mainly rely on transition or noble metals, utilizing their special *d*-orbitals to bond with substrate molecules for the formation of transition states with lower energy barriers. For non-metals, it is generally believed that they have no empty orbits and are difficult to participate in the catalytic process. In fact, the p-block elements lacking electronic flexibility and tend to certain oxidation states may endow the prepared catalysts with attractive stability and adjustability.[77] The light p-block with natural abundance and low toxicity, such as carbon, oxygen, nitrogen, sulfur, or phosphorus, are ideal candidates for the fabrication of heteroatom-doped catalysts. Introducing heteroatoms (such as N, S, P) into the supports has been proved an efficient strategy for regulating the coordination environment. On the one hand, heteroatom-doping sites can be employed as coordination centers to stabilize metal atoms. On the other hand, the atomic radius and electronegativity of heteroatoms can be also used to adjust the electronic structure of metal atoms.[78] Especially for carbon-based supports, heteroatom dopants can remedy their lack of suitable sites to form strong MSI. For example, graphitic carbon nitride (g-C_3N_4) treated by phosphating can promote the separation of photogenerated carriers,[79] and the electron density of the Pd-SAs anchored on the C_3N_4 support was substantially depleted by the coordination N atom.[80] Since the difference in position and bonding state, the types of heteroatoms are also different. For example, N dopants are divided into pyridinic-N, pyrrolic-N, graphitic-N, quaternary-N, sp-N, oxidized-N and quaternaryN,[81] and S dopants are divided into thiophene-S as well as oxidized-S.[82]

It has been reported that the functionality of carbon support can be changed via N atoms doping. In the meantime, the N atom is one of the most widely used ligand dopants at present, which can help to solve the problem that the weak bonding between Mo_2C and metal atoms leads to the latter being prone to irreversible agglomeration during the synthesis, as well as the dissolution loss in the catalytic process.[83] Ru-SAs could be well dispersed on N-doped Mo_2C nanosheets via an anti-Ostwald ripening strategy. The surface digging effect produced by N-doping further prevented the aggregation of Ru-SAs.[84] For N-doped carbon supports, since the electronegativity of N atoms is higher than that of C atoms, more electrons can be obtained. This negative charge transfer induced by the N dopants can be the main reason accounting for the decrease of the electron accumulation on the H atoms and thus the reduction of ΔG_{H*}. Sun and co-workers modified graphene nanosheets with N-doping (NGNs) to support Pt-SAs.[85] Partial density of states (pDOS) and Bader charge analysis illustrated that Ndoping atoms caused the charge transfer between Pt atoms and the support, and, consequently, the chemical bonding of Pt and NGNs resulted in unique electronic properties of Pt-SAs (Figure 7b,c). At the same time, the Pt-SAs adsorbed on the NGNs still had a positive charge and the N atoms obtained electrons, which suggested that these Pt-SAs contained more unoccupied 5*d* density of states. In this case, the H atom would interact strongly with the Pt atoms, resulting in electron pairing and hydride formation.[85] In the Ru and N codoped carbon nanowires (Ru-NC) obtained by high-temperature pyrolysis using Te nanowires as sacrificial templates, N existed in the carbon substrate in four forms, that is, pyridinic-, pyrrolic-, graphitic-, and oxidized-N (Figure 7d).[86] The total N content in Ru-NC decreased with the reduction of pyrolysis temperature. First-principles calculations speculated that the active site of HER was probably the atomic Ru centers (RuC_xN_y) related to the coordination of N and C. In other words, the formation of RuC_2N_2 molecules was the key to the high catalytic activity. Notably, Ru and adjacent C atoms were possible active sites.[86c] Of particular note is that N plays a critical role in the formation of catalytic active sites, and the N-doping level is significantly affected by doping temperature. According to a report, a doping temperature above 550 °C was a necessary condition for inducing Co-NG SAC to form Co—N active sites.[16a]

The reported P-doped SACs are mainly applied in various hydrogenation,[16i,87] photocatalytic,[55b] and electrocatalytic reactions.[88] P-doped SACs for H_2 evolution are rarely reported compared to the doping of N and S heteroatoms. Generally speaking, pure carbon-based supports have low electrochemical activity, which is unfavorable for H_2 generation. Among carbon-based supports, such as typical g-C_3N_4, the introduction of P can dramatically enhance their delocalized p bonds to improve conductivity.[89] Wei's group changed the coordination environment of Co-SAs on g-C_3N_4 through a facile phosphidation method (denoted as Co_1phosphide/PCN).[55b] XPS results in Figure 7e showed that there were two peaks in Co_1-phosphide/PCN, which can represent the characteristic of phosphide species (129.5 eV) and P—N coordination (133.1 eV). It means that partial P atoms may substitute the C atoms in the triazine rings to form P—N bonds in the g-C_3N_4 framework. The formation of the isolated Co_1—P_4 structure was confirmed by XANES spectra (Figure 7f). Remarkably, the PHE activity of the Co_1-phosphide/PCN sample was 274 times higher than before phosphating.

In addition, multicomponent heteroatoms codoping also has great potential to boost H_2 evolution catalytic activity. For example, isolated Ru SAs could be stabilized on 2D titanium carbide MXene ($Ti_3C_2T_x$) support by forming Ru—N and Ru—S bonds with N and S atoms, respectively.[90] It was demonstrated through the control experiment that the catalytic properties of MXene doped with both S and N atoms were higher compared to single component doping. This is reasonable because the strong electronegativity and varying atomic radii of N and S atoms allow them to form two different binding sites with single Ru atoms. In this case, the HER process, which occurs at the interface between this Ru-MXene SAC and electrolyte, can be more effective. Although S and N are both p-block elements, the larger atomic radius and lower electronegativity of the S atoms can spontaneously create defects on the carbon supports and alter the electronic structure of the active sites.[91] In another report on Mo-based SACs, the introduction of S atoms as a dopant into N-doped carbon could further control the electron density distribution of the support, which is conducive to H_2 generation.[92] Specifically, on the one hand, S/N codoping caused tensile strain to the carbon supports and

© 2022 Wiley-VCH GmbH

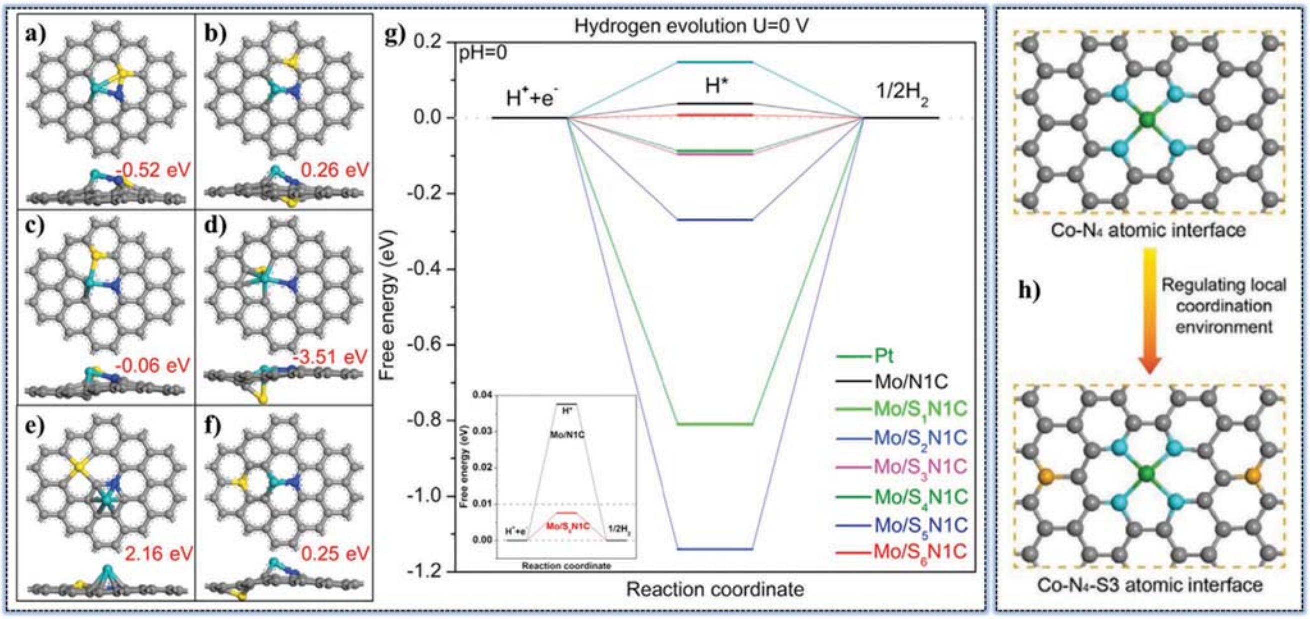

Figure 8. The optimized six different S and N codoped carbon structures and formation energies of a) Mo/S_1N1C, b) Mo/S_2N1C, c) Mo/S_3N1C, d) Mo/S_4N1C, e) Mo/S_5N1C, and f) Mo/S_6N1C. Grey sphere: C, blue sphere: N, cyan sphere: Mo, yellow sphere: S. g) Calculated Free energy versus the reaction coordinates of different S and N codoped carbon supported Mo SAs electrocatalysts at a potential U = 0. The inset indicates the significant difference in free energy between Mo/S_1N1C and Mo/S_6N1C. Reproduced with permission.[92] Copyright 2019, Elsevier Inc. h) Optimized configuration of Co—N_4 and Co—N_4—S_3 atomic interface models. Reproduced with permission.[93] Copyright 2020, John Wiley and Sons.

simultaneously reduced ΔG_{H^*}. On the other hand, the relatively high electronegativity of S and N atoms would also increase the negative charge on adjacent C atoms, leading to the increase of charge on H atoms, and at the same time reducing the bonding strength of Mo atoms and hydrogen bonds.[92] Besides, the binding energy of Mo SAs on this S and N codoped carbon support was quite high, which could well prevent the aggregation of Mo atoms (**Figure 8**a–g). A similar phenomenon was observed on Ru/GO SAC with N, S codoping, in which the dual-coordinated interactions with the Ru—S and Ru—N bonds accelerated the HER kinetics.[66]

Subsequent research further unraveled the dynamic evolution of heteroatoms in the coordination environment. The Multifunctional SAC fabricated by anchoring CoSAs on S/N codoped hollow carbon spheres (N, S-HCS) showed outstanding electrocatalytic activity for ORR, OER, and HER.[93] It was suggested by both experimental characterizations and theoretical calculations that the main reasons for the high activity of the SACs (Figure 8h): i) Co—N_4 sites formed by the coordination of Co atoms with neighboring N atoms; ii) the optimization of the local coordination environment of the active sites owing to S with weaker electronegativity; and iii) the synergistic effect among carbon support, metal atoms and heteroatoms. It is important to highlight that the pivotal atom ratio of N/S is ordinarily constant and difficult to modify. Generally, it is necessary to optimize the synthesis process to better N, S codoping.

2.5. Understanding and Utilizing Metal–Support Interaction

As a special type of supported metal catalyst, the active metal species in SACs are completely dispersed into isolated SAs through chemical bonding with surrounding atoms from the support.[43b] On the one hand, supports are not only employed to disperse and stabilize metals, but also interact with metals, thereby influencing the catalytic activity and selectivity.[94] Notably, the common characteristic of the active sites in the heterogeneous catalytic reaction is the direct contact between interfacial atoms and supports, as well as the generation of interaction.[95] As a result, how to rationally construct the metal–support interface determines whether there can be a significant breakthrough in H_2 evolution efficiency.[96] On the other hand, after the charge transfer caused by the interaction between M-SAs and anchor sites of the support, all the M-SAs as the active centers are partially charged.[97] A representative example, as shown in **Figure 9**, is the strong coordination interaction between the lone pair electrons of N and the *d*-orbital of Ru atom to ensure that Ru-SAs are confined in the voids of MOFs.[98] The easy-to-adjust electronic structure of SACs offers controllability for the selection of ideal catalytic pathways.[99]

The change in the electronic state of the active center atoms usually causes a change in the adsorption state of the reaction substrate, which is also the reason for the high catalytic activity of SACs. It is worth noting that the surface free energy of metal species increases sharply when they are reduced to subnanometer or even atomic scale. Isolated metal atoms with ultra-high surface energy always tend to aggregate into nanoparticles.[100] Therefore, it is necessary to suppress the aggregation of dispersed M-SAs by the MSI. Interestingly, recent studies have found that SACs have low or no activity in certain reactions.[101] The latest research showed that the interaction between metal substrates and the support during the reaction not only affected the catalytic activity by modulating the geometric and electronic characteristics of the metal species, but also promoted the reaction.[102]

© 2022 Wiley-VCH GmbH

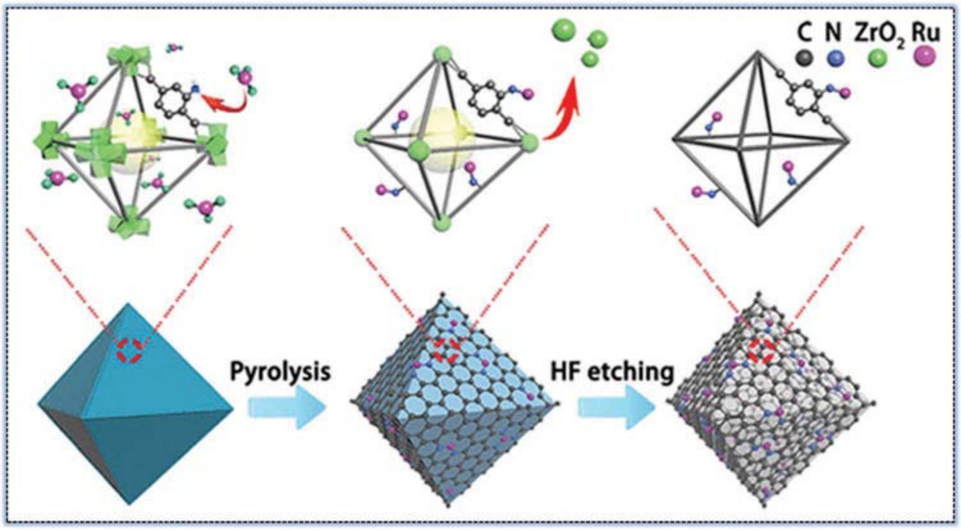

Figure 9. Scheme of the proposed formation mechanisms for Ru SAs/N—C. Reproduced with permission.[98] Copyright 2017, American Chemistry Society.

2.5.1. Strong Metal–Support Interaction

Although it is generally accepted that the as-mentioned properties of the support materials are crucial in catalytic systems, how to control the interaction between metal atoms and the support to design the optimal composition and geometry of the metal sites is still quite challenging.[103] Especially for heterogeneous metal oxide supported catalysts, the mechanisms of support on the reaction activity include the stability of metal atoms, charge transfer properties,[12d,104] direct participation in catalytic reaction,[103a,105] and oxide encapsulation.[94,106] Previous studies showed that the catalytic activity of noble metal particles supported by reducible oxides was greatly improved after high-temperature H_2 treatment. Tauster et al. designated this mechanism for regulating the catalytic performance of active sites as "SMSI".[94] Nevertheless, there are two major challenges in adjusting the reactivity of heterogeneous metal catalysts through SMSI encapsulation state: i) it is difficult to find an intermediate configuration that allows the oxide overlayer to fully interact with most of the exposed active sites;[107] ii) whether SAs and NPs can show similar or even the same SMSI state. The reversible suppression of CO adsorption observed on the Pt/TiO_2 (where Pt-SAs and Pt-NPs coexistence) catalyst helped to unravel the typical SMSI effect in the SACs system.[108] As shown in the in situ DRIFT spectra (**Figure 10**a,b), due to the encapsulation state of Pt-NPs by the TiO_x layer, Pt-NPs lost their CO adsorption strength after reduction at 250 °C, indicating the appearance of SMSI. Pt-SAs and Pt-NPs have common SMSI characteristics such as chemical adsorption and charge transfer. The difference is that, notwithstanding, SMSI occurred between Pt-SAs species and TiO_2 support only after reduction treatment at 600 °C, and the CO adsorption strength could be recovered after oxidation treatment. According to the Low-energy ion scattering (LEIS), different from the physical encapsulation of Pt-NPs by TiO_2 overlayer, single Pt atoms on the surface were neither embedded in the support nor encapsulated. Theoretical calculations further explained that the essence of this difference is that the Pt 18-electron coordination saturated configuration inhibited the CO adsorption of Pt atoms (Figure 10c,d). Briefly, the selective encapsulating of Pt-NPs proved that Pt-SAs provided the main active sites. One of the significant strategies to improve both the reactivity and selectivity of SACs is to solve the structural problem of SMSI overlayer poisoning or collapse during the catalytic reaction.[109]

2.5.2. Electronic Metal–Support Interaction

Further, modulating d-band structure of supported catalysts by the electron transfer can enhance the adsorption of reaction intermediates, decreasing the energy barrier. The "EMSI" induced by this charge transfer is considered to be a superior explanation for the enhancement mechanism of supported catalysts than SMSI.[12d,110] In supported metal nanocatalysts with non-uniform atomic coordination sites, the charge of the support only greatly influences a couple of atomic layers at the metal–support interface.[95,111] Hence, the charge interaction between metal species and the support in SACs, by contrast, is much stronger.[112] Moreover, due to the interference of intrinsic metal effects, including the electronic quantum size effect[12d,104] and structure–sensitivity geometrical effect,[113] it is quite difficult to accurately identify the electronic state of metal particles or clusters. Fortunately, spatially uniform SACs provide an ideal catalytic model for solving the above problems. In turn, the EMSI effect can inhibit the migration of single metal species.

Recently, there are many studies have reported the application of EMSI in hydrogen evolution SACs, for instance, Ni-doped np-G,[114] Pd_1/Co_3O_4,[115] and $Mo_1N_1C_2$.[116] Bao et al. have found that the introduction of Pt-SAs into MoS_2 nanosheets would lead to new electronic states of Pt-MoS_2.[40] As shown in **Figure 11**a, the increase in the electronic state near the Fermi level confirmed the EMSI occurring at the Pt-MoS_2 interface. In other words, the prominent feature of EMSIS is to regulate the d-band centers of active metal sites via the charge transfer between supports and metal atoms.[117] A typical example is that

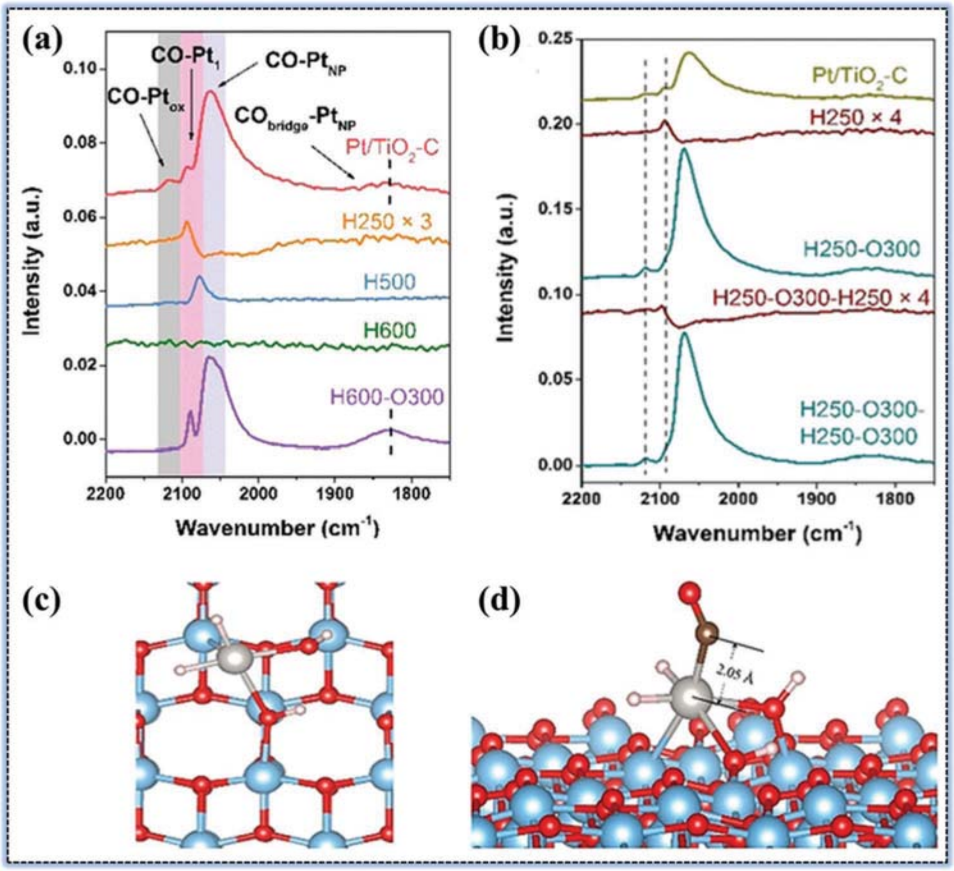

Figure 10. a) In situ CO-DRIFT spectra of Pt/TiO$_2$ after He purging at room temperature. b) Pt/TiO$_2$-C for two redox cycles. Optimized structures obtained from Born–Oppenheimer molecule simulations. c) Top view of (Pt(OH)$_2$(H)$_2$(Ti))-Ti$_{23}$O$_{47}$ and d) side view of (Pt(OH)$_2$(H)$_2$(Ti)(CO))-Ti$_{23}$O$_{47}$. White, brown, red, blue, and silver spheres represent H, C, O, Ti, and Pt. Reproduced with permission.[108] Copyright 2020, Wiley-VCH.

Pt-SAs supported on mesoporous carbon (MC) had a positive charge (+0.270 eV) as well as unoccupied 5d densities of states on a single vacancy, which is critical for HER.[16d] The strong interaction of the 5*d* orbital of Pt-SAs and the highest unoccupied electronic state both indicated the strong EMSI between Pt-SAs and the support (Figure 11b). Subsequent research by Lu et al. confirmed this.[115] They manipulate the unoccupied 5d state of Pt-SAs on Co$_3$O$_4$ through EMSI, which weakened the adsorption of ammonia borane and hydrogen molecules on Pt-SAs to a certain extent. Such an EMSI remarkably enhanced the hydrogen production activity of the SACs. A similar phenomenon has already been observed by Chen's group.[112] They revealed that the electron density around the metal sites could be redistributed when the electronic structure of SAC was tuned by EMSI, which promoted the electron transfer from the metal active sites to the reactants. More intriguingly, EMSI may exhibit differentiated effects on the electrons on diverse orbitals.[85] A similar result is that Pt atoms affect not just the neighboring atoms, they also impact the second and third coordination shells (Figure 11c,d).[118] Since the EMSI effect can greatly disperse and stabilize metal atoms, while significantly adjusting the electronic structure of metal atoms as well as the adsorption energy of intermediate species, EMSI has been extremely crucial in the rational design of catalysts at the atomic level.

The MSI is employed to stabilize the metal atoms on the support and control the coordination structure of SACs.[119] An in-depth study of the difference in electron transfer and adsorption/desorption behavior among different coordination configurations provides valuable insights into the stability of SAs and the superiority of catalytic activity. First-principles calculations can help us find potential SAs active sites, or suitable supports which can introduce active metal centers.[120] First of all, starting from the atomic structure and electronic properties of the supports, the most stable configuration and anchor sites can be calculated. Second, the aggregation induced by excessive surface free energy can be avoided through calculating the cohesive energy and bonding strength of metal atoms. Furthermore, both the electronic conductivity with the substrates and the metallic state of M-SAs can be demonstrated via calculating the total density of states (DOS) of SACs and pristine supports. By combining in situ or operando characterizations to construct the optimized adsorption energy of possible H adsorption sites, the contribution of M-SAs can be better revealed to the catalytic reaction. Especially regarding the characterization techniques of oxidation state, such as XPS and XAFS, are powerful tools to understand the reaction mechanism, because the oxidation state of M-SAs is directly affected by EMSI.

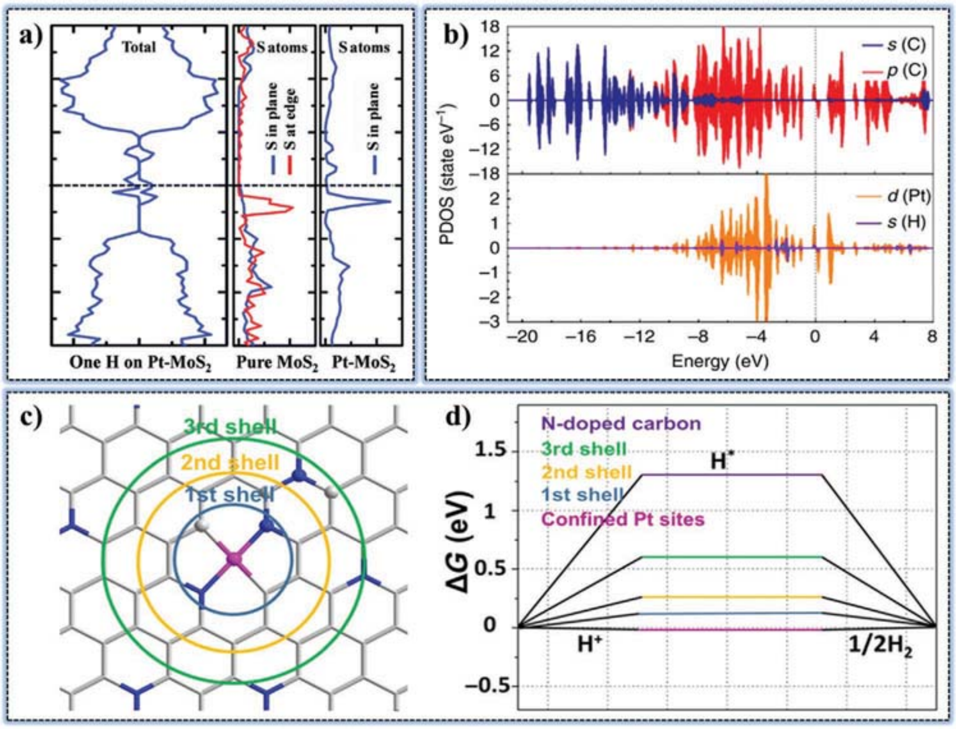

Figure 11. a) Total DOS for one H absorbed on Pt-MoS$_2$, and projected DOS of in-plane and edge sulfur atoms from pure MoS$_2$ and Pt-MoS$_2$. Reproduced with permission.[40] Copyright 2015, Royal Society of Chemistry. b) PDOS of H absorbed on a Pt SA of Pt$_1$/MC. Reproduced with permission.[16d] Copyright 2017, Nature Publishing Group. c) Schematic diagram for the coordination shells for the Pt SAs over the graphene. d) ΔG_{H^*} on pure and Pt-supported graphene in different coordination shells. Reproduced with permission.[118] Copyright 2018, American Association for the Advancement of Science.

3. Interface Engineering of SACs with Different Supports toward H$_2$ Evolution

It must be pointed out it is unreasonable to simply discuss the performance of SACs without combining SAs with supports. As mentioned in the above sections, SAs exhibit excellent catalytic activity by coordinating with their surrounding species. Correspondingly, the HER activity of SACs is closely related to both the composition and properties of the support. In heterogeneous catalysts, the interfacial effect caused by the strong bonding or interactions between two different active components will lead to the reconstruction of active sites.[121] The catalytic performance of such reconstructed active sites far surpasses that of individual components.

The metal–support interface at the atomic scale certainly brings astonishing catalytic performance. Due to the synergistic effect between SA and support, it is of great significance to deeply and comprehensively explore the electronic and geometric effects of supports for both the bonding strength and coordination properties of the metal–support interface. To date, a plethora of experimental and theoretical works have demonstrated that metal oxides, transition metal (TM) compounds, and carbon-base materials can be used as suitable supports to stabilize SAs for H$_2$ production. Based on these great breakthroughs in the design and exploitation, we will comprehensively present the design strategies of M-SAs species stabilized on diverse supports in this section. To help better understand the correlation between geometric structure and electronic structure, as well as their impact on the H$_2$ evolution process, particular attention will be paid to the discussion of electronic regulation, and the relationship between structure and intrinsic activities. It should be pointed out here that we do not simply summarize the synthesis methods of H$_2$ evolution SACs in various reactions, but do attempt to achieve rational designs through the MSIs during specific catalytic reactions.

3.1. Interactions of Metal–Metal Oxide Supports

Among various types of SAC supports, oxide materials have attracted wide attention. Besides the high surface area, oxide supports surface contains abundant oxygen vacancies (O-vacancies, O$_{vac}$) and ·OH groups that can be used as ligands to coordinate with lone pair electrons of oxygen atoms.[21] Particularly, the presence of these O-vacancies can tune the electronic structure of metal species.[122] It can be confirmed that the M-SAs on suitable oxide supports are dispersed and firmly anchored because of the stronger metal–oxide bonding than metal–metal bonding.[109,119b] According to reports, there are currently three main strategies for stabilizing M-SAs on the oxide supports: i) confined to the porous structures or attached to the structural defects; ii) coordinated with surface functional groups (such as O^{2-} or OH$^-$) or metal cations; iii) confined in the surface or lattice of the oxide supports by MSI.[45,123] In the following discussion, we would like to reveal the MSIs that occurred in the SACs supported by metal oxide materials during H$_2$ production reaction.

3.1.1. TiO_2-Supported SACs

TiO_2, especially anatase- and rutile-phase TiO_2, is the most widely studied semiconductor material owing to its good electronic band structure. Traditional TiO_2-based catalysts usually support noble metals. Assembling noble metal nanoparticles on the TiO_2 surface can form a Schottky junction at the interface, thereby inhibiting the recombination of photo-generated electrons and holes in TiO_2 to boost the PHE activity.[124] TiO_2 has been proved to be a suitable support for photochemical applications of SACs as well. Yang's group found that compared with Pt-NPs, Pt-SAs on the TiO_2 surface contribute much more to the activity of photocatalytic H_2 evolution.[125] After metallic Pt_0 nanoparticles were removed by the NaCN leaching method ($2Pt \rightarrow 2[Pt(CN)_4]^{2-}$), there were commonly only extremely small clusters such as single Pt atoms or dimers remain on TiO_2(101). The PHE activity, however, was almost unaffected. In addition, single Pt atoms preferred to bond with two surface two-coordinated O_{2c} (**Figure 12**a), and Bader charge analysis showed that single Pt atoms was in the oxidation state (denoted as $Pt^{\delta+}$ with $\delta = 0.16$). The above results suggested that the oxidation state $Pt^{\delta+}$ on the TiO_2 surface were the real catalytic active center. Subsequently, they further constructed a catalytic model for which isolated metal atoms (Pt, Pd, Rh, or Ru) are anchored on TiO_2.[57] It is not feasible to separate atomically dispersed Pt sites by adsorption method or to introduce additional oxygen atoms to stabilize Pt atoms. The reason is that the former needs to expose a large amount of lattice oxygen coordination environment for anchoring, whereas Pt—O sites of the latter are easily dissociated by hydrogen molecules to form Pt—H bonded lattice OH species.

The dynamic step structure allows Pt-SAs to be doped at the specific step edges of TiO_2 (Figure 12b), where the Pt atoms are in the oxidation state $Pt^{\delta+}$ ($\delta = 1.50$), representing the catalytically real active site.[57] Recently, much attention has been paid to the study of anchoring SAs at the surface defects of hydrothermally grown anatase sheets with large (001) faces.[60a,126] Two main disadvantages of this kind of thin sheet can be overcome by controlling the annealing parameter (defects control): i) it is easy to be fluoride-terminated after hydrothermal synthesis and ii) it will deform at a very low sintering temperature.[60a,127] On the one hand, Pt-SAs could promote the generation of surface O-vacancy sites in neighboring TiO_2 units, thereby forming $Pt—O—Ti^{3+}$ atomic interface. This interface could effectively facilitate the photogenerated electrons transfer from Ti^{3+} defect sites to Pt-SAs, thus promoting the separation of electron–hole pairs.[48] On the other hand, the annealing parameter control can effectively adjust the defect density of Ti^{3+} centers located in the regular lattice position and Ti^{3+} exposed on the surface, to optimize the PHE activity.[60a,128] Another alternative strategy to improve the hydrogen evolution activity of Pt/TiO_2 SAC was to construct TiO_2 nanocrystals with (001) and (101) crystal planes exposed in an appropriate proportion (Figure 12c). The selective anchoring of Pt-SAs on the (101) plane could further enhance the "surface heterojunction" effect between the (001) and (101) planes.[129] According to the reports, Pt-SAs would coordinate with its trap environment (i.e., oxygen atoms on the oxide surface) to form a Pt^{4+} state.[130] This result proved the strong Pt atom—TiO_2 support interaction induced by the covalent bonding. Furthermore, DFT calculation provided a reliable model for designing suitable binding sites to stabilize non-noble metal atoms on TiO_2 anatase (101) surface.

The TM atoms anchored in TiO_2 have great application potential as well. Hyeon et al. predicted the electronic structure of Cu/TiO_2 single-atom photocatalyst through DFT calculations.[131] They thoroughly revealed that Cu-SAs acted as oxidative redox-active metal cofactors could reversibly regulate the local TiO_2 lattice during the process of dynamic photocatalysis (**Figure 13**a). Specifically, the photoexcited electron localized into the Cu $d_z{}^2$ state altered the valence state of the Cu atom after photo-excitation (Figure 13b). To balance the surface charge, an extra proton requires to be adsorbed on the surface (Figure 13c). The photogenerated electrons on pure TiO_2 surface in the absence of Cu redox sites remained delocalized in the conduction band (CB) rather than at the metal sites (Figure 13d). More interestingly, the lattice distortion near TiO_2 induced by Cu $d_z{}^2$ state with an axial antibonding character immobilized the localized electron at Cu, where the backside oxygen coordination was elongated from 1.959 to 2.113 Å (Figure 13e). These results suggested the fundamental similarities of the atomic-level cooperative effect with metalloenzymes and homogeneous catalysis, which was usually disregarded in heterogeneous catalysis systems. A modified wrap-bake-peel process used in this study designed a type of MT/TiO_2 (MT = Co, Fe, Ni, Cu, and Rh) SACs with special positions (Figure 13f). The order of hydrogen production performance of these single-atom metal catalysts was Cu > Rh> Co > Ni > Fe. Interestingly, this experimental result was different from the report of the Yao's group.[132] It may

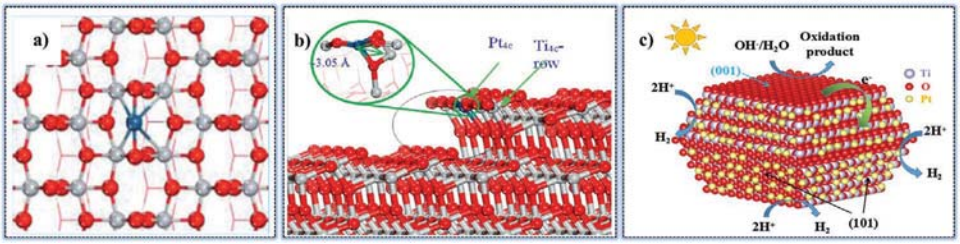

Figure 12. a) The optimized structure of single Pt atom on TiO_2 surface. Reproduced with permission.[125] Copyright 2013, RSC Publishing. b) Pt doping at the specific step-edge represented by the (302) vicinal surface consisting (100) surface and (101) surface. Pt_{4c} represents that a Ti_{4c} is replaced by a Pt atom. Reproduced with permission.[57] Copyright 2014, John Wiley and Sons. c) The model of single Pt atoms selectively dispersed on the (101) facets of TiO_2 Crystals. Reproduced with permission.[126b] Copyright 2017, Elsevier Inc.

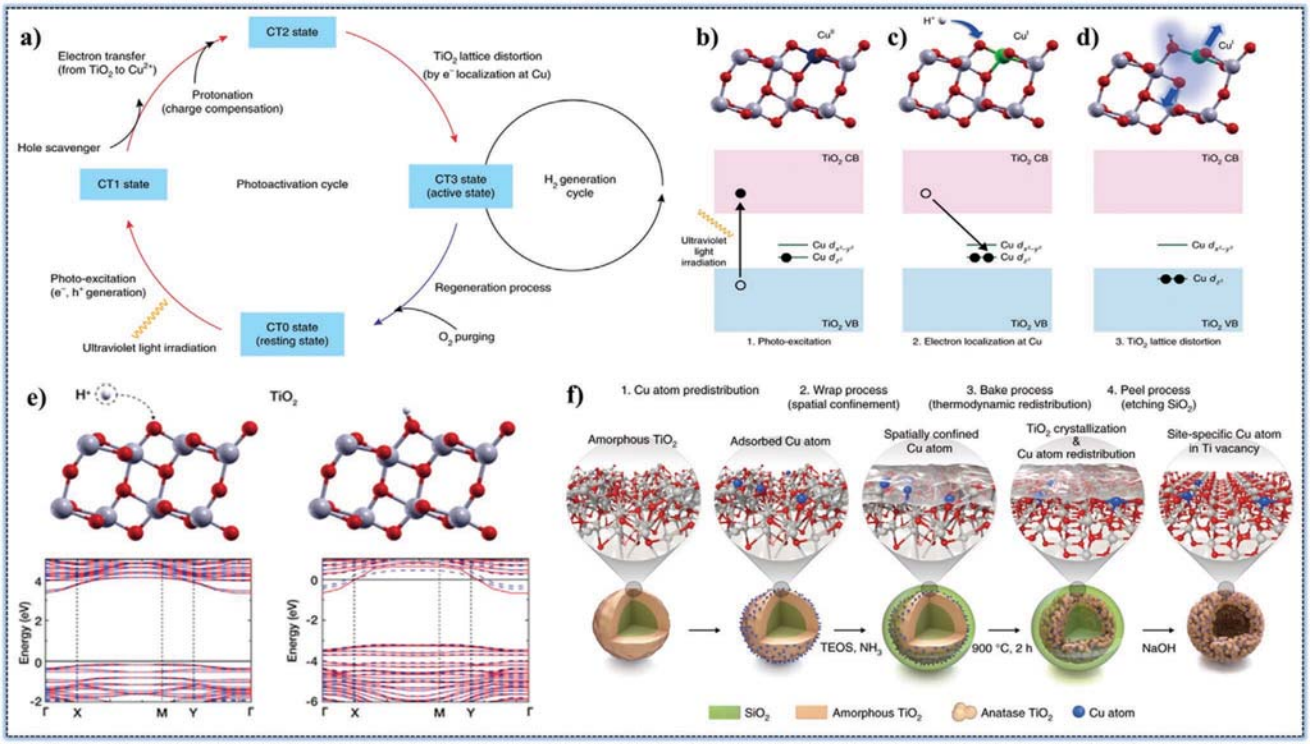

Figure 13. a) Illustration of Cu/TiO$_2$ in various states of photoactivation cycle. CT0: resting state; CT1: photoexcited state; CT2: valence change of the redox-active Cu-SAs; CT3: active state. Schematic illustrations of the photo-excitation process of b) photo-electron formation, c) its localization to Cu d_{z^2} antibonding state with surface protonation, and d) local structural distortion. The top panels show the DFT-optimized structure for each procedure. VB, valence band; CB, conduction band. e) DFT-optimized structures and band structures of TiO$_2$ surfaces in a pristine state (left) and modified with an additional electron and a surface proton (right). The additional electron is delocalized at the CB of the TiO$_2$ surface, which significantly elevates the Fermi level. f) Schematic diagram of Cu/TiO$_2$ SACs synthesized by modified wrap-bake-peel process. Reproduced with permission.[131] Copyright 2019, Nature Publishing Group.

be ascribed to the difference in potential at support crystal sites induced by different synthesis approaches. The change of potential would lead to charge-transfer modification, which affected the catalytic performance.

3.1.2. FeO$_x$-Supported SACs

Iron oxide, as a 3d-metal-based support with abundant oxygen coordination, is a kind of representative material for stabilizing M-SAs. Nevertheless, surface OH groups and the uncertainty of iron oxide composition are influential in the stability, which poses a challenge to accurately anchoring M-SAs. Besides, owing to the redox properties of iron oxides, different reaction conditions and the introduction of single metal atoms can easily change the activity of the oxides. In Ir$_1$/FeO$_x$ SAC, the introduction of Ir-SAs significantly decreased the reduction temperature of FeO$_x$ support, thereby greatly promoting the reduction of FeO$_x$. As a result, abundant oxygen vacancies were further generated, which provided sites for reactive oxygen species and the H$_2$O dissociation to produce hydrogen.[53a] According to the report, Ir-SAs stabilized in the form of Ir—O—Fe played a leading role during the catalytic hydrogen generation reaction. Recently, Li and co-workers reported an Ir$_1$/FeO$_x$ SAC with "dual-metal sites" for WGSR.[123] The investigation by the combination of a theoretical and experimental study that the O atoms bonding with Fe species can be abstracted from the FeO$_x$ support by CO during WGSR, and then generate O-vacancies and promote the conversion of Fe^{3+} to Fe^{2+} (**Figure 14**a). When Ir$_1$/FeO$_x$ with O-vacancies was used for WGSR (Figure 14b), the oxidation state of Ir$_1$-SAs and surrounding Fe sites (denoted as Fe$^{(a)}$) would change from Fe^{3+}—O···Ir^{2+}—O$_{vac}$ to Fe^{2+}—O$_{vac}$···Ir^{3+}—O. As shown in Figure 14c, Ir$_1$-SAs in FeO$_x$ with O$_{vac}$ occupy exactly the positions of Fe atoms. The above results suggest that the O$_{vac}$ near the Ir$_1$-SAs on the FeO$_x$ surface is the key to the formation of the dual-metal sites. This is similar to the results of their previous study.[53a] Such a dual-metal site composed of Ir$_1$ and neighboring Fe atom synergistically promoted the production of H$_2$.

The primitive rhombohedral unit cell of Fe$_2$O$_3$ with a magnetic configuration of (+ − − +) proved to be the most advantageous magnetic configuration of α-Fe$_2$O$_3$ in terms of energy, which can be employed to construct surface slab.[133] Based on this, choosing the O$_3$-terminated surface of Fe$_2$O$_3$ (001) can better stabilize Ir-SAs, in which each Ir atom coordinated with the third layer of Fe atoms below and three surface oxygen atoms (i.e., O$_3$) (Figure 14d), meaning that Ir atoms substituted the Fe atoms on the O$_3$-terminated surface.[123] It has been reported that CO adsorption in WGS could be weakened by reducing the size of the Pd species to increase the ratio of the

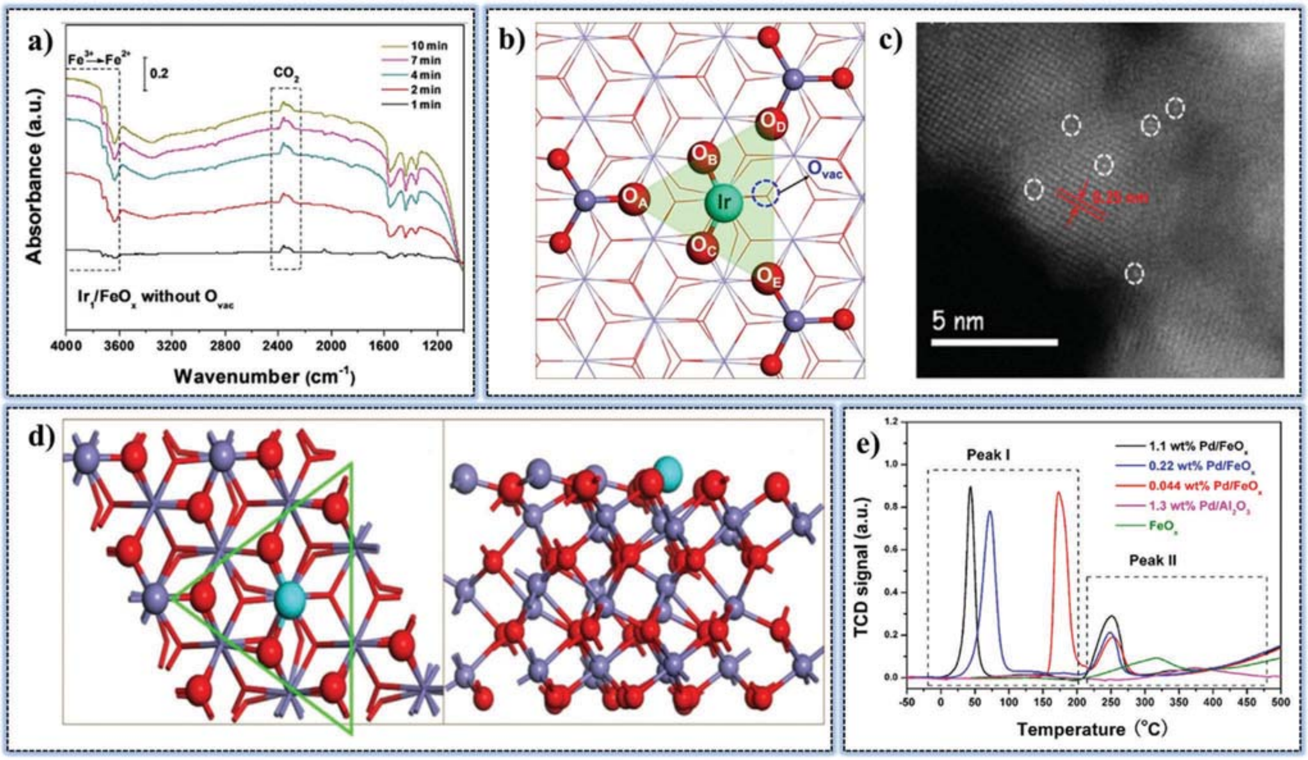

Figure 14. a) In situ DRIFTS spectra of Ir_1/FeO_x samples with O_{vac} during WGSR. b) Illustration of the dual-metal sites ($Fe^{(a)}$ and Ir_1) and two intermediates (ii and ii-a) during the redox process on Ir_1/FeO_x for WGSR. c) HAADF-STEM images of Ir_1/FeO_x with O_{vac}. Reproduced with permission.[123] Copyright 2020, John Wiley and Sons. d) Model of Ir_1/FeO_x with O-vacancy from top view (left) and side view (right), where the O atoms are positioned at a triangle on the surface of Ir_1/FeO_x SAC. Blue: Ir SA; Purple: Fe atom; Red: O atom. Reproduced with permission.[123] Copyright 2019, John Wiley and Sons. e) H_2-TPR profiles of FeOx, Pd/Al_2O_3, and Pd/FeO_x SAC with different Pd loadings. Reproduced with permission.[135] Copyright 2017, American Institute of Chemical Engineers.

onefold adsorption mode of CO at Pb sites.[134] The influence of Pb-SAs on the formation of oxygen vacancies on FeO_x can be evaluated by H_2-TPR experiments (Figure 14e).[135] The main reason may be that the reduction temperature of the catalyst decreased with the addition of Pd, as well as the spillover effect of hydrogen from the metal to the support.[136] Moreover, the H_2 consumption ratio of 0.044 wt.% FeO_x/Pd is about 22 times higher than that of 1.1 wt.% FeO_x/Pd, indicating that Pd-SAs promoted the formation of O-vacancies. The H_2 consumption amounts of PdO reduction to Pd demonstrated the support effect: the strong interaction between single Pd atoms and FeO_x accelerates WGSR.

It can be seen from the above examples that M-SAs in SACs with oxides as supports are usually anchored on the support surface through binding with the metal cations or occupying the vacancies in the support, which is in the form of metal—O–support.[137] M-SAs are neutral atoms and have weak interaction with support. The preparation process, therefore, requires relatively harsh reduction reaction conditions. In addition, the metal–oxide interface sites have been recognized as catalytic reaction zones. Nevertheless, it is almost impossible to reveal the real appearance of the MSI owing to the difficulty in controlling well the O-vacancies at the metal–oxide interface. In summary, it is necessary to systematically study the microchemical environment and acid/alkaline properties in the interface.

3.2. Single Atoms on Transition Metal Compound Supports

3.2.1. Anchoring SACs by Transition Metal Dichalcogenides

Transition metal dichalcogenides (TMDs), a graphene-like 2D nanomaterial possessing excellent chemical/physical properties and low prices, have been widely used in hydrogen generation, energy storage, and various catalysis.[138] The strong spin-orbit coupling (SOC) effect in 2D TMDs MX_2 (M stands for Mo, Nb, W, or V; X represents S, Se, or Te) brings new physical properties, such as the quantum spin Hall (QSH) effect observed in single-layer $1T'-MX_2$,[91c,139] the superconductivity of few-layer $1T_d-MoTe_2$,[140] as well as $2H-NbSe_2$,[141] which make them the focus of physics and materials science. TMDs offer a superior flexible and variable coordination environment, in which the chalcogen and adjacent TMs can synergistically modulate the electronic structure of SACs through the EMSI effect.[112,142]

Generally, single metal atoms can be immobilized on TMDs through doping or adsorption, thus significantly improving the catalytic performance.[143] Sulfur vacancy defects are crucial for TMDs in tuning both the arrangement and electronic structure of adjacent atoms. Consequently, enough attention should be paid to the precise control of S-vacancy parameters, for example, both the concentration and distribution of S-vacancy, and the coordinated regulation of the two. In recent reports, the introduction of a single Svacancy uniformly distributed on MoS_2 surface is expected to be one of the effective ways to further improve the catalytic performance of TMD SACs.[144]

MoS_2-Based SACs: 2D MoS_2 is a typical representative of TMD nanomaterials in H_2 evolution. In particular, MoS_2 shows splendid HER performance in water owing to the hydrogen binding energy close to that of Pt, which is regarded as a high-activity and low-cost alternative to Pt-based metal electrocatalysts.[145] Previous studies have shown that the unsaturated Mo and S atoms located at the edges of the MoS_2 (010) and (100) crystal planes were the active sites in HER.[146] However, the small number of active sites and the high proportion of electrochemically inactive basal planes of MoS_2 greatly limit its HER performance. It is commonly believed that the introduction of metal atoms, such as Co,[147] Ni,[148] Ru,[149] Pt,[40,150] and Zn,[151] can enhance the conductive charge on the basal plane and accelerate the charge transfer on the catalytic electrode, which is an effective strategy to improve the catalytic activity of MoS_2. For example, the isolated Ni atoms modified to the lattice structure of MoS_2 can substitute partial Mo atoms, thus effectively activating S atoms in the basal plane to adjust the electronic structure of the catalyst (**Figure 15**a).[152] Specifically, electrons transferred from Ni to S through the Ni—S bond after Ni atoms modification, and the resulting positively charged Ni centers would significantly increase the content of high-valence Mo (Mo^{6+})[153] According to previous reports, the HER performance of Pt-SAs doped on MoS_2 (Pt_1-MoS_2) was similar to that of Pt-SAs supported on MoS_2 (Pt_1/MoS_2), but Pt_1-MoS_2 had superior stability as well as resistance to toxicity.[40] It should be noticed that the true active sites were S instead of Pt. Due to the special S—Mo—S threelayer unit structure of MoS_2, Pt atoms in the doping layer could be protected from contact with the reaction medium and reactants, which is the main reason for the stability of Pt_1-MoS_2.[154] The above examples indicate that suitable M-SAs doping can dramatically enhance the HER activity of the 2H phase MoS_2.

Doping metal atoms into the MoS_2 lattice, nevertheless, will inevitably lead to excessive hydrogen adsorption at the edge. Given that this excessive activation of the MoS_2 edge is not beneficial to HER, there is a solution that exploits the three-layer atomic structure of MoS_2 to multi-dimensionally regulate the surface and inner layer of the MoS_2 lattice simultaneously, which can selectively activate the basal plane while stabilizing the edge without quenching the activity. MoS_2 co-doped with Co and Se atoms is an ingenious modification strategy. DFT calculations showed that Se atoms doped in the surface S-layer could stabilize both the basal plane and edge sites by forming Co—Se bonds (Figure 15b–d). Meanwhile, they were able to weaken the excessive hydrogen adsorption on the Mo-edge S sites induced by the Co-confined in the inner Mo-layer significantly

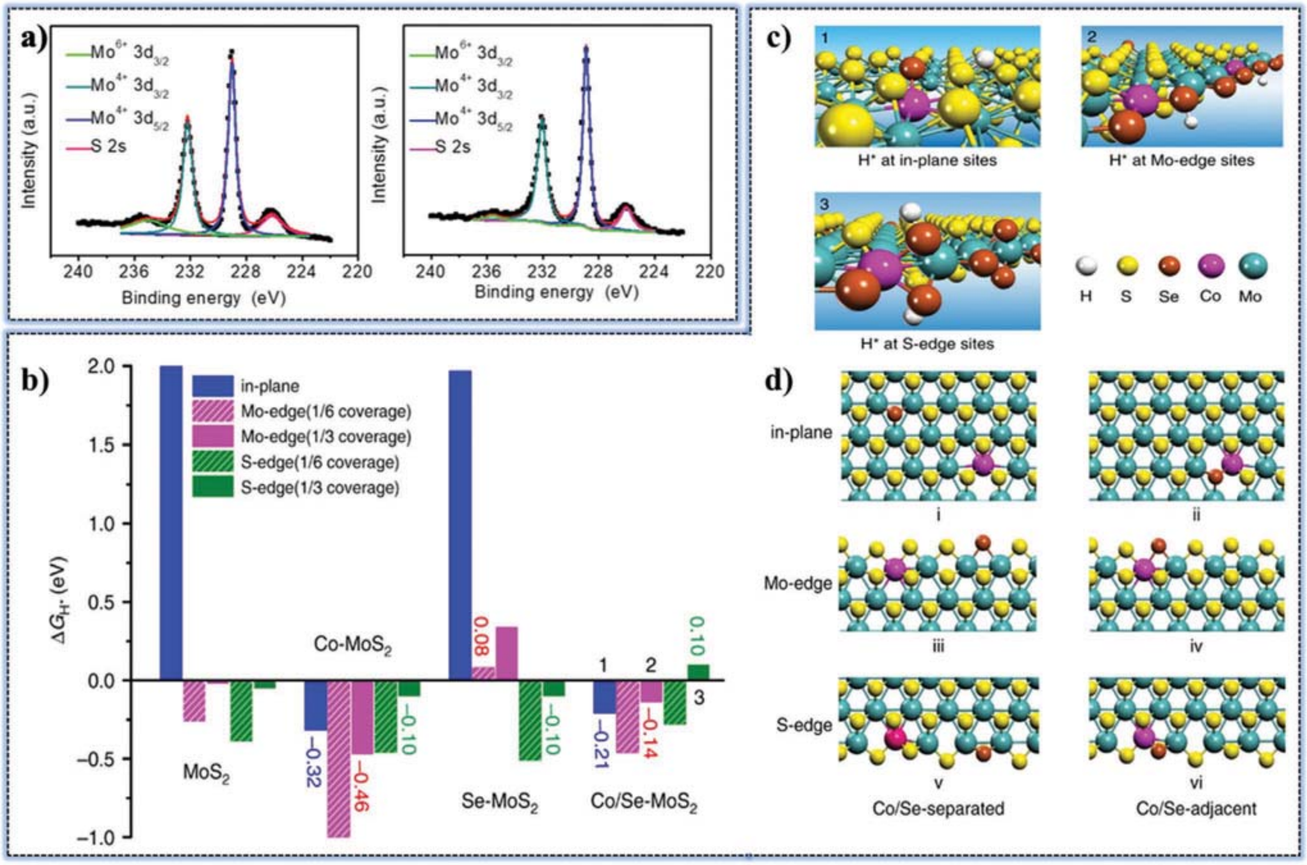

Figure 15. a) High resolution Mo 3d spectra of MCM@MoS_2-Ni (left) and MCM@MoS_2 (right). Reproduced with permission.[152] Copyright 2018, John Wiley and Sons. b) Adsorption free energies of H* (ΔG_H) and c) adsorption structures of H* at the in-plane, Mo-edge, and S-edge sites of Co/SeMoS_2. d) Structures of Co/Se co-confining basal plane, Mo-edge, and S-edge. Reproduced with permission.[155] Copyright 2020, Nature Publishing Group.

enhancing the hydrogen adsorption on the basal plane S sites (ΔG_{H^*} = –0.47 eV).[155] Interestingly, these results mean that the activation effect of Co atoms and the stabilization effect of Se atoms are synergistic, and both enrich the active sites and optimize the hydrogen adsorption activity. In any case, defect engineering is always an important strategy to maximize the catalytic activity of SACs.

Regarding the crystal structure of the MoS_2 supports, there is a semiconductor 2H phase (2H—MoS_2) and metallic 1T phase (1T—and 1T'—MoS_2) in MoS_2 crystal. 2H—MoS_2 is composed of two S—Mo—S layers, presents a triangular prism shape, and naturally exists in bulk MoS_2. On the contrary, 1T—phase MoS_2 is an octahedron composed of a single S—Mo—S layer, and the crystal needs to be exfoliated.[156] 1T phase MoS_2 has greater potential than 2H—MoS_2 in terms of activating the inert basal plane, because the active sites of the former exist both on the edge and in-plane domains.[157] What cannot be ignored is how to modulate and stabilize the phase transition from 2H phase to 1T phase. According to DFT calculations, the strain induced by the lattice mismatch and the bonding of metal atoms with S is considered feasible methods for the phase transition of MoS_2.[158] In 2018, Xing et al. have reported for the first time that the redox characteristic of MoS_2 was employed to induce interfacial heteroatoms doping.[159] They took advantage of a thermodynamic spontaneous interfacial redox reaction approach to chemically activate the surface basal plane of MoS_2 by doping with low content of atomic Pd. According to the combination of characterization and theoretical calculation, the Pd substitution occurs at the surface Mo sites, where the covalent bonding between Pd and S atoms (with the Pd—S coordination number of 4.3) leads to the generation of S-vacancies and the transformation to the 1T phase (**Figure 16**a). It has been confirmed that 1T—MoS_2 exhibited superior stability than 2H—MoS_2, and S atop site next to Pd atom showed ultralow hydrogen adsorption energy (ΔG_H = –0.02 eV), as illustrated in Figure 16b,c. Based on this study, Tan and co-workers have revealed that the bending strain induced from the nanotube-shaped ligament of nanoporous 1T—MoS_2 could increase the Mo—Mo radial distance, changing the atomic arrangement of the resulting SAC (Figure 16d). The formation energy of S-vacancies after Ru doping decreased to 0.832 eV, lower than that before Ru doping, suggesting the feasibility of creating SVs by Ru doping. It is assumed that the introduction of Ru-SAs into MoS_2 would lead to the loss of surrounding S atoms, and the Mo atoms in these formed S-vacancies could directly bind with H_2O molecules.[76]

More interestingly, M-SAs doped in 1T phase usually become the active sites in HER, which is far cry from the pristine 2H phase. For example, Pt-SAs have been proved to be ideal active sites after being doped into 1T'—MoS_2 via the interface engineering method (**Figure 17**a,b).[150] Experimental investigations and theoretical calculations revealed that Pt-SAs located at the top of MoS_2 would continue to concentrate hydrogen owing to the tip effect. Moreover, in acidic and alkaline media, Ni-SAs on the 1T—MoS_2 basal edge served as active sites directly or after forming NiO species (Figure 17c).[160] Certainly, the electronic properties and catalytic activity of MoS_2 doped with different TMs will be varied greatly because of the difference in geometric characteristics and the binding tendency of surface sites.[148b] Taking Co and Ni atoms as an example, Co tends to bind on the S–phase exposed on MoS_2 surface. However, the geometric constraints induced by the large size of Co atoms make it impossible to form Co—Mo interaction. Instead, due to the stereospecificity formed through metal–metal bonds, Ni allows the establishment of the Ni-Mo interactions to modify Mo sites. Nonetheless, the potential cost is the ΔG_{H^*} at the surface exposed Mo sites will deviate from zero under high hydrogen coverage, resulting in decreased activity.

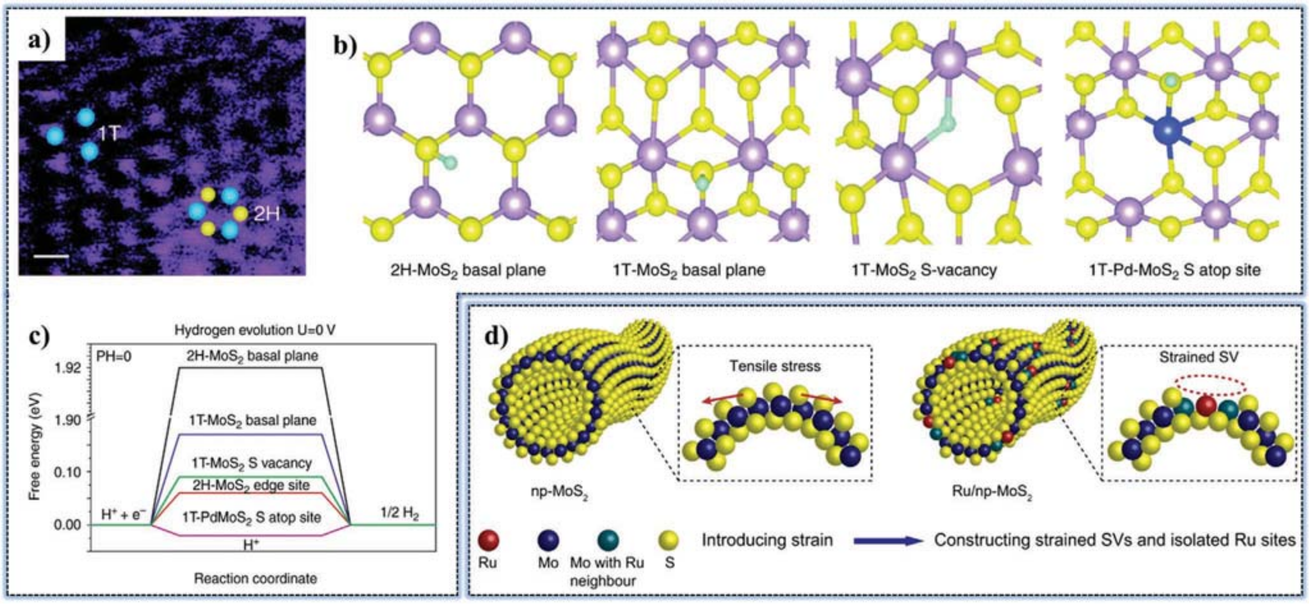

Figure 16. a) TEM image of 1%Pd-MoS_2. Blue and yellow spheres represent Mo and S atoms, respectively. Scale bar: 1 nm. b) Adsorption positions for a single H atom absorbing on pristine MoS_2 and 1T—Pd-MoS_2. Purple sphere: Mo; yellow sphere: S; blue sphere: Pd. c) Calculated free energy diagram for hydrogen evolution of different active sites. Reproduced with permission.[159] Copyright 2018, Nature Publishing Group. d) Illustration of the construction Ru/np-MoS_2. Reproduced with permission.[76] Copyright 2021, Nature Publishing Group.

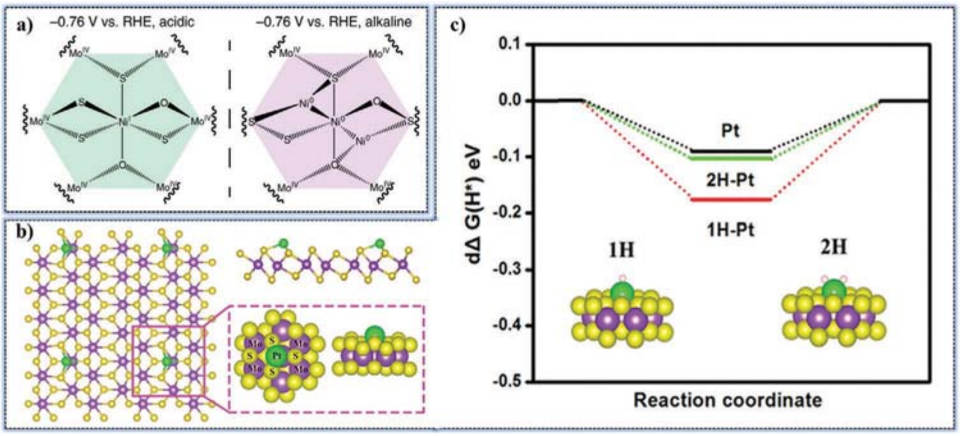

Figure 17. a) Optimum structure of Pt-1T'−MoS_2. b) Differential adsorption free energy ΔG_H diagram of the H atom absorbed on the Pt atom. Reproduced with permission.[150] Copyright 2019, American Chemical Society. c) Schematic illustration of Ni@1T−MoS_2 active species under acidic (left) and alkaline (right) conditions, in which the structure under alkaline conditions is representative. Reproduced with permission.[160] Copyright 2020, Nature Publishing Group.

VS_2-Based SACs: VS_2, which belongs to TMDs nanomaterials as well, has the same 2D layered structure as MoS_2, but its intrinsically metallic phase conductivity is entirely different. There are fewer reports on the introduction of single metal atoms in VS_2 compared to MoS_2. However, the advantage of VS_2 is that the stable 1T phase structure can be constructed only by means of a facile preparation method (a one-step hydrothermal treatment at 160 °C).[59] The photothermal reaction method can anchor Pt-SAs on VS_2 well, and it is easy to control the structure of the catalyst. Characterization analysis showed that Pt atoms were mainly stabilized on the VS_2 surface through Pt−S bond, which was similar to the way 1T−MoS_2 fixed metal atoms. It has been demonstrated that Pt-SAs can exist as a substitute for V atoms or adsorbed species on the surface of VS_2 via a combination of DFT calculations, and either method is favorable for the adsorption and desorption process of hydrogen.

Except for MoS_2, there are few reports on the application of other TMDs as SAC supports toward H_2 production. Given the special electronic band structure of TMDs, such as charge density wave, topological phases, and semiconductor (superconductivity) properties,[161] we believe that there are still many such kinds of materials that have the potential to boost the H_2 evolution activity of single metal/metal-free atoms catalysts.

3.2.2. Anchoring SACs by Transition Metal Carbides

Owing to the properties of metallic electrical conductivity, chemical stability, and corrosion resistance, transition-metal carbides (TMCs) have been widely studied in H_2 production applications.[162] It has been reported that TMCs with noble metallike electronic structure exhibit HER activity similar to Pt.[163] Besides, the high electronic conductivity produced by interstitial alloys gives TMCs inherent advantages as electrocatalysts. More significantly, for electrocatalytic HER, especially in acidic media, TMCs are ideal supports for SACs because of their corrosion resistance, toxicity resistance, and strong interaction with metals.[69b,164]

The first problem to be solved is that the HER kinetics will be slowed down due to the excessively strong binding between TMCs and H intermediates.[165] Effective electronic modulation is a key step in the design of TMCs-supported SACs. The electronic structure of TMCs is affected by the interaction between the *spd* orbitals of metal atoms and *sp* orbitals of C atoms (**Figure 18**). Hence, the variable crystal structures of TMCs generally have different catalytic properties.[162b,166] For example, among a dozen different phases of Mo_xC (including α-Mo_2C, α-MoC_{1-x}, β-Mo_2C, γ-MOC, η-MOC, δ-MoC), β-Mo_2C(011) is more suitable for the electrocatalytic process closely related to the electron transfer in the surface adsorption.[167] Likewise, the electronic deployment of SACs largely determines the HER performance as well. The tunable d-band of TMCs that depends on composition and crystallography can optimize H-binding, thereby accelerating the HER kinetics. Besides, another challenge is to stabilize M-SAs on TMCs while maximizing the exposure of metal sites with high activity.

Stabilizing SACs by Mo_2C and TiC: To design SACs rationally, Sahoo et al. introduced single M (M = Cu, Ag, Au, Ni, Pd, or Pt) atoms on the perfect or defective TiC(001) surface.[168] As the previous report, carbon top (CT) on a perfect surface acted as a more favorable adsorption site than titanium top (TT) and hollow (H).[169] Notwithstanding, the energy barriers of M atoms were lower than the binding energy, indicating that the tendency of metal atomic aggregation and migration on perfect TiC(001) was not stable (**Figure 19**a). After creating the C-vacancy defects on the TiC surface, they calculated that the Ti-rich environment (−0.95 eV) was more energetically favorable than that C-rich (2.50 eV) condition.[168] From a thermodynamic point of view, the carbon chemical potential ($\Delta\mu c$) ranged from −1.76 (Ti-rich) to 0 eV (C-rich), which demonstrated that M atoms were preferentially stabilized on the Ti-rich surface (i.e., C-vacancy state). Moreover, combined with the DOS analysis, it could be concluded that M-SAs embedded in the C-vacancies on the TiC surface reveal higher charge transfer as well as stronger interaction with the support. This research provides guidelines for the establishment of the SACs catalytic system.

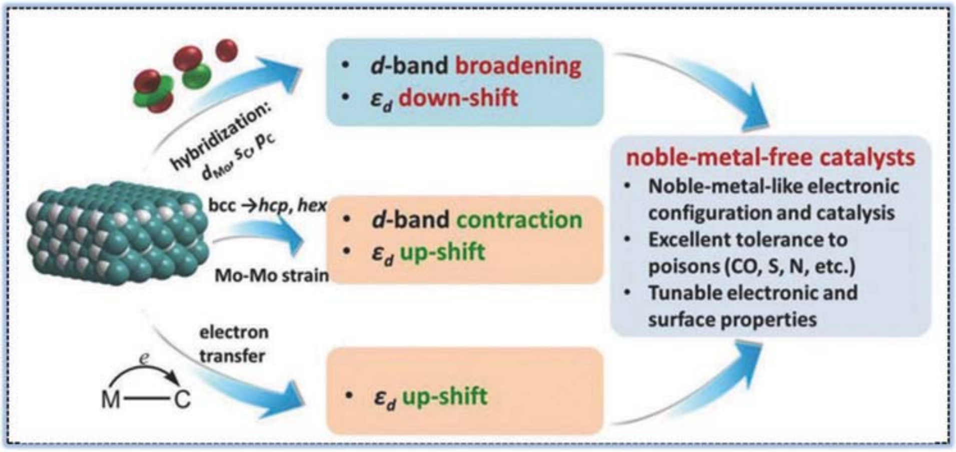

Figure 18. Schematic diagram of the catalytic properties of TMCs depending on the metal–carbon interaction. Reproduced with permission.[162b] Copyright 2018, Wiley-VCH.

Mo_2C has been developed as one of the supports of high-performance single-atom electrocatalysts (SAECs). The unoccupied *d*-orbitals with a large density in Mo are the crucial reason for limiting the HER performance of Mo_2C.[170] The introduction of group VIII metals into Mo_2C can make up for this deficiency and significantly improve its electrocatalytic activity.[171] Thermal annealing of Mo/Zn bimetallic imidazole framework is the latest developed method for the synthesis of

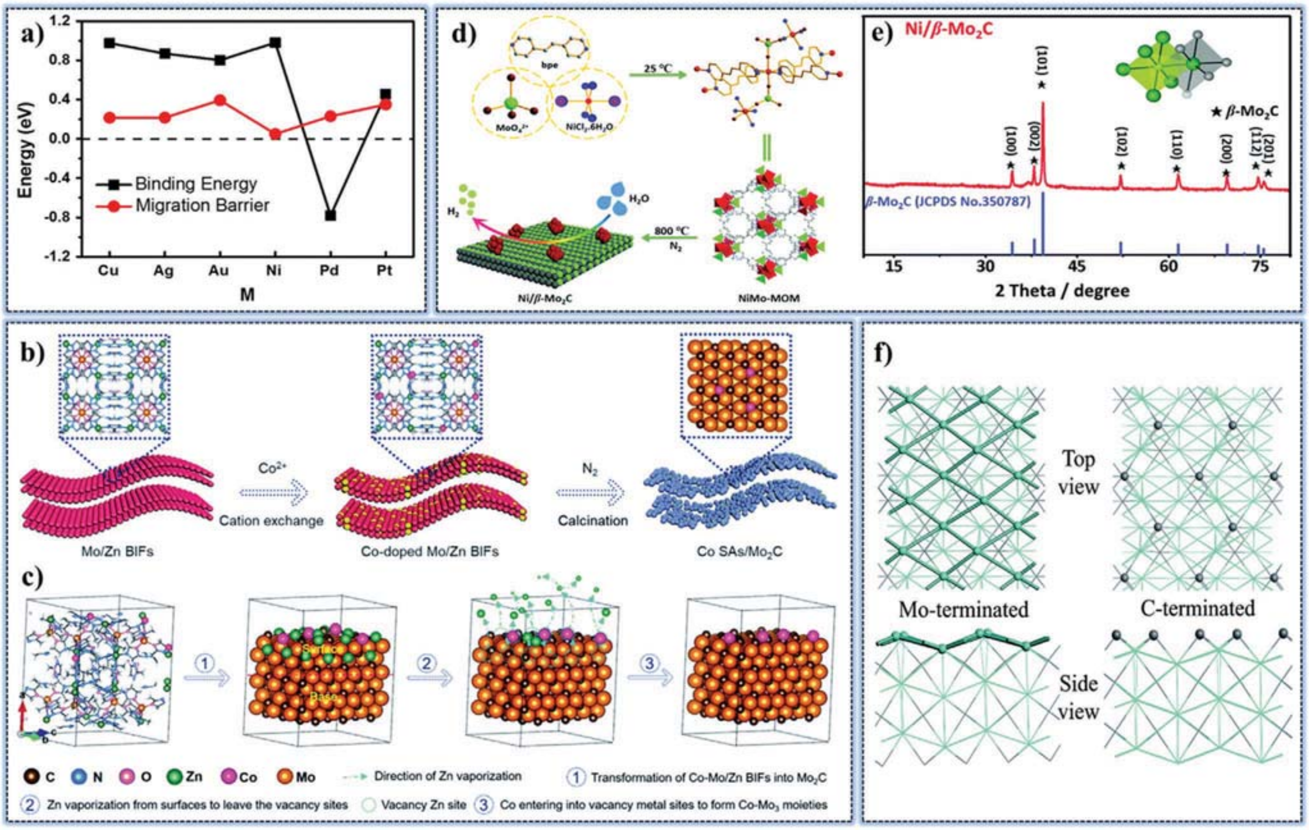

Figure 19. a) Binding energies of single M atoms on the CT site of perfect TiC(001) and the diffusion barriers from the CT site to the nearest CT site. Reproduced with permission.[168] Copyright 2019, American Chemical Society. b) Schematic illustration of the synthesis of Co/Mo_2C. c) Schematic formation mechanism of Co—Mo_3 moieties on the surface of Mo_2C. Reproduced with permission.[172] Copyright 2020, Royal Society of Chemistry. d) Schematic illustration of the synthesis and e) XRD pattern of Ni/β-Mo_2C. Reproduced with permission.[173a] Copyright 2018, Royal Society of Chemistry. f) Optimized geometry of the Mo termination and C termination of β-Mo_2C(001) surface. Blue and gray spheres represent Mo and C atoms, respectively. Reproduced with permission.[173b] Copyright 2017, Royal Society of Chemistry.

porous 2D Mo_2C support (Figure 19b).[172] The sacrificial Zn at high temperatures would leave a large number of metal vacancies to introduce atomically dispersed TM (such as Co, Ni, and Cu) to anchor accurately on the exposed Mo termination surface (Figure 19c). XANES and EXAFS analysis indicated that each metal atom was coordinated with three adjacent Mo atoms. As a representative bifunctional catalyst for both HER and OER, Co/Mo_2C SAC had moderate bonding strength with H and OH species in alkaline OER and HER, which is beneficial to the dissociation of H_2O. Recent studies have found that only SACs fabricated with β-Mo_2C as support were the most effective for HER among the various crystal structures of Mo_2C.[173] Not only that, β-Mo_2C is generally considered to be the most stable as well. Ni/β-Mo_2C SAC was obtained via the use of metal–organic materials (MOMs) containing metal ions (Ni^{2+}) and organic ligands (MoO_4^{2-} groups) as precursors and subsequently high-temperature annealing (Figure 19d).[173a] XRD characterization revealed that Mo_2C was a hexagonal closed-packed phase (Figure 19e). The Ni-Mo bonds in the MOMs precursor were critical to the formation of Ni/β-Mo_2C structure, and the Ni—N_4 bonds favored the stability of isolated Ni atoms on Mo_2C.

Furthermore, β-Mo_2C(001) allows two different terminations, namely Mo termination or C termination (Figure 19f). Specifically, Mo termination of β-Mo_2C (001) surface appeared to be more active oxides,[174] while the C termination was more stable.[175] Compared with C termination, the Mo termination surface supported PtSAs exhibited lower formation energy, meaning that it was energetically favorable to substitute Mo with Pt atoms.[173b] It should be noted that the best adsorption structure was H species located at the vacancies with three Mo atoms. Pt@Mo_2C(001) SAC can effectively overcome the activation barrier of water dissociation to generate enough H and OH species for WGS reaction. According to previous studies, Mo_2C-based catalysts possessed high activity in WGSR and methanol steam reforming (MSR).[176] Hence, the introduction of M-SAs into Mo_2C support can greatly expand and advance the application of WGS or MSR in industrial hydrogen production.[173b] Additionally, to solve the intrinsic structure issue of the unoccupied *d*-orbitals with a large density in Mo, heteroatoms (such as N, P, S) can be introduced into Mo_2C to efficiently adjust the Mo *d*-orbitals, thereby providing an extra active center for HER.

Stabilizing SACs by MXenes: Another TMC support, MXenes (structural formula of $M_{n+1}X_n$ and the other $M_{n+1}X_nT_x$), is a large family of 2D materials, where M represents TM (such as Sc, Ti, V, Cr, Zr, Hf, Nb, Mo, Ta, and W), and X is C and/or N.[177] MXenes supported M-SAs have shown extraordinary competitiveness in electrocatalytic applications owing to its excellent electrochemical activity as well as hydrophilicity.[178] Mxenes, different from TMDs, possess many surface sites that can be chemically modified.[179] This special property makes MXenes good solid support for dispersing isolated metal atoms. Ru ions will be adsorbed due to the interaction with the O and OH groups on Ti_3C_2Tx, which facilitates the bonding of Ru SAs and Ti_3C_2Tx support.[90,180] By forming covalent metal—C bonds with surrounding C atoms, M-SAs can be stably anchored into the vacancies on the MXenes surface. In particular, the abundant Mo vacancies constructed on the surface of double transition-metal MXene ($Mo_2TiC_2T_x$) nanosheets via electrochemical exfoliation approach, providing a large number of anchor sites for capturing M-SAs.[26d] In acidic media, this electrochemical process (including exfoliation and formation of Pt-SAs) changed the surface chemical composition of MXene. Moreover, the MXene layer was disintegrated into defects and base planes that could be employed to fix Pt-SAs (**Figure 20**a–c). In $Mo_2TiC_2O_2$-Pt MXene lattice, Pt-SAs substituting Mo atoms can enhance the HER performance through redistributing the electronic structure.

In addition, another report used Cr_2CO_2 and Mo_2CO_2 MXenes as supports to investigate the activity of SACs with 16 different metal sites for HER.[120] Interestingly, a previous report has shown that Cr_2CO_2 and Mo_2CO_2 are inert materials for HER,[181] which highlights the great contribution of anchored M-SAs to the corresponding catalytic activity. As shown in Figure 20d,e, Fcc sites and hcp sites were two possible adsorption sites for the termination groups, and the corresponding atomic configuration of the latter was more stable.[120] The adsorption energy and bond length of M—O at II and III

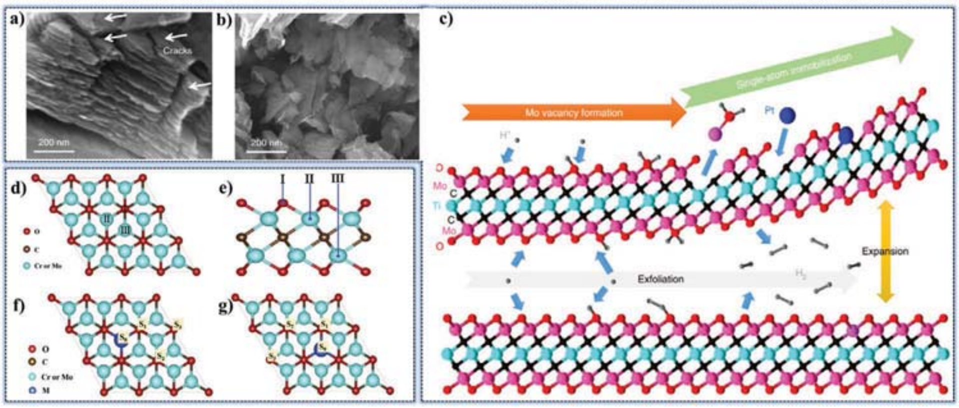

Figure 20. a,b) SEM images of MXene (a) during and (b) after the electrochemical exfoliation process. c) Fabrication mechanism of $Mo_2TiC_2O_2$-Pt during the HER. Reproduced with permission.[26d] Copyright 2018, Nature Publishing Group. Top and side views for the atomic structure of d) hcp sites and e) fcc sites. I, II, and III represent the possible anchoring sites, respectively. f,g) Schematic illustration of four possible H adsorption sites on the Cr_2CO_2 and Mo_2CO_2 surfaces with several metal atoms anchoring. Reproduced with permission.[120] Copyright 2020, Elsevier Inc.

locations were very close, suggesting that both of them could be employed as anchoring sites for atomically dispersed metal species. Figure 20f,g showed four possible H adsorption sites on Cr_2CO_2 and Mo_2CO_2 with corresponding M-SAs anchoring. The calculated ΔG_H of H adsorption demonstrated that the S_1 site on M-Cr_2CO_2 (M = Sc, Ti, V, and Cr) and the S_0 on Cu-Cr_2CO_2 were largely positive.[120] The above results indicated that Cr_2CO_2 with the introduction of Sc, Ti, Cr, Fe, Zn, and Mo_2CO_2 with the introduction of Sc, V, Fe, and Zn exhibited a significant increase in HER activity.

In summary, SACs with MXenes as support have been considered as ideal electrochemical HER systems. While continuously developing strategies to stabilize M-SAs, it is also necessary to further systematically comprehend the role of coordination interactions between M-SA and MXene during the catalytic reaction.

3.3. Interactions between Single Atom Species and the Carbon-Based Supports

Carbon-based materials have been extensively applied as catalyst support owing to their remarkable properties, including low prices, diverse and controllable structures, as well as high stability, conductivity, and surface area.[182] Nevertheless, the performance of pure carbon-based materials as electrocatalysts is not ideal. As mentioned in Section 2.4, the most direct strategy to solve this issue is to introduce metal atoms or heteroatoms into carbon-based materials.[183] Specifically, the introduction of heteroatoms with different electronegativity will optimize the charge state of adjacent C atoms, while the introduction of metal atoms can favor the catalytic reaction by reducing the energy barrier.[184] Notably, unlike the role of introducing heteroatoms, these metal atoms are commonly considered to directly participate in the reaction or even become the active center.

We have reviewed the rational design strategies of SACs with TMCs as supports in Section 3.2. Apart from TMCs, several allotropes of carbon, such as carbon nanotubes (CNTs), graphene, GDY, and carbon nanospheres, are ideal supports as well, since their molecular structures can be further tuned. In the following subsections, we will focus on the breakthroughs made in the design of H_2 evolution SACs by carbon allotropes. Furthermore, we also pay special attention to the interfacial interactions of M-SAs anchored on the N-rich carbon supports, namely M—N—C and graphitic carbon nitride (g-C_3N_4).

3.3.1. Graphdiyne

Recently, GDY, a novel synthetic carbon allotrope with abundant triple bonds, has been believed to be an ideal candidate material for SAC support. GDY is composed of adjacent benzene rings (sp2-hybridized carbon) connected by butadiyne linkages (−C≡C−C≡C−), which have strong reducibility and can directly provide highly stable anchor sites for M-SAs.[185] On the basis of the unique properties of GDY, Li's group successfully reduced Fe and Ni metal ions to zero-valent SAs via electrochemical deposition technology, and they anchored these SAs in GDY for the first time.[26e] They proposed that the key to achieving low loading but high HER activity was the synergistic effect between the acetylene bonds of graphyne, the pore structure of the super-large surface, and Fe/Ni atoms. EXAFS spectra combined with theoretical calculations provided support for studying the geometry of Fe/Ni SAs adsorption sites on GDY (**Figure 21**a). First of all, Fe or Ni atoms at the S1 site were more energetically favorable, where the binding energies were

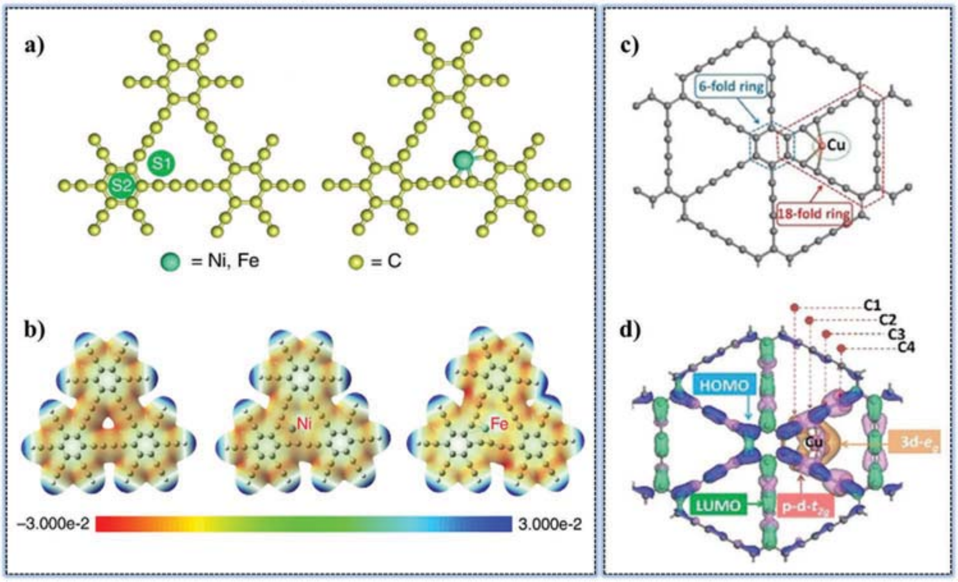

Figure 21. a) Adsorption of Fe/Ni SAs on GDY (left: possible adsorption sites; right: optimized configuration). b) Electrostatic potential maps of pure GDY, Ni/GDY, and Fe/GDY, respectively. Reproduced with permission.[26e] Copyright 2018, Nature Publishing Group. c) Schematic of the unit structures of Cu^0/GDY. d) Schematic of for the coupled p and the d-t_{2g} component (pink isosurface) and the d-e_g component (brown isosurface) of Cu of Cu0/GDY, and contour plots where real-space HOMO and LUMO were depicted in blue isosurface and green isosurface, respectively. (C1, C2, C3, and C4 represent the active H-adsorbed C-sites). Reproduced with permission.[186] Copyright 2020, Wiley-VCH.

–1.22 and –3.72 eV, respectively. The strong charge transfer from Fe/Ni to GDY indicated that both had strong chemisorption characteristics (Figure 21b). Second, taking Ni-3d as an example, the Ni-3*d* orbital in GDY exhibited a larger closed-shell effect than the fcc–Ni orbital overlaps. Meanwhile, stable Ni had almost the same orbital energy in both the nearest neighbor and second neighboring Ni-C environments.[26e] These results meant that the C bonding with Fe or Ni atoms in the Fe/Ni SAs-GDY system was not covalent or ionic bonds in the conventional sense, but should be understood as orbital charge overlaps. Later, Li's group used a similar electrochemical method to successfully anchor Cu-SAs (1.01% loading) on GDY for HER.[186] Similar to Fe/Ni-GDY SACs, Cu preferred to stabilize at the corner of the 18-fold ring (i.e., acetylenic ring) next to the edge of the sixfold ring (Figure 21c). The on-site Cu-3*d* orbital potential energy variations revealed that the strong *p-d* coupling effect was responsible for the connection of local charges, which offered high charge exchange performance for HER. Furthermore, as shown in Figure 21d, the C2 site was more energetically favorable for H adsorption, which could probably be one of the potential reasons for high HER activity.

It has been reported that GDY, toward H_2 generation, is ideal catalyst support for stabilizing various M-SAs, including TMs and noble metals.[46b] Accordingly, it is reasonable to believe that GDY has great research significance as well as potential application value.

3.3.2. Graphene

Graphene is a typical representative of carbon-based materials for hydrogen production, and it has good processability and functionality.[187] Theoretically, there are three stable models of Ni-SAs anchored on graphene. **Figure 22**a shows respectively: i) Ni-SAs were located in the hollow sites of the six-membered C rings as the adsorbed atoms (denoted as $\mathrm{Ni_{ab}}$); ii) Ni-SAs were employed as dopants in the substitutable lattice sites (Nisub), and iii) Ni-SAs anchored to the lattice defects of graphene (denoted as $\mathrm{Ni_{def}}$).[114] As shown in Figure 22b, the $\mathrm{Ni_{sub}}$-doped graphene had the smallest $|\Delta G_{\mathrm{H}*}|$ value (0.10 eV), which was similar to that of the Pt catalyst (0.09 eV). This result indicated that $\mathrm{Ni_{sub}}$, which occupied the carbon sites of graphene, was the most effective active center. The chemical interaction of the metal–support interface in SACs would produce unique electronic structures. According to DFT calculations, Ni-SAs-doped nanoporous graphene (Ni/np-G) exhibited the highest stability with a binding energy of –7.54 eV owing to the strong C—Ni binding. Besides, its special H_2 evolution performance was attributed to the charge transfer between the *d*-orbital of Ni atoms and the *sp* orbital of coordinated C atom, which favors the formation of vacant C—Ni hybrid orbital at the local interface.[114]

Owing to the existence of intrinsic carbon defects, the unsaturated coordination of zigzag carbons or arm-chair carbons in graphene will lead to metal atoms being trapped by

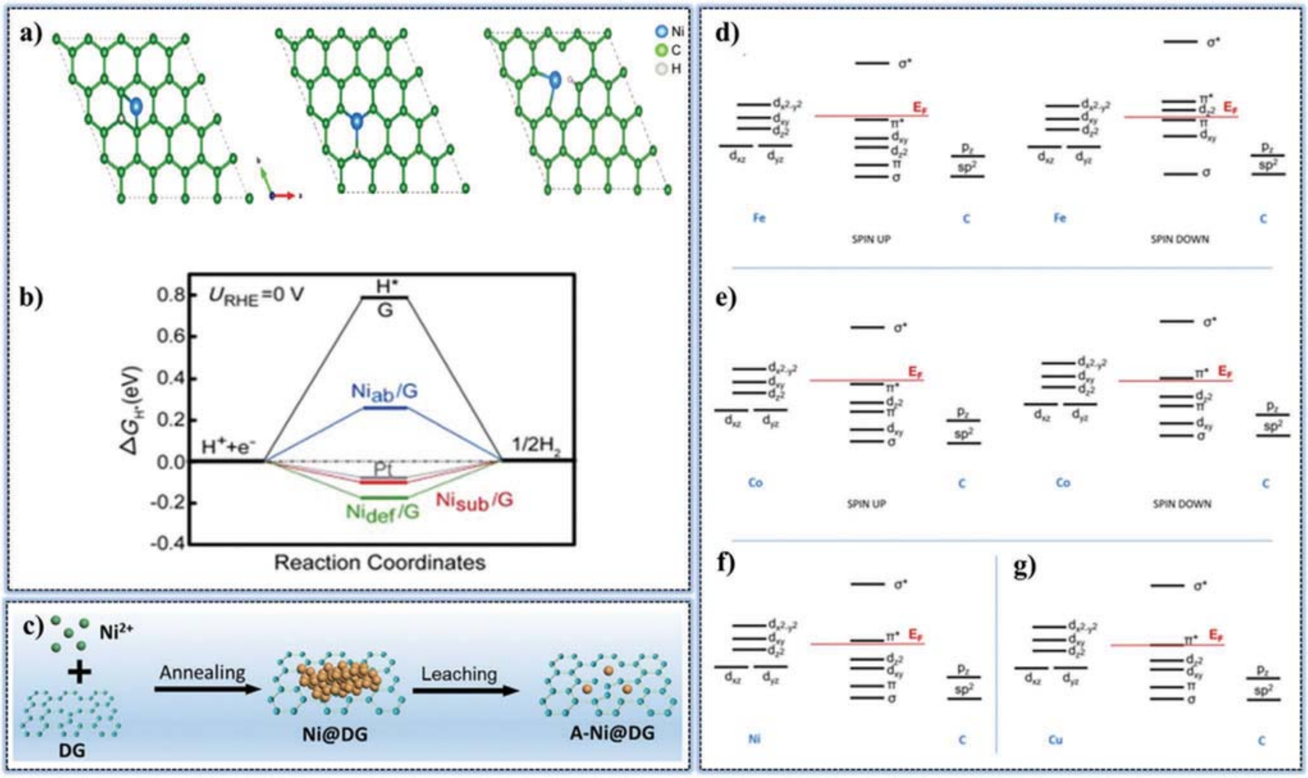

Figure 22. a) Three theoretical configurations of Ni-doped graphene. Ni atom anchored in a hollow center of the graphene lattice (left), Ni atom occupying C site in the graphene lattice (middle), and Ni atom anchored on defect site (right). b) Calculations of $G_{\mathrm{H}*}$ at equilibrium potential for Pt catalyst and Ni/np-G SAC with three possible configurations. Reproduced with permission.[114] Copyright 2015, John Wiley and Sons. c) Synthesis and structure characterizations of aNi@DG. Reproduced with permission.[56] Copyright 2018, Elsevier Inc. Molecular orbital diagrams of free-standing d) Fe@2VG, e) Co@2VG, f) Ni@2VG, and g) Cu@2VG. Reproduced with permission.[193] Copyright 2021, Elsevier Inc.

the edge sites.[183a,188] Unfortunately, the anchor sites provided by the edge sites are limited, so the loading capacity of metal atoms on graphene is usually low. By using the strategy of combining an incipient wetness impregnation (IWI) approach combined with subsequent acid leaching, a large amount of the isolated atomic Ni (aNi) could be stably confined in the defects of defective graphene (DG) (Figure 22c).[56] The key step in the synthesis process was to convert $Ni(OH)_2$ into NiO through high-temperature pyrolysis, while NiO was reduced by carbon to metallic Ni. It is foreseeable that the strong charge transfer between the metal atoms and the 2π antibonding state of C atoms in the DG support can provide effective sites for anchoring M-SAs.[189] Alkaline electrocatalytic experiments showed that the performance of aNi@DG was significantly higher than that of Ni@DG.[56] According to a previous study, it can be inferred that Ni-SAs coordinated with C atoms regulated the electronic environment at the metal–nonmetal interface, strengthening the interactions between the substrate and the adsorbates.[190] This phenomenon was different from the catalytic mechanism of the typical metal—N—C system, because Ni-SAs in the defect were considered to be the unique active center of HER and OER. Recently, to form the volatile $Pt(NH_3)_x$ species that can be anchored on the DG surface, the dicyandiamide was added in the pyrolysis process to generate ammonia gas which can establish strong coordination interaction with Pt atoms.[191] EXAFS analysis demonstrated the oxidation state of isolated Pt ($Pt^{\delta+}$, $0 < \delta < 4$) as well as the proposed coordination structure of Pt—C_4 in this as-prepared SAC. Notably, the DG formed after removing the most O species on the graphene oxide surface via the thermal treatment could further trap the $Pt^{\delta+}$ species, fabricating the atomically dispersed Pt SAC. Subsequently, DFT calculations revealed that the charge transfer between Pt-SAs and DG was larger than that of Pt-SAs anchored on pristine graphene.

The above-mentioned Ni-SAs, as non-noble metal atoms, are trapped at Cvacancies and defects, which significantly improves the electrochemical activity. Nevertheless, the C–metal atom bonds in graphene-based SACs cannot remain stable in the catalytic reaction. As fully discussed in Section 2.4, one of the solutions to this issue is introducing N atoms. Studies have shown that N doping can not only increase the bonding strength between M-SAs and graphene, but also reduce the activation barrier of SACs during the reaction,[192] as well as the overpotential for HER at atomically active sites.[16a] Inspired by the above unique phenomenon, Valentin's group trapped various MT atoms (Fe, Co, Ni, and Cu) at single (1VG) or double (2VG) Cvacancies in DG with N doping, and systematically investigated their structural, electronic, and energetic properties by DFT calculations.[193] Of particular note is that the defect size of the 2VG hole was large enough to accommodate TM atoms compared to the 1VG. As shown in Figure 22d–g, the spin-up component of the π^* of Co@2VG was filled and Cu@2VG got almost filled, while that of Ni@2VG remained unoccupied.[193] Besides, the d states of Cu were the deepest in energy. These results were also proved by N-doped 2VG in free-standing graphene SAC, namely TM@4N2VG, in which four C atoms bonded with TM atoms were substituted by four N atoms. More importantly, in the free-standing N-doped system, the d states of Fe and Co atoms are close to the Fermi level, whereas the d states of Cu atoms are very deep, and the σ^* state is just above the Fermi level.[193] Therefore, it is more reasonable to employ Fe and Co as the active sites of these SACs.

So far, there is still a lack of profound insight into the interaction between metal atoms and defects. The carbon defects in the DG support will be able to help us better understand the structure–performance correlation in the SAC system for H_2 production.

3.3.3. M—N—C

Different from N-doped carbon-based supports, N-rich carbon-based materials have more precise structures. Currently, M—N—C (M refers to non-noble metals, such as Fe, Co, and so on) are hot materials as SAC support for energy storage as well as conversion. In these materials, the abundant M_x—N_y active sites formed by the coordination of M-SAs with N atoms provide splendid electrocatalytic activity.[194]

It is challenging to improve the stability and catalytic activity of M—N—C catalysts at the same time, which is attributed to the leaching of metal sites and protonation of active sites.[195] The recently developed M—N—C SACs for H_2 production mainly used *2*-methylimidazole zinc salt (ZIF8) as the precursor and template and anchored Pt-SAs into Fe—N—C catalysts via IWI method. Generally, the Fe centers of Fe—N_x moieties in Fe—N—C catalysts would be oxidized when absorbing a negatively charged O_2 from the air.[196] However, after atomic Pt was grafted onto the Fe atom at Fe—N_4 center through a bridging oxygen molecule (denoted as Pt_1@Fe—N—C), the negatively charged O_2 further captured the positively charged Pt^{4+} ions at the other end, forming the $Pt_1{*}O_2{*}Fe_1$—N_4 configuration.[197] Then, during mild heat treatment, Fe- and Pt-SAs would form a new stable Pt_1—O_2—Fe_1—N_4 with neighboring O_2 molecules (**Figure 23**a). As a three-function (ORR, HER, and OER) catalyst with excellent performance, the HER activity of Pt_1@Fe—N—C was equivalent to that of Pt-NPs and exhibited long-term stability. Its favorable performance came from the abundant micro/mesopores, heteroatom pairs, and the grafting of Pt_1—O_2—.[198] Subsequently, Li and coworkers also employed the IWI approach to anchor Pt atoms on the Fe—N—C material, but the fabrication method of the Fe—N—C substrate was different.[199] They first synthesized MOF via doping Fe into ZIF8, and then synthesized Fe—N—C by solid-state pyrolysis (Figure 23b). XPS characterization results suggested that the Pt atoms were located at the pyridinic N (py-N) sites. This may be derived from the protonation, the py-N tended to form $[C_x(NH)_2]^{2+}[PtCl_6]^{2-}$ as the anchoring sites of Pt under the electrostatic force.[200] Furthermore, XANES at the L_3 edge of Pt confirmed the existence of Pt 5d state in the sample. A large number of vacant *d*-orbitals of these anchored Pt atoms accelerated the electrons transfer from Pt atoms to Fe—N—C interface, which enhanced the catalytic activity and stabilized Pt-SAs.

At present, the fabrication strategies of M—N—C SACs are mainly based on the high-temperature pyrolysis of metal salts and nitrogen-containing precursors at >700 °C. Notably, the catalysts obtained by this fabrication strategy often have high structural heterogeneity because of the existence of atomically dispersed M_x—N_y and inorganic metal particles.[194b] As a result,

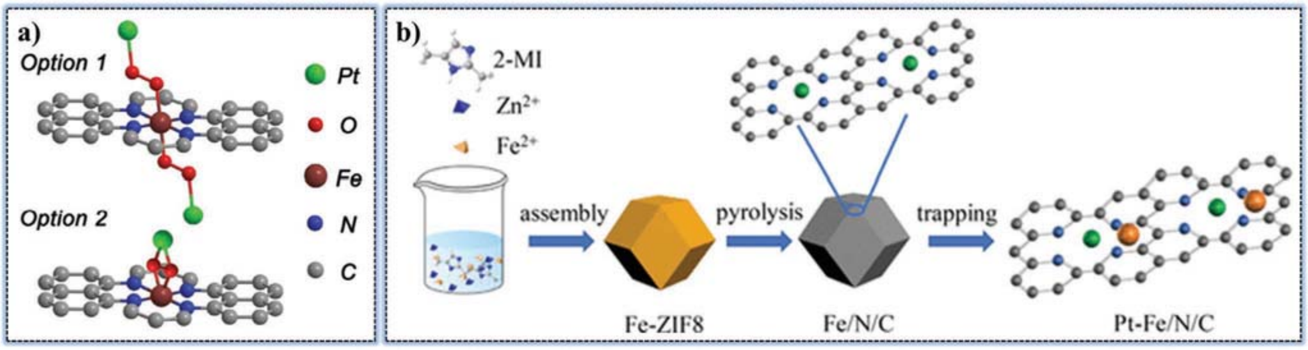

Figure 23. a) Two possible configurations for the new moiety of $Pt_1-O_2-Fe_1-N_4$. Reproduced with permission.[197] Copyright 2017, John Wiley and Sons. b) Synthesis procedure for the Pt-Fe/N/C and the corresponding structural model. Reproduced with permission.[199] Copyright 2020, American Chemical Society.

the atomic utilization is reduced and the difficulty of determining active sites is increased. The post-treatment approaches, such as chemical annealing with acids,[28] or concentrated H_2O_2,[201] can help to remove inorganic metal-containing nanoparticles. Nevertheless, the structure of active M_x-N_y moieties may be damaged on this account. It is obvious that the complicated operation processes of preparing M—N—C SACs are an urgent issue. Therefore, researchers should carefully consider the reaction conditions of each procedure.

3.3.4. g-C_3N_4

In addition to M—N—C, other N-rich materials, such as g-C_3N_4, are also useful supports for anchoring M-SAs. It is well known that g-C_3N_4 is the most stable carbon nitride allotrope during the polymerization process of common N-rich precursors under ambient conditions.[202] The g-C_3N_4 photocatalyst with O and N species was synthesized by the strategy of controlling the doping position for a polymer, showing strong visible light utilization and charge separation efficiency.[203] It is expected to provide a feasible scheme for constructing M_x-N_y sites with single activity on g-C_3N_4. Moreover, it is easy to form the unsaturated coordination containing four in-plane nitrogen atoms (i.e., N-vacancy) during the preparation of g-C_3N_4.[204] Based on the above, the isolated Co atoms could be well supported on phosphorized g-C_3N_4 (PCN) by atomic layer deposition (ALD) technique, which was able to effectively promote the photogenerated e^- at the Co sites to get involved in the H^+ reduction reaction.[79] On the one hand, on the basis of the enhancement of charge density through four N atoms around the Co atom, the Co_1-N_4 active centers constructed at the interface between Co atoms and g-C_3N_4 significantly promoted the transfer of photogenerated electrons from N atoms to Co-SAs, and inhibited the electron–hole recombination (**Figure 24**a,b). On the other hand, N atoms in Co_1-N_4 moiety contributed to the formation of crucial hydride intermediates, thus accelerating the production of H_2. It has been reported that strengthening the reactive metal–support interaction (RMSI) was an effective method to optimize the catalytic active sites.[205] The ideal growth of Pt-SAs species anchored on g-C_3N_4 could be promoted, while selectively inhibiting the Pt precursor at the N-vacancy, by controlling the annealing temperature as well as freezing the precursor solution. The formation of N-rich vacancies in g-C_3N_4 would cause obvious electrondeficiency effects, which enhanced RMSI. Under this strong RMSI, Pt-SAs preferred to combine with the two-coordinated C (C_{2C}) in the N-vacancies to maintain stability (Figure 24c,d).[206] Furthermore, a single atomic Pt introduced into g-C_3N_4 as a cocatalyst could improve the photocatalytic activity by inducing an intrinsic change in the surface trap states of g-C_3N_4.[16f]

Admittedly, the in-plane charge transfer of g-C_3N_4 can be promoted by introducing TM atoms on the π-conjugated planes and doping nonmetal atoms in the lattice. However, these efforts failed to solve the problem of effective charge transfer among the adjacent layers of g-C_3N_4. According to a recent report, it was a feasible strategy to intercalate Pd-SAs into the adjacent layers of g-C_3N_4 and simultaneously anchor Pd-SAs onto the g-C_3N_4 surface.[207] Specifically, Pd atoms in adjacent layers can be regarded as a bridge to induce the directional charge transfer between adjacent layers by constructing vertical channels (Figure 24e). Then, these electrons transferred from bulk to the outermost surface undergo directional in-plane migration to the surface Pd atoms (acted as the reaction centers). It is worth mentioning that the g-C_3N_4 nanosheets (CN-NS) with an ultra-thin structure and multiple interlayers are the key to realizing the directional transfer of electrons to the active centers.[208] In addition, before the Pd^{2+} ions were reduced to metallic Pd atoms by photoirradiation, the stability of surface- and interlayer-Pd^{2+} ions was the result of the interaction between the Pd^{2+} and sp^2hybridized N atoms.[209]

Subsequently, Zhang et al. gave promising insights into the enhancement of the catalytic performance of Pd-SAs supported on bulk C_3N_4 materials as well as the mechanism of water splitting reactions.[210] The authors pointed out that Pd atoms with different oxidation states on the g-C_3N_4 surface would interfere with the analysis of their role in the reaction. Only after the surface layer was removed via an Ar^+ beam etching, the metallic Pd^0 and the oxidation state $Pd^{\sigma+}$ could be detected on the Pd/gC_3N_4 surface. Such a phenomenon was quite different from the results of previous studies.[207] It can be predicted that this distinction may contribute to the different surface characteristics caused by diverse preparation methods influence. Besides, as shown in Figure 24f,g, the C_3N_4 cavity

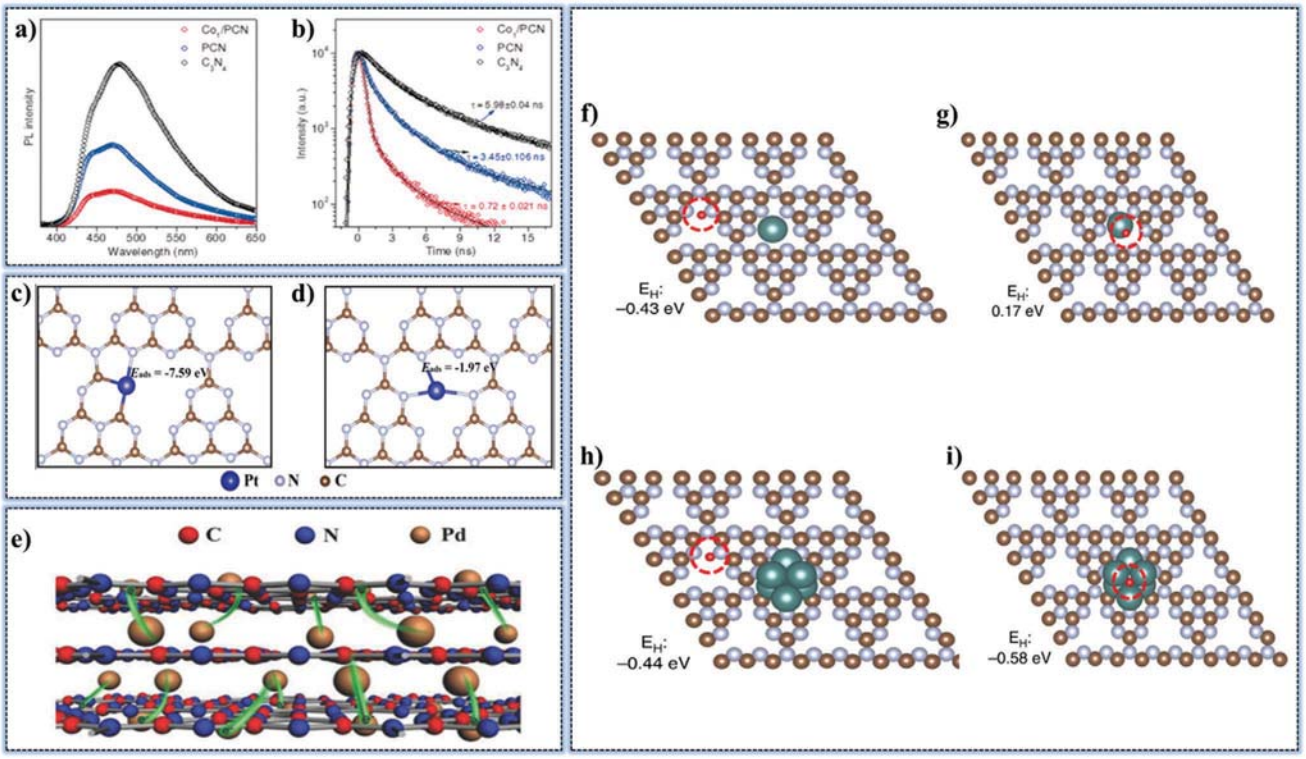

Figure 24. a) Steady-state fluorescence (SSF) spectra at 298 K for Co_1/PCN, PCN, and C_3N_4. b) Time-resolved fluorescence (TRF) kinetics at corresponding steady-state emission peaks. Reproduced with permission.[79] Copyright 2017, John Wiley and Sons. Theoretical configurations of Pt SA trapped at the c) C_{2C} and d) N_{2C} sites. The adsorption energy of Pt SA at the C_{2C} site is more negative than that at the N_{2C} site, suggesting that the Pt SAs are more likely to be anchored at the C_{2C} site. Reproduced with permission.[206] Copyright 2018, Elsevier Inc. e) Conceptual illustration of the isolated Pb atoms intercalated and anchored in the adjacent layers and on the surface of g-C_3N_4, respectively. Reproduced with permission.[207] Copyright 2018, John Wiley and Sons. Geometrical configuration and adsorption energies of hydrogen adsorption on the f) N and g) Pd atoms in Pd-SA/C_3N_4, and the h) N atoms and i) Pd cluster in Pd-cluster/C_3N_4. Reproduced with permission.[210] Copyright 2019, Nature Publishing Group.

adjacent to Pd-SA cavity instead of atomic Pd (–0.43 vs 0.17 eV) provided the most stable adsorption site for hydrogen as well as the aggregation site for activated electrons.[210] More interestingly, as the increase of Pd size, hydrogen atoms tended to be adsorbed on large-sized Pd clusters rather than pyridine N (Figure 24h,i). Obviously, this is not conducive to the improvement of photocatalytic H_2 evolution activity.

3.3.5. Modified Carbon-Based Supports

The atomically distributed metal active sites on SAC support allow the tip structure, namely corner and edge sites, to dramatically enhance the local concentration of reactants and obtain excellent catalytic performance. Inspired by this unique phenomenon, Song's group designed a nanosized onion-like carbon (OLC) support with a high curvature quasi-0D architecture for anchoring atomically dispersed Pt species.[26b] Such an ingenious design of anchoring M-SAs with highly curved supports imitated the metal sites at the corners and edges of particles. The PtO_2C_{295} model was constructed by encapsulating C_{60} fullerene in C_{235} defect fullerene. It can be seen that the pattern to stabilize Pt-SAs was by bonding with one C atom and two O atoms on the surface, as shown in **Figure 25**a. Moreover, the interfacial O species allowed PtSAs to form strong interaction with OLC, thus maintaining high stability in acidic media. More intriguingly, theoretical calculations revealed that an in situ strong local electric field around the Pt site formed a protuberant tip (Figure 25b). Such a similar tip effect also appeared in the previously reported electrocatalytic CO_2 reduction system[211] and the H concentration by Pt-SAs at the top of MoS_2.[150] Actually, before then Fan et al. fabricated Ni@C nanomaterials encapsulated by hollow onion-like nanoshell and graphene layers after HCl leaching treatment with Ni-MOF as a precursor (Figure 25c).[212] They performed constant potential and cyclic voltammetric to activate the Ni@C sample, and unexpectedly found that Ni nanoparticles downsized to Ni-SAs, which were isolated on the carbon support. Arguably, the findings of these studies are a milestone for SACs which were still in their infancy stage.

In addition to the above-mentioned OLCs, we will also introduce another type of carbon allotrope, namely CNTs. The CNTs with integrated carbon network architecture have been also interesting support that can immobilize M-SAs well. It has been reported that Pt-SAs can be firmly anchored on single-walled carbon nanotubes (SWCNTs) through a similar electroplating method with a facile process.[213] Compared with graphene supports, SWCNTs with extremely low loading of Pt-SAs exhibited superior catalytic performance for two major reasons (Figure 25d): i) the high adsorption ability of SWCNTs allowed

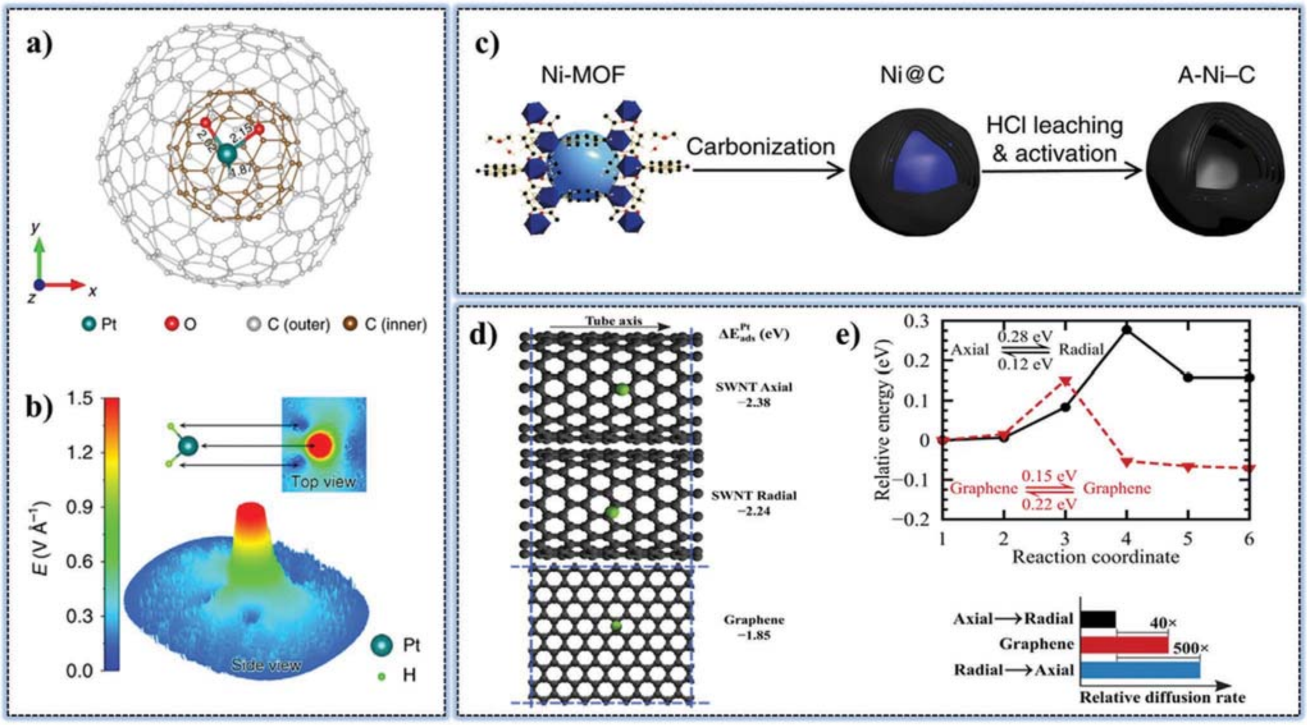

Figure 25. a) The optimized atomic model of PtO_2C_{295}. b) Localized electric field of the H_2Pt_1/OLC system at the tip-like Pt site under an equilibrium potential. Reproduced with permission.[26b] Copyright 2019, Nature Publishing Group. c) Schematic diagram of the synthesis of Ni SACs anchored on graphitized carbon. Reproduced with permission.[212] Copyright 2016, Nature Publishing Group. d) Adsorption of Pt onto (14,0) SWCNT and graphene. Carbon is shown in gray sphere and Pt in green sphere, and periodic boundaries are depicted in blue dotted line. e) The above figure shows a comparison of minimum energy profiles for Pt diffusion between two adjacent sites on graphene and SWCNT. The graph below suggests the activation energies and relative diffusion rates at room temperature. Reproduced with permission.[213] Copyright 2017, American Chemical Society.

them to immobilize dispersed Pt atoms on the surface and inhibit their aggregation; ii) The high surface area of SWCNTs allowed them to be decorated with more Pt atoms on the surface, increasing the loading capacity. It should be noted that the high surface area of SWCNTs made the surface diffusion process of Pt atoms more important.[214] The interactions between Pt and different carbon substrates were calculated by DFT. It was found that the absorption of Pt at the axial sites (parallel to the tube axis) of SWCNTs was more stable than at the radial sites.[213] Furthermore, as shown in Figure 25e, the activation energy diffused along the axial site (0.28 eV) to the radial direction (0.12 eV) was asymmetric, suggesting the stronger tendency of axial sites to bind Pt. As expected, the as-prepared SWNT/at-Pt SAC with an ultralow amount of Pt exhibited notably outstanding HER performance.

4. Atomic Metal–Metal Interactions

As discussed in the above sections, MSIs play an important role in the geometric and electronic properties of supported active metal sites in SACs. It can be seen that enhancing the interactions between metal and support is not only the key to ensuring the stability of M-SAs, but also the key to unraveling the structure–properties relationship at the atomic level. However, this is not the whole process of designing SACs rationally. Recent studies have revealed that heterogeneous bimetallic catalysts have inter-atom interactions that can enhance catalytic performance, which is also known as the synergistic effect. Such a special behavior of synergetic catalysis provides a novel idea for the design of SACs. For instance, “dual-atom catalysts (DACs)” are designed to further increase the density of active sites and loading mass. Especially for “single-atom alloys (SAAs)” composed of bimetals, the TM scaling relationship in traditional alloys will be resolved by the synergistic effect. Based on the above, this section will briefly discuss the role of the synergistic effect between neighboring atoms in the catalytic system. Besides, we will show the metal–metal interactions in SAAs and DACs from electronic effect, interfacial effect, and steric effect.

4.1. Synergistic Effects of Neighboring Single Atoms

The interaction between adjacent SAs is another major discovery in the atomically chemical environment of SACs. Some studies in recent years have shown that decreasing the distance between two singly atomic active sites to sub-nanometer level will bring a surprising impact on the catalytic behavior. Similar to biological catalysis chemical reactivity of biological catalysis, there are synergistic effects between the neighboring active sites in SACs as well.

For example, when two single Fe atoms were fixed on the same graphene material through N atoms to form

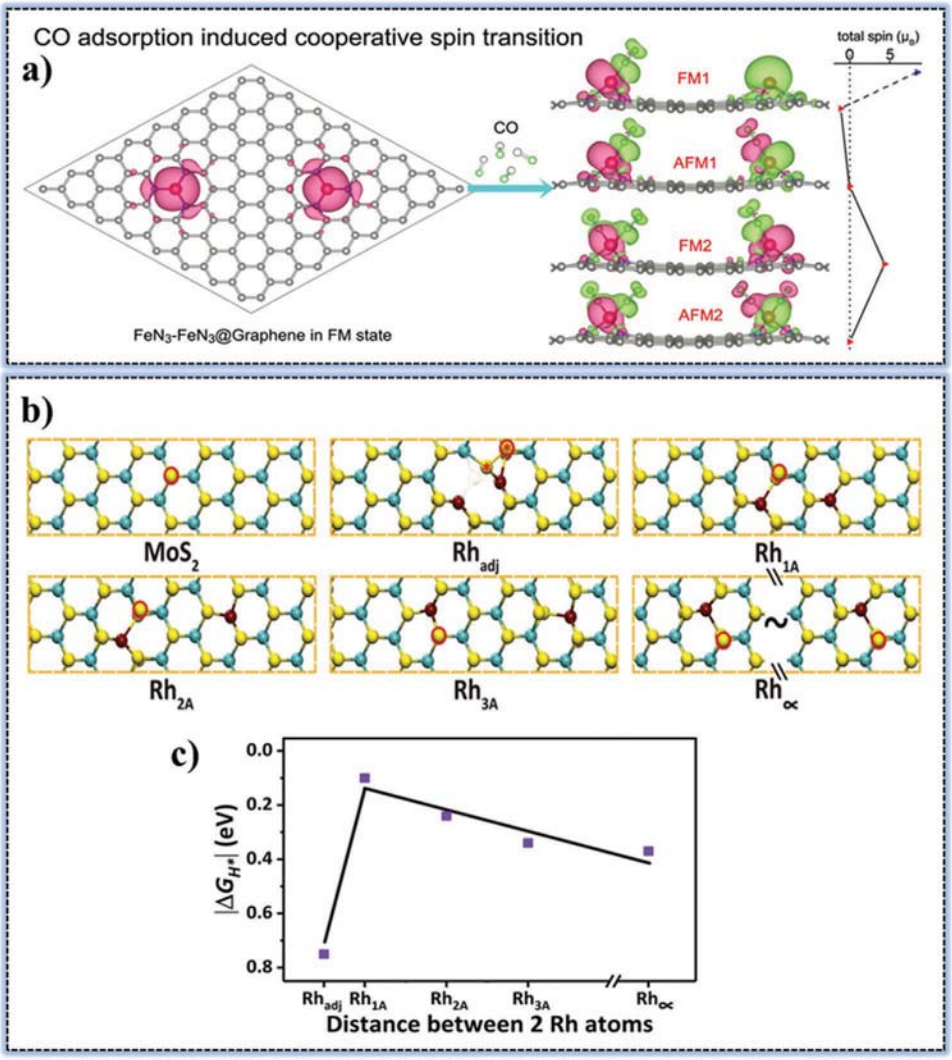

Figure 26. a) Schematic of coordinated electron spin transition occurs between neighboring Fe SACs. Ferromagnetic (FM_1), antiferromagnetic (AFM_1), ferromagnetic (FM_2), antiferromagnetic (AFM_2). Reproduced with permission.[139] Copyright 2018, American Chemical Society. b) Optimized models of two Rh atoms with different inter-Rh distance confined in 2D MoS_2. The yellow, cyan, and brown spheres represent S, Mo, and Rh respectively. c) The relation between the absolute values of ΔG_{H^*} and the inter-Rh distances. Reproduced with permission.[216] Copyright 2020, John Wiley and Sons.

FeN_3—FeN_3@graphene SACs, there was an unusual phenomenon in the CO adsorption on adjacent Fe atoms.[139] Specifically, an atomic Fe would send charge transfer signals to another nearby Fe atom through the graphene support when absorbing Co, and induced it to change synchronously (**Figure 26**a). This is an interesting phenomenon, and such a synergistic effect between adjacent active sites was called cooperative spin transition. There is another report on Ir/FeO_x SAC that the microscopic process of synergistic valence changes between supported Ir-SAs and neighboring Fe atoms was observed.[53a] Furthermore, Liu et al. have demonstrated that the synergistic effect between two adjacent Pt atoms in closely distanced three-coordinated PtC_2N_1 moieties had an important contribution to enhancing HER activity.[215]

Generally, the density of single atomic positions was a key factor in whether the active sites preferred to be close to each other, which would influence the catalytic activity.[43b] This effect also provides a rational strategy for the design of H_2 evolution SACs. By adjusting the concentration of Rh, Meng et al. found that there was a distance synergy between the Rh atoms embedded in the MoS_2 lattice.[216] In this catalytic model, the distance between confined Rh atoms changed with the concentration of Rh, which could modulate the electronic structure of adjacent S atoms and optimize the adsorption energy of H atoms at S sites, thereby adjusting the reactivity of nearby inplane S atoms. As illustrated in Figure 26b,c, with the distance between Rh atoms decreased, the ΔG_{H^*} on the neighboring S site presented a volcanic curve that first activated and then weakened. This study revealed and proved that proper modulation of an inter-single-atom distance confined in the support lattice can trigger the optimal activity of SAC system.

Besides the above-mentioned synergistic effects observed among atomically dispersed active sites, M-SAs can also be employed to isolate metal nanoparticles (M-NPs). Very recently,

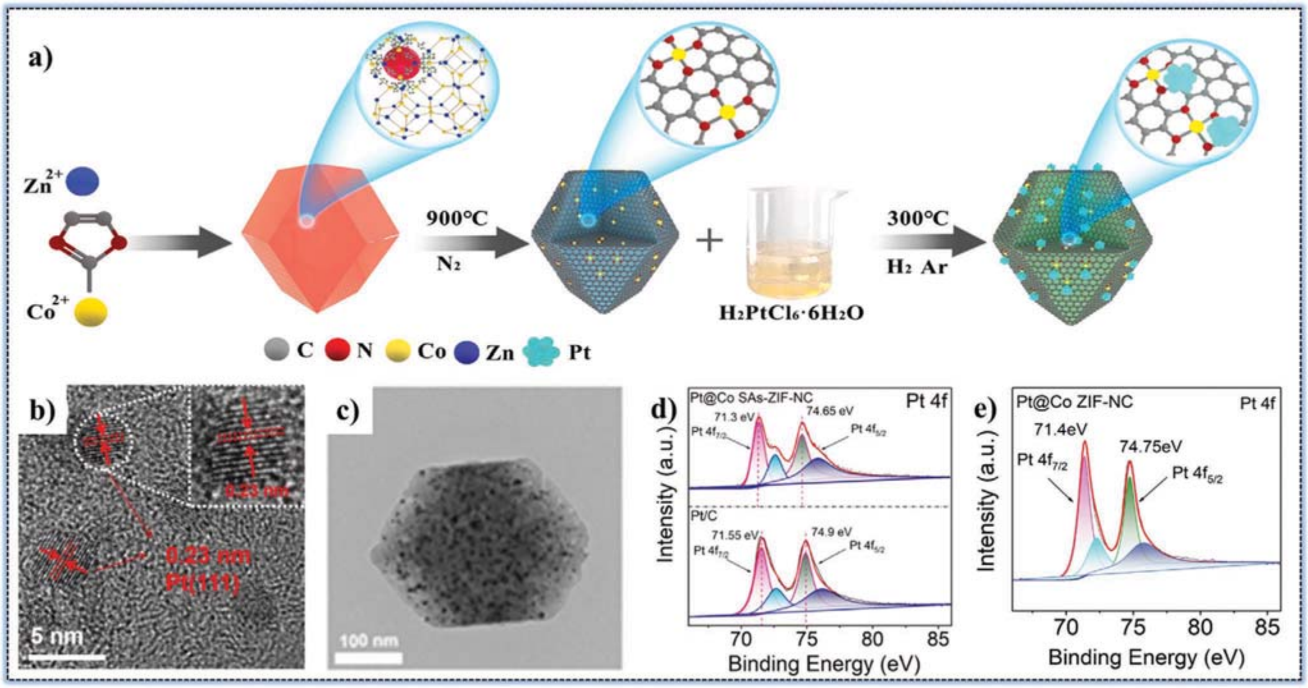

Figure 27. a) Illustration of the synthesis protocols of Pt@Co SAs-ZIF-NC. b,c) HRTEM image of Pt@Co SAs-ZIF-NC. d,e) XPS spectrum of Pt 4f for Pt@Co SAs-ZIF-NC, Pt@Co ZIF-NC, and commercial Pt/C. Reproduced with permission.[217] Copyright 2021, Elsevier Inc.

an outstanding Pt@Co SAs-ZIF-NC electrocatalyst with rich Co-SAs as multiple active sites has been obtained by Mu and co-workers (**Figure 27**a).[217]In their work, Pt NPs were uniformly immobilized on ZnCo-ZIF-derived porous N-doped carbon substrate through the isolating effect of Co site to Pt, the strong interaction between Co and Pt, as well as the confinement of the MOFs. High-resolution imaging and spectroscopy tools displayed that Pt-NPs were fixed in the carbon substrate (Figure 27b,c), and the increased graphitic N in this catalyst can provide more electrons to Co and Pt. As compared to the Pt@Co SAs ZIF-NC, there were massive agglomerated Co particles, too large and randomly arranged Pt particles in Pt@Co ZIF-NC without Co-SAs, resulting in its structural damage and irregularity. Moreover, for the Pt 4f peak in Pt@Co SAs-ZIF-NC, the negative shift of the binding energy was 0.25 eV relative to commercial Pt/C, whereas that of Pt@Co ZIF-NC was 0.15 eV (Figure 27d,e), indicating the stronger interaction between Co-SAs and Pt-NPs. These evidences suggested that Co-SAs and the confinement of porous carbon favored the relatively uniform growth of Pt-NPs. More importantly, the introduction of Co-SAs offered more active sites in HER, and the synergistic effect between Co-SAs and Pt-NPs further enhanced the electrocatalytic performance.

It is worth mentioning that introducing M-SAs into metal supports can solve the problem of irregular morphology or complex composition of mainstream SACs, which is favorable to fully understanding the relationship between atomically dispersed metal centers and H_2 evolution performance. In a previous work, isolated Co atoms were doped into Ru nanosheets (NSs) via co-reduction of Ru(acac), which exhibited higher catalytic activity than pristine Ru and RuCo alloy.[218] As shown in **Figure 28**a, CoSAs substituted some of the atoms in Ru NSs, and dispersed in the hexagonal closepacked (hcp) Ru lattice positions, where Ru: Co atomic ratio was 94:6. Furthermore, DFT studies have shown that the substitution of a single Co atom extraordinarily reduced the energy barrier of water dissociation, resulting in better performance. Nevertheless, as the number of Co atom substitutions increased, the SA dispersion was destroyed, which lead to sluggish water dissociation. In addition, a higher amount of substitution also increased the electron density in the groove around Co atom, bringing difficulty to OH desorption (Figure 28b).

As a general rule, a relatively low loading amount of M-SAs in obtained SACs is a common issue. Due to the little distribution of M-SAs on the support and the long isolation distance between them, there are not enough active sites in the catalytic reaction. One of the feasible strategies to overcome this challenge is to make rational use of the synergy between the isolated active site.

4.2. Surface Chemistry of Single-Atom Alloys and Dual-Atom Catalysts

The synergistic effect of adjacent metal atoms also occurs on the surface layer of another metal host with isolated M-SAs stabilizing. Such a type of catalysts, in which M-SAs are doped into a less reactive metal host and no bonding interactions between adjacent active sites, are typically called “bimetallic single-site catalysts” or SAAs. As shown in **Figure 29**, there are four main geometric structures of the metal–metal interaction.[219] The rapid development of surface science, characterization techniques, as well as first-principles calculations, has reversed the embarrassing situation of synthesizing alloy

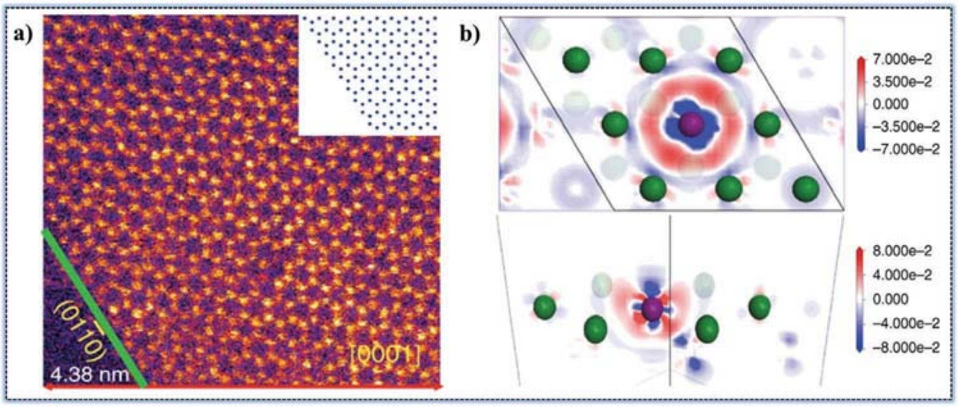

Figure 28. a) Atomic resolution HAADF-STEM images of Ru NSs were substituted by Co. Inset is a surface model of the Ru NSs. b) Top view (up) and side view (down) of the electron density alter after Co SA substitution. Green sphere: Ru; purple sphere: Co; red sphere: O; white sphere: H. Reproduced with permission.[218] Copyright 2018, Nature Publishing Group.

catalysts through chemical intuition and experience for many years. At the same time, it provides a foundational platform for controlling the catalytic activity of atomic surface chemistry and rationally designing heterogeneous catalysts.[220] Moreover, in recent studies involving the synergistic effect of adjacent MSAs, the chemical environment, and active species are the same, which limits the diversity of catalytic behaviors. The special alloy interface of SAAs can make the electronic structure of M-SAs change significantly. As a result, the *d*-orbitals of metal atoms become close to the narrow degree of homogeneous catalysts. It has been reported that such a characteristic can combine the performance of homogeneous and heterogeneous catalysts.[221]

Assuming that the bonding between heterometals is stronger than homometallic bonding, then in principle, it is generally possible to isolate one metal atom (denoted as A) in the atomic array of a less reactive "metal host" (denoted as M). When M is more inert than A, the concentration of M will increase, which ensures that there is no bonding between A atoms.[43b] In comparison, the alloy catalysts have shown dissimilar structures and properties from pristine metal clusters, including different structures at the same size as well as synergistic effects. Other examples have also demonstrated that the synergistic effects between metal and metal can change the catalytic behavior of catalysts.[222] For example, Au-Pd nanoparticles supported on TiO_2 had very high activity for H_2O_2 production,[223] alcohol oxidation,[224] and toluene oxidation.[225] The introduction of Pt-SAs into CoO_x/TiO_2 could improve the selectivity toward the target product (i.e., cinnamaldehyde) and enhance the hydrogenation performance.[226] Besides, the addition of Sn to Raney-Ni catalyst reduced the formation of methane during the H_2 evolution from biomass conversion and favored the bond-breaking of C—C bonds to promote H_2 generation.[227] It is worth noting that the characteristic of such SAAs is that there can be one or more A atoms but only one M.

The common feature of the above-discussed SAAs and typical SACs is that their catalytic reactions are both driven by single metallic sites. DACs, a type of catalysts with "dual-metal sites" reported in recent years, have attracted great attention as well.[228] For DACs, the structural characteristics of their multiatom components provide unique as well as remarkable catalytic performance. The active sites of DACs can be flexibly adjusted by regulating the ligand atom, coordination number, and structural distortion.[229] Such a strong chemical interaction between adjacent heteronuclear metal atoms is favorable to further improve the intrinsic activity and stability of SACs.[230] A phenomenon similar to SAAs is that the catalytic system of DACs also relies on synergistic effects between metals. Depending on the composition of the catalytic sites, dual-atom metal catalysts can generally be divided into i) isolated dual-metal atomic pairs; ii) binuclear homologous (also known as homonuclear) dual-metal atomic pairs and iii) binuclear heterologous (also called heteronuclear) dual-metal atomic pairs. The detailed information about these definitions has been extensively reviewed by Xu and co-workers very recently.[230b] Undoubtedly, until now, the research on DACs is still at the starting stage, especially in the hydrogen evolution.

Accordingly, taking full advantage of the synergistic effect between heterometals brings new opportunities to further control the catalytic properties of SACs. In this section, the dynamic evolution of bimetallic catalysts in H_2 production is explored from the following three aspects.

4.2.1. Electronic Effect

The "crown-jewel (CJ)" structure synthesized by substituting Au atoms at the apex of the Pd cluster showed high catalytic activity in hydrogen peroxide decomposition (**Figure 30**a). The researchers claimed that this phenomenon was attributed to the electron transfer process caused by the alloying effect, which made the gold atoms partially negatively charged.[231] This research finding provides promising guidance for the development of SAAs. In the design of SAAs, it is the key to enhancing the reaction activity that controls the electronic structure of the alloy by the introduced M-SAs. The electronic structure of solute atoms in metal will be largely tuned owing to the unique bond geometry of SAAs, which is usually characterized by the shift of the d-band center relative to the Fermi level.[232] For SAAs, the electronic states of highly dispersed metal atoms tend to be broadened after coupling with their solute metal, and finally, show an averaging effect.

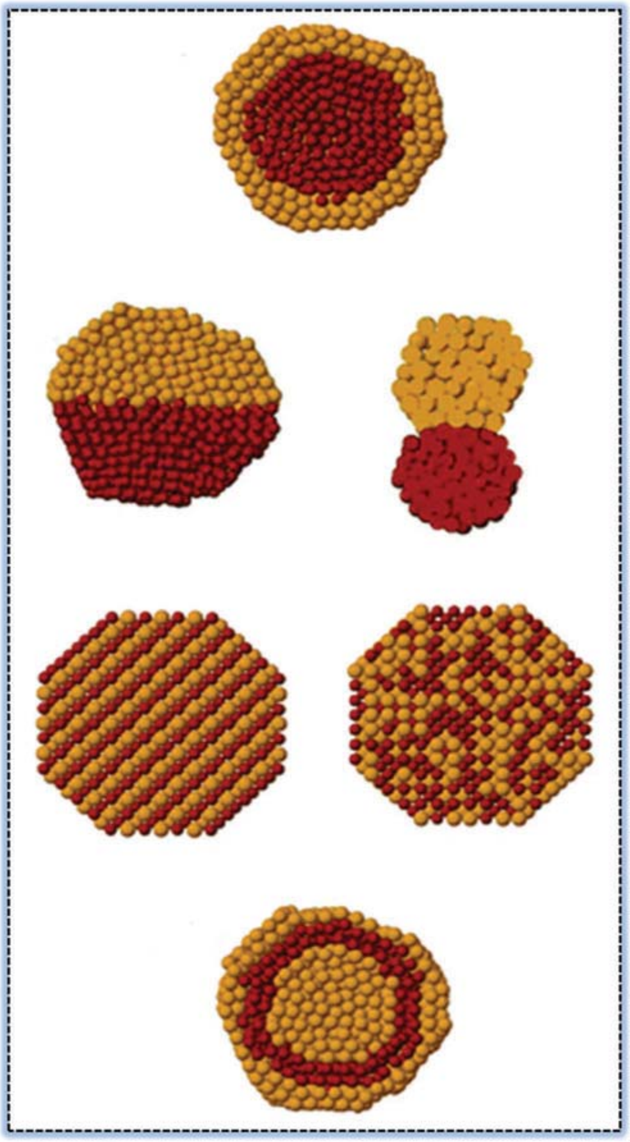

Figure 29. Schematic representation of some possible mixing patterns (cross sections). Top to bottom: Core–shell, linked monometallic nanoparticles, alloy (left) and mixed (right), three shells. The pictures show the clusters. Reproduced with permission.[219] Copyright 2008, American Chemical Society.

However, M-SA in some alloys still has a very narrow bandwidth in the substrate, and the adsorption behavior of the substrate on these M-SAs also deviates from the results predicted by the averaging effect of the two heterometals. There are some works have shown that the electronic structure of some SAAs appeared as the d-band of the solute metal became atomically narrow. In a previous report, using AgCu SAAs as a model catalyst, the narrowing of the Cu 3d state promoted the binding of adsorbed oxygen with π bonds so that the overall bonding strength of adsorbed oxygen was increased.[36] First, PDOS calculations suggested that the d-band of Cu was not disturbed by the surrounding coordination elements and maintained an electronic state similar to a “free atom”. The Cu center in the AgCu alloy was more electron-rich compared with the pure Cu center. Cu L_3 NEXAFS demonstrated the increase in the electron density of the Cu d-band. The charge density difference plots in Figure 30b showed that the charge density around the Cu ions increased. Furthermore, as shown in Figure 30c, the relatively concentrated DOS of AgCu made pz, px, and y all have two intersection points, bonding, and antibonding orbitals in the form of σ and π bonds, respectively. In this case, the adsorption of oxygen on AgCu can be greatly enhanced. Notably, the altering of electron density of the Cu center in these SAAs affected the adsorption process. Specifically, when the adsorbate electronegativity was less than that of Cu, the binding strength between adsorbate and alloy was weaker than that with element Cu. Otherwise, its binding strength with alloy was stronger than that with element Cu.[233] The above results revealed that adsorbate bonding can be weakened by the free-atom-like electronic structure, depending on the electronegativity of adsorbate and the population of valence electrons.

In addition to SAAs, the superior activity of DACs with “biatomic metal sites” is also attributed to the synergistic effects between the electronic structures of the two elements.[229c,234] In a recent work, XANES spectrum demonstrated that the total unoccupied density of states of Pt 5d character in Pt-Ru dimer was higher than that in the Pt foil, which meant that Pt-Ru dimer had better catalytic properties.[235] EXAFS spectrum confirmed that Pt existed in the form of SA, thus the dimer structure was prepared from Pt-SAs. Moreover, the change of the Ru electronic structure in this dimer catalyst was displayed in Figure 30d, Pt—Ru dimer had a higher energy shift of the edge than Ru metal, indicating that charge redistribution had occurred. DFT calculations revealed that Pt atoms had a noticeable influence on the electronic structure of Ru atoms. The simultaneous adsorption of two hydrogen atoms on Pt and Ru (Pt(2H)—Ru(2H)) would make both Pt and Ru gradually lose the metallicity, resulting in more vacancy states (Figure 30e). Furthermore, Pt could regulate the inertness of Ru to H through the synergistic effect between heterometals. In this case, H adsorption would induce the transformation of bimetallic dimer from metal to semiconductor, which should be the key reason for enhancing the performance of HER. Recently, Fan et al. developed W_1Mo_1-NG heteronuclear DAC based on polyoxometalates (POMs) self-assembly chemistry.[230a] This DAC was composed of O-coordinated W—Mo heterodimer anchored in N-doped graphene, where heteronuclear W—Mo was stabilized in the NG vacancies via W—O and Mo—O bonds. XPS survey spectrum demonstrated that the electronic structure of the W—Mo heterodimer changed owing to its local structural perturbation, meaning that its local electronic structure could be significantly regulated by adjusting the W/Mo ratio. EXAFS fitting also proved this point. Combined with theoretical calculations and the optimum configuration of heteronuclear W—Mo atoms was W—O—Mo—O—C configuration with strong covalent interaction. The electron delocalization of this unique O-coordinated W—Mo heterodimer improved HER kinetics.

4.2.2. Interfacial Effect

SAAs, as a type of catalyst with a small amount of dispersed and isolated M-SAs on the surface of the metal host, represents

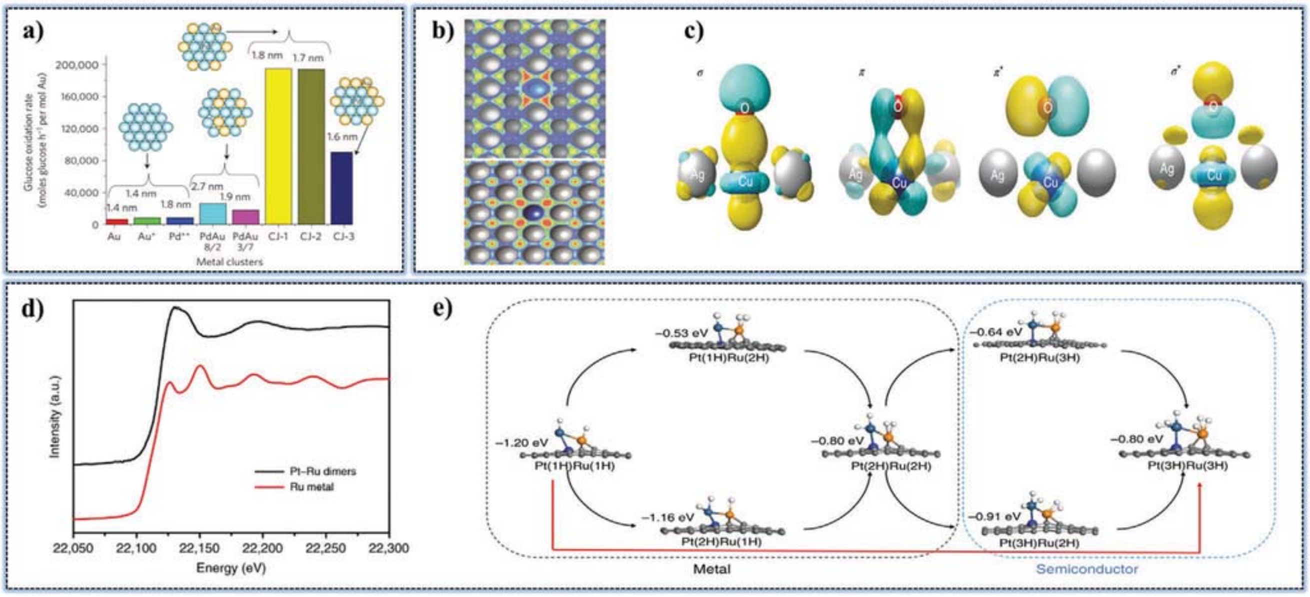

Figure 30. a) Comparison of the catalytic activity of CJ-Au/Pd, Au, Pd, and Pd/Au alloy NCs for aerobic glucose oxidation. Reproduced with permission.[231] Copyright 2012, Nature Publishing Group. b) Computed charge density difference plots along the (110) and (100) planes in $Ag_{31}Cu_1$ and c) Schematic diagram of real space bonding between O and Cu in AgCu. Reproduced with permission.[36] Copyright 2018, Nature Publishing Group. d) Normalized XANES spectra at the Ru K-edge. e) Influence of adsorption energies on the atom structures of different H adsorption. Reproduced with permission.[235] Copyright 2019, Nature Publishing Group.

the complementary surface science model of two metals, which provides a promising research platform for catalytic activity and selectivity.[236] Such SAAs with isolated bimetallic centers can provide a unique surface process, promoting the dissociation of reactant molecules to form intermediates.[222a] As early as 1998, Besenbacher and co-workers introduced Au to the surface of Ni catalyst to improve the efficiency of the steam reforming reaction.[237] The combination of scanning tunneling microscope and DFT calculation confirmed that the alloying Au atoms were favorable to inhibit the formation of carbon-containing compounds on Ni catalyst surface and prevent the Ni catalyst from being poisoned. There are many studies since then that have shown that the more active metal elements in the alloy were stabilized on the surface by adsorbate. Such an interesting phenomenon, that adsorbates had stronger binding with metals, was explained as a reverse segregation effect.[220b] Later, Tierney et al. found that H_2 activation preferred to be at the isolated Pd sites, and hydrogen atoms diffused to the weaker Cu center.[238]

As for Pt-based SAAs, almost all reports are about anchoring atomic Pt on the Cu surface, and few of them have been applied to electrocatalytic reactions. Pd, which has a lattice constant similar to that of Pt, may be an ideal substrate for electrocatalytic Ptbased SAAs.[239] Zhang and co-workers successfully deposited Pt-SAs on the (100) and (111) surfaces of Pd-NPs through ALD method and synthesized octahedral Pt/Pd SAAs.[240] HAADF-STEM images illustrated that there were both Pt clusters (**Figure 31**a) and isolated Pt-SAs (Figure 31b) on the surface of octahedral Pd particles, which was confirmed by subsequent XANES spectra. Such a different deposition phenomenon was caused by the difference in surface energy of (111) and (100). Then, they determined the occupancy of the 5d states of Pt. The results indicated that the total unoccupied density of states of Pt 5d character in octahedral Pt/Pd SAA (0.8176) was higher than that in Pt foil sample (0.6754), suggesting that the interaction between PtSAs and Pd-NPs surfaces was much stronger. Moreover, EXAFS spectra analysis demonstrated that the coordination number of Pt—Pd and Pt—Pt in the octahedral Pt/Pd SAA were 0.8 and 1.7, respectively, which were lower than that of the cubic Pd@Pt catalyst (2.7 and 3.3, respectively). These results revealed that Pt existed on the octahedral Pd surface in the form of SAs and clusters, whereas did not diffuse into the Pd lattice. By comparison, a thin Pt shell was formed on cubic Pd. DFT calculation was employed to study the enhancement mechanism of Pt atoms on the Pd surface with different structures for the electrocatalytic HER and ORR. Pt-SAs on octahedral Pd(111) could strongly absorb H^+ during the Volmer step ($H^+ + e^- \rightarrow H^*$), and the second and third H adsorptions on Pt were promoted, as shown in Figure 31d. Depending on the above characteristics, the HER activity of this Pt/Pd SAA (23.5 A mg^{-1}) at an overpotential as low as 0.05 V is 54.6 times higher than that of commercial Pt/C (0.43 A mg^{-1}). Earlier, Li and co-workers reported that Cu-Pt dual sites alloyed with Pd NRs (Pd/Cu-Pt NRs) were a more attractive catalyst for HER than commercial Pt/C catalysts.[241] The characterization results showed that Cu and Pt existed in the form of atomic dispersion, and coordinated with each other or Pd atoms. In the Pt EXAFS curve of the sample, the Pt—O distance was shorter than that of PtO_2, suggesting the unsaturated coordination of Pt on the surface of Pd/Cu-Pt NRs. The remarkable HER activity of this SAA was attributed to the Cu atoms adjacent to Pt-SAs that balance the interaction between H and Pt atoms.

The interfacial effects can optimize the chemisorption of precursor molecules (such as H^+ or H_2O) and reactive

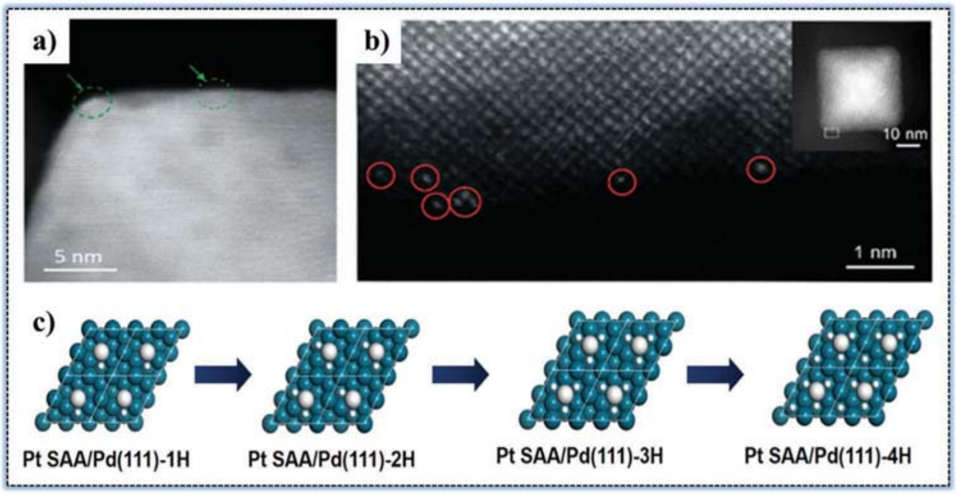

Figure 31. HAADF-STEM image of octahedral Pt/Pd SAA. a) Brighter atoms (dashed circles) show the presence of Pt clusters and b) Individual bright spots (solid circle) indicate the presence of isolated Pt SAs, where inset shows an individual octahedral Pt/Pd SAA particle. c) Optimized adsorption configurations of H atoms on Pt/Pd(111) SAA. The coverages of hydrogen are 0.25, 0.50, 0.75, and 1.00 ML, respectively. Reproduced with permission.[240] Copyright 2019, American Chemical Society.

intermediates (i.e., H*) to accelerate HER kinetics.[13] A prominent example is RuAu SAA, where the incompatibility between Au and Ru created unique electronic and geometric structures.[232b] To establish the catalysis model of RuAu SAA for HER, DFT calculations were performed on RuAu(001), Ru(001), and Pt(111) facets. The H_2O dissociation on RuAu(001) and Ru(001) was easier than that of Pt(111), and the higher energy barrier of RuAu(001) was ascribed to structural perturbation induced by alloying. Due to the interfacial effect of Ru-Au, the adsorption of H_2O and protons achieved an outstanding balance. Specifically, Ru atoms acted as the first active sites for capturing and dissociating water molecules, while Au atoms served as the second active sites to achieve the absorption of protons and promote the formation of H_2 (**Figure 32**a–d). In another report, Wang and co-workers found that the dual-metal Rh—Fe interbond formed by Rh-SAs adjacent to Fe could encourage the conversion of Fe-NPs to Fe-SAs at low temperatures.[242] As illustrated in Figure 32e,f, Fe embedded in nitrogendoped carbon hollow spheres (NCS) inhibited the formation of Rh-NPs. Furthermore, the Rh—Fe—N_4 interface formed after introducing Rh-SAs into the crystal lattice would reversely detach Fe clusters, which resulted in the shrinkage of Fe_{10} to Fe_9 (Figure 32g,h). Such synergistic effect in the bimetallic Rh-Fe interface significantly optimized ΔG_H.

4.2.3. Steric Effect

The particle size of TM-based catalysts generally prefers to be in the range of nanometer.[243] This makes it more difficult to study the influence of metal particle size on electrochemical performance at the atomic scale. Fortunately, the bimetallic active sites introduced by adding two cations can not only regulate the coordination environment of the metal sites to enhance the catalytic activity, but also provide a steric hindrance to alleviate agglomeration during the pyrolysis process.[51,244] In particular, such a steric effect between heterogeneous atoms can enlarge the distance between adjacent atoms,

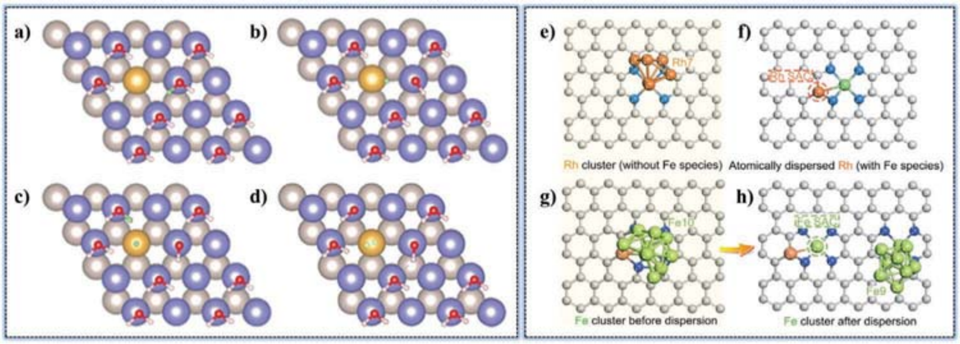

Figure 32. a,b) Schematic illustration of H_2 evolution on RuAu SAA. (a) Adsorption of water molecule on Ru atom. (b) H_2O dissociation on Ru atom and H adsorption on Au atom. c) H_2O activation on another Ru atom nearby, and d) H_2 formation on Au atom. Spheres: blue, top layer of Ru; gray, side layer of Ru; golden, Au; red, O; white and green, hydrogen. Reproduced with permission.[232b] Copyright 2019, John Wiley and Sons. e–h) Mechanism of the interaction between adjacent Fe and Rh atoms on the stability. (e) Rh_7 cluster without Fe species adding. (f) Rh-SA formed with the assistance of Fe species. (g) Fe_{10} clusters and NCS linked by Rh-SA and (h) the formation of Rh—Fe dual-metal bonds. Reproduced with permission.[242] Copyright 2020, John Wiley and Sons.

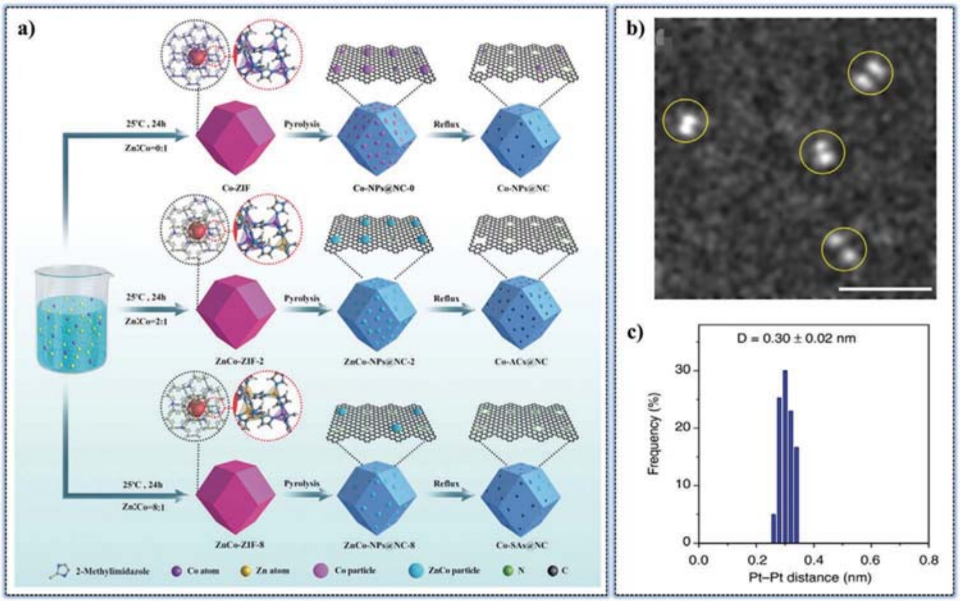

Figure 33. a) The synthesis and structure diagram of ZnCo-ZIFs with different Zn/CO molar ratios. Reproduced with permission.[245] Copyright 2019, John Wiley and Sons. b) Aberration-corrected HAADF-STEM images of Pt_2 dimers. Scale bars, 1 nm. c) Statistical Pt—Pt distance in more than 80 pairs of Pt_2 dimers. Reproduced with permission.[246] Copyright 2017, Nature Publishing Group.

controlling the metal atoms with different aggregation degrees. After precisely adjusting the doping amount of Zn in the bimetallic ZnCo-ZIFs precursor, it was found that Co atoms can be geometrically isolated by the introduced Zn atoms to varying degrees during pyrolysis.[245] As shown in **Figure 33**a, when the molar ratio of Zn/Co was 0:1, 2:1, and 8:1, the isolation degree was the smallest (nanoparticle size), middle (atomic cluster size), and highest (atomic level), respectively. The subsequent HAADF-STEM images confirmed the formation of Co clusters and SAs. Surprisingly, this steric effect caused by doping with heterometallic atoms acted like a fence. More interestingly, the steric hindrance could be observed in DACs with homo-metal sites as well.[246] First, in order to obtain Pt_1/graphene SAC, $MeCpPtMe_3$ was anchored on the graphene surface with a lot of defect sites. Then, Pt_1SAs were employed as the nucleation sites for the selective deposition of the secondary Pt atom during the second ALD cycle, and finally obtaining a Pt-Pt dimer DAC (Pt_2/graphene). It can be clearly observed through aberration-corrected HAADF-STEM measurements that the steric hindrance induced during synthesis well isolated the Pt_1-SAs, where the Pt—Pt distance in dimers was longer than the Pt—Pt bond in Pt bulk (Figure 33b,c).

The development of pluralistic catalysts to achieve high reactivity and selectivity for complex reactions is the general trend of the future development of energy applications. In this case, SAA_S and DACs with unique properties provide a new idea for the design of SACs.

5. Recent Advances in SACs for Hydrogen Generation

Hydrogen is an earth-abundant element and mainly exists in the form of water, hydrocarbons, and biomass in nature. However, to make these H elements into H_2 fuel, it is first necessary to extract them through other forms of energy, such as light, electricity, or heat.[247] Noble metal nanocatalysts have been widely applied in H_2 production. Unfortunately, shortcomings such as high price, poor durability, and low utilization limit their commercial applications. As mentioned above, SACs can utilize precious metal and non-precious metal atoms with maximum efficiency, greatly reducing the use and cost of precious metals. Furthermore, the excellent performance of SACs in activity, selectivity, and stability provides a feasible way for large-scale production and industrial application of hydrogen energy. Based on this, this section will comprehensively review the current progress of SACs in the common hydrogen generation reactions, including WGSR, electrocatalytic HER, and photocatalytic H_2 evolution. The future prospect and development direction of SACs are revealed from both experimental and theoretical aspects.

5.1. Hydrogen Production from Water Gas Shift Reaction

WGSR ($CO + H_2O \leftrightarrow CO_2 + H_2$) is a type of crucial energy conversion reaction that employs fossil fuels as raw materials to produce H_2, MeOH, and synthetic ammonia.[248] Besides, it is also used to remove CO pollution. Up to now, the major source of H_2 is still the catalytic steam reformation relying on fossil energy.[249] Nevertheless, the weaknesses of this H_2 production strategy are also very obvious, for example, low thermal stability, complicated operation, and working at high temperatures or high H_2O/CO ratio.[250] The catalytic performance plays a decisive role in solving this issue. In this case, the emergence of supported SACs is expected to substitute for the convent commercial catalysts.

As early as 2003, Professor Maria Flytzani-Stephanopoulos skillfully used NaCN to wash away the NPs on the catalyst, and

© 2022 Wiley-VCH GmbH

found that the WGSR activity of this catalyst was still maintained, which fully proved that singly dispersed Pt and Au atoms were the real active sites.[8a] Such a catalyst with excellent performance is recognized as a milestone, leading to the rapid development of other SACs for WGSR. Fe-based SACs are generally used for high-temperature WGSR, while Cu-based or MoS_2-based SACs are mostly employed for low-temperature WGSR. In recent years, a large number of SACs that produce hydrogen through WGSR have been reported, including Ir/FeO_x,[53a,123,242] Au/FeO_x,[68] Pb/FeO_x,[135] Rh/TiO_2,[251] Pt/TiO_2,[252] as well as Au/TiO_2.[253] In WGSR, the Mo_2C surface that is doped with Pt-SAs has similar activity as the Pt catalytic system. Unlike Pt(111), the inhibition of CO_2 desorption by Mo_2C promotes the separation of H. On the contrary, introducing Pt-SAs into Mo_2C can significantly increase the release of H_2. For Pt@Mo_2C(001) SAC, the synergistic effect of bimetallic Mo—Pt is beneficial to H_2 evolution.[173b] The initial adsorption and activation process of H_2O occurs at the Mo site. Subsequently, H_2O dissociates spontaneously to form H species, and migrates to unstable Pt sites to release H_2. Interestingly, the major product on the Pt@Mo_2C(001) surface is the trans-COOH species (**Figure 34**a). In another report, the total CO conversion rate of Rh/TiO_2 SAC with 0.37% loading was as high as 95%, and the WGSR activity was about four times higher than that of NPs catalyst (Figure 34b).[251] Such excellent performance can be ascribed to the fact that H_2 generated in WGSR does not react with CO and CO_2 to form CH_4.

In general, oxides are the most commonly used as SAC support for H_2 production from WGSR, and H_2O is dissociated at the oxygen vacancy sites in oxide support. The introduction of M-SAs into oxides can promote the formation of O-vacancies on the oxide support, and thus the enhancement of the reactivity. It is worth noting that the mechanisms of WGSR are not identical. It has been generally accepted that the WGSR follows three mechanisms, including i) surface redox, ii) carboxyl, and iii) formate mechanism.[176a,254] Temperature-programmed surface reaction (TPSR-MS) experiment under WGS flow is a common method to distinguish the three mechanisms.[255] In the redox pathway, SACs always generate H_2 first and then CO_2, such as Ir/FeO_x[53a] and Pd/FeO_x.[135] CO is oxidized through the Mars–van Krevelen mechanism. The absorbed CO reacts directly with the lattice O near SAs to form CO_2. For the carboxyl/formate mechanism, COOH/HCOO intermediates are produced by the reaction of absorbed CO with OH groups adjacent to SAs. It can be seen from Figure 34c that the priorities of the three reaction pathways are not the same at different reaction temperatures.[252] Moreover, the generation step of OCOH* is similar to transalkylation in the formate pathways. An Ir_1/FeO_x SAC with synergistic dualmetallic sites has been reported, which provides a redox mechanism different from the typical associative mechanism for the formation of formate or carboxyl intermediates.[242] Typically, H_2O is decomposed into OH* and H* on Ir_1-SAs and the first adjacent O atom that is bonded with Fe, respectively.

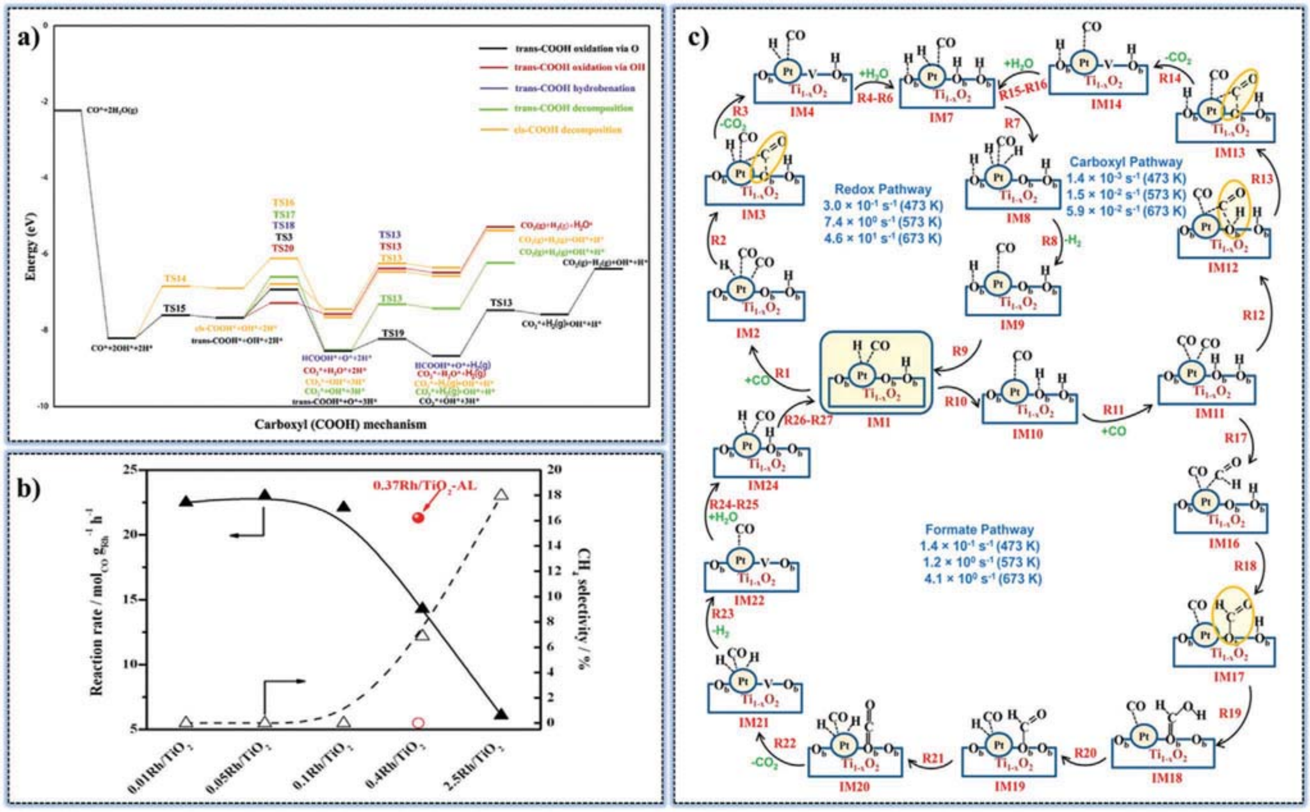

Figure 34. a) Diagram of the WGS reaction on the Pt@Mo_2C(001) surface, potential energy had been Calculated. Reproduced with permission.[173b] Copyright 2017, American Chemical Society. b) Specific reaction rate (solid symbol) and CH_4 selectivity (open symbol) Rh/TiO_2 catalysts. Reproduced with permission.[251] Copyright 2017, John Wiley and Sons. c) Various WGS reaction steps on Pt/TiO_2 SAC. Reproduced with permission.[252] Copyright 2017, American Chemical Society.

Next, the O-vacancies on the support surface are formed by the adsorbed CO on Ir_1. Subsequently, H will migrate from absorbed OH* to Ir_1, and eventually react with another H* to produce H_2.

5.2. Hydrogen Evolution by Water Electrolysis

Water splitting (H_2O (l) → H_2 (g) + 1/2 O_2 (g), $\Delta G^\circ = +237.2$ kJ mol^{-1}, $\Delta E^\circ = 1.23$ V vs normal hydrogen electrode (NHE)) is believed to be the most promising and sustainable way toward H_2 production with zero-carbon-emission. The HER ($2H^+$ (aq) + $2e^-$ → H_2 (g)) is a half reaction of water electrolysis/electrochemical water splitting at the cathode, as illustrated in **Figure 35**a. In comparison with the reforming of fossil fuels, there are many advantages of H_2 generation through the HER, including i) abundant and renewable raw materials, that is, water, ii) pollution-free production process, iii) high purity of H_2, iv) storable energy, and v) complementary advantages with other renewable energy sources. However, the energy consumption and cost of H_2 evolution by water splitting are relatively high, because the water splitting reaction is not prone to occur in thermodynamics and kinetics, and great reaction barriers require to be overcome for high efficiency.[256] In other words, energy input is needed to overcome the barriers in HER from water, namely the overpotential (η, the potential difference between the value required for a given electrochemical reaction and the thermodynamic value). Therefore, developing high-electrode catalysts to minimize the overpotentials for generating H_2 efficiently is of great significance to the application of water electrolysis. As mentioned above, the HER is an electron transfer process in electrochemical water splitting that occurs at the cathode. Protons in acidic media or H_2O molecules in alkaline media are reduced to H_2 on the electrode surface with minimum external potential applied (Figure 35b). The difference in pH value of electrolytes will affect the reaction steps of HER. Volmer–Heyrovsky (Equation (1)) or Volmer–Tafel (Equation (2)) routes are involved to investigate the HER mechanisms in acidic and alkaline electrolytes.[257]

$$H^+ + e^- \rightarrow H^*, H^* + H^+ + e^- \rightarrow H_2 \quad (1)$$

$$H^+ + e^- \rightarrow H^*, H^* + H^* \rightarrow H_2 \quad (2)$$

where H_{ads} represents the adsorbed H atoms on the catalytically active sites (*) of the electrode surface.

In particular, the Gibbs free energy of H adsorption (ΔG_{H^*}) is typically a key indicator to evaluate the HER activity. According to the Sabatier principle,[259] if the interaction between catalysts and the reactive intermediates is too strong or too weak, the reaction will be slowed down. In the "volcano-type" plot established by Parson, the $j0$ value is associated with ΔG_{H^*}.[260] As shown in **Figure 36**a,b, the closer the ΔG_{H^*} value is to zero, the higher

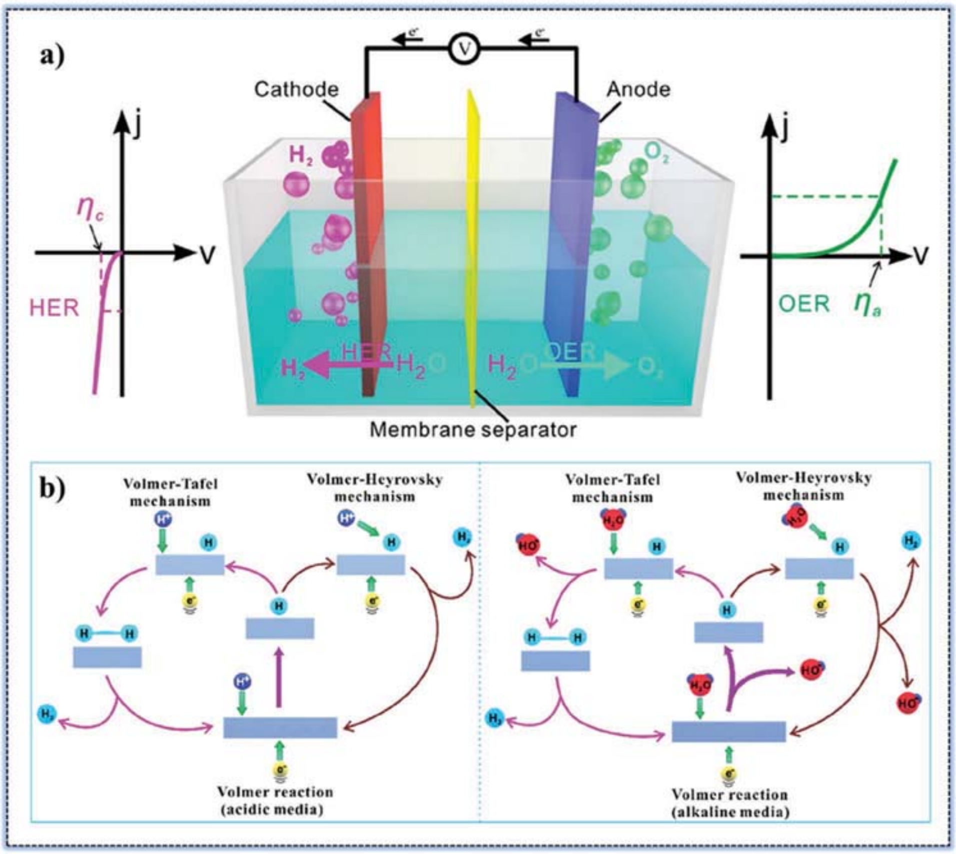

Figure 35. a) Schematic diagram of water electrolysis involved HER and OER. b) Mechanistic illustration of H_2 evolution on the surface of an electrode in acidic (left) and alkaline (right) environment. Reproduced with permission.[258] Copyright 2020, American Chemical Society.

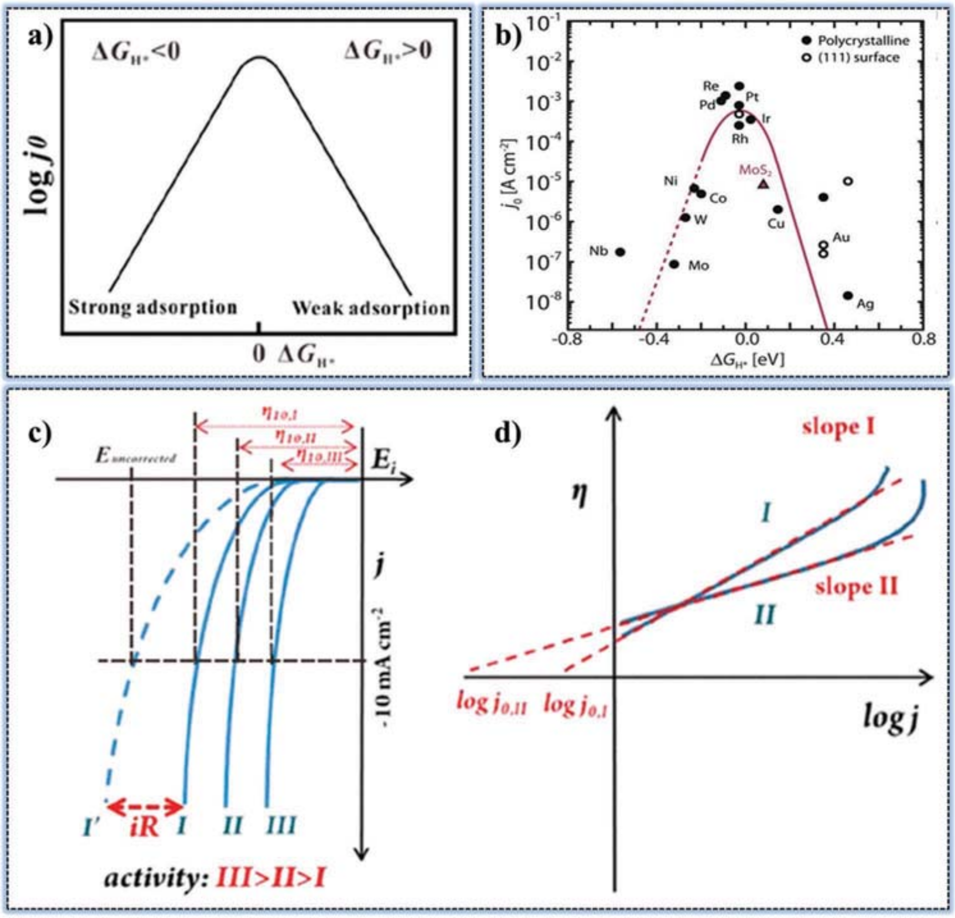

Figure 36. a) Relationship between $j0$ and ΔG_{H*} under the assumption of a Langmuir adsorption model. Reproduced with permission.[260] Copyright 1958, Royal Society of Chemistry. b) HER volcano plot for metals-supported MoS_2. Reproduced with permission.[13] Copyright 2017, The American Association for the Advancement of Science. c) Her polarization curve for *iR* correction and overpotential measurement. d) Tafel plots of Tafel slopes and exchange current densities. Reproduced with permission.[162b] Copyright 2019, John Wiley and Sons.

the H_2 evolution activity (HER log $j0$) is. Meanwhile, it should be noted that the adsorption and desorption of H atoms on the catalyst are in competition with each other. With the rapid development of computer science, DFT calculation has become a momentous tool to obtain the ΔG_{H*} value.[23b,258,261] Specifically, the indicators for evaluating HER catalyst performance also include overpotential (η), Tafel slope (b), faradaic efficiency, turnover frequency (TOF), hydrogen bonding energy, etc. Among them, η_1 (onset overpotential), η_{10}, and η_{100} correspond to current densities of 1, 10, and 100 mA cm^{-2}, respectively.[4a,162b,165] In particular, η_{10} is usually used to evaluate HER activity, and a smaller η_{10} indicates higher activity (Figure 36c). Moreover, the Tafel slope is closely related to HER rate. As shown in Figure 36d, the smaller the Tafel slope, the faster the electron transfer kinetics. More evaluation approach of HER catalysts has been discussed thoroughly in the work by Wong and co-workers.[258]

As is shown above in our paper, three main factors that can influence the SACs activity have been summarized: the geometric structure and electronic properties of the support, the coordination environment of the metal atom, as well as the uniformity of the active site. Because the electronegativity of M-SAs is different from that of coordination atoms, the electrons of M-SAs will migrate to the support. This electron transfer will lead to more unoccupied *d*-orbitals, which favors the adsorption of hydrogen species. On the basis of above mechanism, for a complex electrochemical environment, especially under alkaline conditions, the efficient HER SACs boost the process of industrial H_2 production. All in all, SACs have been extensively studied in HER and exhibited exciting performance (**Table 1**).

5.2.1. HER in Acidic Media

The HER in acidic environment is carried out by the reduction of protons in the electrolyte ($2H^+ + 2e^- \rightarrow H_2$).[23f] Specifically, acidic HER involves three key steps (Equations (3)–(5)):

$$H^+ + e^- + * \rightarrow H*(\text{Volmer}) \tag{3}$$

$$H^+ + e^- + H* \rightarrow H_2 + *(\text{Heyrovsky}) \tag{4}$$

$$2H* \rightarrow H_2 + *(\text{Tafel}) \tag{5}$$

Under acidic conditions, the HER precursor is a proton, which can easily receive electrons from the cathode. As a result,

Table 1. HER Performance of State-of-the-Art SAECs in different reaction environments.

Electrocatalyst	Single active species	Loading	$-\eta_{10}$ [mV]	mass activity [A mg^{-1}@mV]	Tafel slope [mV dec^{-1}]	Stability	TOF [s^{-1}@mV]	Electrolyte	Ref.
Pt-MoS_2	Pt	1.7 wt.%	60		96	5000 CV cycles		0.1 м H_2SO_4	[40]
Pt-1T′ MoS_2	Pt	1.04 wt.%	180		88.4	5000 CV cycles or 20 h		0.5 м H_2SO_4	[150]
Pt-SAs/MoS_2	Pt	5.1 wt.%	≈59	17.14@50	31	1000 CV cycles or 2 h	47.3@100	0.5 м H_2SO_4	[67]
SA Co-D 1T MoS_2	Co	3.54 wt.%	42		32	10 000 CV cycles or 240 h	7.82@100	0.5 м H_2SO_4	[158c]
Pt_1@Fe—N—C	Pt	2.1 wt.%	60		42			0.5 м H_2SO_4	[197]
K_2PtCl_4@NC-M	Pt	≈1.92 wt.%	11	5.8@20	21	40 h	6.1@20	0.5 м H_2SO_4	[262]
$Mo_2TiC_2T_x$—Pt_{SA}	Pt	≈1.2 wt.%	30	8.3@77	30	10 000 CV cycles or 100 h		0.5 м H_2SO_4	[26d]
			61		36	5000 CV cycles		0.5 м PBS	
Pt SAs/DG	Pt	2.1 wt.%	23	26.2@50	25	5000 CV cycles or 24 h		0.5 м H_2SO_4	[191]
Pt SASs/AG	Pt	0.44 wt.%	12	22.4@50	29.33	2000 CV cycles or 24 h		0.5 м H_2SO_4	[263]
Pt/NiS@Al_2O_3	Pt	2.8 wt.%	≈34		≈35	120 h		0.5 м H_2SO_4	[264]
400-SWNT/at-Pt	Pt	0.75 at %	27		38	5000 CV cycles		0.5 м H_2SO_4	[213]
Ru_{SA}-N-S-$Ti_3C_2T_x$	Ru	1.2 wt.%	76		90	3000 CV cycles or 16 h	0.52@100 0.87@150 1.50@200	0.5 м H_2SO_4	[90]
Pd-MoS_2	Pd	1.0 wt.%	78		80	5000 CV cycles or 100 h	2.77@100	0.5 м H_2SO_4	[159]
Ru SAs@PN	Ru	0.33 wt.%	24		38	5000 CV cycles or 24 h	1.67@25 4.29@50	0.5 м H_2SO_4	[88a]
Co-NG-MW	Co	≈1.1 wt.%	127		80	1000 CV cycles or 120 h	0.385@100	0.5 м H_2SO_4	[265]
Ni/np-G	Ni	≈4–8 at %	≈180		45	1000 CV cycles or 120 h	0.8@300	0.5 м H_2SO_4	[114]
A-Ni—C	Ni	1.5 wt.%	34		41	4000 CV cycles or 25 h		0.5 м H_2SO_4	[212]
SAP-Mo_2C-CS	P	3.6 wt.%	36		38.1	1000 CV cycles or 11 h	0.23@50 1.12@100	0.5 м H_2SO_4	[266]
SANi-I	I	1.2 wt.%	34.6			10 000 CV cycles or 24 h		1.0 м KOH	[24]
Ru/N,S-GO	Ru	7.2 wt.%	26	0.352@100	30	10 000 CV cycles or 50 h		1.0 м KOH	[66]
Ru SAs/NCNFs	Ru	2.96 wt.%	η_{20} = 34	0.39@100	71	20 h		1.0 м KOH	[267]
Ru/np-MoS_2	Ru	7.94 at %	30		31	40 h		1.0 м KOH	[76]
Ni_5P_4-Ru	Ru	3.83 wt.%	54	1.601@50	52	120 h		1.0 м KOH	[63]
Ru-NC-700	Ru	2.01 at %	47		14			0.1 м KOH	[86c]
			12			10 000 CV cycles		1.0 м KOH	
			29		28			0.5 м H_2SO_4	
Pt/NiRu-OH	Pt	≈1.0 wt.%	38	1.01@50	39	5000 CV cycles or 30 h		1.0 м KOH	[268]
PtSA-NiO/Ni	Pt	1.14 wt.%	26	20.6@100	27.07	5000 CV cycles or 30 h	5.71@50	1.0 м KOH	[269]
			27		31.94			1.0 м PBS (pH = 7.0)	
Pt@PCM	Pt	0.53 wt.%	139		73.6	1000 CV cycles or 5 h		1.0 м KOH	[118]
			105		65.3		43.6@500	0.5 м H_2SO_4	
Co_1/PCN	Co	≈0.3 wt.%	151		52		0.22@50, 5.98@100	0.5 м H_2SO_4	[33]
			89			5000 CV cycles or 24 h		1.0 м KOH	
$Mo_1N_1C_2$	Mo	1.32 wt.%	154		86	1000 CV cycles	0.082@50, 0.262@100 0.842@150, 2.59@200	0.5 м H_2SO_4	[116]
			132		90		0.148@50, 0.465@100, 1.46@150	0.1 м KOH	

© 2022 Wiley-VCH GmbH

Table 1. Continued.

Electrocatalyst	Single active species	Loading	$-\eta_{10}$ [mV]	mass activity [A mg^{-1}@mV]	Tafel slope [mV dec^{-1}]	Stability	TOF [s^{-1}@mV]	Electrolyte	Ref.
W-SAC	W	1.21 wt.%	105		58	10 000 CV cycles or 11 h			
			85		53		1.16@40 3.40@80 6.35@120	0.1 M KOH	[270]
Ni/β-Mo$_2$C	Ni		155		79	1000 CV cycles or 10 h		0.5 M H$_2$SO$_4$	[173a]
			149		66			1.0 M PBS (pH = 7.0)	
			157		61			1.0 M KOH	
Pt/np-Co$_{0.85}$Se	Pt	≈1.03 wt.%	58	1.28@100	39			1.0 M KOH	[271]
			55	1.32@100	35	3000 CV cycles or 40 h	3.93@100	1.0 M PBS (pH = 7.0)	
			58	13.57@100	26			0.5 M H$_2$SO$_4$	
PtSA-NT-NF	Pt	1.76 wt.%	24	0.07@50	30	5000 CV cycles		1.0 M PBS (pH = 7.2)	[26a]
Pt-SAs/MoSe$_2$	Pt	4.7 wt.%	67	43.65@100	28		151@200	0.5 M H$_2$SO$_4$	[112]
			29	34.37@100	34	1000 CV cycles	6.21@50	1.0 M KOH	
Pt-SAs/MoS$_2$		5.1 wt.%	59	47.47@100	31		172@200	0.5 M H$_2$SO$_4$	
			65	6.75@100	50	1000 CV cycles	1.02@50	1.0 M KOH	
Pt-SAs/WS$_2$		4.1 wt.%	32	130.21@100	28		273@200	0.5 M H$_2$SO$_4$	
			108	2.46@100	55	1000 CV cycles	0.56@50	1.0 M KOH	
Pt-SAs/WSe$_2$		4.9 wt.%	118	11.20@100	41		101@200	0.5 M H$_2$SO$_4$	
			126	2.20@100	59	1000 CV cycles	0.52@50	1.0 M KOH	

the activity of HER in acidic media is relatively high when there are enough protons in the electrolyte. By comparison with alkaline and neutral conditions, the acidic HER is usually the first choice for H_2 evolution by water reduction.[155,186] In addition, the powerful and flexible proton exchange membrane electrolyzers in acidic media allow water electrolysis to couple with wind and solar energy.[272] Up to now, many SACs toward acidic HER have been reported.[26d,40,264,265]

Pt-based materials have been believed to be the most effective HER catalysts in acidic environments.[273] Especially, Pt-based SACs are able to maximize the HER activity of Pt metal sites. Deng et al. proposed for the first time that doping Pt-SAs into the in-plane domain of MoS_2 nanosheets can significantly enhance the acidic HER activity and stability of MoS_2.[40] According to the DFT calculations, Pt-MoS_2 formed a new electronic state, and the adsorption behavior of H atoms on adjacent S sites can be well regulated by isolated Pt atoms. Yi et al. reported a site-specific electrodeposition (SSED) technique that can be used to synthesize SACs supported with various metals (e.g., Pt, Pd, Rh, Cu, and so on).[67] MoS_2 was chosen as support to deposit metals at the characteristic site through surface-limited reaction, namely UPD process, and the metals were confined at the atomic scale (**Figure 37**a,b). Compared with the most advanced SAECs, the as-fabricated Pt-SAs/MoS_2 SAC exhibited competitive activity with low η_{10} of ≈59 mV and stability in acidic HER. Amorphous Mobased oxides may also be outstanding supports for Pt-based SAECs.[274] The Pt-SA/α-MoO_x electrocatalyst was synthesized by anchoring dispersed Pt-SAs on amorphous MoO_x through a wet chemical-calcination hybrid strategy.[275] As shown in Figure 37c, the mass activity of Pt corresponds to 40 times (52 A mg_{Pt}^{-1}) and 47.6 times (161.7 A mg_{Pt}^{-1}) over Pt/C at an overpotential of 50 and 100 mV, respectively. The synergistic effect between unsaturated Pt-SAs and α-MoO_x with abundant oxygen-vacancies is the key to the remarkable catalytic performance of Pt-SA/α-MoOx. Furthermore, the successful loading of other M-SAs such as Ir, Au, and Pb atoms on α-MoO_x reflected the universality of the synthesis method as well. In another recent report, Pt-SAs were anchored on N-doped mesoporous hollow carbon sphere (Pt_1/NMHCS).[276] Due to the strong EMSI effect induced by the unique $N_1{-}Pt_1{-}C_2$ coordination structure, this Pt_1/NMHCS SAC exhibited an outstanding HER performance in acidic solution with an ultralow η_{10} of 40 mV and a Tafel slope of 56 mV dec^{-1}. According to DFT calculations, the $N_1{-}Pt_1{-}C_2$ structure with the electron-rich state and strong reduction ability favored the reduction of absorbed H^+. Additionally, Pt-SAs dispersed in tungsten suboxide (denoted Pt SA/m-WO_{3-x}) accelerated the kinetics of H insertion/extraction ($Pt + H^+ + e^- \leftrightarrow Pt{-}H$, $Pt{-}H + H^+ + e^- \leftrightarrow Pt + H_2 \uparrow$).[277] According to the experimental measurements, the as-prepared SAC could deliver a current density of 10 mA cm^{-2} at a super low overpotential of only 38 mV, while the mass activity was 16 times that of commercial Pt/C. The authors claimed that this work was a strategy combining electronic effect and spillover effect, in which the support effect was the key to the enhancement of HER activity (Figure 37d). It may be reasonable because the interface between Pt-SAs and WO_{3-x} strengthens the H spillover effect and shortens the H diffusion length.[278]

Recently, Sun et al. designed a mild and facile approach to anchored atomically dispersed Pt atoms on aniline-stacked graphene (AG) support for HER.[263] As depicted in **Figure 38**a, graphene was modified via strong $\pi{-}\pi$ interaction of aniline molecules. DFT suggested that the edge-to-face configuration in aromatic $\pi{-}\pi$ interactions was thermodynamically preferred compared with the face-to-face configuration. Subsequently,

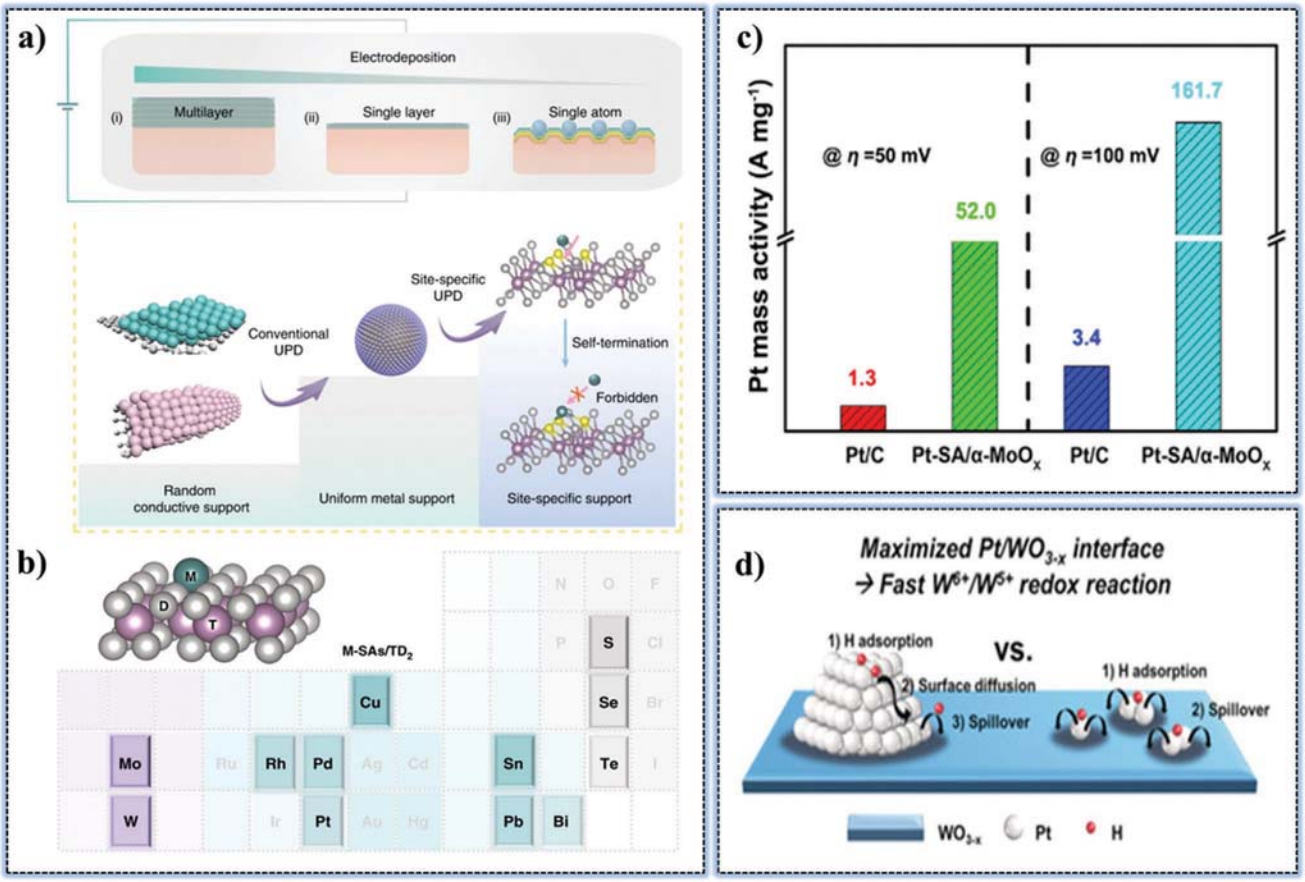

Figure 37. a) Schematic diagram of electrodeposition method for depositing M-SAs on TMCs. b) A SACs library of various supporting TMD substrates and precursor metals for SSED. Reproduced with permission.[67] Copyright 2020, Nature Publishing Group. c) HER mass activities of Pt-SA/α-MoO$_x$ at $\eta = 50$ and 100 mV. Reproduced with permission.[275] Copyright 2020, Elsevier Inc. d) Illustration of the HER for Pt SA/m-WO$_{3-x}$ and Pt NP/m-WO$_{3-x}$. Reproduced with permission.[277] Copyright 2019, John Wiley and Sons.

H_2PtCl_6 aqueous solution with 0.44 wt.% Pt content and as-obtained AG were fully mixed, then $PtCl_6^{2-}$ ions were electrostatically fixed on AG. After microwave irradiation, these $PtCl_6^{2-}$ ions anchored on AG support were eventually reduced to Pt-SAs. Interestingly, the maximum protonation of aniline limited the maximum $PtCl_6^{2-}$ loading amount of 0.44 wt.%, preventing excess Pt from being anchored to form NPs or clusters. Images from in situ TEM characterizations demonstrated that Pt SASs/AG well maintained the wrinkle structure of graphene, and Pt-SAs were uniformly dispersed on AG without visible agglomeration (Figure 38b–e). According to HAADF-STEM and XAFS measurements, Pt-SAs were coordinated with four aniline molecules to form a Pt-N configuration (the coordination number was about 4), as shown in Figure 38f. The as-prepared Pt SASs/AG catalyst exhibited nearly zero onset potential and a super low η_{10} of only 12 mV, as well as a remarkable mass activity of 22 400 A g_{Pt}^{-1}, which is 46 times higher than that of the commercial 20% Pt/C. The structure–performance relationship between Pt coordination and H_2 evolution activity was studied by DFT calculations. On the one hand, the d-band center of Pt-SAs anchored by aniline downshifted to −2.465 eV (Figure 38g), which is close to that of Pt(111) (−2.687 eV), suggesting that the synergistic effects between aniline and Pt were responsible for HER performance. On the other hand, the ΔG_{H^*} of this catalyst was −0.127 eV, which is almost the same as that of Pt(111) (Figure 38h). Moreover, Li's group successfully prepared a Pt SAs/DG SAC from bulk Pt net through a facile thermal emitting approach.[191] The obtained SAC with 2.1 wt.% loading of Pt can serve as a high-performance catalyst toward HER and selective oxidation of various organosilanes. In another study, the Pt/NiS@Al_2O_3 SAC containing ≈2.8 wt.% Pt loading was synthesized by anchoring Pt-SAs on a 3D flower-like NiS@Al_2O_3 heterostructure.[264] For HER electrocatalysis in 0.5 M H_2SO_4, this obtained catalyst achieved a low η_{10} of ≈34 mV and Tafel slope of ≈35 mV dec^{-1}, superior to Pt/MnS@Al_2O_3 and Pt/CoS_2@Al_2O_3 and comparable to commercial 20 wt.% Pt/C sample. It was believed that the high catalytic performance of Pt/NiS@Al_2O_3 was derived from the rich redox reaction sites generated by the introduction of Pt-SAs, as well as the active area of γ-Al_2O_3 nanosheets enlarged by highly dispersed NiS NPs.

Conventional solution chemistry and photochemical reduction are the common methods for metal nanocatalysts. However, the liquid phase and reaction products are prone to nucleation, growth, agglomeration, and diffusion, which seriously hinder their application in the synthesis of SACs.[16f,85,279] In this case, freezing the precursor solution to limit the photochemical

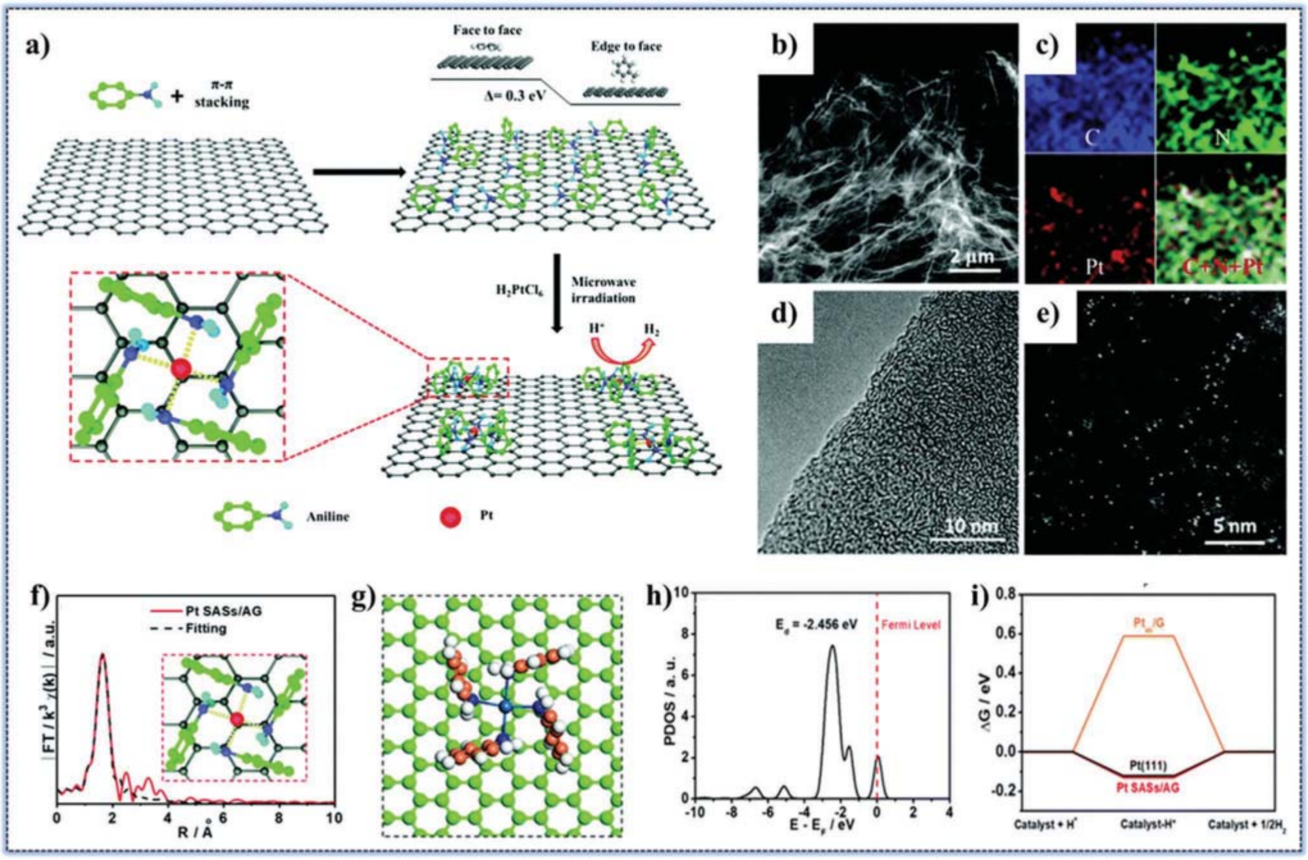

Figure 38. a) Illustration of fabricating Pt SASs/AG. b) TEM image and c) corresponding elemental maps of Pt SASs/AG. d) HR-TEM image and e) HAADF-STEM images of Pt SASs/AG. f) EXAFS fitting curve of the Pt SASs/AG. The inset shows the optimized model. g) DFT calculation models (top views) of Pt SASs/AG and h) Corresponding PDOSs of the 5*d* orbitals of Pt. i) ΔG_{H*} on Pt(111), Pt_{ab}/G, and Pt SASs/AG. Reproduced with permission.[263] Copyright 2019, Royal Society of Chemistry.

reduction products is an effective solution. Wei et al. successfully prepared dispersed Pt-SAs that can be anchored on various substrates through this method.[16d] The electrochemical H_2 evolution activity of the as-obtained Pt_1/MC had a low overpotential of only 65 mV at $\eta = 100$ mA cm^{-2}, which is superior to the state-of-the-art Pt/C. On this basis, Huang et al. revealed the heterogeneous nucleation process of Pt—Pt dimers at −40 °C and room temperature via ab initio molecular dynamics (AIMD) simulations.[280] As shown in **Figure 39**a, the low-temperature environment forces the nucleation process of Pt—Pt to overcome larger nucleation barriers, promoting the formation of highly dispersed Pt-SAs. This atomically dispersed Pt supported on the surface of N-doped mesoporous carbon (Pt/NMC-LT) was synthesized by a circulating cooling system (Figure 39b). The interactions between the Pt atom and the support make Pt species present the oxidation state of $Pt^{\delta+}$.[16d,281] Unfortunately, the above-mentioned synthesis strategies are relatively complex, low-yield, and require expensive equipment, which cannot be employed in industrial reparation. The recently developed ball milling process provides a feasible scheme for the large-scale automated production of SACs and SAAs.[282] In a study by Jin and co-workers, a Pt SAC (K_2PtCl_4@NC-M) was fabricated quickly and easily by ball milling Pt precursor and N-doped carbon support.[262] In 0.5 м H_2SO_4 solution, the overpotential of K_2PtCl_4@NC-M ($\eta_{10} = 11$ mV) was lower than that of the commercial 20 wt.% Pt/C ($\eta_{10} = 14$ mV), while the mass activity in electrochemical HER was increased by 17 times (Figure 39c,d). XAFS data demonstrated that the superior H_2 evolution activity of K_2PtCl_4@NC-M was ascribed to the maximum utilization of uniformly dispersed PtSAs as well as the introduction of Pt—N_2C_2 active sites. Furthermore, this ball milling procedure is generally applicable to fabricate other M-SAs with similar structures (Mt—N_2C_2) for large-scale energy storage and conversion application scenes, such as Rh SAC ($RhCl_3$@NC-M) and Ru SAC ($RuCl_3$@NC-M).

It should be pointed out that the strong corrosiveness of acidic media will decrease the stability of carbon-based supports. Besides, the application of Pt in industrial H_2 production from water electrolysis is greatly limited due to its high price and easy poisoning. Therefore, it is necessary to develop novel SACs to replace Pt-based electrocatalysts. It has been found that Ru exhibits a similar metal–hydrogen (M—H) bonding strength to Pt, and its price is relatively low.[283] To this regard, Yang et al. prepared Ru SAC through a typical co-reduction approach, in which Ru-SAs coordinated with four N atoms on the P-vacancies of a novel carbon-free PN nanotube support.[88a] The as-prepared RuSAs@PN catalyst contained merely 0.33 wt.% Ru loading but exhibited similar catalytic performance compared with commercial 20 wt.% Pt/C. Only ultralow overpotential

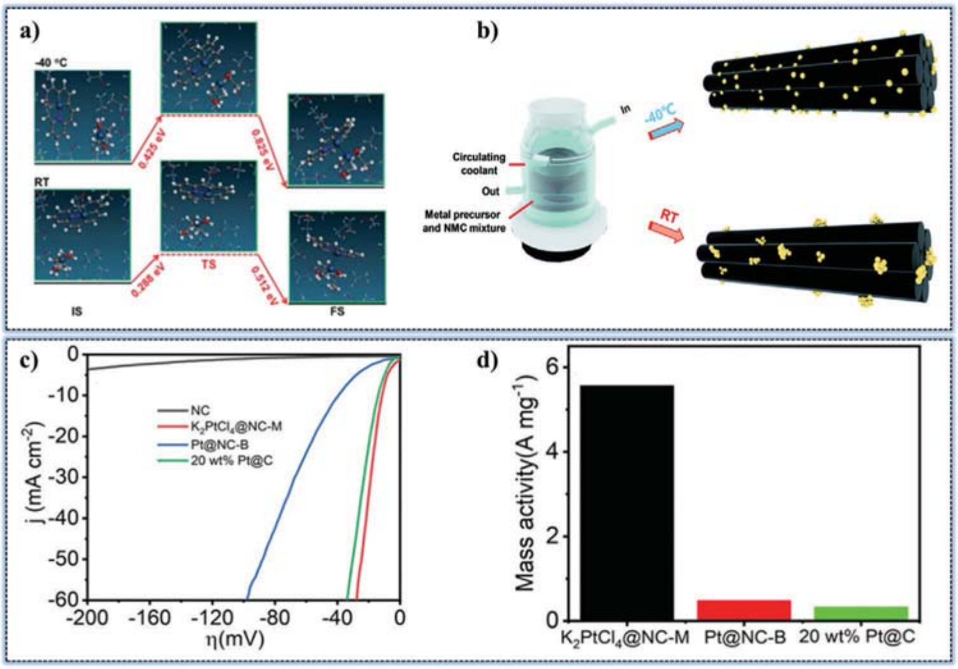

Figure 39. a) Energy diagram of Pt—Pt dimer formation at −40 °C and RT. The initial state (IS), transition state (TS), and final state (FS) are indicated from left to right. C: gray; N: blue; Pt: light blue; O atoms: red; H atoms: white. b) Schematic illustration of the atomically dispersed Pt on NMC substrates. Reproduced with permission.[280] Copyright 2019, Royal Society of Chemistry. c) HER polarization curves of K_2PtCl_4@NC-M and other samples. d) Mass activity of K_2PtCl_4@NC-M and other samples at an overpotential of 20 mV. Reproduced with permission.[262] Copyright 2020, John Wiley and Sons.

of 24 mV was needed for Ru-SAs@PN to provide the current density of 10 mA cm^{-2}, with the Tafel slope being 38 mV dec^{-1}. Furthermore, it showed good stability at a high current density of 100 mA cm^{-2}. The PN substrate with distorted spatial structure and polar P—N bond is considered to be an ideal support for isolating the metal sites. Another example by He et al. stabilized Ru-SAs on the N and S doped $Ti_3C_2T_x$ MXene.[90] DFT calculations based on XPS and XAFS results showed that the obtained Ru_{SA}-N-S-$Ti_3C_2T_x$ endowed an optimized H adsorption free energy close to zero (0.08 eV) (see **Figure 40**a). As shown in 40b and c, the Ru_{SA}-N-S-$Ti_3C_2T_x$ was reported to exhibit a low η_{10} of 76 mV and η_{100} of 237 mV in acidic electrolyte, with a Tafel slope of 90 mV dec^{-1}. For comparison, the Tafel value of such Ru-MXene SAC is higher than that of the previously reported Ru-based electrocatalyst,[283] while similar to that of other 2D MXenes catalysts for HER.[284] This phenomenon can be attributed to the synergistic effect of Ru-SAs and $Ti_3C_2T_x$ MXene and the regulation of electronic structure by N, S doping. In another graphene-supported SAC work, Duan and co-workers reported a simple and universal microwave heating strategy that can stabilize a series of M-SAs (M = Co, Ni, and Cu).[265] The characterization results suggested that microwave radiation can remove the oxygen functional groups, and meanwhile, restore the ordered graphene structure. Additionally, the defects or vacancies produced in the thermal reduction process from microwave radiation also play a major role in the anchoring sites for metal atoms.

As discussed in Section 2.4, the strong electronegativity of non-metal atoms allows them to couple with metal atoms on the support surface, thereby modulating the electrocatalytic activity of catalysts. Recently, a non-metal-based SAC with single P atoms as active sites has shown great potential for HER. Fu et al. have successfully fabricated a phosphorus SAC on Mo_2C-based hexagonal nanosheet arrays supported by carbon sheet (SAP-Mo_2C-CS).[266] In contrast to P-doped Mo_2CCS without SAs, the positive charge of Mo increases in SAP-Mo_2C-CS (Figure 40d). A high-intensity P—Mo peak appeared in the front edge region (about 2146.8 eV), which suggested that P atoms mainly coordinated with Mo atoms (Figure 40e). This metal-free SAC required a low overpotential of only 36 mV at 10 mA cm^{-2} in acidic electrolyte, with a corresponding Tafel slope of 38.1 mV dec^{-1}, which is comparable to commercial Pt/C. Particularly, the electrocatalytic activity of SAPMo$_2$CCS with 3.6 wt.% of P content was even superior than the commercial Pt/C at a higher potential range. Theoretical calculations suggested that the P-SAs, as highly active sites, gave rise to chemical coupling effects and electron redistribution on Mo_2C, accelerating the HER kinetics.

5.2.2. HER in Alkaline Solution

In an alkaline environment, HER is carried out by the reduction of water in the electrolyte ($2H_2O + 2e^- \rightarrow H_2 + 2OH^-$) (Equations (6)–(8)).[23f]

$$H_2O + e^- + * \rightarrow H* + OH^- \,(\text{Volmer}) \tag{6}$$

$$H_2O + e^- + H* \rightarrow H_2 + OH^- \,(\text{Heyrovsky}) \tag{7}$$

$$2H* \rightarrow H_2 + * \,(\text{Tafel}) \tag{8}$$

Because there is only a small amount of H^+ in alkaline media, it is necessary to dissociate the water molecules through

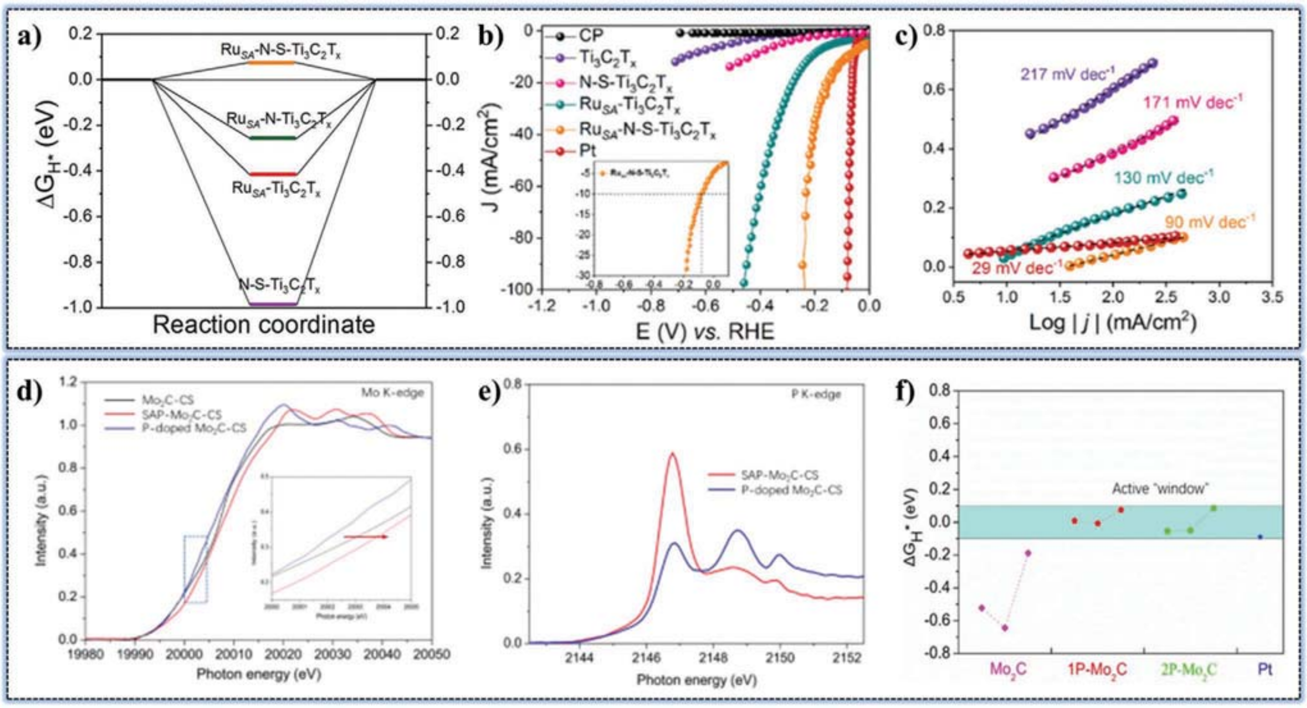

Figure 40. a) Schematic diagram of the calculated ΔG_{H^*} of Ru$_{SA}$-N-S-Ti$_3$C$_2$T$_x$ catalyst. b,c) Electrocatalytic HER performance of the Ru$_{SA}$-N-S-Ti$_3$C$_2$T$_x$ catalyst. Reproduced with permission.[90] Copyright 2019, John Wiley and Sons. d,e) XANES spectra of SAP-Mo$_2$C-CS and other samples. f) The calculated ΔG_{H^*} of different H* adsorption sites on various samples. Reproduced with permission.[266] Copyright 2020, John Wiley and Sons.

constant and high current densities to obtain H$^+$.[285] In general, the Tafel slope of alkaline HER is larger than that of acidic HER, which means that the kinetic rate of H_2 evolution in an alkaline media is much slower than that in acidic media. Taking the state-of-the-art Pt electrocatalysts as an example, their relatively slow HER behavior exhibited in alkaline environment has become the main bottleneck for large-scale applications.[38b,198c,286] From another perspective, although the electrocatalysis under acidic conditions has superior activity, it will inevitably produce acid mist during high-temperature operation, resulting in hydrogen pollution and equipment corrosion.[184a] The HER behavior demonstrates the opposite in alkaline media, and the electrocatalysts can maintain stable operation. Accordingly, the development of SACs with high H_2 evolution properties in alkaline media possibly has greater value in practical application.

For alkaline HER, decreasing the H_2O dissociation energy in the Volmer step (Equation (6)) for electrocatalysts is crucial for H_2 evolution due to the energy barrier for splitting a strong OH—H bond. In general, in order to improve the H_2 evolution activity of SACs, it is necessary to achieve the optimal adsorption energy of H atoms, while also increasing the dissociation efficiency of water molecules on the catalyst surface.[287] It is well known that noble-metals active species, such as Pt, Ru, and Pd, have a relatively strong H adsorption but weak H_2O dissociation in the alkaline HER catalysts.[4a,163] Introducing single noble metal atoms into electrocatalysts is an effective approach to designing high-performance HER catalysts. For example, introducing atomically dispersed Ru species into N-doped Mo_2C nanosheets could significantly enhance the electrocatalytic activity.[84] The electronic state of Ru sites on this fabricated Ru SAs/N-Mo_2C NSs catalyst was investigated by XAFS and XPS characterizations. As shown in **Figure 41**a, the Ru peaks of the sample supported Ru-SAs presented more negative binding energies than that of the sample supported Ru-NPs, suggesting the strong electron transfer between Ru-SAs and support. XANES spectra showed an obvious shift to lower energy of pre-edge centroid of Ru SAs/N-Mo_2C catalyst, indicating the decrease of the oxidation state (Figure 41b). In 1.0 м KOH electrolyte, this Ru SAC exhibited a remarkable mass activity of 6.44 A mg $^{-1}$, which is 7 times higher than that of the 20 wt.% Pt/C catalyst (0.91 A mg^{-1}). DFT results further demonstrated the strong synergistic effect between atomic Ru species and N-Mo_2C in this electrocatalyst. According to another previous study, S-vacancies in MoS_2 basal plane could be created via the introduction of Pd-SAs, and these S-vacancies adjacent to M-SAs were regarded as the real active sites during HER.[159] Inspired by the above findings, Tan's group designed a nanoporous MoS_2 (np-MoS_2) with bicontinuous structure to stabilize atomic Ru species, in which the synergistic effect between S-vacancies and Ru-SAs dramatically boosted the alkaline HER.[76] The rational design scheme of this Ru SAC was predicted through theoretical calculations first. Notably, for alkaline HER, the active sites were the Mo sites located below the S-vacancies. By comparison, the ΔG_{H^*} value of the Ru sites and S sites after the introduced strain decreased to nearly zero (Figure 41d), demonstrating the desirable binding strength to hydrogen. As expected, the synergistic effect between Ru-SAs and S-vacancies could be enhanced via applying strain in MoS_2. According to these theoretical results, a Ru/np-MoS_2 SAC with 3D bicontinuous nanoporous structure and nanotube-shaped

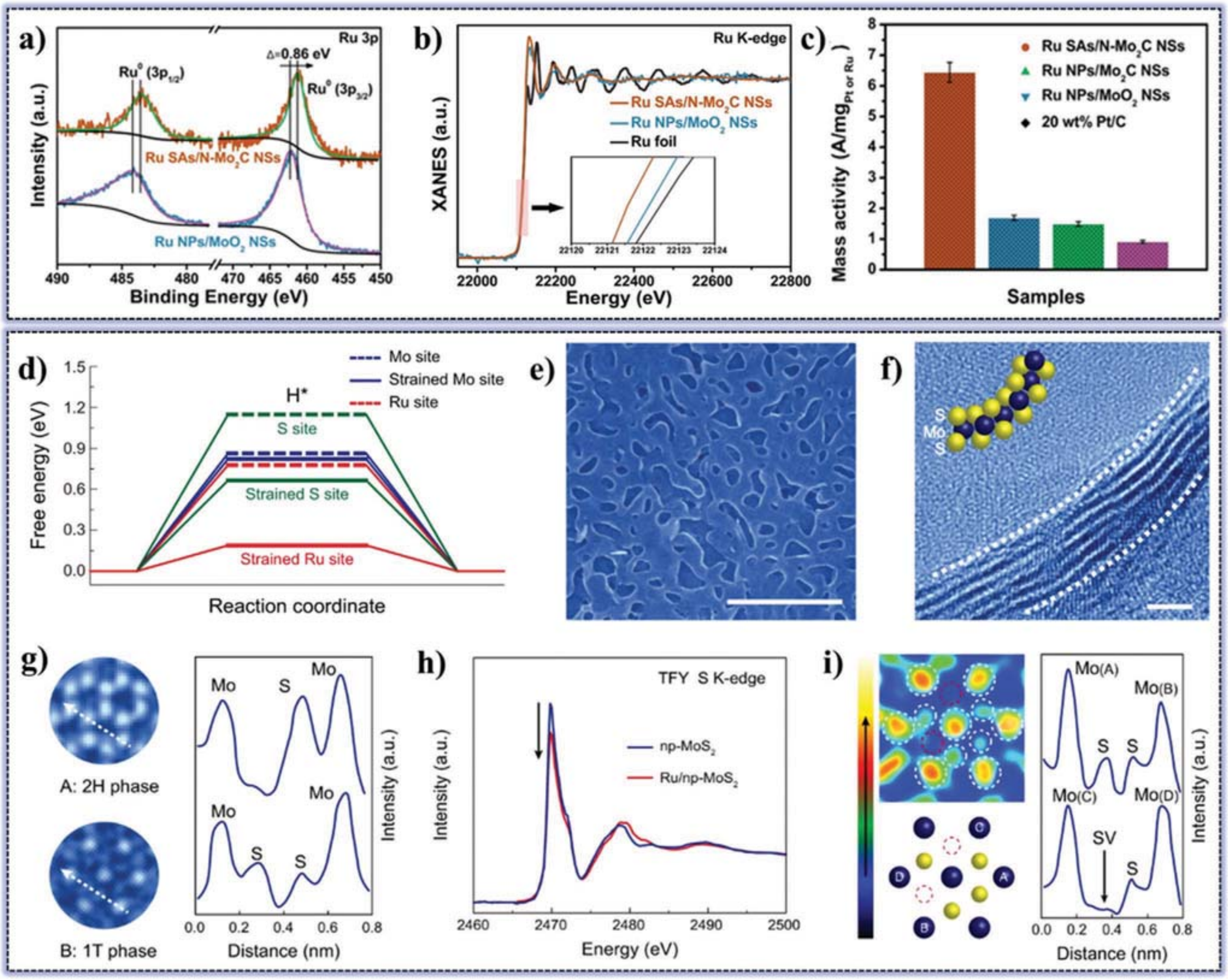

Figure 41. a) Ru 3d for Ru NPs/MoO_2 NSs and Ru SAs/N-Mo_2C NSs. b) XANES spectra for Ru K-edge of Ru NPs/MoO_2 NSs, Ru SAs/N-Mo_2C NSs, and Ru foil. c) Mass-specific activity at overpotentials of 100 mV. Reproduced with permission.[84] Copyright 2020, Elsevier Inc. d) Free energy diagrams for hydrogen adsorption at different sits. e) SEM image of Ru/np-MoS_2. f) HRTEM image of Ru/np-MoS_2 from the cross-sectional view. g) Magnified HAADF-STEM image and corresponding intensity line profiles. h) S K-edge XANES spectra of np-MoS_2 and Ru/np-MoS_2. i) S-vacancies characterization. Reproduce with permission.[76] Copyright 2021, Nature Publishing Group.

ligaments were fabricated successfully via spontaneous reduction strategy (Figure 41e,f). HAADF-STEM and XANES spectra confirmed the 2H—1T phase transition in np-MoS_2 induced by Ru doping (Figure 41g,h). The S-vacancies formed by the loss of S atoms after Ru substituting were proved by the magnified HAADF-STEM image and corresponding intensity profile analysis, as illustrated in Figure 41i. Furthermore, ambient pressure XPS and operando XAS comprehensively revealed the mechanism of the improvement of HER performance, as well as the identification of the active sites. Briefly, the applied strain of Ru/np-MoS_2 enhanced the accumulation of OH^- and H_2O in SVs adjacent to Ru atoms, accelerating the H_2O mass transfer for the subsequent alkaline HER. Meanwhile, the bending strain of these catalysts effectively tuned the electronic structure of Ru-SAs, which plays a crucial role in the water dissociation and H—H coupling. Surprisingly, the Ru/np-MoS_2 SAC exhibited an extremely low overpotential of 30 mV at current densities of 10 mA cm^{-2} and a Tafel slope of 31 mV dec^{-1} in 1.0 M KOH electrolytes, which surpasses the state-of-the-art electrocatalyst and commercial 20 wt.% Pt/C catalyst for H_2 evolution. On the basis of these design principles, it may be a promising way to maximize the catalytic performance of SACs by constructing a synergistic center to assist the SA site.

The above-discussed strategies achieve highly efficient H_2 generation through independently modulating the binding energy of reactants (i.e., OH and H*) on different catalytic sites. Inspired by this, other materials with superior HER performance as well as coordination environment should be thoroughly investigated as SAC support. Contrary to noble metals, oxides/hydroxides possess weaker H adsorption properties, but stronger H_2O dissociation under alkaline conditions.[288] Consequently, it can be predicted that the composite SACs formed by combining both the single noble-metal atoms and oxide/hydroxide supports are a feasible approach to simultaneously promote the H adsorption and the H_2O dissociation. In this regard, Li et al. have designed a novel type of hybrid electrocatalyst, namely Pt/NiRu-OH, where the amorphous surface of NiRu-OH had abundant functional groups, which can fix highly dispersed Pt-SAs.[268] Theoretical calculations and experimental results revealed that the NiRu-OH sites accelerated water splitting while the atomic Pt species promoted hydrogen recombination, which were the crucial reason for the superior performance of this hybrid catalyst under alkaline conditions. Surprisingly, Pt/NiRu-OH can drive a typical current density of 10 mA cm_{geo}^{-2} at a low overpotential of 38 mV (**Figure 42**a). Likewise, Li's group recently fabricated a Ru SAC (Ni_5P_4-Ru) through stabilizing Ru^{3+} species into Ni-vacancy defects of $Ni(OH)_2$ via impregnation method (Figure 42b).[63] The as-prepared Ni_5P_4-Ru sample exhibited an impressive HER activity with a low η_{10} of 54 mV and a small Tafel slope of 52 mV dec^{-1}. DFT calculations investigated that the incorporated Ru-SAs improved the conductivity, which boosted the HER process. As shown in Figure 42c, the charge density redistributions have been demonstrated. Such a localized structural polarization induced an environment with electron-rich Ru sites, decreasing the energy barrier of H_2O dissociation. The calculation results further proved that the energy barrier on the Ru site in Ni_5P_4-Ru (1.28 eV) was lower than that on pristine Ni_5P_4 (1.97 eV), as shown in Figure 42d.

In addition to the above-mentioned hydroxide supports, the binding energy of reaction intermediates (including OH* and H*) can be independently regulated by the dual active sites created at the metal oxide/metal interface, efficiently facilitating the water dissociation step with a low energy barrier.[269] In this as-synthesized Pt_{SA}-NiO/Ni heterostructure nanosheets on Ag nanowires conductive network, metallic Ni sites and NiO sites at the NiO/Ni interfaces served as dual active sites (**Figure 43**a,b). Specifically, the crystal-lattice dislocation and phase transition generated abundant O-vacancies at the surface of NiO/Ni interfaces, which offered anchoring sites for Pt-SAs. As depicted in Figure 43c, Ni and NiO sites possessed strong binding with OH* and H*, respectively, promoting the H—OH bond destabilization, and then Volmer step would be accelerated. Particularly, NiO/Ni-supported atomic Pt sites favored the H reactants' adsorption and transfer because of the wider 5d band and higher density near the Fermi level (Figure 43d). HAADF-STEM, XPS, and XAFS analyses confirmed the Pt-SAs dispersed uniformly on NiO/Ni nanosheets. Combining the DFT calculations, the fitting results of EXAFS spectra indicated that the Pt atoms coordinated with one O atom and five Ni atoms in this Pt SAC, stabilizing at the interfacial Ni positions. As expected, Pt_{SA}-NiO/Ni exhibited a minimum energy barrier of 0.31 eV compared with that of Pt_{SA}-Ni (0.47 eV) and Pt_{SA}-NiO (1.42 eV), which demonstrated that the NiO/Ni interface played a critical role in the H_2O dissociation (Figure 43e). In particular, an ideal H binding energy (ΔG_{H^*}, −0.07 eV) was obtained (Figure 43f). Subsequent experiments revealed that the Pt_{SA}-NiO/Ni SAC exhibited a remarkable HER activity with an ultralow overpotential η_{10} and η_{100} of 26 and 85 mV, respectively, and a small Tafel slope of 27 mV dec^{-1} in alkaline media. Furthermore, this Pt_{SA}-NiO/Ni SAC displayed remarkable stability that there was negligible change in the HER polarization curves after 5000 cycles or 30 h.

As we all know, CO is irreversibly adsorbed on the Pt surface, resulting in the deactivation of Pt-based catalysts.[289] Therefore, great efforts have been made to fabricate CO-tolerant Pt catalysts. It is of great significance to further study the influence mechanism of CO-absorbed metal species on HER activity to reduce the toxicity of CO to the catalyst.[290] Recent studies have shown that, contrary to the common poisonous behavior

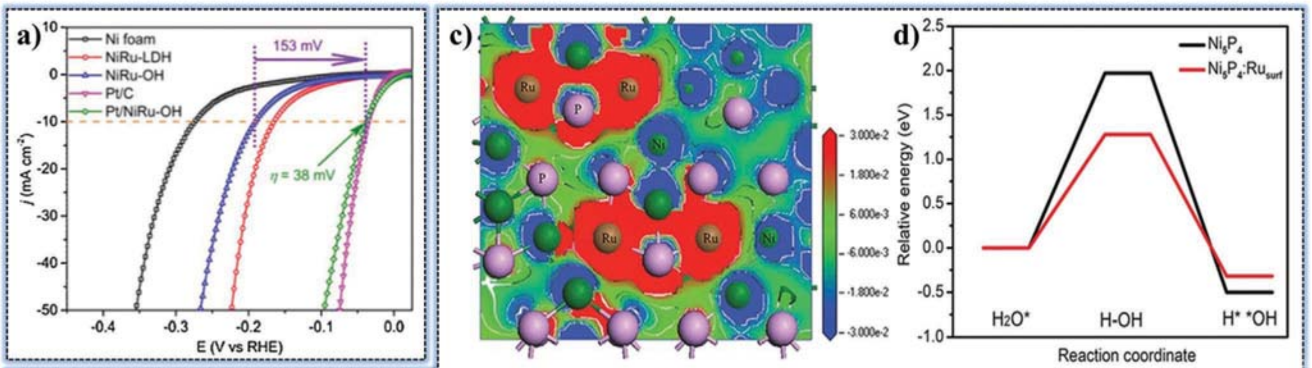

Figure 42. a) Polarization curves of the Ni foam, NiRu-LDH, NiRu-OH, Pt/C, and Pt/NiRu-OH. Reproduced with permission.[268] Copyright 2020, Elsevier Inc. b) Schematic diagram for the fabrication of Ni_5P_4-Ru. c) Bader analysis of Ni_5P_4-Ru. d) The energy barriers for H_2O dissociation on optimized sites in Ni_5P_4 with Ru doping. Reproduced with permission.[63] Copyright 2020, John Wiley and Sons.

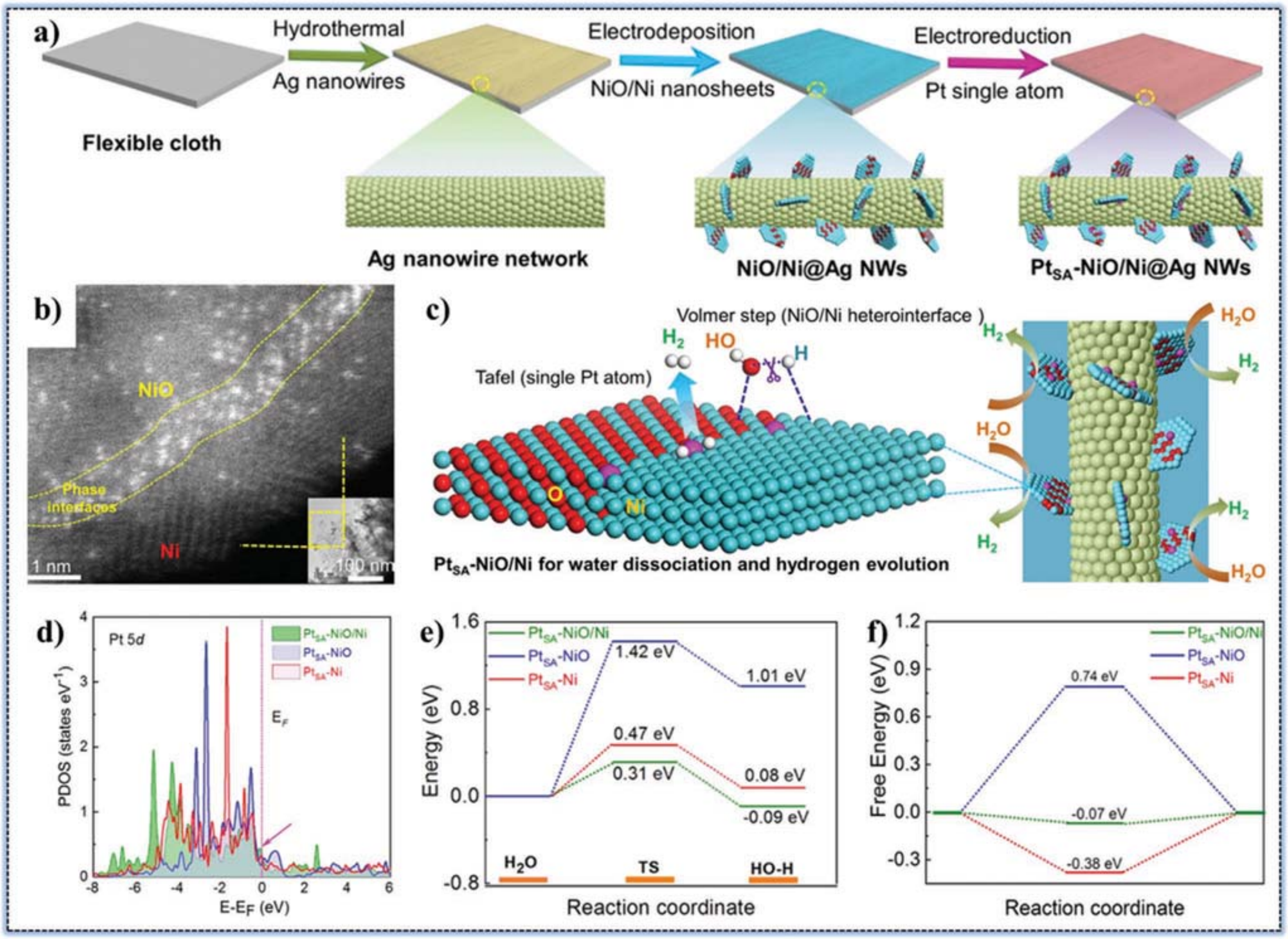

Figure 43. a) Fabrication procedure of Pt_{SA}-NiO/Ni nanosheets on Ag nanowires. b) HAADF-STEM image of Pt_{SA}-NiO/Ni. c) Mechanism of Pt_{SA}-NiO/Ni catalyst for H_2O dissociation and H_2 production in alkaline electrolyte. d) Calculated Pt 5d band of Pt_{SA}-NiO/Ni and other samples. e) Calculated energy barriers of H_2O dissociation kinetic and f) Free energy diagrams for hydrogen adsorption on the surface of three catalysts. Reproduced with permission.[269] Copyright 2021, Nature Publishing Group.

in conventional electrocatalysis, the adsorption of CO on Au can enhance the catalytic performance.[291] However, since Pt is more active than Au, the strong donor-acceptor binding ability of CO is easier to decrease the activity of Pt-based catalysts in electrocatalysis.[292] As a result, CO is usually considered a strong poisoning agent of Pt.[293] Surprisingly, when Pt in the Pt—S_4 species downsizes to the atomic scale, the activity of Pt toward alkaline HER can be effectively enhanced by CO-adsorption.[294] Electrocatalytic HER characterizations showed that in the presence of CO, Pt-NPs supported by purely carbonaceous zeolite-templated carbon (denoted Pt/ZTC) and Pt-SAs supported by carbon with a high sulfur content (denoted Pt/HSC) were both significantly deactivated (**Figure 44**a–c). Interestingly, the kinetics of Pt/HSC was improved in CO-saturated electrolytes. Such a special phenomenon is explained by the irreversible binding of CO to the atomic Pt site as an HER promoter. In addition, compared with pristine Pt SAC, the reduction current on the CO-modified catalyst increased significantly, and CO reduction products were not formed. DFT calculations suggested that two H_2O molecules (employed as reactants and spectator) on Pt^{2+} were replaced by two CO molecules (Figure 44d). Notably, the enhanced effect of absorbed CO molecules on Pt/HSC on the HER performance was observed in an alkaline environment. By comparison, CO will induce rapid deactivation of this catalyst under acidic or neutral conditions. Actually, the electrode/electrolyte interface chemistry modulated by the change of pH value can obviously improve the HER kinetics.

Besides the tungsten oxide supports discussed above, the combination of W atoms and carbon supports (i.e., graphene and CNTs) is also one of the strategies widely used to adjust the conductivity of materials.[209,210] Inspired by these works, Chen and co-works reported a synthesis approach that first anchored atomic W species on MOF-derived N-doped carbon (**Figure 45**a).[270] During the pyrolysis process, the uncoordinated amine group contained in the MOF (UiO-66-NH_2) played a vital role in suppressing the aggregation of W species. It can be seen in the TEM images that this obtained W-SAC maintained the polyhedral shape and size distribution (Figure 45b). HADDF-STEM image showed the atomically dispersed W in the sample (Figure 45c). As shown in Figure 45d, this result was also confirmed by XAFS measurements, where FT-EXAFS

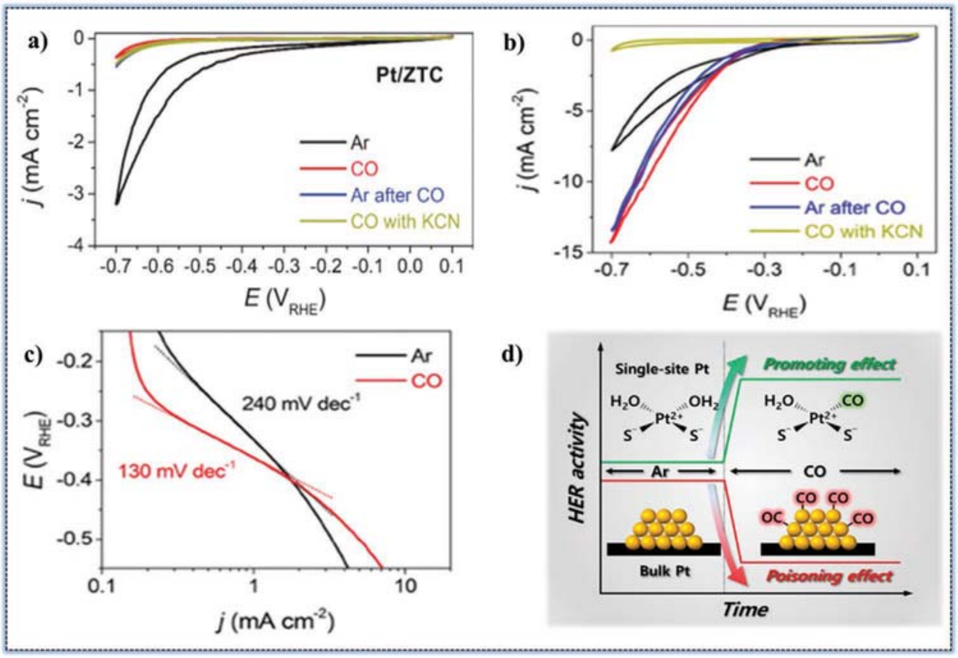

Figure 44. HER polarization curves of a) Pt/ZTC and b) Pt/HSC. c) Tafel plots of Pt/HSC obtained from the potentiodynamic. d) Model structure of Pt—S$_4$ with Pt^{2+} center coordinated by two strong thiolates and two labile thioethers. Reproduced with permission.[294] Copyright 2018, American Chemical Society.

peaks assigned to W—W coordination were not detected. Subsequently, DFT calculations further demonstrated the $W_1N_1C_3$ moiety was the optimized configuration toward HER. In comparison, W-SAC possessed the lowest ΔG_{H*} of 0.033 eV than that of other W-based catalysts (Figure 45e). This single-W-atom material exhibited promising HER performance with η_{10} of 85 mV and a Tafel slope of 53 mV dec^{-1} in an alkaline electrolyte, similar to that of commercial Pt/C. Actually, the high HER activity of W-SAC is mainly attributed to the increase of electron density on C atoms after W doping.

The first synthesis of SAC with nonmetal active sites came from the work of Zhao and co-workers, who fabricated a nickel iodide single-atom electrocatalyst with atomically dispersed iodide species, termed SANi-I.[24] After substituting the excess iodine atoms in Ni-I precursor with O atoms and hydroxide ions, I-SAs will be immobilized at the interface between the

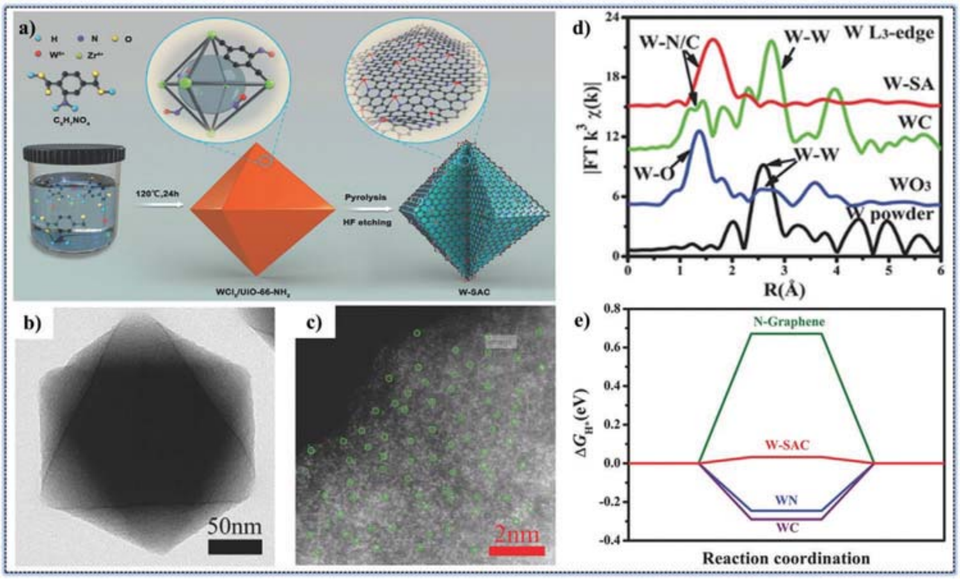

Figure 45. a) Illustration of the formation of W SAC. b) TEM characterizations of the W-SAC. c) The HAADF-STEM image of the W-SAC. d) k^3-weight FT-EXAFS curves of the W-SAC at W L$_3$-edge. e) ΔG_{H*} diagram of the W-SAC, WC, WN, and N-doped graphene samples. Reproduced with permission.[270] Copyright 2018, John Wiley and Sons.

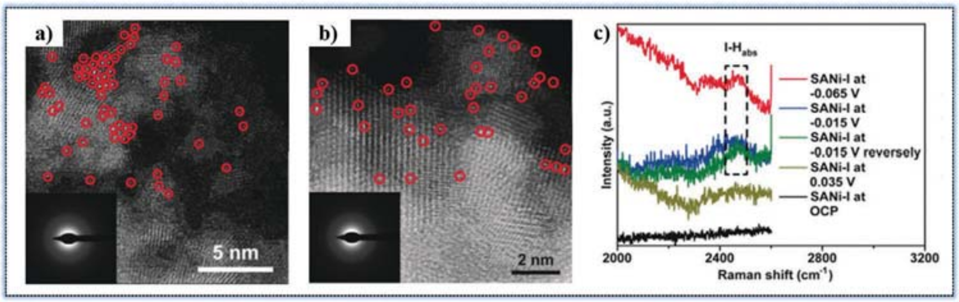

Figure 46. Magnified HAADF-STEM image and (inset) corresponding SAED pattern of a) SANi-I and c) SANi-I sample after activation for 96 h, where red circles highlight I-SAs. HAADF-STEM image, corresponding mapping images as well as line-scanning profile (along the highlighted green line) for b) SANi-I and d) SANi-I sample after activation for 96 h. Schematic illustration of in situ Raman spectra for e) SANi-I and f) A-Ni-OH sample. For SANi-I, the broad peak of about 2460 cm^{-1} at a potential of –0.015 and –0.065 V is ascribed to the I-H vibrational band. Reproduced with permission.[24] Copyright 2019, John Wiley and Sons.

Ni support and the Ni-I precursor through chemical bonding with Ni atoms. During this synthesis procedure, the Ni-I precursor was activated in cyclic voltammetry scanning under alkaline conditions, obtaining highly stable SANi-I with uniformly dispersed I-SAs (**Figure 46**a–d). EXAFS and XANES measurements demonstrated that the O atoms would be inserted between Ni and I sites to form I—O bonds during the activation process, thereby isolating the I atoms. This nonmetal SAC predominantly consisted of nickel hydroxide has exhibited a low η_{10} of only 60 mV in alkaline solution, which is even lower than that of Pt/C (61 mV) and bulk nickel hydroxide clusters with no iodine (A-Ni-OH) (285 mV). Meanwhile, SANi-I also showed excellent stability with a negligible loss after 10 000 CV sweeps or 24 h operation at –20 mA cm^{-2}, indicating its promising potential in practical application. In situ Raman spectroscopy revealed the HER mechanism of SANi-I. As shown in Figure 46e, an I-H vibrational band was observed at approximately 2460 cm^{-1}, and the peak intensity increased due to the application of more negative potentials (from –0.015 V to –0.065 V vs RHE). On the contrary, no such peak was presented under the same condition (Figure 46f). The above experimental results suggested that boosted H_2O dissociation and H adsorption via forming I-H$_{ads}$.

5.2.3. HER Under Neutral Conditions

Compared with HER in acidic environments and alkaline environments, the advantages of neutral electrolytes are environment-friendly, less corrosive as well as low requirements for hydrolysis equipment. Nevertheless, due to the larger Ohmic loss and low proton concentration, the kinetics of neutral HER is relatively slow.[295] Therefore, a higher applied voltage should be needed to achieve the same current density as in acidic or alkaline media. Fortunately, SAECs with maximum atom utilization open up a new avenue for the solution of this challenge.

Commercial Pt/C is believed to be the most effective H_2 evolution electrocatalyst in a neutral environment.[296] Recently, with the rapid development, SAECs have represented a type of promising alternative for practical applications. It has been reported that the Pt-SAs, whose electronic structure underwent positive modulation by support, showed extremely high HER activity.[40,297] Moreover, some works have demonstrated that M-SAs can be dissolved from Pt anodes into acidic or alkaline media under high voltages, and then transferred to the cathodes.[298] Inspired by above works, a potential-cycling approach has been reported by Luo and co-workers,[26a] who attached Pt species to CoP-based nanotube arrays by Ni foam, fabricating SAECs containing Pt-SAs (PtSA-NT-NF) (**Figure 47**a). This binder-free electrocatalyst was atomic-scale and scalable, while its great advantage was that each PtSA-NT-NF piece could be directly employed as an HER cathode. In neutral media, the as-obtained SAEC exhibited a satisfactory HER performance with a low η_{10} of 24 mV, comparable to that of commercial Pt/C (Figure 47b). Meanwhile, this catalyst could maintain a stable current density at an overpotential of 100 mV over 24 h with a negligible decrease, as shown in Figure 47c.

Later on, a similar synthesis strategy was reported by Jiang and co-workers.[271] They embedded Pt atoms at the electrochemical vacancy sites created in nanoporous cobalt selenide via a cycle voltammetry method, successfully fabricating Pt-SAs doped electrocatalyst, namely Pt/np-Co$_{0.85}$Se (**Figure 48**a). The electronic and structure of the obtained SAC was revealed by XAFS analysis. FT-EXAFS spectra in Figure 48b exhibited a conspicuous peak at 2.03 Å, which could be attributed to the contributions from Pt—Se coordination, suggesting the single-atom nature of Pt. As shown in Figure 48c, the peak intensity decreased from 2.13 to 2.09 Å after the introduction of the Pt-SAs in np-Co$_{0.85}$Se, which means the formation of Se vacancies for the partial rearrangement of Co atoms. In 1.0 M PBS solutions, the HER activity of Pt/np-Co$_{0.85}$Se with low Pt loading of 1.03 wt.% could far surpass that of commercial Pt/C at high overpotentials (>19 mV), as depicted in Figure 48d. In particular, this catalyst exhibited a remarkable mass activity of 1.32 A mg^{-1} at an overpotential of –100 mV, which is 11 times higher than that of the commercial 10 wt.% Pt/C (0.12 A mg^{-1}). More insights on the origins of the outstanding activities of this Pt-based SAC were investigated via the in situ and operando Co K-edge XANES and FT-EXAFS spectra. The Pt-SAs could cooperate with the surrounding Co atoms to promote the thermodynamic and kinetic process of HER, as illustrated in Figure 48e. DFT calculation was employed to further demonstrate the electronic interactions between Pt-SAs and support. The strong induction of charge redistribution at the Pt/np-Co$_{0.85}$Se

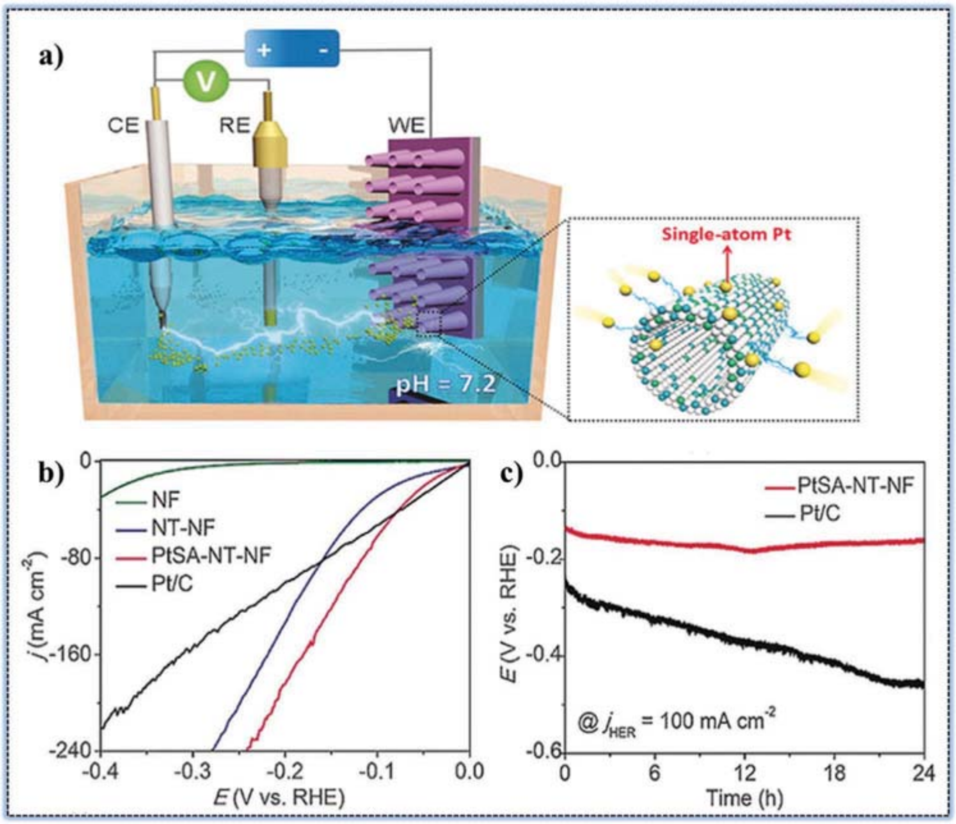

Figure 47. a) Schematic illustration of the synthesis procedure of PtSA-NT-NF, where CE represents counter electrode. RE represents reference electrode, WE represent working electrode. b) HER polarization curves of PtSA-NT-NF and other samples, acquired with 5 mV s^{-1} in N_2-saturated 1.0 M PBS at 25 °C. c) Current density versus time (*i*–*t*) curves of PtSA-NT-NF and Pt/C at a constant $j_{HER} = 100$ mA cm^{-2}. Reproduced with permission.[26a] Copyright 2017, John Wiley and Sons.

interface by single Pt atoms favored the H_2O dissociation process, while improving the adsorption/desorption of hydrogen, thus accelerating the HER kinetics.

5.2.4. HER Over a Wide pH Range

Electrocatalytic H_2 evolution is an electron transfer process as well as a proton transfer process. Since the water electrolysis process will inevitably lead to changes in the concentration of protons, the operating environment of different electrolysis equipment is not the same. As a result, there is an urgent need to develop electrocatalysts that can operate efficiently and sustainably over a wide pH range. We believe that the stability and catalytic activity of the active phase in different pH environments must be considered in the design of SACs. For example, near-free Pt SAs formed as a result of the weakened interaction and charge transfer between Pt and N-C framework displayed superior HER activity in wide-pH electrolytes.[37] Unfortunately, at present, the report of H_2 evolution SACs operating at all pH values has not constituted a complete system.

Generally, it is difficult to immobilize Pt-SAs onto porous carbon supports via traditional wet-chemistry technique. This is because the charge-balancing double layer generated by the precursors prevents the diffusion of Pt species.[10] To solve this issue, Lou's group reported a facile and universal synthesis strategy for the introduction of Pt-SA into the porous carbon matrix (PCM).[118] They found that when atomic Pt species migrated from the surface of the parent carbon sphere into the interior of the carbon matrix, the traction induced by PCM would make Pt ions gradually fuse into the crystal lattice of the PCM. Specifically, pyrolysis of the mesostructured polydopamine (PDA) particles incorporated with the Pt species can induce the mesopores formation, progressively fusing Pt ions into PCM owing to the internal dynamic force (**Figure 49**a). EXAFS spectrum demonstrated that the Pt—N/O bonds showed a square-pyramidal configuration. XANES spectra suggested that the d-electron transfer from Pt to PCM was due to the higher electronic density of unoccupied d states of the obtained Pt@PCM (Figure 49b). Additionally, they confirmed these results by using XPS, and there are no Pt-NPs existing in Pt@PCM sample. Despite a low Pt content of merely 0.53 wt.%, this Pt SAC exhibited promising stability and performance toward HER with a η_{10} of 105 mV and 139 mV in acidic and alkaline conditions, respectively. Especially, the decrease of Pt loading amount (from 0.53% to 0.095%) induced the presence of negative-shifted onset potential, indicating that the atomic Pt sites significantly contributed activity toward HER. DFT results revealed that there were some new hybrid electronic states between Pt (4*f* and 5*d* orbitals) and adjacent atoms

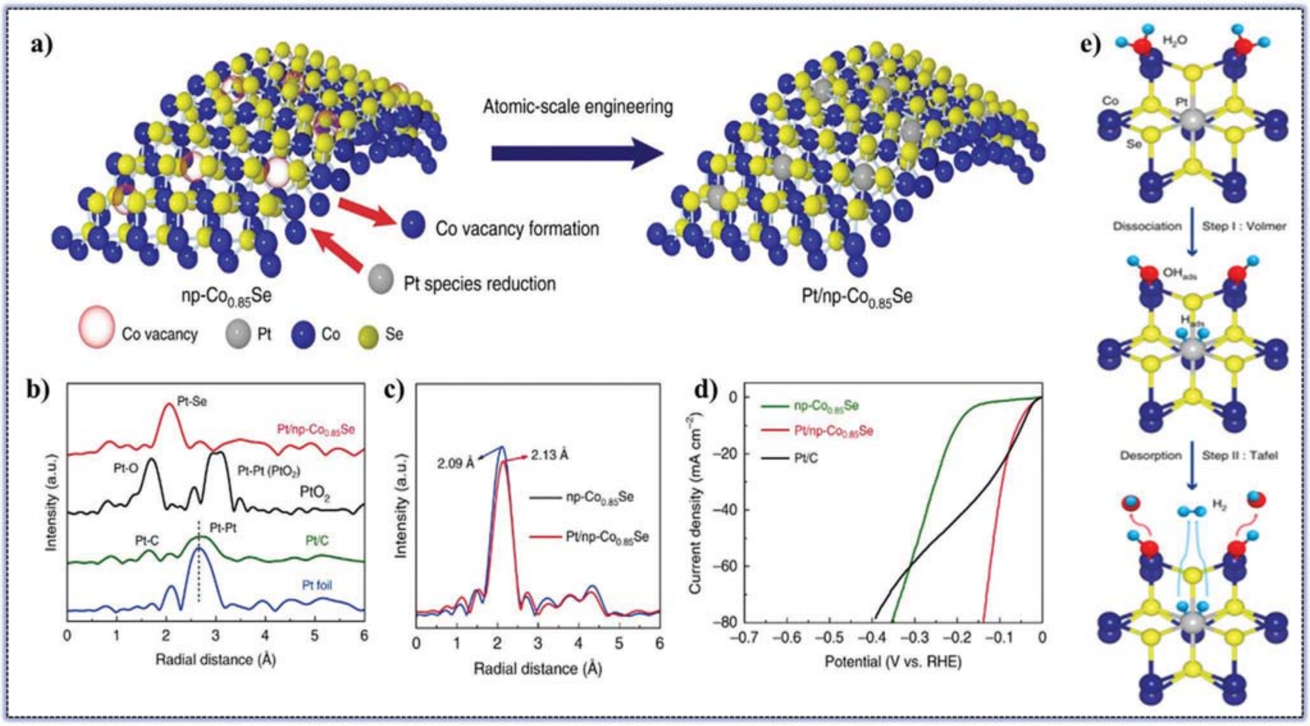

Figure 48. a) Schematic diagram of the manufacturing process of np-$Co_{0.85}$Se. b) Corresponding FT-EXAFS spectra for the normalized XANES at the Pt L_3-edge of Pt/np-$Co_{0.85}$Se and other samples. c) Corresponding FT-EXAFS spectra from the normalized XANES spectra at the Co K-edge of Pt/np-$Co_{0.85}$Se and other samples. d) HER polarization curves of Pt/np-$Co_{0.85}$Se and Pt/C. e) Schematic diagram of the HER mechanism revealed by in situ and operando XAFS measurements of Pt/np-$Co_{0.85}$Se in neutral solution. Reproduced with permission.[271] Copyright 2019, Nature Publishing Group.

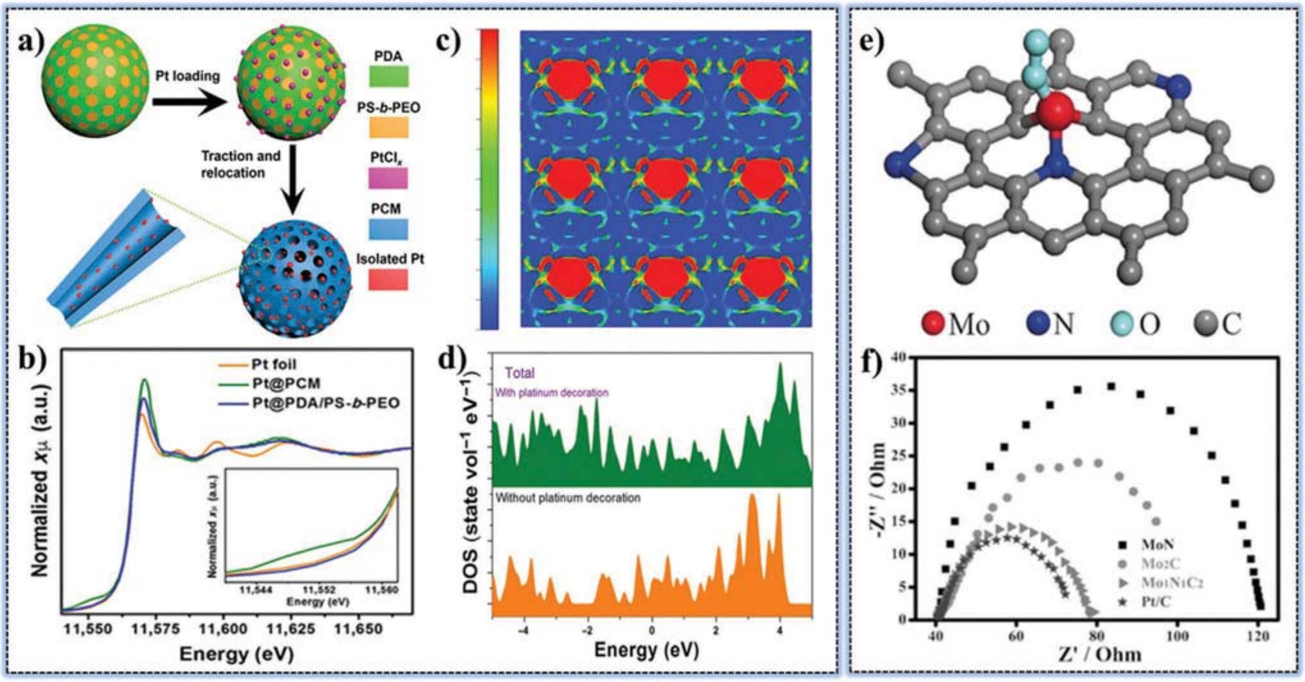

Figure 49. a) Schematic diagram of the fabrication procedure of Pt@PCM. First, Pt@PDA/PS-b-PEO is prepared by loading Pt component onto the PDA/PS-*b*-PEO. Second, Pt@PCM is obtained through pyrolysis of Pt@PDA/PS-*b*-PEO. b) Pt 4f XPS spectra of Pt@PCM and Pt/C-20%. c) Calculated DOS and d) Distribution of charge density of Pt@PCM. Reproduced with permission.[118] Copyright 2018, American Association for the Advancement of Science. e) Structure model of the $Mo_1N_1C_2$. f) Nyquist plots of the $Mo_1N_1C_2$, Mo_2C, MoN, and 20% Pt/C. Reproduced with permission.[116] Copyright 2017, John Wiley and Sons.

(Figure 49c). In addition, most of the charge density originated from Pt atoms, which can indicate that these Pt atoms enhance the catalytic activity through the distribution of charge density (Figure 49d).

In order to find an alternative material for Pt-based electrocatalyst, Tour et al. introduced dispersed Co-SAs into N-doped graphene (termed Co-NG) via simply heat-treating graphene oxide and a small number of cobalt salts in atmosphere of gaseous NH_3.[16a] Experimental and theoretical results showed that the Co-SAs in Co-NG could coordinate with N atoms on graphene, and had considerable H_2 evolution activity as well as stability in both acidic and alkaline media. In another work, Chen and co-workers prepared a SAEC that Mo-SAs were anchored on N-doped carbon via template and pyrolysis methods using sodium molybdate and chitosan as precursor.[116] AC-STEM and XAFS characterizations indicated that the Mo-SAs in the as-obtained catalyst were threefold coordinated $Mo_1N_1C_2$ moiety by one N atom and two C atoms, denoted as. Under alkaline conditions (0.1 м KOH), the as-fabricated SAEC exhibited an onset overpotential of 13 mV and required only an overpotential of 132 mV to deliver the current density of 10 mA cm^{-2}, which is much lower than that of Mo_2C and MoN. Figure 49f shows the Nyquist plots where the charge transfer of $Mo_1N_1C_2$ was relatively low, suggesting the faster charge transfer capacity of $Mo_1N_1C_2$ during HER. Meanwhile, $Mo_1N_1C_2$ also displayed good HER activity and stability in acidic solutions. As revealed by DFT calculations, the excellent electrocatalytic performance of $Mo_1N_1C_2$ for HER was mainly attributed to its unique coordination environment optimizing the d-electron domination near the Fermi level. Besides, MoS_2 nanosheets array supported by a carbon cloth (MoS_2/CC) provided abundant anchoring sites for Ru-SAs.[299] The unique 3D porous structure of MoS_2/CC can serve as co-catalyst for synergetic reaction and increase the electrical conductivity of this SAC. Owing to these properties, the as-prepared Ru-MoS_2/CC exhibited interesting HER activities under pH-universal conditions with a low η_{10} and Tafel slope. Among them, the values for Ru-MoS_2/CC at η_{10} were 41, 61, and 114 mV in alkaline, acidic and neutral media, respectively.

As discussed in the foregoing Section 2.5.2, from the structure–performance relationship, fine-tuning the oxidation state of SACs by EMSI is a feasible and promising strategy to achieve the regulation of the catalytic activities in both acidic and alkaline HER. Based on this, acidic/alkaline HER activity correlated with the oxidation state of Pt-SAs and the Pt—H/Pt—OH interaction was recently studied by Chen's group.[112] They used TMDs (e.g., MoS_2, WS_2, $MoSe_2$, and WSe_2) as supports for stabilizing Pt-SAs, where the chalcogen (S, Se) and the adjacent TM (Mo, W) could synergistically modulate the electronic structure of SAC via EMSI (**Figure 50**a). The synthesis method employed to immobilize Pt-SAs on various TMDs supports was similar to the work of Li and co-workers,[67] that is, UPD technique. As illustrated by XPS in Figure 50b, the conspicuous peak altered at approximately 71.8–72.8 eV was attributed to the increase of the binding energies of Pt $4f_{7/2}$ of Pt-SAs/TMDs.[112] This result indicated that the Pt species in Pt-SAs/TMDs has been partially oxidized with 0–+4 valence state because of the electronic interactions between Pt atoms and various TMDs supports (i.e., $Pt^{\delta+}$). By combining the magnified HAADF-STEM and DFT results, XAFS measurements demonstrated that Pt atoms coordinated with three nearest neighboring S or Se atoms were straddled atop Mo atoms, as shown in Figure 50c–f. As expected, the designed Pt-SA/TMDs exhibited remarkable HER activity with negligible overpotentials in both 1.0 м KOH and 0.5 H_2SO_4 solutions. In alkaline media, the trend of HER activities was Pt-SAs/$MoSe_2$ > Pt-SAs/MoS_2 > Pt-SAs/WS_2 > Pt-SAs/WSe_2, especially for Pt-SAs/$MoSe_2$ that exhibited the lowest $\eta_{10,\mathrm{HER}}$ of merely 29 mV and an exceptional mass activity of 34.4 A mg^{-1} at 200 mV, which is 73.4 times greater than that of commercial Pt/C (Figure 50g). By comparison with alkaline HER, these Pt SACs showed different activity orders in acidic media. Among them, Pt-SA/WS_2 exhibited the greatest HER activity with a superb mass activity of 130.2 A mg^{-1} at 100 mV, much better than most of the state-of-the-art SAECs (Figure 50h). More interestingly, when the average oxidation state of Pt-SAs was increased, the H adsorption ability would enhance almost linearly under acidic conditions, whereas the alkaline HER activity showed a volcano-type relationship (Figure 50g). Such phenomena further suggested that the adsorption energy of H* intermediates and Pt-OH interaction was modulated by the EMSI during HER.

5.3. Photocatalytic Water Splitting for Hydrogen Generation

Photocatalysis for the removal of pollutants and the production of renewable energy sources has become an increasingly promising technology to support the sustainable development of human being.[300] In addition to the above-mentioned techniques, converting photon energy into chemical energy to produce H_2 from water is also believed to be another promising energy conversion strategy.[3,301] Different from electrochemical water splitting requiring an applied voltage, photocatalytic water splitting/water photolysis can directly utilize solar energy to produce H_2. Mechanistically, owing to the semiconductor nature, photocatalysts can adsorb UV and/or visible-light (Vis) irradiation from sunlight or other light sources. As schematically depicted in **Figure 51**, when the energy of incident light is greater than that of the band gap, the electrons in the valence band (VB) will be excited to CB, while the holes are generated in the VB. These photogenerated electrons and holes separate and migrate to the photocatalyst surface through photoexcitation, leading to redox reactions similar to electrolysis. The produced negative electron (e^-) and positive hole (h^+) pairs act as reducing and oxidizing agents to form H_2 and O_2 for overall water splitting. As mentioned in Section 5.2, water splitting is an uphill reaction, which requires the standard Gibbs free energy change ΔG^0 of 237 kJ mol^{-1} or 1.23 eV. Accordingly, the theoretical band gap energy (E_g) of the photocatalyst for water splitting should be >1.23 eV when the wavelength of light irradiation (λ) is longer than 1000 nm, whereas E_g should be <3.0 eV (λ > 400 nm) to use visible light.

Obviously, it is important to match the band gap and the potentials of the conduction and VBs for both the reduction and oxidation of H_2O. Furthermore, the process of photocatalytic water splitting involves complex multi-electronic and multistep reactions. Typically, due to the low efficiency of water photolysis using pure water, the sacrificial reagents (also known as hole scavengers) are usually introduced to effectively

© 2022 Wiley-VCH GmbH

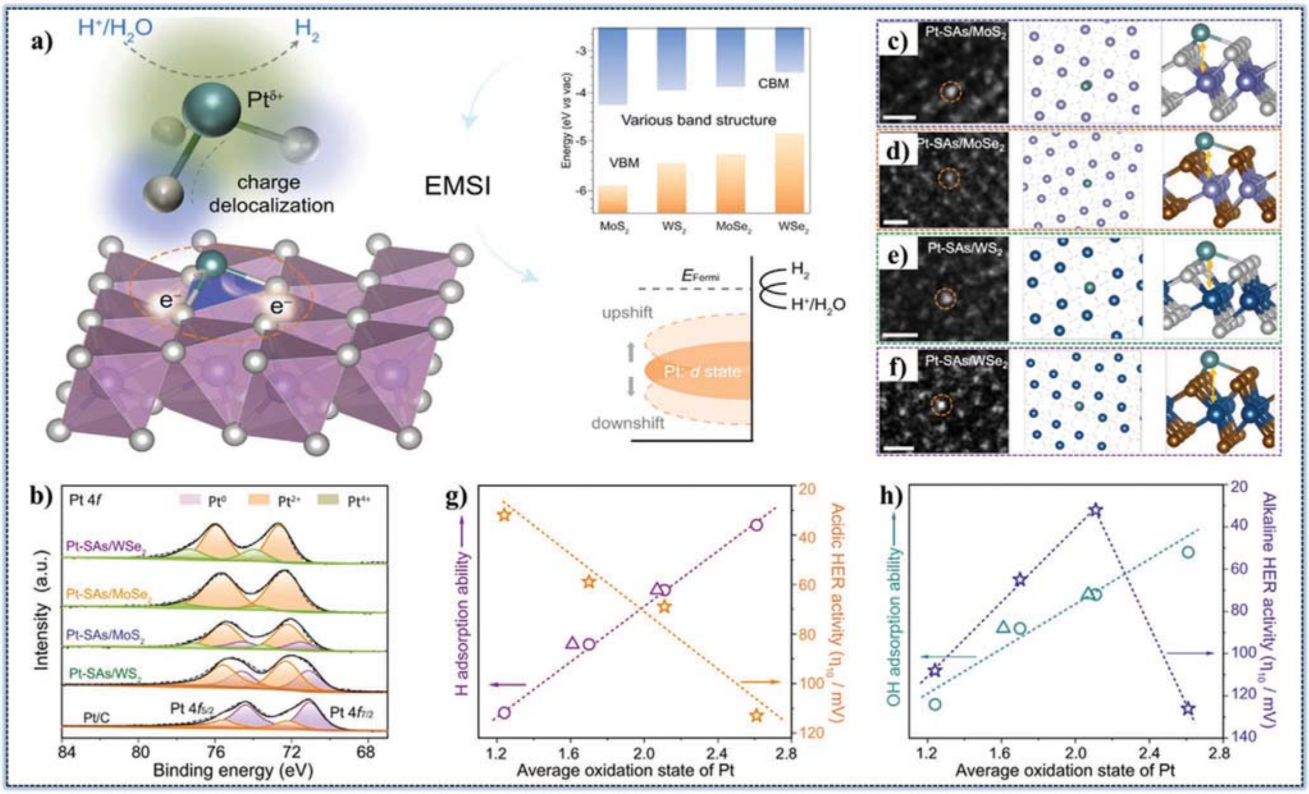

Figure 50. a) EMSI regulation of Pt-SAs for HER. Left: structure illustration of Pt-SAs on TMDs material. Gray spheres: chalcogen (S/Se); purple spheres: TM (Mo/W); green spheres: platinum. The electronic structure of Pt-SAs was tuned by 2D TMDs through charge delocalization, enabling the Pt-SAs to take a slightly positive charge ($Pt^{\delta+}$). The structural unit of Pt-SAs was circled by the orange dashed line and further enlarged above. Top right: schematic illustration of the band edges of TMDs. Bottom right: Schematic diagram shows that the *d*-state shift of Pt-SAs induced by EMSI modulates the HER performance. b) Pt 4*f* XPS spectra of the Pt-SAs/TMDs samples and commercial Pt/C. Magnified HAADF-STEM images and corresponding top and front views of optimized structural models for c) Pt-SAs/MoS_2, d) PtSAs/$MoSe_2$, e) Pt-SAs/WS_2, and f) Pt-SAs/WSe_2 samples. scale bars: 2 nm. purple spheres: Mo; gray spheres: S; brown spheres: Se; green spheres: Pt; blue spheres: W. Relationships of average oxidation state, HER activities, as well as H adsorption ability or Pt—OH interaction of Pt-SAs/TMDs g) under acidic conditions and h) under alkaline conditions. The circle and triangle represent the average oxidation state of Pt-SAs obtained from XPS and XANES, respectively. Reproduce with permission.[112] Copyright 2021, Nature Publishing Group.

promote the separation of electron-hole pairs, enhancing photocatalytic activity for hydrogen generation. Specifically, during the water photolysis process, photogenerated holes irreversibly oxidize sacrificial agents instead of water, so as to enrich electrons in photocatalysts for activity enhancement.[302] In other words, the electron donor sacrificial reagents (such as alcohol and sulfide ions) can be employed as an external force to drive the surface chemical reactions, then the formation of H_2O from H_2 and O_2 is inhibited. These sacrificial reagents can be divided into two types: organic (e.g., MeOH, organic acids, and hydrocarbons) and inorganic (e.g., sulfides and sulfites) electron donors. So far, methanol (MeOH) and triethanolamine (TEOA) have been widely reported as sacrificial reagents added in SACs for photocatalytic H_2 generation (**Table 2**). Notably, MeOH is commonly involved in the H_2 production reaction carried out by TiO_2-based photocatalysts, as well as for SACs.[126b,131,303] As an electron donor, methanol can react with photogenerated VB holes to improve quantum efficiency.[302a] Carbon-based[304] and MOFs-based SACs[41,70,71,305] are reported to be active for PHE in the presence of TEOA as the sacrificial reagent. Besides, Na_2SO_3/Na_2S,[58] ascorbic acid,[70] $(NH_4)_2SO_3$,[306] and lactic acid[49] have been used as sacrificial reagents for SACs toward PHE.

It should not be ignored that there are two major drawbacks in PHE driven by sacrificial reagents. On the one hand, it is necessary to continuously add fresh sacrificial agents in the reaction to maintain catalytic activity, which makes it difficult to achieve large-scale industrial H_2 production. On the other hand, sacrificial reagents such as sulfide (S^{2-}) and sulfite (SO_3^{2-}) are by-products of fossil energy.[307] These weak points are in contradiction to the strategic significance of clean energy and sustainable production. Unless photocatalysts with high light-to-hydrogen conversion efficiency are developed to compensate. Therefore, improving the absorption of visible light by the semiconductor photocatalyst, as well as reducing the recombination rate of photo-generated carriers and accelerating the surface reaction are necessary tasks in the study of H_2 evolution photocatalysts. As we have discussed before, the unique nature and exceptional performance of SACs provide great opportunities for practical PHE. Indeed, single-atoms photocatalysts (SAPCs) toward H_2 production are still in their infancy. Most of these studies focused on the synthesis, characterization, and

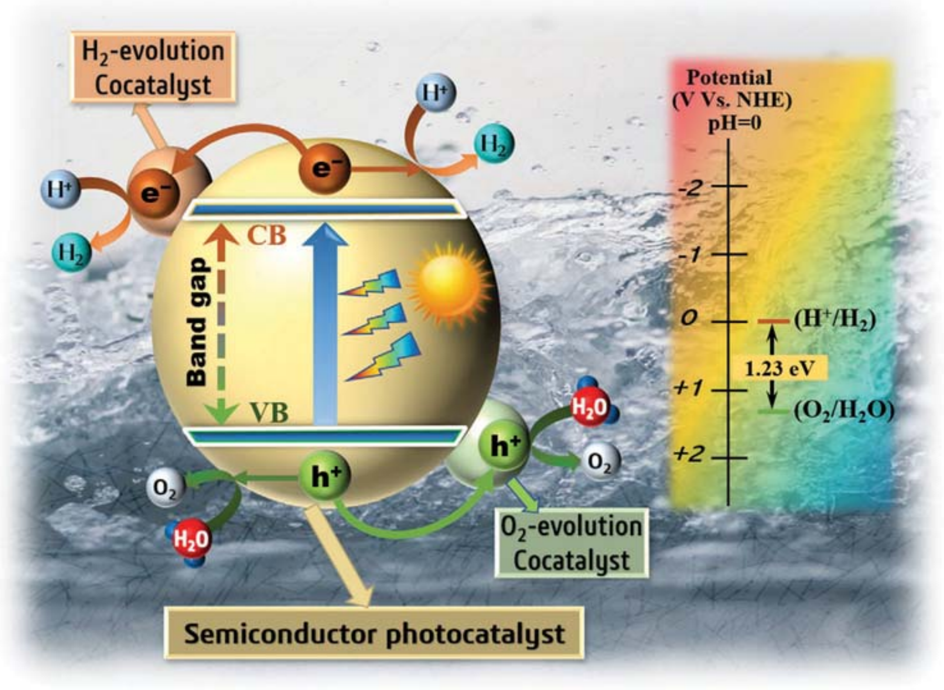

Figure 51. Principle of water splitting using semiconductor-based photocatalysts with cocatalyst loading.

activity evaluation of the catalysts. Accordingly, there is still no report on the mechanistic insights and detailed evaluation of the specific single-atom photocatalytic system by different sacrificial reagents. Of note, the effects of different sacrificial agents on specific PHE activity are not the same.[308] The redox potential of sacrificial reagents is the key to the study of water photolysis because of its effect on quantum efficiency and stability. For instance, in Pt-decorated CdS nanorods, the hole removal rate of SO_3^{2-} and TEOA with higher oxidation potential is faster than that of disodium ethylenediaminetetraacetic acid ($EDTA^{4-}$) and MeOH, whose relative low photooxidation leads to the loss of semiconductor materials and ligands, thus unfavorable for promoting kinetics.[302a] Furthermore, too high a concentration and the corrosive effect on catalysts will also influence the overall efficiency of the catalytic reactions to a certain extent. In general, besides continuing breakthroughs in the development of novel visible-light-driven photocatalysts, we believe that the investigation of sacrificial reagents into SAC systems toward PHE should be further strengthened to promote industrialization. Future directions of H_2 generation SAPCs should focus on the selection of appropriate sacrificial reagents, as well as the reducing or even not using sacrificial reagents.

In this section, two subsections according to the following basis: i) For Subsection 5.3.1, as a cocatalyst, M-SAs usually works synergistically with the adjacent environment to enhance the activity of PHE, such as modulating the electronic structure of support, reducing the interface resistance of carrier migration, modifying the intrinsic structure of support;[16f,131,309] ii) regarding Subsection 5.3.2, M-SAs served as primary active sites, and adsorbed H* directly originates from single metal sites.[79,207]

5.3.1. Single-Atoms-Derived Species as Cocatalysts

It is one of the effective strategies to improve the activity and stability of photocatalysts by introducing cocatalyst into photocatalytic systems, which can inhibit charge carrier recombination and electron capture, and meanwhile offer extra active sites for protons.[311] Figure 51 illustrated the principle of water splitting using semiconductor-based photocatalysts with cocatalyst loading. Specifically, i) cocatalyst can decrease the energy barrier of charge separation and migration for hydrogen or OERs; ii) cocatalyst can provide more reaction active sites; iii) the appropriate hetero-junction interface formed by cocatalyst and semiconductor shortens the necessary charge transfer distance, thus effectively accelerating the charge separation and transfer, as well as inhibiting both surface and bulk recombination; and iv) some specific cocatalysts loaded on semiconductors can inhibit their decomposition to enhance the stability of these photocatalysts.[312] Due to the unique coordination structure of single-atom catalysts, in which metal atoms coordinate with neighboring coordination atoms, M-SAs act as isolated active sites while also altering the electronic structure of the semiconductor support. In this case, M-SAs may be more suitable as a cocatalyst in photocatalysis.

As has been discussed in this paper before, the size of catalysts is a crucial factor influencing catalytic performance, and cocatalysts are no exception. Regarding the metal nanocatalysts, a large number of studies have demonstrated that the supported cocatalysts with small size and high dispersion exhibited superior photocatalytic activity. Certainly, M-SAs acting as a cocatalyst can further significantly boost the activity of photocatalysts because of the atomically dispersed

© 2022 Wiley-VCH GmbH

Table 2. Comparison of State-of-the-Art SACs for Photocatalytic H_2 Evolution.

Single-atom Photocatalyst	Metal Loading [wt.%]	Role of Single Atomic Species	Sacrificial Reagent	Light source	quantum efficiency [%]	Rate of H_2 Evolution	Ref.
Pt_1/black TiO_2	0.254	/	MeOH	300 W Xe lamp (> 420 nm)	1.37% at 420 nm	800.3 μmol h^{-1} g^{-1}	[303]
Pt/TiO_2-A	0.6	Active sites	MeOH	300 W Xe lamp		84.5 μmol h^{-1}	[126b]
Pt/TiO_2	0.2	Cocatalyst	MeOH			169.6 μmol h^{-1}	[57]
Pt_1/def-TiO_2	0.02	Cocatalyst	MeOH	300 W Xe lamp		52 720 μmol h^{-1} g^{-1}	[48]
Cu/TiO_2	0.75	Cocatalyst	MeOH	300 W Xe lamp (> 400 nm)	45.5% at 340 nm	16.6 mmol h^{-1} g^{-1}	[131]
Pt-CN	0.16	Cocatalyst	TEOA	300 W Xe lamp		318 μmol h^{-1}	[16f]
Pt-CN	0.1	Cocatalyst	MeOH	300 W Xe lamp (> 420 nm)		473.82 μmol mg^{-1}	[16g]
Pt-SACs/MBT	0.98	Cocatalyst	TEOA	300 W Xe lamp (> 420 nm)	67.6% at 420 nm	68.33 mmol h^{-1} g^{-1}	[305]
Pt_1Ag_{24}/g-C_3N_4	0.016	Cocatalyst	TEOA	300 W Xe lamp (> 420 nm)		39.7 μmol h^{-1}	[304a]
Pd/C_3N_4	0.1	Cocatalyst	TEOA	300 W Xe lamp (> 400nm)		728 mmol h^{-1} g^{-1}	[210]
Pd/g-CN	0.33	Active sites	TEOA		4% at 420 nm	6688 μmol h^{-1} g^{-1}	[207]
Al-TCPP-0.1Pt	0.07	Cocatalyst	TEOA	300 W Xe lamp (> 380 nm)		129 μmol h^{-1} g^{-1}	[41]
CN-Ni-OH	0.2 at %	Active sites	TEOA	300 W Xe lamp		354.9 μmol h^{-1} g^{-1}	[310]
Ag-N_2C_2/CN	3.7	Active sites	TEOA	300 W Xe lamp (> 420 nm)		1866 μmol h^{-1} g^{-1}	[304b]
Co_1/PCN	1.0	Active sites	TEOA	300 W Xe lamp (≥300 nm)	3.02% at 450 nm, 1.25% at 500 nm	10.8 μmol h^{-1}	[79]
				300 W Xe lamp (≥420 nm)		9.1 μmol h^{-1}	
Co_1-phosphide/PCN	0.4	Active sites	Pure water	300 W Xe lamp (≥300 nm)	3.6% at 420 nm, 2.2% at 500 nm, 0.35% at 580 nm	410.3 μmol h^{-1} g^{-1}	[55b]
				300 W Xe lamp (≥420 nm)		126.8 μmol h^{-1} g^{-1}	
CdS@CDs/Pt-SAs	1.15	Cocatalyst	Na_2SO_3/Na_2S	300 W Xe lamp	29.8% at 400 nm	45.5 mmol h^{-1} g^{-1}	[58]
PtSA-MNSs	12.0	Active sites	ascorbic acid	300 W Xe lamp (> 420 nm)		11 320 μmol h^{-1} g^{-1}	[70]
Ni-NG/CdS	0.0013	Cocatalyst	$(NH_4)_2SO_3$	300 W Xe lamp (> 420 nm)	48.2% at 420 nm	1351.1 μmol h^{-1}	[306]
Pt/CdS	0.27	Cocatalyst	lactic acid	300 W Xe lamp (> 420 nm)		19.77 μmol h^{-1} g^{-1}	[49]

active sites. For example, when Pt-SAs were anchored on the ultrathin porous CdS@carbon Dots (CDs) nanosheet as a cocatalyst, the H_2 production rate is 133 times higher than that of pristine CdS@CDs, up to 45.5 mmol h^{-1} g^{-1} (**Figure 52**a).[58] In this work, the Pt-SAs were immobilized on CdS@CDs through in situ reductions of the Pt precursor (H_2PtCl_6 $6H_2O$), while XAFS spectra demonstrated that the Pt-SAs were bonded as four-coordinated Pt—S. Noting that the Pt-SAs could not only enhance the photocatalytic performance of CDs nanosheets, but also accept electrons as the active sites for water reduction under light irradiation. In another report, anchoring the atomically dispersed Pt atoms could remarkably improve the PHE activity of g-C_3N_4.[16f] While the loading amount of atomic Pt species was 0.16 wt.%, the H_2 generation rate of the as-obtained SAC (318 μmol h^{-1}) was ≈50 and 8.3 times higher than that of pure g-C_3N_4 and Pt nanoparticles, respectively (Figure 52b). This is ascribed to the synergistic effect induced by isolated Pt-SAs inducing intrinsic change of the surface trap states the support. A similar work was reported by Zhang et al. that the photocatalytic H_2 evolution activity of g-C_3N_4 with low Pd-SAs loading (0.1 wt.%) was up to 728 μmol h^{-1} g^{-1} compared with that of pristine g-C_3N_4 (1.4 μmol h^{-1} g^{-1}).[210] The atomically dispersed Pb atoms bring about more efficient charge separation and faster charge transfer, strengthening the adsorption ability of hydrogen. Notably, the pyridine N in the adjacent cavity to the Pb atom was the real active site. In addition,

Li's group has reported a highly efficient SAPC with Pt loading content of merely 0.02 wt.% (denoted as Pt_1/def-TiO_2).[48] Experiments and characterizations demonstrated that Pt-SAs can promote the neighboring TiO_2 units to produce the surface O_{vac}. Remarkably, the photocatalytic H_2 evolution rate of the as-prepared SAPC was 78.5 times than that of pristine def-TiO_2 in the presence of MeOH, which was attributed to the unique structure of the constructed Pt—O—Ti^{3+} interface. Jiang et al. employed Al-TCPP MOFs as support to anchor Pt-SAs to fabricate a photocatalyst for H_2 evolution.[41] The atomic Pt species that strongly interact with the Pyrroic N atom in the as-prepared catalyst can maintain good stability, and the TOF (35 h^{-1}) of the Pt-SAs is 30 times that of the corresponding Pt-NPs, obtaining an amazing photocatalytic hydrogen production efficiency. This study has proved that MOFs possess the potential to be ideal support for SACs.

Ag clusters or NPs were regarded as one of the alternative materials for precious metal-based semiconductors.[313] The strong synergistic effect induced by SAs can eliminate the sluggish interfacial electron transfer of Ag. Hua et al. have found that introducing Pt-SAs as a dopant into Ag_{25} nanocluster

© 2022 Wiley-VCH GmbH

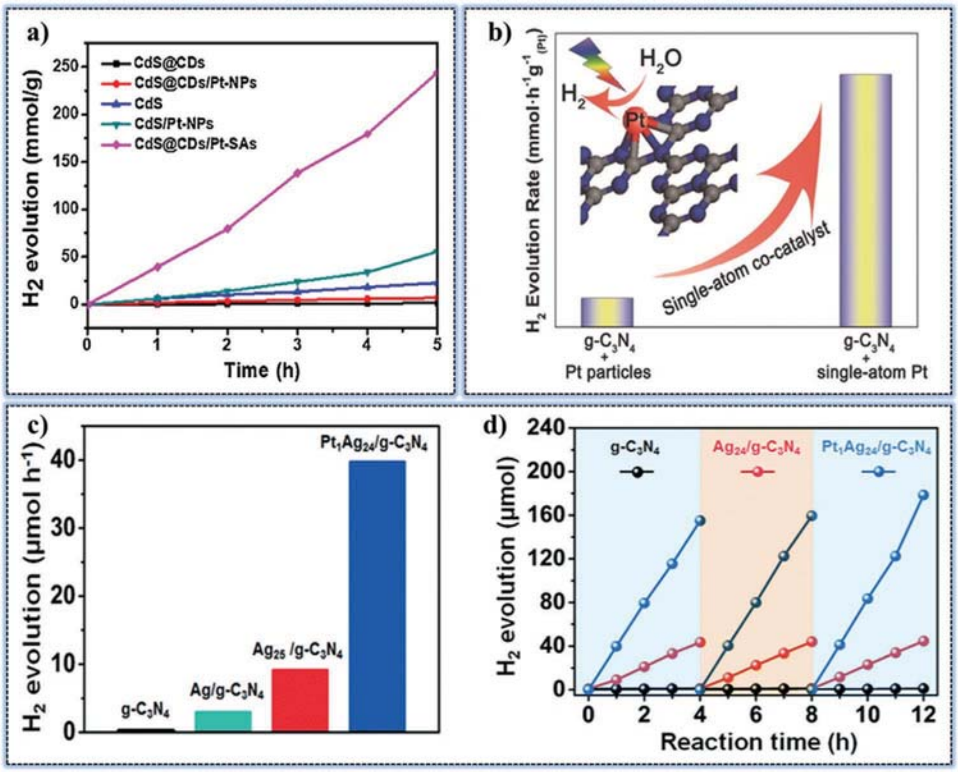

Figure 52. a) Photocatalytic H_2 evolution over CdS@CDs/Pt and other catalysts under simulated sunlight irradiation. Reproduced with permission.[58] Copyright 2019, Elsevier Inc. b) The photocatalytic activity of g-C_3N_4 was greatly enhanced due to Pt SAs. Reproduced with permission.[16f] Copyright 2016, John Wiley and Sons. c) Photocatalytic H_2 evolution performance of g-C_3N_4, Ag_{25}/g-C_3N_4, and Pt_1Ag_{24}/g-C_3N_4. d) Cycling runs for the H_2 evolution of g-C_3N_4, Ag_{25}/g-C_3N_4, and Pt_1Ag_{24}/g-C_3N_4. Reproduced with permission.[304a] Copyright 2020, Royal Society of Chemistry.

anchored on g-C_3N_4 (Pt_1Ag_{24}/g-C_3N_4) could strengthen the ability for trapping electrons, thus finely controlling the charge-carrier dynamics.[304a] Under visible-light irradiation, the H_2 evolution rate of Pt_1Ag_{24}/g-C_3N_4 was more than 4 times that of Ag_{25}/g-C_3N_4 without Pt-SAs in the presence of TEOA, and it could be reused within the cycle time, which exhibited considerable activity and stability (Figure 52c,d). It has been proved that the uniformly dispersed Pt-SAs cocatalyst creates a new surface state for charge trapping, thereby enhancing the interface charge transfer and electron-hole separation efficiency.[312b]

The non-noble metal SAs employed as cocatalysts have shown good PHE efficiency.[306] For example, catalytically active Pt-SAs were successfully anchored onto N-doped graphene by routine wet impregnation method, and then coupled with CdS, obtaining Ni-NG/CdS SAC. This catalyst with Ni loading of 0.0013 wt.% exhibited robust and highly active PHE in the presence of $(NH_4)_2SO_3$ as a sacrificial agent, especially an extremely high quantum efficiency of 48.2% at 420 nm. As investigated by photoluminescence (PL), the lower PL intensity of this photocatalyst indicated a stronger inhibition effect for the recombination of charge carriers, thus increasing the photocatalytic activity. Additionally, EIS and photocurrents measurement further verified the promotion effect of charge separation and transfer in Ni-NG/CdS compared to NG/CdS and bare CdS. These results demonstrated that Ni-SAs dispersed in NG played critical roles in the proton reduction reaction. According to DFT calculations (**Figure 53**a,b), the Ni-SAs confined in single vacancy +3 pyridinic-N (SV+3N) structures provided H adsorption sites and weakened the H adsorption $|\Delta G_{H^*}|$ at N sites, thus obtaining preferable ΔG_{H^*} value.

There is no doubt that M-SAs as cocatalysts could well regulate the electronic band structure and the interaction with semiconductors, which alters the intrinsic light-absorbing properties of photocatalysts.[314] More importantly, these single-atom cocatalysts can significantly increase the PHE activity with a fairly low metal loading amount.

5.3.2. Single Atoms as Active Sites toward Hydrogen Generation

In addition to acting as cocatalysts, M-SAs usually play the role of active sites in photocatalytic reactions as well. In the work of Chen' group, single Pd atoms were simultaneously anchored onto surface and intercalated into the space among the adjacent layers of the g-C_3N_4 support. The results of electrochemical impedance spectroscopy (EIS), steady-state, and time-resolved photoluminescence (TRPL) spectroscopy demonstrate that the photoexcited electrons transferred from the bulk to the surface are finally captured by the surface Pd atoms, indicating that the Pd atoms are the active sites.[207] Wang and co-workers stabilized a series of noble metal SAs on zirconium-porphyric MOF hollow nanotubes (HNTM) by a simple solvothermal method (**Figure 54**a).[71] The authors used porphyrin–Pt units as a catalyst and cleverly introduced Ir complexes as photosensitizers

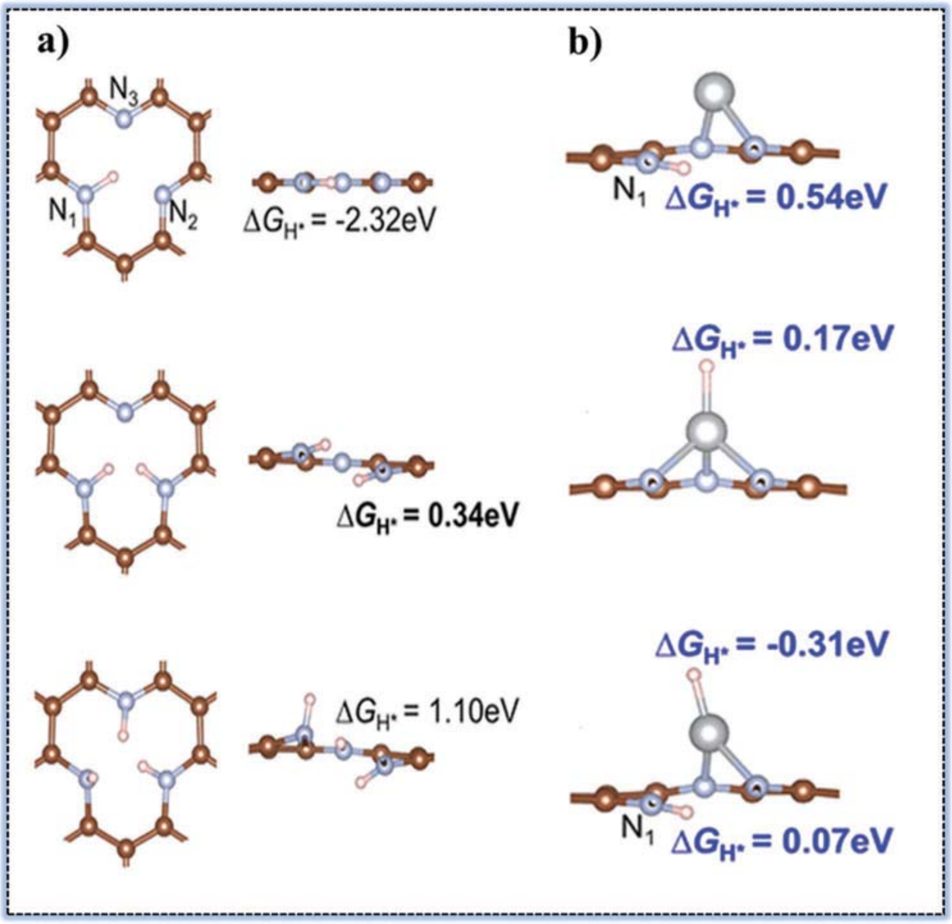

Figure 53. Optimized structure with various H adsorbed on a) SV+3N and b) SV+3N+Ni structures. Reproduced with permission.[306] Copyright 2018, American Chemical Society.

into the HNTM structure. Interestingly, the formed porphyrin-Ir units have a synergistic effect with the catalyst, which contributes to improving the catalytic performance. In another work, dispersed Pt-SAs at ultrahigh loading could be immobilized onto ultrathin 2D MOF nanosheet (MNSs) through a surfactant-stabilized coordination strategy, fabricating a PtSA-MNSs SAPC.[70] HAADF-STEM images showed a uniform distribution of Pt-SAs on the MNSs, and this result was confirmed via XAFS measurements. XANES spectra of Pt L_3-edge demonstrated the oxidation state of Pt species due to the white-line intensity of the obtained catalyst was between those of Pt foil and PtO_2, as shown in Figure 54b. By combining the XPS results, EXAFS analysis further gave predominantly Pt—N coordination for the atomic Pt sites with a bond length of ≈1.5 Å (Figure 54c), indicating that Pt-SAs were immobilized by N atoms with the absence of Pt nanoparticles or clusters. This photocatalyst exhibited a surprising H_2 evolution rate of 11 320 μmol h^{-1} g^{-1} (Figure 54d). Correspondingly, DFT calculations revealed that these Pt-SAs favored efficient proton/electron transfer and optimized H binding (Figure 54e).

Carbon nitride is currently one of the major supports of photocatalysts, including SAPCs. By a phosphidation approach, Wei's group constructed a stable single Co-phosphide structure (namely Co_1—P_4 site) on g-C_3N_4 nanosheets for the immobilization of Co-SAs.[55b] Such coordinatively unsaturated Co sites against the charge recombination could significantly prolong the average lifetimes of photogenerated carriers, as well as favor the adsorption and activation of water molecules compared to the N sites in g-C_3N_4. Soon afterwards, they successfully anchored Co-SAs on g-C_3N_4 nanosheets for efficient PHE via ALD (**Figure 55**a).[79] In this work, the single Co_1—N_4 sites formed by the grafting of dispersed Co-SAs with N atoms acted as active sites for promoting H—H coupling to facilitate H_2 production. In the presence of TEOA as the sacrificial electron donor, the obtained SAC showed an outstanding photocatalytic performance up to 10.8 μmol h^{-1} under UV-Vis light, which is 11 times higher than that of pristine counterpart (**Figure 56**d). This work provided an ideal model to unravel the mechanism of enhanced H_2 evolution for the typical Co_1-N_4 structure. In recent work, the oxidized Ni SAC constructed on polymeric carbon nitride (denoted CN-0.2 Ni-HO) achieved a 30-fold improvement in the photocatalytic H_2 evolution activity, as compared to pure CN.[310] Intriguingly, the addition of Ni component had little effect on the intrinsic structure and functional groups of CN, while the coordination environments of Ni-SAs could be finely modulated through different

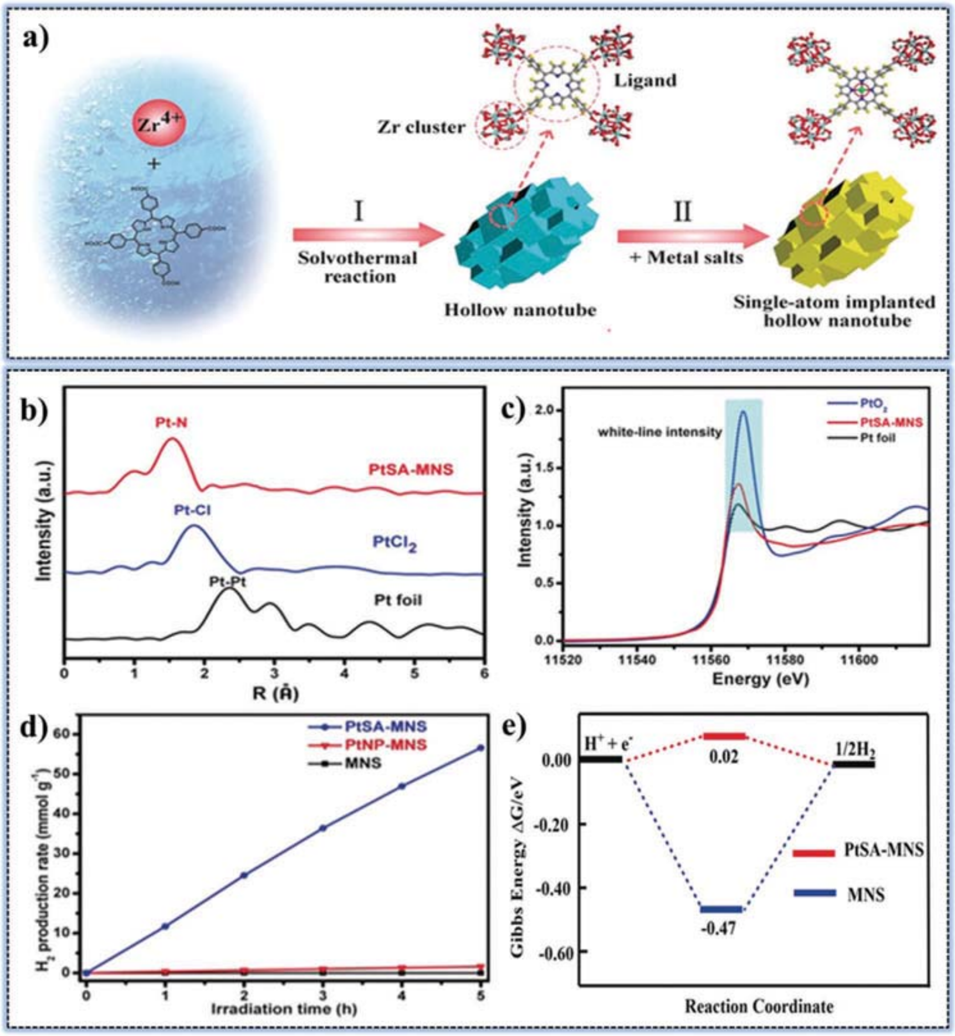

Figure 54. a) Illustration of the synthetic route toward the single-atom-immobilized hollow nanotube MOF (HNTM-M). Reproduced with permission.[71] Copyright 2018, John Wiley and Sons. b) Aberration-corrected HAADF-STEM image of the PtSA-MNSs. The Pt L_3-edge c) XANES and d) EXAFS spectra for PtSA-MNSs, $PtCl_2$, and Pt foil. e) ΔG_{H*} on MNSs and PtSA-MNSs. Reproduced with permission.[70] Copyright 2019, John Wiley and Sons.

calcination procedures. DFT calculations and XAFS spectroscopy confirmed that each Ni-SAs dispersed on CN substrate was coordinated with four N atoms and one C atom (Figure 55b). The fitting results gave the coordination number of circa 5 at 2.06 Å (Figure 55c). Particularly, the partial oxide state of the single-atom active sites was essentially the intermediate valence state with Ni^{2+}/Ni^0 ratio of about 2:1. Particularly, the partially oxidized single Ni sites had more *d*-orbital unpaired electrons occupying the VB (Figure 55d), and the CB crossed the Fermi surface, which reduced the electron work function (from 4.76 to 3.69 eV). As a result, electrons are more easily excited by light. As shown in Figure 55e–g, the investigation into the photocatalytic H_2 evolution performance demonstrated that the as-prepared SAC possessed robust activity and stability.

Of note that C atoms are the central storage rooms for the excited electrons of CN, but the metal atoms in SACs prefer to bind with N atoms to form $M-N_x$.[79,315] This means that when the excited electrons in CN are transferred to metal atoms, a high energy barrier needs to be overcome, especially for metals with low work function (such as Ag).[316] Regarding this, Chen et al. propose a supermolecular approach to modulating the Ag-SAs coordinated with C and N atoms, constructing an $Ag-N_2C_2/CN$ photocatalyst which could lower the energy barriers of electron transfer (Figure 56a).[304b] As illustrated in Figure 56b,c, XAFS measurements revealed that the dispersed Ag-SAs were coordinated with C and N atoms in CN substrate at the coordination number of 1.8 and 2.3, respectively. Similar to CN-0.2 Ni-HO SAC mentioned above, there was no obvious influence on the structure of CN after the introduction of Ag atoms, whereas Ag atoms could enhance the light absorption by band gap narrowing. Impressively, the as-fabricated catalyst exhibited much better H_2 evolution activity than Pt-NPs supported on CN, with robust stability even after 15 cycles (Figure 56d,e). Experimental characterizations and DFT calculations demonstrated that the atomically dispersed Ag species co-coordinated with C and N atoms modulated the electronic structure and improved charge transfer, thus boosting the photocatalytic H_2 evolution of CN (Figure 56f).

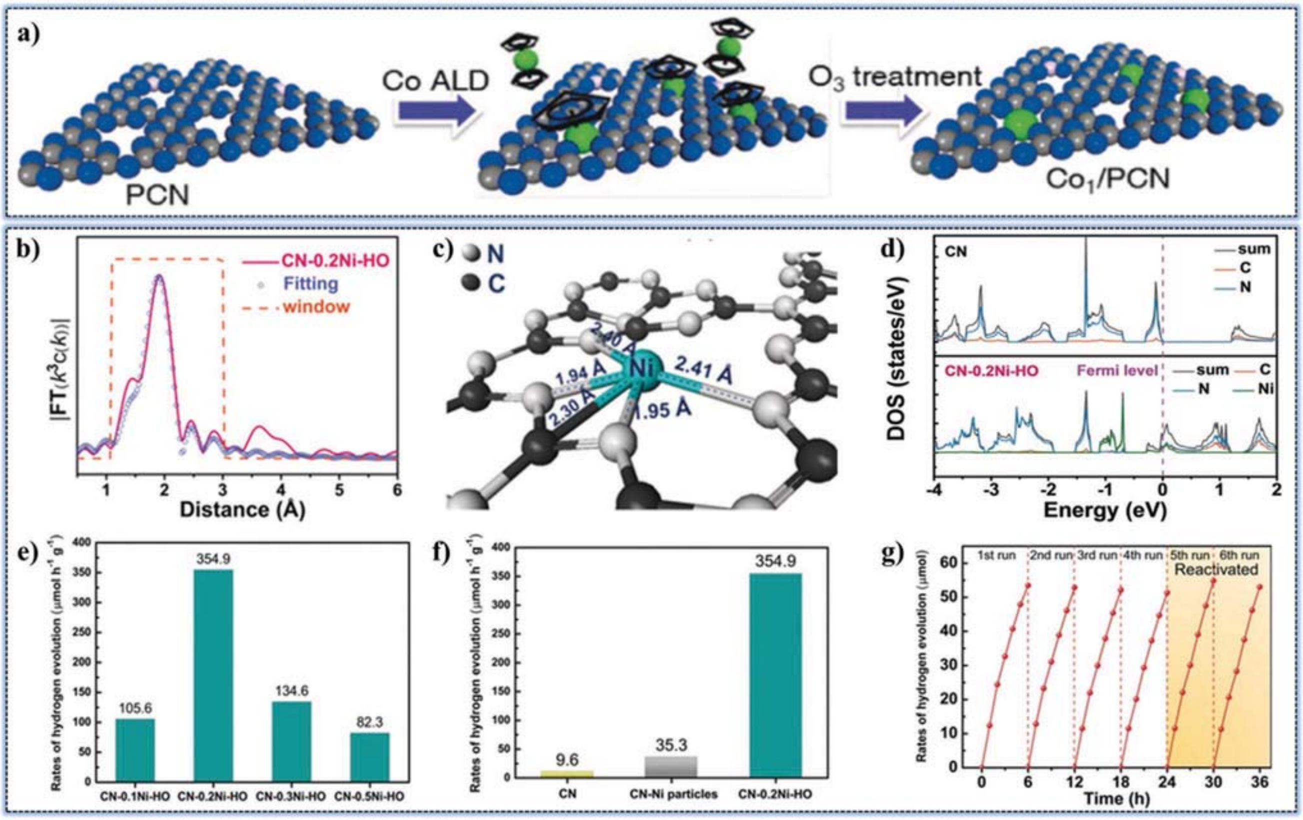

Figure 55. a) Illustration of the preparation for Co$_1$/PCN SAC by the ALD method. Reproduced with permission.[79] Copyright 2017, John Wiley and Sons. b) Structural model for single Ni site in CN. Black, light, and green spheres represent C, N, and Ni atoms, respectively. c) Fitting results of FT-EXAFS for CN-0.2 Ni-HO. d) Density of states of CN and Ni/CN. Photocatalytic H$_2$ production rates on Ni-SAC e) with different concentrations of Ni, and f) in comparison to those of pristine CN and CN-Ni particles. g) Cycling stability on CN-0.2 Ni-HO. Reproduced with permission.[310] Copyright 2020, John Wiley and Sons.

6. Conclusions and Perspective

Single-atom catalysts have been a hot topic in the field of sustainable energy transformations. In the course of H$_2$ evolution, SACs have exhibited the following three outstanding advantages. First, the ultrahigh catalytic efficiency of SACs provides the best scheme for saving preparation costs. The second is that their machinability and versatility can broaden the scope of application. Particularly, in addition to electrocatalysis and photocatalysis, SACs can also get involved in various biomedical research (e.g., cancer treatment, wound disinfection, biosensing, and oxidative-stress cytoprotection),[317] as well as the enzyme catalysis[318] and the synthesis of fine chemicals.[319] Third, it is not limited to noble and non-noble metals, even nonmetal SACs can also display excellent catalytic performance.[24] Throughout the full paper, to rationally design H$_2$ production SACs, we highlight the guidelines involved in structural and electronic modulation: i) designing highly uniform single active sites to maximize the atom-utilization efficiency; ii) constructing specific geometric configuration to stabilize and expose a large density of active sites on the surface, thus enhancing the HER activity; iii) optimizing the density/loading of SAs to suppress their migration and agglomeration; iv) tuning the coordination environment by doping heteroatoms to adjust electronic structure and promote electrons transfer, thereby facilitating the adsorption/desorption of hydrogen on the catalyst surface; v) taking advantages of the interactions between metal and support to regulate the adsorption energy of intermediate species, which can lower the kinetic reaction barriers for water dissociation. Since the supports are not only used to immobilize M-SAs but also participate in catalytic reactions, the rational design of metal atom–support interface is of great significance for H$_2$ evolution. It has been demonstrated that metal atoms, supports, and anchor sites are the key factors affecting the H$_2$ generation performance of SACs in different catalytic systems. In particular, due to the intrinsic limitations, SACs cannot fully exploit their advantages in certain catalytic systems. In this regard, we believe that the proximity effects in SACs, that is, the synergistic effects between metal and metal, is one of the effective ways to overcome this problem. From the three perspectives of intermetallic electronic, interface, and steric effects, the static regulation and dynamic evolution of bimetallic catalysts, that is, SAAs and DACs, are briefly described. The successful design from SACs to SAAs/DACs can help us survey the diversified development of catalysts for H$_2$ production.

Regarding PHE or HER, an ideal catalyst system for H$_2$ production should possess the following typical advantages: i) low costs, which means that non-noble metal and even metal-free sites show the high efficiency of H$_2$ evolution similar to that of noble metal, apart from the low noble metal loading;

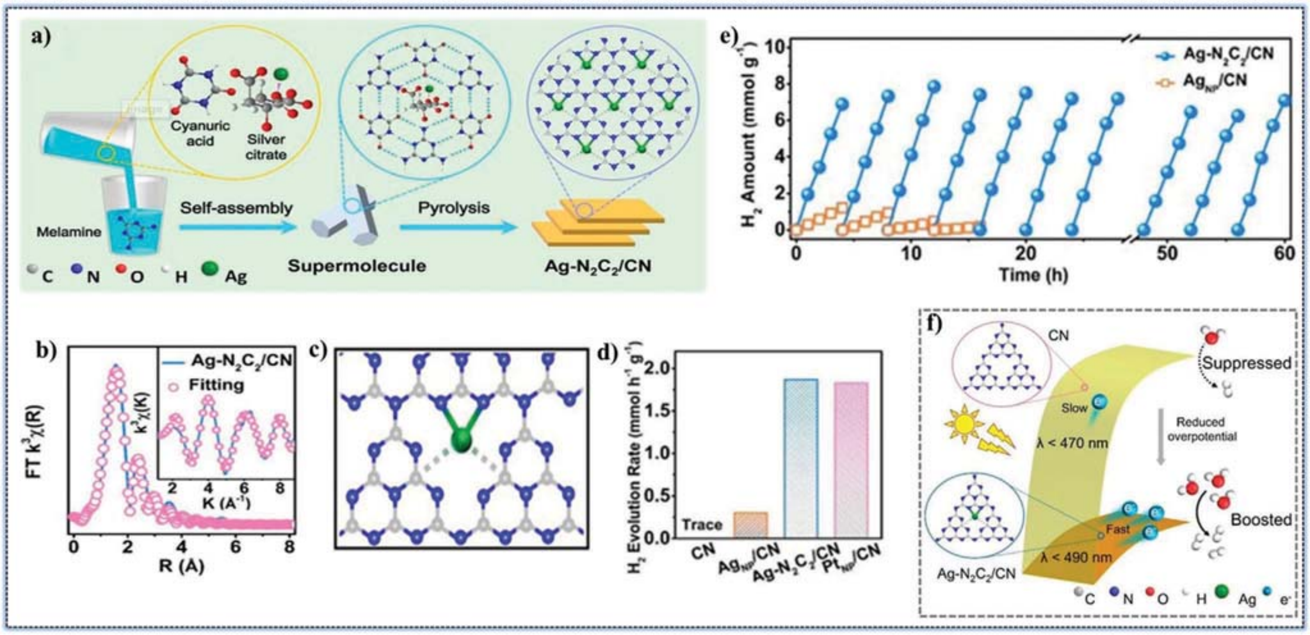

Figure 56. a) Synthesis process of Ag-N$_2$C$_2$/CN. b) EXAFS fitting curve in R space and c) Schematic structural model of Ag-N$_2$C$_2$/CN. Green, blue, and grey spheres represent Ag, N, and C atoms, respectively. d) H$_2$ generation rates and e) the cycling activity of Ag-N$_2$C$_2$/CN and other samples. f) proposed mechanism for photocatalytic H$_2$ generation over CN and Ag-N$_2$C$_2$/CN. Reproduced with permission.[304b] Copyright 2020, John Wiley and Sons.

ii) facile and universal fabrication route for industrial production; iii) good durability and high catalytic stability in complex electrolytes during HER electrocatalysis, or continuously generating excited charges by the use of absorbed photons during PHE; iv) robust HER activity over a wide pH range, or efficient separation of the photoactive sites without any sacrificial reagents during PHE; v) necessary mouldability and easy recycling to ensure reutilization; and vi) integrating with other renewable energy utilization devices, such as the wind generator, hydroelectric power system, and solar energy photovoltaic power system, etc. Unfortunately, during practical applications, almost none of the known can have all the above advantages at the same time, because of poisoning deactivation induced by trace environmental impurities and the aggregation of active sites. It has been demonstrated that SACs can integrate the advantages of homogeneous catalysts (including dispersedly isolated active sites, maximum metal utilization, and high selectivity) with heterogeneous catalysts (including good stability and easy separation).[18] Consequently, SACs with significant size effect have been believed to serve as a kind of promising catalysts to achieve new breakthroughs in H$_2$ production. Young SACs have won the favor of many scholars in just ten years. However, the impressive research fruits in SACs cannot cover up the fact that it is still a challenge to achieve a wide range of industrial applications, especially there are some issues to be solved, such as stability, preparation universality, and suitable catalytic system. Despite the vigorous advances in SACs, it is suggested that more research efforts should be devoted to getting deep insight into the numerous challenges still existing for their future applications in H$_2$ production:

(1) Attaching great importance to the role of support: As compared to nanocatalysts, SACs show more distinct metal–support effects.[320] The key factors affecting the H$_2$ production activity of SACs include but not limited to the electronic structure of support, the number and isolation distance of vacancies, as well as the electronic properties of M-SAs. For example, the electron transfer on the d_{z^2} orbital of Cu could lead to lattice distortion of TiO$_2$, thereby improving the PHE activity through the cooperative interaction of atomic catalysts and neighboring environments.[131] In another example, the unique configurations formed by trapping Ni-SAs into graphene defects could modulate the local electronic structure to optimize electrochemical activity for OER and HER, respectively.[56] It should be pointed out that the presence of a small amount of subnanometric metal clusters or nanoparticles can mislead the active sites and reaction pathways of SACs. Therefore, the conditions for judging whether SACs are successfully prepared are relatively stringent. Strictly speaking, all metal atoms in SAC are expected to be fully dispersed and isolated on the support, in which the aggregation of metal atoms is not allowed. It can be seen that the real active sites for activating reactants should be "single metal atoms". The key to achieving this goal is the coordination interactions between active metal atoms and ligand species (such as O^{2-}, OH$^-$, C^{4-}, N^{3-}, and S^{2-} species on the ionic supports) on the support surface. Particularly, the coordinating species at the metal–support interface can participate in the water redox process or proton transfer process, thus promoting the electrocatalytic HER. Actually, such a coordination relationship is similar to that of homogeneous catalysts. The geometric character is the biggest difference between SACs and homogeneous catalysts, especially the limitation of inorganic solid support on the geometric configuration of complexes. In this regard, the use of supports with flexible geometry, such as polymer, is one of the feasible methods to overcome the geometric limitation. It should be emphasized that in some

catalytic systems, the support can directly get involved in the catalytic reaction and establish a prominent proximity effect with M-SAs. These research findings indicate that it is necessary to thoroughly explore the mechanism of the metal–support interface in the reaction.

The stability of SACs is another index that must be paid attention to, in which the influence of the supports cannot be ignored. First, because of the intrinsic heterogeneity of most supports, the interactions between SAs and supports present uncertain spatial ordering. That is, SAs are highly sensitive to the surface structure of the supports, which greatly increases the difficulty of practical production.[230b] The non-uniform active sites of SACs lead to a significant decrease in their hydrogen production performance. Second, atomically dispersed metal species tend to agglomerate into nanoparticles or clusters due to their high surface energy as well as the strong chemical interactions between adsorbates and metal sites on supports, losing excellent activity. It is challenging to fabricate high-performance SACs with highly uniform active sites in large-scale industrial applications. In Section 3, we reviewed metal oxide supports (TiO_2, Fe_xO) and TM compounds (TMDs, TMCs) that can be used to stabilize M-SAs, and showed outstanding hydrogen production activity. Nevertheless, these SACs have low conductivity and/or poor stability toward HER under strong acid or alkaline environment.[29,321] In contrast, carbon-based SACs can work well over a wide pH range. There also exists the disadvantage of being unstable high-temperature oxidation and high-oxidation potential environments.[322] Based on the current research and understanding, SACs with adaptive structures need to be designed according to the actual reaction conditions toward efficient PHE and HER. Adjusting the coordination structure between SAs and substances to strengthen the interaction with the coordinatively unsaturated sites, such as heteroatom doping, loading mass/density, is a common means to control the adaptability of the support. Furthermore, the combination of operando spectroscopic studies and computational simulations can help us to deeply dissect the mechanisms and phenomena in various reactions, which is of great significance for the rational design of highly stable SACs toward H_2 production.

(2) Performance and practicability improvement: In energy-related applications, the low-cost operation depends on the development of catalysts with high activity and selectivity. Improving the density and intrinsic activity of active sites are considered to be effective strategies to enhance the activity of SACs. The peculiar MSIs in SACs provide a confinement effect to stabilize more M-SAs as active sites. Meanwhile, the exposure of active sites can be increased by functionalizing the support, for instance, heteroatoms doping and the introduction of defects. Notably, although the density of active sites increases to a certain extent when raising the metal loading, the excessive increase may lead to agglomeration, thus reducing catalytic activity. Considering the costs, the activity enhancement dependent on the loading amount does not apply to noble metal-based catalysts.

The intrinsic activity of active sites has a more significant impact on the catalytic activity as compared to the density of active sites. The difference in intrinsic activity between good catalysts and poor catalysts can exceed more than 10 orders of magnitude, but the difference between high-loading and low-loading catalysts might only be 1 to 3 orders of magnitude.[13,323] The intrinsic activity of SACs can be regulated by the coordination environment, the interactions between metals and the support, and the synergistic effect between metals and metals, as well as the nature of the metals and supports, especially the H-binding strength is determined by the electronic structure of active sites. This means that there is an urgent need to further combine theoretical calculations with experimental results in order to deeply study and understand the relationship between the electronic and geometric effect of SACs and the catalytic activity. Generally speaking, because the active sites in SACs are isolated, their catalytic activity tends to weaken as the selectivity increases. Constructing SACs with a controllable coordination environment is the optimal scheme to maintain high activity and high selectivity at the same time. The site-isolated atoms in SACs provide high chemical selectivity, while the electronic modification of the active sites by the coordination environment can effectively activate the reactant. Compared to the regulation of metal–support coordination for minimizing ΔG_{H*}, it is still experimentally challenging to promote both the H_2O dissociation and H recombination under alkaline conditions via the optimization of single-atom active sites. As discussed in Section 4.2, owing to the atomic-level cooperative interactions between metal and metal, bimetallic single-site catalysts (i.e., SAAs) or bimetallic dual-site catalysts (i.e., DACs) have been expected to be ideal model catalysts for controllable optimization of the balance between H_2O dissociation and H recombination, thus further improving the rate of H_2 evolution.

(3) Developing novel synthesis approaches and design strategies: In the single-atom catalyst systems, the coordination atoms have a great influence on the electronic structure of the center atoms, which leads to the active sites exhibiting different catalytic performance. This finding suggests that finely designing the local atomic structure of the active sites with a regulable coordination environment at atomic scale has become the focus and challenge of research area. On the one hand, most reported synthesis strategies of H_2 evolution SACs are only applicable to small-size preparation in the laboratory. On the other hand, the high catalytic efficiency of these SACs is the result of sacrificing the loading amount. In addition, we also noticed that the research on non-metal-based SACs has been almost neglected as compared to metal-based SACs. The primary advantage of non-metal-based SACs is low cost and facile fabrication. We advocate that the development of the study on SACs should be diversified. It is of great economic and scientific significance to further develop the large-scale production technologies for non-metallic SAC in the field of H_2 production. Obviously, to meet industrial needs, it is of great practical significance to further develop superior support materials and synthesis strategies to achieve low cost, fast, integrated control, high efficiency, and stable large-scale application standards. In 2019, Zhang's group employed a "ligand-mediated" approach for large scale synthesis (>1 kg) of transition-metal SACs containing Cr, Mn, Fe, Co, Ni, Cu, Zn, Ru, Pt, or combinations thereof.[324]

Subsequently, Ma and co-workers reported a feasible strategy that allowed the kilogram-scale fabrication of noble-metal SACs via the ball-milling and calcination treatment of commercial acetylacetonate precursors at ambient conditions.[282] These works pave the way for cost-effective mass production of SACs, opening a window for their industrial application.

Actually, the activity of SACs is not always superior to that of nanocatalysts in some HER systems.[102] Interestingly, the presence of a moderate number of M-NPs in SACs may be able to maintain the high conductivity of the active site, promoting rapid charge transfer. For example, Kim and co-workers reported that there was a synergistic effect between M-SAs and M-NPs loaded on melamine-derived graphitic tubes, which boosted the electrocatalytic HER.[325] Lin et al. found that the dispersed Pt-SAs and clusters immobilized on functionalized MWCNTs together endowed the electrocatalyst with ultrahigh HER activity.[326] Besides, the recently produced Ru-NPs/SAs@N-TC has been demonstrated to exhibit excellent performance in both electrocatalytic and photocatalytic H_2 evolution, which is attributed to the synergistic coupling between Ru-NPs and Ru-SAs.[327] Undoubtedly, researchers need to make reasonable choices based on the realistic reaction demands to give full play to the advantages of SAs or NPs/clusters. However, there are many barriers to be overcome regarding the preparation and application of supported catalysts in the presence of M-SAs and NPs/clusters. On the one hand, the precise identification of active sites is a huge challenge. On the other hand, the optimal proportion of SAs and NPs/clusters should be adjusted according to the reaction system as well as the nature of the active site and support.

(4) The combination of advanced characterization technologies, theoretical calculations, and simulation systems: The development of advanced characterization technologies, such as AC-STEM, XAFS, etc., provides support for the visualized characterization of SACs. Undoubtedly, in the complex H_2 generation reaction, the supported catalysts will undergo corresponding structural changes as the reaction proceeds. Meanwhile, this dynamic change in geometry or electronic structure will result in different reaction pathways. However, the catalytic models usually established in studies are static, which cannot reveal the true reaction mechanism and regulate the reaction, especially important information such as the microstructure evolution at atomic scale and the adsorbed reaction intermediates during the H_2 generation process. Therefore, in situ monitoring of the dynamic evolution of SACs plays a great role in the accurate detection of active sites under practical reaction conditions and in-depth understanding of the relationship between structure and performance. In situ characterization techniques, including but not limited to TEM, EXAFS, XANES, Raman spectroscopy, XRD, etc., allow researchers to investigate the subsequent evolution of SACs during or after the reaction.

In addition, combining experimental results with theoretical calculations can help us unravel or even predict the catalytic behavior and mechanism of SACs for H_2 generation reactions, which builds a basic platform for the advances of efficient catalysts. Generally, the H-binding strength obtained by theoretical calculations will deviate from the actual liquid condition to some extent. Accordingly, we would like to emphasize that the theoretical calculations and molecular simulations should match the working conditions as much as possible, otherwise it is difficult to make a reliable explanation of the experimental phenomena. With the continuous development of computing hardware and software resources, it is expected that the theoretical calculation results for SACs in H_2 generation reaction will be basically consistent with the practical catalytic reaction results in the near future. Given the good development impetus, SACs will be a fruitful area.

Arguably, SACs have offered an ideal model and research platform for understanding the catalytic reactions mechanism at the molecular level. More importantly, SACs with broad application prospects create unprecedented opportunities for the promotion of renewable energy technology, which not only marks a new era in the field of catalysis, but also presents new challenges to researchers. To deal with the unresolved problems in SAC system, there is an urgent need to build a research system that should not just cater to a specific catalytic reaction. We should systematically combine the knowledge of physics and chemistry, rationally integrate the existing theoretical basis of homogeneous or heterogeneous catalysis in photochemistry, electrochemistry, and photoelectrochemistry, and make a global explanation from the molecular scale.

Acknowledgements

C.Z. and H.W. contributed equally to this work. This work was supported by the National Natural Science Foundation of China (51909089, 22178091, 21776066, 51739004, and 51578222), Natural Science Foundation of Hunan Province, China (2020JJ5252), and China Postdoctoral Science Foundation (2019M662781).

Conflict of Interest

The authors declare no conflict of interest.

Keywords

active site immobilization, electro-/photo-chemical hydrogen evolution, single-atom catalysts, structure–performance relationship, surface chemistry

Received: March 14, 2022
Revised: May 5, 2022
Published online:

---

[1] M. S. Dresselhaus, I. L. Thomas, *Nature* **2001**, *414*, 332.
[2] Y. Jiao, Y. Zheng, M. Jaroniec, S. Z. Qiao, *Chem. Soc. Rev.* **2015**, *44*, 2060.
[3] A. Kudo, Y. Miseki, *Chem. Soc. Rev.* **2009**, *38*, 253.
[4] a) X. Zou, Y. Zhang, *Chem. Soc. Rev.* **2015**, *44*, 5148; b) J. Wang, W. Cui, Q. Liu, Z. Xing, A. M. Asiri, X. Sun, *Adv. Mater.* **2016**, *28*, 215.
[5] a) W. R. Patterson, J. J. Rooney, *Catal. Today* **1992**, *12*, 113; b) M. Boudart, in *Advances in Catalysis*, Vol. *20*, Academic Press, New York, USA **1969**, p. 153.

© 2022 Wiley-VCH GmbH

[6] a) J. J. Ronney, *J. Mol. Catal.* **1985**, *31*, 147; b) J. J. Rooney, G. Webb, *J. Catal.* **1964**, *3*, 488.

[7] a) K. Asakura, H. Nagahiro, N. Ichikuni, Y. Iwasawa, *Appl. Catal., A* **1999**, *188*, 313; b) S. Abbet, U. Heiz, H. Häkkinen, U. Landman, *Phys. Rev. Lett.* **2001**, *86*, 5950; c) S. Abbet, A. Sanchez, U. Heiz, W. D. Schneider, A. M. Ferrari, G. Pacchioni, N. Rösch, *J. Am. Chem. Soc.* **2000**, *122*, 3453.

[8] a) Q. Fu, H. Saltsburg, M. Flytzani-Stephanopoulos, *Science* **2003**, *301*, 935; b) X. Zhang, H. Shi, B.-Q. Xu, *Angew. Chem., Int. Ed.* **2005**, *44*, 7132.

[9] a) S. F. J. Hackett, R. M. Brydson, M. H. Gass, I. Harvey, A. D. Newman, K. Wilson, A. F. Lee, *Angew. Chem., Int. Ed.* **2007**, *46*, 8593; b) A. Uzun, V. Ortalan, N. D. Browning, B. C. Gates, *J. Catal.* **2010**, *269*, 318; c) A. Uzun, V. Ortalan, N. D. Browning, B. C. Gates, *Chem. Commun.* **2009**, 4657, https://doi.org/10.1039/B823171K.

[10] X. F. Yang, A. Wang, B. Qiao, J. Li, J. Liu, T. Zhang, *Acc. Chem. Res.* **2013**, *46*, 1740.

[11] a) C. Wang, Y. Hu, C. M. Lieber, S. Sun, *J. Am. Chem. Soc.* **2008**, *130*, 8902; b) P.-p. Wang, Y. Yang, J. Zhuang, X. Wang, *J. Am. Chem. Soc.* **2013**, *135*, 6834.

[12] a) M. Turner, V. B. Golovko, O. P. H. Vaughan, P. Abdulkin, A. Berenguer-Murcia, M. S. Tikhov, B. F. G. Johnson, R. M. Lambert, *Nature* **2008**, *454*, 981; b) W. E. Kaden, T. Wu, W. A. Kunkel, S. L. Anderson, *Science* **2009**, *326*, 826; c) M. Valden, X. Lai, D. W. Goodman, *Science* **1998**, *281*, 1647; d) C. T. Campbell, *Nat. Chem.* **2012**, *4*, 597.

[13] Z. W. Seh, J. Kibsgaard, C. F. Dickens, I. Chorkendorff, J. K. Nørskov, T. F. Jaramillo, *Science* **2017**, *355*, eaad4998.

[14] J. M. Thomas, R. Raja, D. W. Lewis, *Angew. Chem., Int. Ed.* **2005**, *44*, 6456.

[15] B. Qiao, A. Wang, X. Yang, L. F. Allard, Z. Jiang, Y. Cui, J. Liu, J. Li, T. Zhang, *Nat. Chem.* **2011**, *3*, 634.

[16] a) H. Fei, J. Dong, M. J. Arellano-Jiménez, G. Ye, N. Dong Kim, E. L. G. Samuel, Z. Peng, Z. Zhu, F. Qin, J. Bao, M. J. Yacaman, P. M. Ajayan, D. Chen, J. M. Tour, *Nat. Commun.* **2015**, *6*, 8668; b) L. Wang, H. Li, W. Zhang, X. Zhao, J. Qiu, A. Li, X. Zheng, Z. Hu, R. Si, J. Zeng, *Angew. Chem., Int. Ed. Engl.* **2017**, *56*, 4712; c) H. Wang, J. X. Liu, L. F. Allard, S. Lee, J. Liu, H. Li, J. Wang, J. Wang, S. H. Oh, W. Li, M. Flytzani-Stephanopoulos, M. Shen, B. R. Goldsmith, M. Yang, *Nat. Commun.* **2019**, *10*, 3808; d) H. Wei, K. Huang, D. Wang, R. Zhang, B. Ge, J. Ma, B. Wen, S. Zhang, Q. Li, M. Lei, C. Zhang, J. Irawan, L.-M. Liu, H. Wu, *Nat. Commun.* **2017**, *8*, 1490; e) K. Ding, A. Gulec, A. M. Johnson, N. M. Schweitzer, G. D. Stucky, L. D. Marks, P. C. Stair, *Science* **2015**, *350*, 189; f) X. Li, W. Bi, L. Zhang, S. Tao, W. Chu, Q. Zhang, Y. Luo, C. Wu, Y. Xie, *Adv. Mater.* **2016**, *28*, 2427; g) Y. Zhu, T. Wang, T. Xu, Y. Li, C. Wang, *Appl. Surf. Sci.* **2019**, *464*, 36; h) G. Dong, Z. Ai, L. Zhang, *RSC Adv.* **2014**, *4*, 5553; i) Y. Ma, B. Chi, W. Liu, L. Cao, Y. Lin, X. Zhang, X. Ye, S. Wei, J. Lu, *ACS Catal.* **2019**, *9*, 8404.

[17] C. Gao, J. Low, R. Long, T. Kong, J. Zhu, Y. Xiong, *Chem. Rev.* **2020**, *120*, 12175.

[18] X. Cui, W. Li, P. Ryabchuk, K. Junge, M. Beller, *Nat. Catal.* **2018**, *1*, 385.

[19] M. W. McKittrick, C. W. Jones, *J. Am. Chem. Soc.* **2004**, *126*, 3052.

[20] a) C. H. Choi, M. Kim, H. C. Kwon, S. J. Cho, S. Yun, H.-T. Kim, K. J. J. Mayrhofer, H. Kim, M. Choi, *Nat. Commun.* **2016**, *7*, 10922; b) J. Liu, *Chin. J. Catal.* **2017**, *38*, 1460.

[21] B. C. Gates, M. Flytzani-Stephanopoulos, D. A. Dixon, A. Katz, *Catal. Sci. Technol.* **2017**, *7*, 4259.

[22] Y. Lei, Y. Wang, Y. Liu, C. Song, Q. Li, D. Wang, Y. Li, *Angew. Chem., Int. Ed.* **2020**, *59*, 20794.

[23] a) M. Khalid, P. A. Bhardwaj, A. M. B. Honorato, H. Varela, *Catal. Sci. Technol.* **2020**, *10*, 6420; b) H. Liu, X. Peng, X. Liu, *ChemElectroChem* **2018**, *5*, 2963; c) J. Cai, R. Javed, D. Ye, H. Zhao, J. Zhang, *J. Mater. Chem. A* **2020**, *8*, 22467; d) Z. Pu, I. S. Amiinu, R. Cheng, P. Wang, C. Zhang, S. Mu, W. Zhao, F. Su, G. Zhang, S. Liao, S. Sun, *Nano-Micro Lett.* **2020**, *12*, 21; e) J. Zhang, C. Liu, B. Zhang, *Small Methods* **2019**, *3*, 1800481; f) Y. Wang, H. Su, Y. He, L. Li, S. Zhu, H. Shen, P. Xie, X. Fu, G. Zhou, C. Feng, D. Zhao, F. Xiao, X. Zhu, Y. Zeng, M. Shao, S. Chen, G. Wu, J. Zeng, C. Wang, *Chem. Rev.* **2020**, *120*, 12217; g) C. Zhu, Q. Shi, S. Feng, D. Du, Y. Lin, *ACS Energy Lett.* **2018**, *3*, 1713; h) Y. Wang, X. Zheng, D. Wang, *Nano Res.* **2022**, *15*, 1730.

[24] Y. Zhao, T. Ling, S. Chen, B. Jin, A. Vasileff, Y. Jiao, L. Song, J. Luo, S.-Z. Qiao, *Angew. Chem., Int. Ed.* **2019**, *58*, 12252.

[25] F. Lu, D. Yi, S. Liu, F. Zhan, B. Zhou, L. Gu, D. Golberg, X. Wang, J. Yao, *Angew. Chem., Int. Ed.* **2020**, *59*, 17712.

[26] a) L. Zhang, L. Han, H. Liu, X. Liu, J. Luo, *Angew. Chem., Int. Ed.* **2017**, *56*, 13694; b) D. Liu, X. Li, S. Chen, H. Yan, C. Wang, C. Wu, Y. A. Haleem, S. Duan, J. Lu, B. Ge, P. M. Ajayan, Y. Luo, J. Jiang, L. Song, *Nat. Energy* **2019**, *4*, 512; c) A. Wang, T. Zhang, *Nat. Energy* **2016**, *1*, 15019; d) J. Zhang, Y. Zhao, X. Guo, C. Chen, C.-L. Dong, R.-S. Liu, C.-P. Han, Y. Li, Y. Gogotsi, G. Wang, *Nat. Catal.* **2018**, *1*, 985; e) Y. Xue, B. Huang, Y. Yi, Y. Guo, Z. Zuo, Y. Li, Z. Jia, H. Liu, Y. Li, *Nat. Commun.* **2018**, *9*, 1460.

[27] Z. Weng, Y. Wu, M. Wang, J. Jiang, K. Yang, S. Huo, X.-F. Wang, Q. Ma, G. W. Brudvig, V. S. Batista, Y. Liang, Z. Feng, H. Wang, *Nat. Commun.* **2018**, *9*, 415.

[28] W. Liu, L. Zhang, X. Liu, X. Liu, X. Yang, S. Miao, W. Wang, A. Wang, T. Zhang, *J. Am. Chem. Soc.* **2017**, *139*, 10790.

[29] D. Zhao, Z. Zhuang, X. Cao, C. Zhang, Q. Peng, C. Chen, Y. Li, *Chem. Soc. Rev.* **2020**, *49*, 2215.

[30] a) M. Emmrich, F. Huber, F. Pielmeier, J. Welker, T. Hofmann, M. Schneiderbauer, D. Meuer, S. Polesya, S. Mankovsky, D. Ködderitzsch, H. Ebert, F. J. Giessibl, *Science* **2015**, *348*, 308; b) H. Wei, X. Liu, A. Wang, L. Zhang, B. Qiao, X. Yang, Y. Huang, S. Miao, J. Liu, T. Zhang, *Nat. Commun.* **2014**, *5*, 5634; c) F. S. Hage, G. Radtke, D. M. Kepaptsoglou, M. Lazzeri, Q. M. Ramasse, *Science* **2020**, *367*, 1124.

[31] a) R. Long, Y. Li, Y. Liu, S. Chen, X. Zheng, C. Gao, C. He, N. Chen, Z. Qi, L. Song, J. Jiang, J. Zhu, Y. Xiong, *J. Am. Chem. Soc.* **2017**, *139*, 4486; b) P. N. Duchesne, G. Chen, N. Zheng, P. Zhang, *J. Phys. Chem. C* **2013**, *117*, 26324; c) T. Zhang, Z. Chen, A. G. Walsh, Y. Li, P. Zhang, *Adv. Mater.* **2020**, *32*, 2002910.

[32] a) F. Tao, M. Salmeron, *Science* **2011**, *331*, 171; b) T. Yao, Z. Sun, Y. Li, Z. Pan, H. Wei, Y. Xie, M. Nomura, Y. Niwa, W. Yan, Z. Wu, Y. Jiang, Q. Liu, S. Wei, *J. Am. Chem. Soc.* **2010**, *132*, 7696; c) J. Dou, Z. Sun, A. A. Opalade, N. Wang, W. Fu, F. Tao, *Chem. Soc. Rev.* **2017**, *46*, 2001.

[33] L. Cao, Q. Luo, W. Liu, Y. Lin, X. Liu, Y. Cao, W. Zhang, Y. Wu, J. Yang, T. Yao, S. Wei, *Nat. Catal.* **2019**, *2*, 134.

[34] X. Zheng, B. Zhang, P. De Luna, Y. Liang, R. Comin, O. Voznyy, L. Han, F. P. García de Arquer, M. Liu, C. T. Dinh, T. Regier, J. J. Dynes, S. He, H. L. Xin, H. Peng, D. Prendergast, X. Du, E. H. Sargent, *Nat. Chem.* **2018**, *10*, 149.

[35] a) K. Gong, F. Du, Z. Xia, M. Durstock, L. Dai, *Science* **2009**, *323*, 760; b) J. Greeley, I. E. L. Stephens, A. S. Bondarenko, T. P. Johansson, H. A. Hansen, T. F. Jaramillo, J. Rossmeisl, I. Chorkendorff, J. K. Nørskov, *Nat. Chem.* **2009**, *1*, 552.

[36] M. T. Greiner, T. E. Jones, S. Beeg, L. Zwiener, M. Scherzer, F. Girgsdies, S. Piccinin, M. Armbrüster, A. Knop-Gericke, R. Schlögl, *Nat. Chem.* **2018**, *10*, 1008.

[37] S. Fang, X. Zhu, X. Liu, J. Gu, W. Liu, D. Wang, W. Zhang, Y. Lin, J. Lu, S. Wei, Y. Li, T. Yao, *Nat. Commun.* **2020**, *11*, 1029.

[38] a) W. Sheng, Z. Zhuang, M. Gao, J. Zheng, J. G. Chen, Y. Yan, *Nat. Commun.* **2015**, *6*, 5848; b) I. Ledezma-Yanez, W. D. Z. Wallace, P. Sebastián-Pascual, V. Climent, J. M. Feliu, M. T. M. Koper, *Nat. Energy* **2017**, *2*, 17031.

[39] Q. Sun, N. Wang, T. Zhang, R. Bai, A. Mayoral, P. Zhang, Q. Zhang, O. Terasaki, J. Yu, *Angew. Chem., Int. Ed.* **2019**, *58*, 18570.

© 2022 Wiley-VCH GmbH

[40] J. Deng, H. Li, J. Xiao, Y. Tu, D. Deng, H. Yang, H. Tian, J. Li, P. Ren, X. Bao, *Energy Environ. Sci.* **2015**, *8*, 1594.

[41] X. Fang, Q. Shang, Y. Wang, L. Jiao, T. Yao, Y. Li, Q. Zhang, Y. Luo, H.-L. Jiang, *Adv. Mater.* **2018**, *30*, 1705112.

[42] a) N. Kornienko, Y. Zhao, C. S. Kley, C. Zhu, D. Kim, S. Lin, C. J. Chang, O. M. Yaghi, P. Yang, *J. Am. Chem. Soc.* **2015**, *137*, 14129; b) K. Manna, T. Zhang, W. Lin, *J. Am. Chem. Soc.* **2014**, *136*, 6566.

[43] a) H. Li, M. Wang, L. Luo, J. Zeng, *Adv. Sci.* **2019**, *6*, 1801471; b) A. Wang, J. Li, T. Zhang, *Nat. Rev. Chem.* **2018**, *2*, 65.

[44] D. A. Bulushev, M. Zacharska, A. S. Lisitsyn, O. Y. Podyacheva, F. S. Hage, Q. M. Ramasse, U. Bangert, L. G. Bulusheva, *ACS Catal.* **2016**, *6*, 3442.

[45] R. Qin, K. Liu, Q. Wu, N. Zheng, *Chem. Rev.* **2020**, *120*, 11810.

[46] a) Y. Ren, Y. Tang, L. Zhang, X. Liu, L. Li, S. Miao, D. Sheng Su, A. Wang, J. Li, T. Zhang, *Nat. Commun.* **2019**, *10*, 4500; b) X.-P. Yin, H.-J. Wang, S.-F. Tang, X.-L. Lu, M. Shu, R. Si, T.-B. Lu, *Angew. Chem., Int. Ed.* **2018**, *57*, 9382.

[47] P. Liu, N. Zheng, *Natl. Sci. Rev.* **2018**, *5*, 636.

[48] Y. Chen, S. Ji, W. Sun, Y. Lei, Q. Wang, A. Li, W. Chen, G. Zhou, Z. Zhang, Y. Wang, L. Zheng, Q. Zhang, L. Gu, X. Han, D. Wang, Y. Li, *Angew. Chem., Int. Ed.* **2020**, *59*, 1295.

[49] X. Wu, H. Zhang, J. Dong, M. Qiu, J. Kong, Y. Zhang, Y. Li, G. Xu, J. Zhang, J. Ye, *Chem. Sci.* **2018**, *45*, 109.

[50] a) Q. Fu, W.-X. Li, Y. Yao, H. Liu, H.-Y. Su, D. Ma, X.-K. Gu, L. Chen, Z. Wang, H. Zhang, B. Wang, X. Bao, *Science* **2010**, *328*, 1141; b) J. M. Thomas, W. J. Thomas, *Principles and practice of heterogeneous catalysis*, Wiley-VCH, Mannheim **2014**.

[51] P. Yin, T. Yao, Y. Wu, L. Zheng, Y. Lin, W. Liu, H. Ju, J. Zhu, X. Hong, Z. Deng, G. Zhou, S. Wei, Y. Li, *Angew. Chem., Int. Ed.* **2016**, *55*, 10800.

[52] Y.-N. Gong, L. Jiao, Y. Qian, C.-Y. Pan, L. Zheng, X. Cai, B. Liu, S.-H. Yu, H.-L. Jiang, *Angew. Chem., Int. Ed.* **2020**, *59*, 2705.

[53] a) J. Lin, A. Wang, B. Qiao, X. Liu, X. Yang, X. Wang, J. Liang, J. Li, J. Liu, T. Zhang, *J. Am. Chem. Soc.* **2013**, *135*, 15314; b) H. B. Yang, S.-F. Hung, S. Liu, K. Yuan, S. Miao, L. Zhang, X. Huang, H.-Y. Wang, W. Cai, R. Chen, J. Gao, X. Yang, W. Chen, Y. Huang, H. M. Chen, C. M. Li, T. Zhang, B. Liu, *Nat. Energy* **2018**, *3*, 140; c) J. Gu, C.-S. Hsu, L. Bai, H. M. Chen, X. Hu, *Science* **2019**, *364*, 1091; d) H. Jing, P. Zhu, X. Zheng, Z. Zhang, D. Wang, Y. Li, *Adv. Powder Mater.* **2022**, *1*, 100013.

[54] a) S. Losse, J. G. Vos, S. Rau, *Coord. Chem. Rev.* **2010**, *254*, 2492; b) Z. Chen, H. Jia, J. Yuan, X. Liu, C. Fang, Y. Fan, C. Cao, Z. Chen, *Int. J. Hydrogen Energy* **2019**, *44*, 24342.

[55] a) V. Artero, M. Chavarot-Kerlidou, M. Fontecave, *Angew. Chem., Int. Ed.* **2011**, *50*, 7238; b) W. Liu, L. Cao, W. Cheng, Y. Cao, X. Liu, W. Zhang, X. Mou, L. Jin, X. Zheng, W. Che, Q. Liu, T. Yao, S. Wei, *Angew. Chem., Int. Ed.* **2017**, *56*, 9312.

[56] L. Zhang, Y. Jia, G. Gao, X. Yan, N. Chen, J. Chen, M. T. Soo, B. Wood, D. Yang, A. Du, X. Yao, *Chem* **2018**, *4*, 285.

[57] J. Xing, J. F. Chen, Y. H. Li, W. T. Yuan, Y. Zhou, L. R. Zheng, H. F. Wang, P. Hu, Y. Wang, H. J. Zhao, Y. Wang, H. G. Yang, *Chem. - Eur. J.* **2014**, *20*, 2138.

[58] S. Qiu, Y. Shen, G. Wei, S. Yao, W. Xi, M. Shu, R. Si, M. Zhang, J. Zhu, C. An, *Appl. Catal., B* **2019**, *259*, 118036.

[59] J. Zhu, L. Cai, X. Yin, Z. Wang, L. Zhang, H. Ma, Y. Ke, Y. Du, S. Xi, A. T. S. Wee, Y. Chai, W. Zhang, *ACS Nano* **2020**, *14*, 5600.

[60] a) S. Hejazi, S. Mohajernia, B. Osuagwu, G. Zoppellaro, P. Andryskova, O. Tomanec, S. Kment, R. Zbořil, P. Schmuki, *Adv. Mater.* **2020**, *32*, 1908505; b) A. Naldoni, M. Altomare, G. Zoppellaro, N. Liu, Š. Kment, R. Zbořil, P. Schmuki, *ACS Catal.* **2019**, *9*, 345.

[61] H. Zhang, G. Liu, L. Shi, J. Ye, *Adv. Energy Mater.* **2018**, *8*, 1701343.

[62] R. Senga, K. Suenaga, *Nat. Commun.* **2015**, *6*, 7943.

[63] Q. He, D. Tian, H. Jiang, D. Cao, S. Wei, D. Liu, P. Song, Y. Lin, L. Song, *Adv. Mater.* **2020**, *32*, 1906972.

[64] L. Zhao, Y. Zhang, L.-B. Huang, X.-Z. Liu, Q.-H. Zhang, C. He, Z.-Y. Wu, L.-J. Zhang, J. Wu, W. Yang, L. Gu, J.-S. Hu, L.-J. Wan, *Nat. Commun.* **2019**, *10*, 1278.

[65] M. Babucci, F. E. Sarac Oztuna, L. M. Debefve, A. Boubnov, S. R. Bare, B. C. Gates, U. Unal, A. Uzun, *ACS Catal.* **2019**, *9*, 9905.

[66] M. J. Wang, M. Ji, X. Zheng, C. Jiang, H. Zhao, Z. X. Mao, M. Zhang, C. Zhu, J. Xu, *Appl. Surf. Sci.* **2021**, *551*, 148742.

[67] Y. Shi, W.-M. Huang, J. Li, Y. Zhou, Z.-Q. Li, Y.-C. Yin, X.-H. Xia, *Nat. Commun.* **2020**, *11*, 4558.

[68] M. Flytzani-Stephanopoulos, *Acc. Chem. Res.* **2014**, *47*, 783.

[69] a) Y. Chen, S. Ji, C. Chen, Q. Peng, D. Wang, Y. Li, *Joule* **2018**, *2*, 1242; b) Z. W. Chen, L. X. Chen, C. C. Yang, Q. Jiang, *J. Mater. Chem. A* **2019**, *7*, 3492.

[70] Q. Zuo, T. Liu, C. Chen, Y. Ji, X. Gong, Y. Mai, Y. Zhou, *Angew. Chem., Int. Ed.* **2019**, *58*, 10198.

[71] T. He, S. Chen, B. Ni, Y. Gong, Z. Wu, L. Song, L. Gu, W. Hu, X. Wang, *Angew. Chem., Int. Ed.* **2018**, *57*, 3493.

[72] a) H. Furukawa, K. E. Cordova, M. O'Keeffe, O. M. Yaghi, *Science* **2013**, *341*, 1230444; b) N. Stock, S. Biswas, *Chem. Rev.* **2012**, *112*, 933; c) S. Chen, M. Cui, Z. Yin, J. Xiong, L. Mi, Y. Li, *ChemSusChem* **2021**, *14*, 73; d) L. Jiao, H.-L. Jiang, *Chem* **2019**, *5*, 786.

[73] Y. He, S. Hwang, D. A. Cullen, M. A. Uddin, L. Langhorst, B. Li, S. Karakalos, A. J. Kropf, E. C. Wegener, J. Sokolowski, M. Chen, D. Myers, D. Su, K. L. More, G. Wang, S. Litster, G. Wu, *Energy Environ. Sci.* **2019**, *12*, 250.

[74] P. Peng, L. Shi, F. Huo, C. Mi, X. Wu, S. Zhang, Z. Xiang, *Sci. Adv.* **2019**, *5*, eaaw2322.

[75] Y. Zhou, X. Tao, G. Chen, R. Lu, D. Wang, M.-X. Chen, E. Jin, J. Yang, H.-W. Liang, Y. Zhao, X. Feng, A. Narita, K. Müllen, *Nat. Commun.* **2020**, *11*, 5892.

[76] K. Jiang, M. Luo, Z. Liu, M. Peng, D. Chen, Y.-R. Lu, T.-S. Chan, F. M. F. de Groot, Y. Tan, *Nat. Commun.* **2021**, *12*, 1687.

[77] S. Zhou, W. Pei, Y. Zhao, X. Yang, N. Liu, J. Zhao, *npj Comput. Mater.* **2021**, *7*, 186.

[78] M. Fan, J. Cui, J. Wu, R. Vajtai, D. Sun, P. M. Ajayan, *Small* **2020**, *16*, 1906782.

[79] Y. Cao, S. Chen, Q. Luo, H. Yan, Y. Lin, W. Liu, L. Cao, J. Lu, J. Yang, T. Yao, S. Wei, *Angew. Chem., Int. Ed.* **2017**, *56*, 12191.

[80] X. Huang, H. Yan, L. Huang, X. Zhang, Y. Lin, J. Li, Y. Xia, Y. Ma, Z. Sun, S. Wei, J. Lu, *J. Phys. Chem. C* **2019**, *123*, 7922.

[81] a) W. Ding, Z. Wei, S. Chen, X. Qi, T. Yang, J. Hu, D. Wang, L.-J. Wan, S. F. Alvi, L. Li, *Angew. Chem., Int. Ed.* **2013**, *52*, 11755; b) M. Fan, Z.-Q. Feng, C. Zhu, X. Chen, C. Chen, J. Yang, D. Sun, *J. Mater. Sci.* **2016**, *51*, 10323; c) Y. Zhao, J. Wan, H. Yao, L. Zhang, K. Lin, L. Wang, N. Yang, D. Liu, L. Song, J. Zhu, L. Gu, L. Liu, H. Zhao, Y. Li, D. Wang, *Nat. Chem.* **2018**, *10*, 924.

[82] J. Zhu, W. Li, S. Li, J. Zhang, H. Zhou, C. Zhang, J. Zhang, S. Mu, *Small* **2018**, *14*, 1800563.

[83] a) H. J. Song, M.-C. Sung, H. Yoon, B. Ju, D.-W. Kim, *Adv. Sci.* **2019**, *6*, 1802135; b) Z. Zhang, P. Li, Q. Feng, B. Wei, C. Deng, J. Fan, H. Li, H. Wang, *ACS Appl. Mater. Interfaces* **2018**, *10*, 32171.

[84] J. Yu, A. Wang, W. Yu, X. Liu, X. Li, H. Liu, Y. Hu, Y. Wu, W. Zhou, *Appl. Catal., B* **2020**, *277*, 119236.

[85] N. Cheng, S. Stambula, D. Wang, M. N. Banis, J. Liu, A. Riese, B. Xiao, R. Li, T.-K. Sham, L.-M. Liu, G. A. Botton, X. Sun, *Nat. Commun.* **2016**, *7*, 13638.

[86] a) B. Lu, T. J. Smart, D. Qin, J. E. Lu, N. Wang, L. Chen, Y. Peng, Y. Ping, S. Chen, *Chem. Mater.* **2017**, *29*, 5617; b) F. Zheng, Y. Yang, Q. Chen, *Nat. Commun.* **2014**, *5*, 5261; c) B. Lu, L. Guo, F. Wu, Y. Peng, J. E. Lu, T. J. Smart, N. Wang, Y. Z. Finfrock, D. Morris, P. Zhang, N. Li, P. Gao, Y. Ping, S. Chen, *Nat. Commun.* **2019**, *10*, 631.

[87] R. Gao, L. Pan, H. Wang, X. Zhang, L. Wang, J.-J. Zou, *ACS Catal.* **2018**, *8*, 8420.

[88] a) J. Yang, B. Chen, X. Liu, W. Liu, Z. Li, J. Dong, W. Chen, W. Yan, T. Yao, X. Duan, Y. Wu, Y. Li, *Angew. Chem., Int. Ed.* **2018**, *57*, 9495;

b) K. Yuan, D. Lützenkirchen-Hecht, L. Li, L. Shuai, Y. Li, R. Cao, M. Qiu, X. Zhuang, M. K. H. Leung, Y. Chen, U. Scherf, *J. Am. Chem. Soc.* **2020**, *142*, 2404.

[89] a) S. Guo, Z. Deng, M. Li, B. Jiang, C. Tian, Q. Pan, H. Fu, *Angew. Chem., Int. Ed.* **2016**, *55*, 1830; b) Y. Zhang, T. Mori, J. Ye, M. Antonietti, *J. Am. Chem. Soc.* **2010**, *132*, 6294; c) Y.-j. Sun, J.-y. He, D. Zhang, X.-j. Wang, J. Zhao, R.-h. Liu, F.-t. Li, *Appl. Surf. Sci.* **2020**, *517*, 146192.

[90] V. Ramalingam, P. Varadhan, H.-C. Fu, H. Kim, D. Zhang, S. Chen, L. Song, D. Ma, Y. Wang, H. N. Alshareef, J.-H. He, *Adv. Mater.* **2019**, *31*, 1903841.

[91] a) J.-J. Zeng, Y.-J. Lin, *Appl. Phys. Lett.* **2014**, *104*, 233103; b) Y.-C. Wang, Y.-J. Lai, L. Song, Z.-Y. Zhou, J.-G. Liu, Q. Wang, X.-D. Yang, C. Chen, W. Shi, Y.-P. Zheng, M. Rauf, S.-G. Sun, *Angew. Chem., Int. Ed.* **2015**, *54*, 9907; c) Q. Li, W. Chen, H. Xiao, Y. Gong, Z. Li, L. Zheng, X. Zheng, W. Yan, W.-C. Cheong, R. Shen, N. Fu, L. Gu, Z. Zhuang, C. Chen, D. Wang, Q. Peng, J. Li, Y. Li, *Adv. Mater.* **2018**, *30*, 1800588.

[92] X. Gao, Y. Zhou, Y. Tan, B. Yang, Z. Cheng, Z. Shen, J. Jia, *Appl. Surf. Sci.* **2019**, *473*, 770.

[93] Z. Zhang, X. Zhao, S. Xi, L. Zhang, Z. Chen, Z. Zeng, M. Huang, H. Yang, B. Liu, S. J. Pennycook, P. Chen, *Adv. Energy Mater.* **2020**, *10*, 2002896.

[94] S. J. Tauster, S. C. Fung, R. L. Garten, *J. Am. Chem. Soc.* **1978**, *100*, 170.

[95] T. W. van Deelen, C. Hernández Mejía, K. P. de Jong, *Nat. Catal.* **2019**, *2*, 955.

[96] H. Li, Y. Zhou, W. Tu, J. Ye, Z. Zou, *Adv. Funct. Mater.* **2015**, *25*, 998.

[97] J. C. Fierro-Gonzalez, S. Kuba, Y. Hao, B. C. Gates, *J. Phys. Chem. B* **2006**, *110*, 13326.

[98] X. Wang, W. Chen, L. Zhang, T. Yao, W. Liu, Y. Lin, H. Ju, J. Dong, L. Zheng, W. Yan, X. Zheng, Z. Li, X. Wang, J. Yang, D. He, Y. Wang, Z. Deng, Y. Wu, Y. Li, *J. Am. Chem. Soc.* **2017**, *139*, 9419.

[99] B. Zhang, T. Fan, N. Xie, G. Nie, H. Zhang, *Adv. Sci.* **2019**, *6*, 1901787.

[100] T. W. Hansen, A. T. DeLaRiva, S. R. Challa, A. K. Datye, *Acc. Chem. Res.* **2013**, *46*, 1720.

[101] a) D. I. Kochubey, V. V. Chesnokov, S. E. Malykhin, *Carbon* **2012**, *50*, 2782; b) R. Arrigo, M. E. Schuster, Z. Xie, Y. Yi, G. Wowsnick, L. L. Sun, K. E. Hermann, M. Friedrich, P. Kast, M. Hävecker, A. Knop-Gericke, R. Schlögl, *ACS Catal.* **2015**, *5*, 2740.

[102] L. Liu, D. M. Meira, R. Arenal, P. Concepcion, A. V. Puga, A. Corma, *ACS Catal.* **2019**, *9*, 10626.

[103] a) J. Graciani, K. Mudiyanselage, F. Xu, A. E. Baber, J. Evans, S. D. Senanayake, D. J. Stacchiola, P. Liu, J. Hrbek, J. F. Sanz, J. A. Rodriguez, *Science* **2014**, *345*, 546; b) M. Behrens, F. Studt, I. Kasatkin, S. Kühl, M. Hävecker, F. Abild-Pedersen, S. Zander, F. Girgsdies, P. Kurr, B.-L. Kniep, M. Tovar, R. W. Fischer, J. K. Nørskov, R. Schlögl, *Science* **2012**, *336*, 893.

[104] A. Bruix, J. A. Rodriguez, P. J. Ramírez, S. D. Senanayake, J. Evans, J. B. Park, D. Stacchiola, P. Liu, J. Hrbek, F. Illas, *J. Am. Chem. Soc.* **2012**, *134*, 8968.

[105] J. Saavedra, H. A. Doan, C. J. Pursell, L. C. Grabow, B. D. Chandler, *Science* **2014**, *345*, 1599.

[106] a) O. Dulub, W. Hebenstreit, U. Diebold, *Phys. Rev. Lett.* **2000**, *84*, 3646; b) S. J. Tauster, *Acc. Chem. Res.* **1987**, *20*, 389.

[107] a) T. Uchijima, *Catal. Today* **1996**, *28*, 105; b) S. Bernal, J. J. Calvino, M. A. Cauqui, J. M. Gatica, C. López Cartes, J. A. Pérez Omil, J. M. Pintado, *Catal. Today* **2003**, *77*, 385; c) X. Y. Shi, W. Zhang, C. Zhang, W. T. Zheng, H. Chen, J. G. Qi, *J. Microsc.* **2016**, *262*, 203; d) J. C. Matsubu, S. Zhang, L. DeRita, N. S. Marinkovic, J. G. Chen, G. W. Graham, X. Pan, P. Christopher, *Nat. Chem.* **2017**, *9*, 120.

[108] B. Han, Y. Guo, Y. Huang, W. Xi, J. Xu, J. Luo, H. Qi, Y. Ren, X. Liu, B. Qiao, T. Zhang, *Angew. Chem., Int. Ed.* **2020**, *59*, 11824.

[109] R. Lang, X. Du, Y. Huang, X. Jiang, Q. Zhang, Y. Guo, K. Liu, B. Qiao, A. Wang, T. Zhang, *Chem. Rev.* **2020**, *120*, 11986.

[110] P. Hu, Z. Huang, Z. Amghouz, M. Makkee, F. Xu, F. Kapteijn, A. Dikhtiarenko, Y. Chen, X. Gu, X. Tang, *Angew. Chem., Int. Ed.* **2014**, *53*, 3418.

[111] a) P. Liu, R. Qin, G. Fu, N. Zheng, *J. Am. Chem. Soc.* **2017**, *139*, 2122; b) H. Tang, F. Liu, J. Wei, B. Qiao, K. Zhao, Y. Su, C. Jin, L. Li, J. Liu, J. Wang, T. Zhang, *Angew. Chem., Int. Ed.* **2016**, *55*, 10606.

[112] Y. Shi, Z.-R. Ma, Y.-Y. Xiao, Y.-C. Yin, W.-M. Huang, Z.-C. Huang, Y.-Z. Zheng, F.-Y. Mu, R. Huang, G.-Y. Shi, Y.-Y. Sun, X.-H. Xia, W. Chen, *Nat. Commun.* **2021**, *12*, 3021.

[113] a) J. K. Nørskov, T. Bligaard, B. Hvolbæk, F. Abild-Pedersen, I. Chorkendorff, C. H. Christensen, *Chem. Soc. Rev.* **2008**, *37*, 2163; b) S. Dahl, A. Logadottir, R. C. Egeberg, J. H. Larsen, I. Chorkendorff, E. Törnqvist, J. K. Nørskov, *Phys. Rev. Lett.* **1999**, *83*, 1814.

[114] H. J. Qiu, Y. Ito, W. Cong, Y. Tan, P. Liu, A. Hirata, T. Fujita, Z. Tang, M. Chen, *Angew. Chem., Int. Ed.* **2015**, *54*, 14031.

[115] J. Li, Q. Guan, H. Wu, W. Liu, Y. Lin, Z. Sun, X. Ye, X. Zheng, H. Pan, J. Zhu, S. Chen, W. Zhang, S. Wei, J. Lu, *J. Am. Chem. Soc.* **2019**, *141*, 14515.

[116] W. Chen, J. Pei, C.-T. He, J. Wan, H. Ren, Y. Zhu, Y. Wang, J. Dong, S. Tian, W.-C. Cheong, S. Lu, L. Zheng, X. Zheng, W. Yan, Z. Zhuang, C. Chen, Q. Peng, D. Wang, Y. Li, *Angew. Chem., Int. Ed.* **2017**, *56*, 16086.

[117] a) M. E. Strayer, T. P. Senftle, J. P. Winterstein, N. M. Vargas-Barbosa, R. Sharma, R. M. Rioux, M. J. Janik, T. E. Mallouk, *J. Am. Chem. Soc.* **2015**, *137*, 16216; b) N. Acerbi, S. C. E. Tsang, G. Jones, S. Golunski, P. Collier, *Angew. Chem., Int. Ed.* **2013**, *52*, 7737.

[118] H. Zhang, P. An, W. Zhou, B. Y. Guan, P. Zhang, J. Dong, X. W. Lou, *Sci. Adv.* **2018**, *4*, eaao6657.

[119] a) S. Yang, J. Kim, Y. J. Tak, A. Soon, H. Lee, *Angew. Chem., Int. Ed.* **2016**, *55*, 2058; b) L. Liu, A. Corma, *Chem. Rev.* **2018**, *118*, 4981.

[120] Z. Shen, X. Fan, S. Ma, Y. An, D. Yang, N. Guo, Z. Luo, Y. Hu, *Int. J. Hydrogen Energy* **2020**, *45*, 14396.

[121] J. Zhang, Q. Zhang, X. Feng, *Adv. Mater.* **2019**, *31*, 1808167.

[122] R. Qin, P. Liu, G. Fu, N. Zheng, *Small Methods* **2018**, *2*, 1700286.

[123] J.-X. Liang, J. Lin, J. Liu, X. Wang, T. Zhang, J. Li, *Angew. Chem., Int. Ed.* **2020**, *59*, 12868.

[124] H. Ahmad, S. K. Kamarudin, L. J. Minggu, M. Kassim, *Renewable Sustainable Energy Rev.* **2015**, *43*, 599.

[125] J. Xing, H. B. Jiang, J. F. Chen, Y. H. Li, L. Wu, S. Yang, L. R. Zheng, H. F. Wang, P. Hu, H. J. Zhao, H. G. Yang, *J. Mater. Chem. A* **2013**, *1*, 15258.

[126] a) J. Wan, W. Chen, C. Jia, L. Zheng, J. Dong, X. Zheng, Y. Wang, W. Yan, C. Chen, Q. Peng, D. Wang, Y. Li, *Adv. Mater.* **2018**, *30*, 1705369; b) Y. Sui, S. Liu, T. Li, Q. Liu, T. Jiang, Y. Guo, J.-L. Luo, *J. Catal.* **2017**, *353*, 250; c) T. Wei, Y. Zhu, Y. Wu, X. An, L.-M. Liu, *Langmuir* **2019**, *35*, 391.

[127] M. Bellardita, C. Garlisi, A. M. Venezia, G. Palmisano, L. Palmisano, *Catal. Sci. Technol.* **2018**, *8*, 1606.

[128] a) S. Mohajernia, S. Hejazi, P. Andryskova, G. Zoppellaro, O. Tomanec, R. Zboril, P. Schmuki, *ChemElectroChem* **2019**, *6*, 1244; b) S. Mohajernia, S. Hejazi, A. Mazare, N. T. Nguyen, P. Schmuki, *Chem. - Eur. J.* **2017**, *23*, 12406.

[129] Z. Lian, W. Wang, G. Li, F. Tian, K. S. Schanze, H. Li, *ACS Appl. Mater. Interfaces* **2017**, *9*, 16959.

[130] a) N. Daelman, M. Capdevila-Cortada, N. López, *Nat. Mater.* **2019**, *18*, 1215; b) R. Lang, W. Xi, J.-C. Liu, Y.-T. Cui, T. Li, A. F. Lee, F. Chen, Y. Chen, L. Li, L. Li, J. Lin, S. Miao, X. Liu, A.-Q. Wang, X. Wang, J. Luo, B. Qiao, J. Li, T. Zhang, *Nat. Commun.* **2019**, *10*, 234.

[131] B.-H. Lee, S. Park, M. Kim, A. K. Sinha, S. C. Lee, E. Jung, W. J. Chang, K.-S. Lee, J. H. Kim, S.-P. Cho, H. Kim, K. T. Nam, T. Hyeon, *Nat. Mater.* **2019**, *18*, 620.

[132] D. Yi, F. Lu, F. Zhang, S. Liu, B. Zhou, D. Gao, X. Wang, J. Yao, *Angew. Chem., Int. Ed.* **2020**, *59*, 15855.

© 2022 Wiley-VCH GmbH

[133] L. M. Sandratskii, M. Uhl, J. Kübler, *J. Phys.: Condens. Matter* **1996**, *8*, 983.

[134] a) A. Guerrero-Ruiz, S. Yang, Q. Xin, A. Maroto-Valiente, M. Benito-Gonzalez, I. Rodriguez-Ramos, *Langmuir* **2000**, *16*, 8100; b) T. Lear, R. Marshall, J. Antonio Lopez-Sanchez, S. D. Jackson, T. M. Klapötke, M. Bäumer, G. Rupprechter, H.-J. Freund, D. Lennon, *J. Chem. Phys.* **2005**, *123*, 174706; c) S. Bertarione, C. Prestipino, E. Groppo, D. Scarano, G. Spoto, A. Zecchina, R. Pellegrini, G. Leofanti, C. Lamberti, *Phys. Chem. Chem. Phys.* **2006**, *8*, 3676.

[135] X. Sun, J. Lin, Y. Zhou, L. Li, Y. Su, X. Wang, T. Zhang, *AlChE J.* **2017**, *63*, 4022.

[136] J. Lin, Y. Huang, L. Li, B. Qiao, X. Wang, A. Wang, T. Zhang, *Chem. Eng. J.* **2011**, *168*, 822.

[137] a) D. Pierre, W. Deng, M. Flytzani-Stephanopoulos, *Top. Catal.* **2007**, *46*, 363; b) J. H. Kwak, J. Hu, D. Mei, C.-W. Yi, D. H. Kim, C. H. F. Peden, L. F. Allard, J. Szanyi, *Science* **2009**, *325*, 1670.

[138] a) M. Xu, T. Liang, M. Shi, H. Chen, *Chem. Rev.* **2013**, *113*, 3766; b) X. Liu, T. Xu, X. Wu, Z. Zhang, J. Yu, H. Qiu, J.-H. Hong, C.-H. Jin, J.-X. Li, X.-R. Wang, L.-T. Sun, W. Guo, *Nat. Commun.* **2013**, *4*, 1776; c) S. Zhu, L. Gong, J. Xie, Z. Gu, Y. Zhao, *Small Methods* **2017**, *1*, 1700220.

[139] Q.-K. Li, X.-F. Li, G. Zhang, J. Jiang, *J. Am. Chem. Soc.* **2018**, *140*, 15149.

[140] J. Cui, P. Li, J. Zhou, W.-Y. He, X. Huang, J. Yi, J. Fan, Z. Ji, X. Jing, F. Qu, Z. G. Cheng, C. Yang, L. Lu, K. Suenaga, J. Liu, K. T. Law, J. Lin, Z. Liu, G. Liu, *Nat. Commun.* **2019**, *10*, 2044.

[141] X. Xi, Z. Wang, W. Zhao, J.-H. Park, K. T. Law, H. Berger, L. Forró, J. Shan, K. F. Mak, *Nat. Phys.* **2016**, *12*, 139.

[142] X. Li, H. Rong, J. Zhang, D. Wang, Y. Li, *Nano Res.* **2020**, *13*, 1842.

[143] X. Dai, K. Du, Z. Li, M. Liu, Y. Ma, H. Sun, X. Zhang, Y. Yang, *ACS Appl. Mater. Interfaces* **2015**, *7*, 27242.

[144] X. Wang, Y. Zhang, H. Si, Q. Zhang, J. Wu, L. Gao, X. Wei, Y. Sun, Q. Liao, Z. Zhang, K. Ammarah, L. Gu, Z. Kang, Y. Zhang, *J. Am. Chem. Soc.* **2020**, *142*, 4298.

[145] K. Chang, X. Hai, H. Pang, H. Zhang, L. Shi, G. Liu, H. Liu, G. Zhao, M. Li, J. Ye, *Adv. Mater.* **2016**, *28*, 10033.

[146] a) J. Kibsgaard, Z. Chen, B. N. Reinecke, T. F. Jaramillo, *Nat. Mater.* **2012**, *11*, 963; b) T. F. Jaramillo, K. P. Jørgensen, J. Bonde, J. H. Nielsen, S. Horch, I. Chorkendorff, *Science* **2007**, *317*, 100.

[147] G. Liu, A. W. Robertson, M. M.-J. Li, W. C. H. Kuo, M. T. Darby, M. H. Muhieddine, Y.-C. Lin, K. Suenaga, M. Stamatakis, J. H. Warner, S. C. E. Tsang, *Nat. Chem.* **2017**, *9*, 810.

[148] a) Q. Wang, Z. L. Zhao, S. Dong, D. He, M. J. Lawrence, S. Han, C. Cai, S. Xiang, P. Rodriguez, B. Xiang, Z. Wang, Y. Liang, M. Gu, *Chem. Sci.* **2018**, *53*, 458; b) T. H. M. Lau, X. Lu, J. Kulhavý, S. Wu, L. Lu, T.-S. Wu, R. Kato, J. S. Foord, Y.-L. Soo, K. Suenaga, S. C. E. Tsang, *Chem. Sci.* **2018**, *9*, 4769.

[149] J. Zhang, X. Xu, L. Yang, D. Cheng, D. Cao, *Small Methods* **2019**, *3*, 1900653.

[150] C. Wu, D. Li, S. Ding, Z. u. Rehman, Q. Liu, S. Chen, B. Zhang, L. Song, *J. Phys. Chem. Lett.* **2019**, *10*, 6081.

[151] P. Liu, J. Zhu, J. Zhang, K. Tao, D. Gao, P. Xi, *Electrochim. Acta* **2018**, *260*, 24.

[152] H. Zhang, L. Yu, T. Chen, W. Zhou, X. W. Lou, *Adv. Funct. Mater.* **2018**, *28*, 1807086.

[153] G. Liu, P. Li, G. Zhao, X. Wang, J. Kong, H. Liu, H. Zhang, K. Chang, X. Meng, T. Kako, J. Ye, *J. Am. Chem. Soc.* **2016**, *138*, 9128.

[154] C. Tsai, F. Abild-Pedersen, J. K. Nørskov, *Nano Lett.* **2014**, *14*, 1381.

[155] Z. Zheng, L. Yu, M. Gao, X. Chen, W. Zhou, C. Ma, L. Wu, J. Zhu, X. Meng, J. Hu, Y. Tu, S. Wu, J. Mao, Z. Tian, D. Deng, *Nat. Commun.* **2020**, *11*, 3315.

[156] a) D. Voiry, M. Salehi, R. Silva, T. Fujita, M. Chen, T. Asefa, V. B. Shenoy, G. Eda, M. Chhowalla, *Nano Lett.* **2013**, *13*, 6222; b) Q. H. Wang, K. Kalantar-Zadeh, A. Kis, J. N. Coleman, M. S. Strano, *Nat. Nanotechnol.* **2012**, *7*, 699.

[157] M. A. Lukowski, A. S. Daniel, F. Meng, A. Forticaux, L. Li, S. Jin, *J. Am. Chem. Soc.* **2013**, *135*, 10274.

[158] a) C. Tan, W. Zhao, A. Chaturvedi, Z. Fei, Z. Zeng, J. Chen, Y. Huang, P. Ercius, Z. Luo, X. Qi, B. Chen, Z. Lai, B. Li, X. Zhang, J. Yang, Y. Zong, C. Jin, H. Zheng, C. Kloc, H. Zhang, *Small* **2016**, *12*, 1866; b) S. Song, D. H. Keum, S. Cho, D. Perello, Y. Kim, Y. H. Lee, *Nano Lett.* **2016**, *16*, 188; c) K. Qi, X. Cui, L. Gu, S. Yu, X. Fan, M. Luo, S. Xu, N. Li, L. Zheng, Q. Zhang, J. Ma, Y. Gong, F. Lv, K. Wang, H. Huang, W. Zhang, S. Guo, W. Zheng, P. Liu, *Nat. Commun.* **2019**, *10*, 5231.

[159] Z. Luo, Y. Ouyang, H. Zhang, M. Xiao, J. Ge, Z. Jiang, J. Wang, D. Tang, X. Cao, C. Liu, W. Xing, *Nat. Commun.* **2018**, *9*, 2120.

[160] B. Pattengale, Y. Huang, X. Yan, S. Yang, S. Younan, W. Hu, Z. Li, S. Lee, X. Pan, J. Gu, J. Huang, *Nat. Commun.* **2020**, *11*, 4114.

[161] S. Manzeli, D. Ovchinnikov, D. Pasquier, O. V. Yazyev, A. Kis, *Nat. Rev. Mater.* **2017**, *2*, 17033.

[162] a) J. Huang, J. Wang, R. Xie, Z. Tian, G. Chai, Y. Zhang, F. Lai, G. He, C. Liu, T. Liu, P. R. Shearing, D. J. L. Brett, *J. Mater. Chem. A* **2020**, *8*, 19879; b) Q. Gao, W. Zhang, Z. Shi, L. Yang, Y. Tang, *Adv. Mater.* **2019**, *31*, 1802880.

[163] C. G. Morales-Guio, L.-A. Stern, X. Hu, *Chem. Soc. Rev.* **2014**, *43*, 6555.

[164] Y. C. Kimmel, X. Xu, W. Yu, X. Yang, J. G. Chen, *ACS Catal.* **2014**, *4*, 1558.

[165] R. Michalsky, Y.-J. Zhang, A. A. Peterson, *ACS Catal.* **2014**, *4*, 1274.

[166] H. H. Hwu, J. G. Chen, *Chem. Rev.* **2005**, *105*, 185.

[167] a) C. Wan, Y. N. Regmi, B. M. Leonard, *Angew. Chem., Int. Ed.* **2014**, *53*, 6407; b) J. R. d. S. Politi, F. Viñes, J. A. Rodriguez, F. Illas, *Phys. Chem. Chem. Phys.* **2013**, *15*, 12617.

[168] S. K. Sahoo, Y. Ye, S. Lee, J. Park, H. Lee, J. Lee, J. W. Han, *ACS Energy Lett.* **2019**, *4*, 126.

[169] T. Gomez, E. Florez, J. A. Rodriguez, F. Illas, *J. Phys. Chem. C* **2011**, *115*, 11666.

[170] J. Xiong, J. Li, J. Shi, X. Zhang, N.-T. Suen, Z. Liu, Y. Huang, G. Xu, W. Cai, X. Lei, L. Feng, Z. Yang, L. Huang, H. Cheng, *ACS Energy Lett.* **2018**, *3*, 341.

[171] Z.-Y. Yu, Y. Duan, M.-R. Gao, C.-C. Lang, Y.-R. Zheng, S.-H. Yu, *Chem. Sci.* **2017**, *8*, 968.

[172] Z. Kou, W. Zang, W. Pei, L. Zheng, S. Zhou, S. Zhang, L. Zhang, J. Wang, *J. Mater. Chem. A* **2020**, *8*, 3071.

[173] a) T. Ouyang, A.-N. Chen, Z.-Z. He, Z.-Q. Liu, Y. Tong, *Chem. Commun.* **2018**, *54*, 9901; b) Q. Li, Z. Ma, R. Sa, H. Adidharma, K. A. M. Gasem, A. G. Russell, M. Fan, K. Wu, *J. Mater. Chem. A* **2017**, *5*, 14658; c) Y. Ma, M. Chen, H. Geng, H. Dong, P. Wu, X. Li, G. Guan, T. Wang, *Adv. Funct. Mater.* **2020**, *30*, 2000561.

[174] P. Liu, J. A. Rodriguez, T. Asakura, J. Gomes, K. Nakamura, *J. Phys. Chem. B* **2005**, *109*, 4575.

[175] G. G. Asara, A. Roldan, J. M. Ricart, J. A. Rodriguez, F. Illas, N. H. de Leeuw, *J. Phys. Chem. C* **2014**, *118*, 19224.

[176] a) J. Patt, D. J. Moon, C. Phillips, L. Thompson, *Catal. Lett.* **2000**, *65*, 193; b) N. M. Schweitzer, J. A. Schaidle, O. K. Ezekoye, X. Pan, S. Linic, L. T. Thompson, *J. Am. Chem. Soc.* **2011**, *133*, 2378; c) W. Setthapun, S. K. Bej, L. T. Thompson, *Top. Catal.* **2008**, *49*, 73; d) A. C. Lausche, J. A. Schaidle, L. T. Thompson, *Appl. Catal., A* **2011**, *401*, 29.

[177] H. Wang, Y. Wu, X. Yuan, G. Zeng, J. Zhou, X. Wang, J. W. Chew, *Adv. Mater.* **2018**, *30*, 1704561.

[178] H. Wang, C. Qian, J. Liu, Y. Zeng, D. Wang, W. Zhou, L. Gu, H. Wu, G. Liu, Y. Zhao, *J. Am. Chem. Soc.* **2020**, *142*, 4862.

[179] V. Kamysbayev, A. S. Filatov, H. Hu, X. Rui, F. Lagunas, D. Wang, R. F. Klie, D. V. Talapin, *Science* **2020**, *369*, 979.

[180] C. Zhang, J. Sha, H. Fei, M. Liu, S. Yazdi, J. Zhang, Q. Zhong, X. Zou, N. Zhao, H. Yu, Z. Jiang, E. Ringe, B. I. Yakobson, J. Dong, D. Chen, J. M. Tour, *ACS Nano* **2017**, *11*, 6930.

[181] S. Ma, X. Fan, Y. An, D. Yang, Z. Luo, Y. Hu, N. Guo, *J. Mater. Sci.* **2019**, *54*, 11378.

© 2022 Wiley-VCH GmbH

[182] a) Y. Chen, S. Ji, Y. Wang, J. Dong, W. Chen, Z. Li, R. Shen, L. Zheng, Z. Zhuang, D. Wang, Y. Li, *Angew. Chem., Int. Ed.* **2017**, *56*, 6937; b) X. Yan, Y. Jia, X. Yao, *Chem. Soc. Rev.* **2018**, *47*, 7628.

[183] a) J. Zhu, S. Mu, *Adv. Funct. Mater.* **2020**, *30*, 2001097; b) S. Gao, H. Liu, K. Geng, X. Wei, *Chem. Sci.* **2015**, *12*, 785.

[184] a) J. Wang, F. Xu, H. Jin, Y. Chen, Y. Wang, *Adv. Mater.* **2017**, *29*, 1605838; b) D. Yan, Y. Li, J. Huo, R. Chen, L. Dai, S. Wang, *Adv. Mater.* **2017**, *29*, 1606459.

[185] a) J. He, S. Y. Ma, P. Zhou, C. X. Zhang, C. He, L. Z. Sun, *J. Phys. Chem. C* **2012**, *116*, 26313; b) G. Li, Y. Li, H. Liu, Y. Guo, Y. Li, D. Zhu, *Chem. Commun.* **2010**, *46*, 3256.

[186] L. Hui, Y. Xue, H. Yu, C. Zhang, B. Huang, Y. Li, *ChemPhysChem* **2020**, *21*, 2145.

[187] Y. Shi, J. Huang, G. Zeng, W. Cheng, J. Hu, L. Shi, K. Yi, *Chemosphere* **2019**, *230*, 40.

[188] C. Xie, D. Yan, W. Chen, Y. Zou, R. Chen, S. Zang, Y. Wang, X. Yao, S. Wang, *Mater. Today* **2019**, *31*, 47.

[189] Y. Jia, L. Zhang, A. Du, G. Gao, J. Chen, X. Yan, C. L. Brown, X. Yao, *Adv. Mater.* **2016**, *28*, 9532.

[190] D. U. Lee, B. J. Kim, Z. Chen, *J. Mater. Chem. A* **2013**, *1*, 4754.

[191] Y. Qu, B. Chen, Z. Li, X. Duan, L. Wang, Y. Lin, T. Yuan, F. Zhou, Y. Hu, Z. Yang, C. Zhao, J. Wang, C. Zhao, Y. Hu, G. Wu, Q. Zhang, Q. Xu, B. Liu, P. Gao, R. You, W. Huang, L. Zheng, L. Gu, Y. Wu, Y. Li, *J. Am. Chem. Soc.* **2019**, *141*, 4505.

[192] D. Deng, X. Chen, L. Yu, X. Wu, Q. Liu, Y. Liu, H. Yang, H. Tian, Y. Hu, P. Du, R. Si, J. Wang, X. Cui, H. Li, J. Xiao, T. Xu, J. Deng, F. Yang, P. N. Duchesne, P. Zhang, J. Zhou, L. Sun, J. Li, X. Pan, X. Bao, *Sci. Adv.* **2015**, *1*, e1500462.

[193] A. Baby, L. Trovato, C. Di Valentin, *Carbon* **2021**, *174*, 772.

[194] a) Y. Peng, B. Lu, S. Chen, *Adv. Mater.* **2018**, *30*, 1801995; b) P. Ren, Q. Li, T. Song, Y. Yang, *ACS Appl. Mater. Interfaces* **2020**, *12*, 27210.

[195] G. Zhang, R. Chenitz, M. Lefèvre, S. Sun, J.-P. Dodelet, *Chem. Sci.* **2016**, *29*, 111.

[196] Q. Jia, N. Ramaswamy, U. Tylus, K. Strickland, J. Li, A. Serov, K. Artyushkova, P. Atanassov, J. Anibal, C. Gumeci, S. C. Barton, M.-T. Sougrati, F. Jaouen, B. Halevi, S. Mukerjee, *Chem. Sci.* **2016**, *29*, 65.

[197] X. Zeng, J. Shui, X. Liu, Q. Liu, Y. Li, J. Shang, L. Zheng, R. Yu, *Adv. Energy Mater.* **2018**, *8*, 1701345.

[198] a) Y. Zhang, X. Xia, X. Cao, B. Zhang, N. H. Tiep, H. He, S. Chen, Y. Huang, H. J. Fan, *Adv. Energy Mater.* **2017**, *7*, 1700220; b) M. Ledendecker, G. Clavel, M. Antonietti, M. Shalom, *Adv. Funct. Mater.* **2015**, *25*, 393; c) R. Subbaraman, D. Tripkovic, D. Strmcnik, K.-C. Chang, M. Uchimura, A. P. Paulikas, V. Stamenkovic, N. M. Markovic, *Science* **2011**, *334*, 1256.

[199] H. Li, G. Wang, F. Zhang, L. Zou, Z. Zou, H. Yang, *J. Phys. Chem. C* **2020**, *124*, 11760.

[200] Z. Zhang, Y. Chen, L. Zhou, C. Chen, Z. Han, B. Zhang, Q. Wu, L. Yang, L. Du, Y. Bu, P. Wang, X. Wang, H. Yang, Z. Hu, *Nat. Commun.* **2019**, *10*, 1657.

[201] J. A. Varnell, J. S. Sotiropoulos, T. M. Brown, K. Subedi, R. T. Haasch, C. E. Schulz, A. A. Gewirth, *ACS Energy Lett.* **2018**, *3*, 823.

[202] a) X. Chen, J. Zhang, X. Fu, M. Antonietti, X. Wang, *J. Am. Chem. Soc.* **2009**, *131*, 11658; b) Z. Chen, E. Vorobyeva, S. Mitchell, E. Fako, N. López, S. M. Collins, R. K. Leary, P. A. Midgley, R. Hauert, J. Pérez-Ramírez, *Natl. Sci. Rev.* **2018**, *5*, 642; c) Z. Chen, S. Mitchell, E. Vorobyeva, R. K. Leary, R. Hauert, T. Furnival, Q. M. Ramasse, J. M. Thomas, P. A. Midgley, D. Dontsova, M. Antonietti, S. Pogodin, N. López, J. Pérez-Ramírez, *Adv. Funct. Mater.* **2017**, *27*, 1605785; d) J. Wan, J. Huang, H. Yu, L. Liu, Y. Shi, C. Liu, *J. Colloid Interface Sci.* **2021**, *601*, 229.

[203] a) Y. Wang, M. K. Bayazit, S. J. A. Moniz, Q. Ruan, C. C. Lau, N. Martsinovich, J. Tang, *Energy Environ. Sci.* **2017**, *10*, 1643; b) L. Jiang, X. Yuan, Y. Pan, J. Liang, G. Zeng, Z. Wu, H. Wang, *Appl. Catal., B* **2017**, *217*, 388; c) H. Wang, Y. Wu, M. Feng, W. Tu, T. Xiao, T. Xiong, H. Ang, X. Yuan, J. W. Chew, *Water Res.* **2018**, *144*, 215.

[204] a) Q. Tay, P. Kanhere, C. F. Ng, S. Chen, S. Chakraborty, A. C. H. Huan, T. C. Sum, R. Ahuja, Z. Chen, *Chem. Mater.* **2015**, *27*, 4930; b) X. Wang, S. Blechert, M. Antonietti, *ACS Catal.* **2012**, *2*, 1596; c) W.-J. Ong, L.-L. Tan, Y. H. Ng, S.-T. Yong, S.-P. Chai, *Chem. Rev.* **2016**, *116*, 7159.

[205] S. Penner, M. Armbrüster, *ChemCatChem* **2015**, *7*, 374.

[206] P. Zhou, F. Lv, N. Li, Y. Zhang, Z. Mu, Y. Tang, J. Lai, Y. Chao, M. Luo, F. Lin, J. Zhou, D. Su, S. Guo, *Chem. Sci.* **2019**, *56*, 127.

[207] S. Cao, H. Li, T. Tong, H.-C. Chen, A. Yu, J. Yu, H. M. Chen, *Adv. Funct. Mater.* **2018**, *28*, 1802169.

[208] L. Liu, J. Huang, H. Yu, J. Wan, L. Liu, K. Yi, W. Zhang, C. Zhang, *Chemosphere* **2021**, *282*, 131049.

[209] J. H. Lee, J. Ryu, J. Y. Kim, S.-W. Nam, J. H. Han, T.-H. Lim, S. Gautam, K. H. Chae, C. W. Yoon, *J. Mater. Chem. A* **2014**, *2*, 9490.

[210] L. Liu, X. Wu, L. Wang, X. Xu, L. Gan, Z. Si, J. Li, Q. Zhang, Y. Liu, Y. Zhao, R. Ran, X. Wu, D. Weng, F. Kang, *Commun. Chem.* **2019**, *2*, 18.

[211] a) H. Jiang, Z. Hou, Y. Luo, *Angew. Chem., Int. Ed.* **2017**, *56*, 15617; b) M. Liu, Y. Pang, B. Zhang, P. De Luna, O. Voznyy, J. Xu, X. Zheng, C. T. Dinh, F. Fan, C. Cao, F. P. G. de Arquer, T. S. Safaei, A. Mepham, A. Klinkova, E. Kumacheva, T. Filleter, D. Sinton, S. O. Kelley, E. H. Sargent, *Nature* **2016**, *537*, 382.

[212] L. Fan, P. F. Liu, X. Yan, L. Gu, Z. Z. Yang, H. G. Yang, S. Qiu, X. Yao, *Nat. Commun.* **2016**, *7*, 10667.

[213] M. Tavakkoli, N. Holmberg, R. Kronberg, H. Jiang, J. Sainio, E. I. Kauppinen, T. Kallio, K. Laasonen, *ACS Catal.* **2017**, *7*, 3121.

[214] H. C. Dam, N. T. Cuong, A. Sugiyama, T. Ozaki, A. Fujiwara, T. Mitani, S. Okada, *Phys. Rev. B* **2009**, *79*, 115426.

[215] W. Liu, J. Ji, X. Yan, W. Liu, Y.-C. Huang, K. Wang, P. Jin, X. Yao, J. Jiang, *J. Mater. Chem. A* **2020**, *8*, 5255.

[216] X. Meng, C. Ma, L. Jiang, R. Si, X. Meng, Y. Tu, L. Yu, X. Bao, D. Deng, *Angew. Chem., Int. Ed.* **2020**, *59*, 10502.

[217] L. Liang, H. Jin, H. Zhou, B. Liu, C. Hu, D. Chen, Z. Wang, Z. Hu, Y. Zhao, H.-W. Li, D. He, S. Mu, *Chem. Sci.* **2021**, *88*, 106221.

[218] J. Mao, C.-T. He, J. Pei, W. Chen, D. He, Y. He, Z. Zhuang, C. Chen, Q. Peng, D. Wang, Y. Li, *Nat. Commun.* **2018**, *9*, 4958.

[219] R. Ferrando, J. Jellinek, R. L. Johnston, *Chem. Rev.* **2008**, *108*, 845.

[220] a) J. Zhang, M. B. Vukmirovic, K. Sasaki, A. U. Nilekar, M. Mavrikakis, R. R. Adzic, *J. Am. Chem. Soc.* **2005**, *127*, 12480; b) J. Greeley, M. Mavrikakis, *Nat. Mater.* **2004**, *3*, 810; c) J. Wintterlin, S. Völkening, T. V. W. Janssens, T. Zambelli, G. Ertl, *Science* **1997**, *278*, 1931.

[221] a) A. E. Baber, H. L. Tierney, T. J. Lawton, E. C. H. Sykes, *ChemCatChem* **2011**, *3*, 607; b) G. Rupprechter, *Nat. Chem.* **2017**, *9*, 833; c) J. G. Chen, C. A. Menning, M. B. Zellner, *Surf. Sci. Rep.* **2008**, *63*, 201.

[222] a) S. Zhang, L. Nguyen, J.-X. Liang, J. Shan, J. Liu, A. I. Frenkel, A. Patlolla, W. Huang, J. Li, F. Tao, *Nat. Commun.* **2015**, *6*, 7938; b) G. Kyriakou, M. B. Boucher, A. D. Jewell, E. A. Lewis, T. J. Lawton, A. E. Baber, H. L. Tierney, M. Flytzani-Stephanopoulos, E. C. H. Sykes, *Science* **2012**, *335*, 1209; c) M. Chen, D. Kumar, C.-W. Yi, D. W. Goodman, *Science* **2005**, *310*, 291.

[223] K. Edwards Jennifer, B. Solsona, N. E. Ntainjua, F. Carley Albert, A. Herzing Andrew, J. Kiely Christopher, J. Hutchings Graham, *Science* **2009**, *323*, 1037.

[224] I. Enache Dan, K. Edwards Jennifer, P. Landon, B. Solsona-Espriu, F. Carley Albert, A. Herzing Andrew, M. Watanabe, J. Kiely Christopher, W. Knight David, J. Hutchings Graham, *Science* **2006**, *311*, 362.

[225] L. Kesavan, R. Tiruvalam, A. Rahim Mohd Hasbi, I. bin Saiman Mohd, I. Enache Dan, L. Jenkins Robert, N. Dimitratos, A. Lopez-Sanchez Jose, H. Taylor Stuart, W. Knight David, J. Kiely Christopher, J. Hutchings Graham, *Science* **2011**, *331*, 195.

[226] J. Zhang, Z. Gao, S. Wang, G. Wang, X. Gao, B. Zhang, S. Xing, S. Zhao, Y. Qin, *Nat. Commun.* **2019**, *10*, 4166.

[227] G. W. Huber, J. W. Shabaker, J. A. Dumesic, *Science* **2003**, *300*, 2075.

© 2022 Wiley-VCH GmbH

[228] R. Li, D. Wang, *Adv. Energy Mater.* **2022**, *12*, 2103564.

[229] a) W. I. Choi, B. C. Wood, E. Schwegler, T. Ogitsu, *Adv. Energy Mater.* **2015**, *5*, 1501423; b) A. Grimaud, K. J. May, C. E. Carlton, Y.-L. Lee, M. Risch, W. T. Hong, J. Zhou, Y. Shao-Horn, *Nat. Commun.* **2013**, *4*, 2439; c) Z. Lu, B. Wang, Y. Hu, W. Liu, Y. Zhao, R. Yang, Z. Li, J. Luo, B. Chi, Z. Jiang, M. Li, S. Mu, S. Liao, J. Zhang, X. Sun, *Angew. Chem., Int. Ed.* **2019**, *58*, 2622.

[230] a) Y. Yang, Y. Qian, H. Li, Z. Zhang, Y. Mu, D. Do, B. Zhou, J. Dong, W. Yan, Y. Qin, L. Fang, R. Feng, J. Zhou, P. Zhang, J. Dong, G. Yu, Y. Liu, X. Zhang, X. Fan, *Sci. Adv.* **2020**, *6*, eaba6586; b) C.-C. Hou, H.-F. Wang, C. Li, Q. Xu, *Energy Environ. Sci.* **2020**, *13*, 1658.

[231] H. Zhang, T. Watanabe, M. Okumura, M. Haruta, N. Toshima, *Nat. Mater.* **2012**, *11*, 49.

[232] a) H. Thirumalai, J. R. Kitchin, *Top. Catal.* **2018**, *61*, 462; b) C.-H. Chen, D. Wu, Z. Li, R. Zhang, C.-G. Kuai, X.-R. Zhao, C.-K. Dong, S.-Z. Qiao, H. Liu, X.-W. Du, *Adv. Energy Mater.* **2019**, *9*, 1803913.

[233] D. R. Lide, W. Haynes, *Handbook of chemistry and physics: a ready-reference book of chemical and physical data*, CRC, Boca Raton **2009**.

[234] a) J. Wang, Z. Huang, W. Liu, C. Chang, H. Tang, Z. Li, W. Chen, C. Jia, T. Yao, S. Wei, Y. Wu, Y. Li, *J. Am. Chem. Soc.* **2017**, *139*, 17281; b) X. Fang, L. Jiao, S.-H. Yu, H.-L. Jiang, *ChemSusChem* **2017**, *10*, 3019; c) J. Wang, W. Liu, G. Luo, Z. Li, C. Zhao, H. Zhang, M. Zhu, Q. Xu, X. Wang, C. Zhao, Y. Qu, Z. Yang, T. Yao, Y. Li, Y. Lin, Y. Wu, Y. Li, *Energy Environ. Sci.* **2018**, *11*, 3375.

[235] L. Zhang, R. Si, H. Liu, N. Chen, Q. Wang, K. Adair, Z. Wang, J. Chen, Z. Song, J. Li, M. N. Banis, R. Li, T.-K. Sham, M. Gu, L.-M. Liu, G. A. Botton, X. Sun, *Nat. Commun.* **2019**, *10*, 4936.

[236] R. T. Hannagan, G. Giannakakis, M. Flytzani-Stephanopoulos, E. C. H. Sykes, *Chem. Rev.* **2020**, *120*, 12044.

[237] F. Besenbacher, I. Chorkendorff, B. S. Clausen, B. Hammer, A. M. Molenbroek, J. K. Nørskov, I. Stensgaard, *Science* **1998**, *279*, 1913.

[238] H. L. Tierney, A. E. Baber, J. R. Kitchin, E. C. H. Sykes, *Phys. Rev. Lett.* **2009**, *103*, 246102.

[239] a) X. Wang, S.-I. Choi, L. T. Roling, M. Luo, C. Ma, L. Zhang, M. Chi, J. Liu, Z. Xie, J. A. Herron, M. Mavrikakis, Y. Xia, *Nat. Commun.* **2015**, *6*, 7594; b) S. Xie, S.-I. Choi, N. Lu, L. T. Roling, J. A. Herron, L. Zhang, J. Park, J. Wang, M. J. Kim, Z. Xie, M. Mavrikakis, Y. Xia, *Nano Lett.* **2014**, *14*, 3570.

[240] L. Zhang, H. Liu, S. Liu, M. Norouzi Banis, Z. Song, J. Li, L. Yang, M. Markiewicz, Y. Zhao, R. Li, M. Zheng, S. Ye, Z.-J. Zhao, G. A. Botton, X. Sun, *ACS Catal.* **2019**, *9*, 9350.

[241] T. Chao, X. Luo, W. Chen, B. Jiang, J. Ge, Y. Lin, G. Wu, X. Wang, Y. Hu, Z. Zhuang, Y. Wu, X. Hong, Y. Li, *Angew. Chem., Int. Ed.* **2017**, *56*, 16047.

[242] Y. Zhou, E. Song, W. Chen, C. U. Segre, J. Zhou, Y.-C. Lin, C. Zhu, R. Ma, P. Liu, S. Chu, T. Thomas, M. Yang, Q. Liu, K. Suenaga, Z. Liu, J. Liu, J. Wang, *Adv. Mater.* **2020**, *32*, 2003484.

[243] Z. Cao, S. B. Zacate, X. Sun, J. Liu, E. M. Hale, W. P. Carson, S. B. Tyndall, J. Xu, X. Liu, X. Liu, C. Song, J.-h. Luo, M.-J. Cheng, X. Wen, W. Liu, *Angew. Chem.* **2018**, *130*, 12857.

[244] Y.-Z. Chen, C. Wang, Z.-Y. Wu, Y. Xiong, Q. Xu, S.-H. Yu, H.-L. Jiang, *Adv. Mater.* **2015**, *27*, 5010.

[245] X. Han, X. Ling, Y. Wang, T. Ma, C. Zhong, W. Hu, Y. Deng, *Angew. Chem., Int. Ed.* **2019**, *58*, 5359.

[246] H. Yan, Y. Lin, H. Wu, W. Zhang, Z. Sun, H. Cheng, W. Liu, C. Wang, J. Li, X. Huang, T. Yao, J. Yang, S. Wei, J. Lu, *Nat. Commun.* **2017**, *8*, 1070.

[247] S. Ding, M. J. Hülsey, J. Pérez-Ramírez, N. Yan, *Joule* **2019**, *3*, 2897.

[248] C. Ratnasamy, J. P. Wagner, *Catal. Rev.* **2009**, *51*, 325.

[249] R. M. Navarro, M. A. Peña, J. L. G. Fierro, *Chem. Rev.* **2007**, *107*, 3952.

[250] a) M. Zhu, I. E. Wachs, *ACS Catal.* **2016**, *6*, 722; b) J. L. Ayastuy, M. A. Gutiérrez-Ortiz, J. A. González-Marcos, A. Aranzabal, J. R. González-Velasco, *Ind. Eng. Chem. Res.* **2005**, *44*, 41.

[251] H. Guan, J. Lin, B. Qiao, S. Miao, A.-Q. Wang, X. Wang, T. Zhang, *AIChE J.* **2017**, *63*, 2081.

[252] S. C. Ammal, A. Heyden, *ACS Catal.* **2017**, *7*, 301.

[253] T. Magadzu, J. H. Yang, J. D. Henao, M. C. Kung, H. H. Kung, M. S. Scurrell, *J. Phys. Chem. C* **2017**, *121*, 8812.

[254] a) J. P. Clay, J. P. Greeley, F. H. Ribeiro, W. Nicholas Delgass, W. F. Schneider, *J. Catal.* **2014**, *320*, 106; b) P. Liu, J. A. Rodriguez, *J. Phys. Chem. B* **2006**, *110*, 19418.

[255] J. E. Kubsh, J. A. Dumesic, *AIChE J.* **1982**, *28*, 793.

[256] S. Chu, A. Majumdar, *Nature* **2012**, *488*, 294.

[257] J. Guo, J. Huo, Y. Liu, W. Wu, Y. Wang, M. Wu, H. Liu, G. Wang, *Small Methods* **2019**, *3*, 1900159.

[258] J. Zhu, L. Hu, P. Zhao, L. Y. S. Lee, K.-Y. Wong, *Chem. Rev.* **2020**, *120*, 851.

[259] S. Paul, *Ber. Dtsch. Chem. Ges.* **1911**, *44*, 17.

[260] R. Parsons, *Trans. Faraday Soc.* **1958**, *54*, 1053.

[261] a) J. K. Nørskov, T. Bligaard, A. Logadottir, J. R. Kitchin, J. G. Chen, S. Pandelov, U. Stimming, *J. Electrochem. Soc.* **2005**, *152*, J23; b) V. R. Stamenkovic, B. S. Mun, M. Arenz, K. J. J. Mayrhofer, C. A. Lucas, G. Wang, P. N. Ross, N. M. Markovic, *Nat. Mater.* **2007**, *6*, 241.

[262] H. Jin, S. Sultan, M. Ha, J. N. Tiwari, M. G. Kim, K. S. Kim, *Adv. Funct. Mater.* **2020**, *30*, 2000531.

[263] S. Ye, F. Luo, Q. Zhang, P. Zhang, T. Xu, Q. Wang, D. He, L. Guo, Y. Zhang, C. He, X. Ouyang, M. Gu, J. Liu, X. Sun, *Energy Environ. Sci.* **2019**, *12*, 1000.

[264] Y. Feng, Y. Guan, H. Zhang, Z. Huang, J. Li, Z. Jiang, X. Gu, Y. Wang, *J. Mater. Chem. A* **2018**, *6*, 11783.

[265] H. Fei, J. Dong, C. Wan, Z. Zhao, X. Xu, Z. Lin, Y. Wang, H. Liu, K. Zang, J. Luo, S. Zhao, W. Hu, W. Yan, I. Shakir, Y. Huang, X. Duan, *Adv. Mater.* **2018**, *30*, 1802146.

[266] W. Fu, Y. Wang, W. Tian, H. Zhang, J. Li, S. Wang, Y. Wang, *Angew. Chem., Int. Ed.* **2020**, *59*, 23791.

[267] Z. Zhang, J. Cai, H. Zhu, Z. Zhuang, F. Xu, J. Hao, S. Lu, H. Li, F. Duan, M. Du, *Chem. Eng. J.* **2020**, *392*, 123655.

[268] D. Li, X. Chen, Y. Lv, G. Zhang, Y. Huang, W. Liu, Y. Li, R. Chen, C. Nuckolls, H. Ni, *Appl. Catal., B* **2020**, *269*, 118824.

[269] K. L. Zhou, Z. Wang, C. B. Han, X. Ke, C. Wang, Y. Jin, Q. Zhang, J. Liu, H. Wang, H. Yan, *Nat. Commun.* **2021**, *12*, 3783.

[270] W. Chen, J. Pei, C.-T. He, J. Wan, H. Ren, Y. Wang, J. Dong, K. Wu, W.-C. Cheong, J. Mao, X. Zheng, W. Yan, Z. Zhuang, C. Chen, Q. Peng, D. Wang, Y. Li, *Adv. Mater.* **2018**, *30*, 1800396.

[271] K. Jiang, B. Liu, M. Luo, S. Ning, M. Peng, Y. Zhao, Y.-R. Lu, T.-S. Chan, F. M. F. de Groot, Y. Tan, *Nat. Commun.* **2019**, *10*, 1743.

[272] F. Podjaski, D. Weber, S. Zhang, L. Diehl, R. Eger, V. Duppel, E. Alarcón-Lladó, G. Richter, F. Haase, A. Fontcuberta i Morral, C. Scheu, B. V. Lotsch, *Nat. Catal.* **2020**, *3*, 55.

[273] P. Wang, X. Zhang, J. Zhang, S. Wan, S. Guo, G. Lu, J. Yao, X. Huang, *Nat. Commun.* **2017**, *8*, 14580.

[274] Y. Duan, Z.-Y. Yu, S.-J. Hu, X.-S. Zheng, C.-T. Zhang, H.-H. Ding, B.-C. Hu, Q.-Q. Fu, Z.-L. Yu, X. Zheng, J.-F. Zhu, M.-R. Gao, S.-H. Yu, *Angew. Chem., Int. Ed.* **2019**, *58*, 15772.

[275] J. Xu, C. Zhang, H. Liu, J. Sun, R. Xie, Y. Qiu, F. Lü, Y. Liu, L. Zhuo, X. Liu, J. Luo, *Chem. Sci.* **2020**, *70*, 104529.

[276] P. Kuang, Y. Wang, B. Zhu, F. Xia, C.-W. Tung, J. Wu, H. M. Chen, J. Yu, *Adv. Mater.* **2021**, *33*, 2008599.

[277] J. Park, S. Lee, H.-E. Kim, A. Cho, S. Kim, Y. Ye, J. W. Han, H. Lee, J. H. Jang, J. Lee, *Angew. Chem., Int. Ed.* **2019**, *58*, 16038.

[278] S. Mukherjee, B. Ramalingam, S. Gangopadhyay, *J. Mater. Chem. A* **2014**, *2*, 3954.

[279] M. R. Buck, J. F. Bondi, R. E. Schaak, *Nat. Chem.* **2012**, *4*, 37.

[280] K. Huang, R. Wang, H. Wu, H. Wang, X. He, H. Wei, S. Wang, R. Zhang, M. Lei, W. Guo, B. Ge, H. Wu, *J. Mater. Chem. A* **2019**, *7*, 25779.

[281] L. DeRita, J. Resasco, S. Dai, A. Boubnov, H. V. Thang, A. S. Hoffman, I. Ro, G. W. Graham, S. R. Bare, G. Pacchioni, X. Pan, P. Christopher, *Nat. Mater.* **2019**, *18*, 746.

[282] X. He, Y. Deng, Y. Zhang, Q. He, D. Xiao, M. Peng, Y. Zhao, H. Zhang, R. Luo, T. Gan, H. Ji, D. Ma, *Cell Rep. Phys. Sci.* **2020**, *1*, 100004.

[283] J. Mahmood, F. Li, S.-M. Jung, M. S. Okyay, I. Ahmad, S.-J. Kim, N. Park, H. Y. Jeong, J.-B. Baek, *Nat. Nanotechnol.* **2017**, *12*, 441.

[284] a) Z. W. Seh, K. D. Fredrickson, B. Anasori, J. Kibsgaard, A. L. Strickler, M. R. Lukatskaya, Y. Gogotsi, T. F. Jaramillo, A. Vojvodic, *ACS Energy Lett.* **2016**, *1*, 589; b) A. D. Handoko, K. D. Fredrickson, B. Anasori, K. W. Convey, L. R. Johnson, Y. Gogotsi, A. Vojvodic, Z. W. Seh, *ACS Appl. Energy Mater.* **2018**, *1*, 173.

[285] E. Gülzow, *J. Power Sources* **1996**, *61*, 99.

[286] J. Hu, C. Zhang, L. Jiang, H. Lin, Y. An, D. Zhou, M. K. H. Leung, S. Yang, *Joule* **2017**, *1*, 383.

[287] C. Hu, L. Zhang, J. Gong, *Energy Environ. Sci.* **2019**, *12*, 2620.

[288] a) T. Ling, D.-Y. Yan, H. Wang, Y. Jiao, Z. Hu, Y. Zheng, L. Zheng, J. Mao, H. Liu, X.-W. Du, M. Jaroniec, S.-Z. Qiao, *Nat. Commun.* **2017**, *8*, 1509; b) I. T. McCrum, M. T. M. Koper, *Nat. Energy* **2020**, *5*, 891.

[289] a) Y. J. Tong, *Chem. Soc. Rev.* **2012**, *41*, 8195; b) S. Jiménez, J. Soler, R. X. Valenzuela, L. Daza, *J. Power Sources* **2005**, *151*, 69.

[290] a) M. Escudero-Escribano, M. E. Zoloff Michoff, E. P. M. Leiva, N. M. Marković, C. Gutiérrez, Á. Cuesta, *ChemPhysChem* **2011**, *12*, 2230; b) I.-S. Park, D. O. Atienza, A. M. Hofstead-Duffy, D. Chen, Y. J. Tong, *ACS Catal.* **2012**, *2*, 168.

[291] a) P. Rodriguez, N. Garcia-Araez, M. T. M. Koper, *Phys. Chem. Chem. Phys.* **2010**, *12*, 9373; b) P. Rodriguez, Y. Kwon, M. T. M. Koper, *Nat. Chem.* **2012**, *4*, 177.

[292] J. J. Baschuk, X. Li, *Int. J. Energy Res.* **2001**, *25*, 695.

[293] a) I.-S. Park, Y. Y. J. Tong, *Electrocatalysis* **2013**, *4*, 117; b) C. Susut, D.-J. Chen, S.-G. Sun, Y. J. Tong, *Phys. Chem. Chem. Phys.* **2011**, *13*, 7467.

[294] H. C. Kwon, M. Kim, J.-P. Grote, S. J. Cho, M. W. Chung, H. Kim, D. H. Won, A. R. Zeradjanin, K. J. J. Mayrhofer, M. Choi, H. Kim, C. H. Choi, *J. Am. Chem. Soc.* **2018**, *140*, 16198.

[295] X. Zou, X. Huang, A. Goswami, R. Silva, B. R. Sathe, E. Mikmeková, T. Asefa, *Angew. Chem., Int. Ed.* **2014**, *53*, 4372.

[296] B. Liu, L. Zhang, W. Xiong, M. Ma, *Angew. Chem., Int. Ed.* **2016**, *55*, 6725.

[297] a) S. T. Hunt, M. Milina, Z. Wang, Y. Román-Leshkov, *Energy Environ. Sci.* **2016**, *9*, 3290; b) B. Bayatsarmadi, Y. Zheng, A. Vasileff, S.-Z. Qiao, *Small* **2017**, *13*, 1700191.

[298] a) R. Chen, C. Yang, W. Cai, H.-Y. Wang, J. Miao, L. Zhang, S. Chen, B. Liu, *ACS Energy Lett.* **2017**, *2*, 1070; b) S. Cherevko, A. A. Topalov, A. R. Zeradjanin, G. P. Keeley, K. J. J. Mayrhofer, *Electrocatalysis* **2014**, *5*, 235.

[299] D. Wang, Q. Li, C. Han, Z. Xing, X. Yang, *Appl. Catal., B* **2019**, *249*, 91.

[300] a) H. Yu, J. Huang, L. Jiang, L. Leng, K. Yi, W. Zhang, C. Zhang, X. Yuan, *Appl. Catal., B* **2021**, *298*, 120618; b) H. Yu, J. Huang, L. Jiang, Y. Shi, K. Yi, W. Zhang, J. Zhang, H. Chen, X. Yuan, *Chem. Eng. J.* **2020**, *402*, 126187; c) H. Yu, J. Huang, L. Jiang, X. Yuan, K. Yi, W. Zhang, J. Zhang, H. Chen, *Chem. Eng. J.* **2021**, *408*, 127334.

[301] Y. Wu, H. Wang, W. Tu, Y. Liu, S. Wu, Y. Z. Tan, J. W. Chew, *Appl. Catal., B* **2018**, *233*, 58.

[302] a) M. J. Berr, P. Wagner, S. Fischbach, A. Vaneski, J. Schneider, A. S. Susha, A. L. Rogach, F. Jäckel, J. Feldmann, *Appl. Phys. Lett.* **2012**, *100*, 223903; b) H. Yu, L. Jiang, H. Wang, B. Huang, X. Yuan, J. Huang, J. Zhang, G. Zeng, *Small* **2019**, *15*, 1901008.

[303] T. Wang, Y. Zhu, Z. Luo, Y. Li, J. Niu, C. Wang, *Environ. Chem. Lett.* **2021**, *19*, 1815.

[304] a) X. L. Du, X. L. Wang, Y. H. Li, Y. L. Wang, J. J. Zhao, L. J. Fang, L. R. Zheng, H. Tong, H. G. Yang, *Chem. Commun.* **2017**, *53*, 9402; b) X.-H. Jiang, L.-S. Zhang, H.-Y. Liu, D.-S. Wu, F.-Y. Wu, L. Tian, L.-L. Liu, J.-P. Zou, S.-L. Luo, B.-B. Chen, *Angew. Chem., Int. Ed.* **2020**, *132*, 23312.

[305] J. Li, H. Huang, P. Liu, X. Song, D. Mei, Y. Tang, X. Wang, C. Zhong, *J. Catal.* **2019**, *375*, 351.

[306] Q. Zhao, J. Sun, S. Li, C. Huang, W. Yao, W. Chen, T. Zeng, Q. Wu, Q. Xu, *ACS Catal.* **2018**, *8*, 11863.

[307] R. M. Navarro, M. C. Sánchez-Sánchez, M. C. Alvarez-Galvan, F. d. Valle, J. L. G. Fierro, *Energy Environ. Sci.* **2009**, *2*, 35.

[308] a) S. Cao, B. Shen, Q. Huang, Z. Chen, *Appl. Surf. Sci.* **2018**, *442*, 361; b) V. Kumaravel, M. D. Imam, A. Badreldin, R. K. Chava, J. Y. Do, M. Kang, A. Abdel-Wahab, *Catalysts* **2019**, *9*, 276.

[309] a) M. Xiao, L. Zhang, B. Luo, M. Lyu, Z. Wang, H. Huang, S. Wang, A. Du, L. Wang, *Angew. Chem., Int. Ed.* **2020**, *59*, 7230; b) J. Yan, Y. Ji, M. Batmunkh, P. An, J. Zhang, Y. Fu, B. Jia, Y. Li, S. Liu, J. Ye, T. Ma, *Angew. Chem., Int. Ed.* **2021**, *60*, 2541.

[310] X. Jin, R. Wang, L. Zhang, R. Si, M. Shen, M. Wang, J. Tian, J. Shi, *Angew. Chem., Int. Ed.* **2020**, *59*, 6827.

[311] a) Z. Jiang, J. Liu, M. Gao, X. Fan, L. Zhang, J. Zhang, *Adv. Mater.* **2017**, *29*, 1603369; b) L. Zhu, M. Hong, G. W. Ho, *Chem. Sci.* **2015**, *11*, 28.

[312] a) J. Ran, J. Zhang, J. Yu, M. Jaroniec, S. Z. Qiao, *Chem. Soc. Rev.* **2014**, *43*, 7787; b) J. Yang, D. Wang, H. Han, C. Li, *Acc. Chem. Res.* **2013**, *46*, 1900; c) J. Ran, M. Jaroniec, S.-Z. Qiao, *Adv. Mater.* **2018**, *30*, 1704649; d) A. Meng, L. Zhang, B. Cheng, J. Yu, *Adv. Mater.* **2019**, *31*, 1807660.

[313] Y. Choi, H.-i. Kim, G.-h. Moon, S. Jo, W. Choi, *ACS Catal.* **2016**, *6*, 821.

[314] W. Choi, A. Termin, M. R. Hoffmann, *J. Phys. Chem.* **1994**, *98*, 13669.

[315] a) Z. Guo, Y. Xie, J. Xiao, Z.-J. Zhao, Y. Wang, Z. Xu, Y. Zhang, L. Yin, H. Cao, J. Gong, *J. Am. Chem. Soc.* **2019**, *141*, 12005; b) W. Liu, Y. Chen, H. Qi, L. Zhang, W. Yan, X. Liu, X. Yang, S. Miao, W. Wang, C. Liu, A. Wang, J. Li, T. Zhang, *Angew. Chem., Int. Ed.* **2018**, *57*, 7071.

[316] Z. Chen, M.-R. Gao, Y.-Q. Zhang, N. Duan, T. Fan, J. Xiao, J. Zhang, Y. Dong, J. Li, X. Yi, J.-L. Luo, *Chem. Sci.* **2020**, *73*, 104833.

[317] H. Xiang, W. Feng, Y. Chen, *Adv. Mater.* **2020**, *32*, 1905994.

[318] L. Jiao, H. Yan, Y. Wu, W. Gu, C. Zhu, D. Du, Y. Lin, *Angew. Chem., Int. Ed.* **2020**, *59*, 2565.

[319] L. Zhang, Y. Ren, W. Liu, A. Wang, T. Zhang, *Natl. Sci. Rev.* **2018**, *5*, 653.

[320] Y. Tang, Y. Wei, Z. Wang, S. Zhang, Y. Li, L. Nguyen, Y. Li, Y. Zhou, W. Shen, F. F. Tao, P. Hu, *J. Am. Chem. Soc.* **2019**, *141*, 7283.

[321] M. Liu, L. Wang, K. Zhao, S. Shi, Q. Shao, L. Zhang, X. Sun, Y. Zhao, J. Zhang, *Energy Environ. Sci.* **2019**, *12*, 2890.

[322] a) X. Zheng, P. Li, S. Dou, W. Sun, H. Pan, D. Wang, Y. Li, *Energy Environ. Sci.* **2021**, *14*, 2809; b) T. Sharifi, E. Gracia-Espino, A. Chen, G. Hu, T. Wågberg, *Adv. Energy Mater.* **2020**, *10*, 1902084.

[323] J. D. Benck, T. R. Hellstern, J. Kibsgaard, P. Chakthranont, T. F. Jaramillo, *ACS Catal.* **2014**, *4*, 3957.

[324] H. Yang, L. Shang, Q. Zhang, R. Shi, G. I. N. Waterhouse, L. Gu, T. Zhang, *Nat. Commun.* **2019**, *10*, 4585.

[325] a) J. N. Tiwari, A. M. Harzandi, M. Ha, S. Sultan, C. W. Myung, H. J. Park, D. Y. Kim, P. Thangavel, A. N. Singh, P. Sharma, S. S. Chandrasekaran, F. Salehnia, J.-W. Jang, H. S. Shin, Z. Lee, K. S. Kim, *Adv. Energy Mater.* **2019**, *9*, 1900931; b) J. N. Tiwari, S. Sultan, C. W. Myung, T. Yoon, N. Li, M. Ha, A. M. Harzandi, H. J. Park, D. Y. Kim, S. S. Chandrasekaran, W. G. Lee, V. Vij, H. Kang, T. J. Shin, H. S. Shin, G. Lee, Z. Lee, K. S. Kim, *Nat. Energy* **2018**, *3*, 773.

[326] J. Ji, Y. Zhang, L. Tang, C. Liu, X. Gao, M. Sun, J. Zheng, M. Ling, C. Liang, Z. Lin, *Chem. Sci.* **2019**, *63*, 103849.

[327] B. Yan, D. Liu, X. Feng, M. Shao, Y. Zhang, *Adv. Funct. Mater.* **2020**, *30*, 2003007.

© 2022 Wiley-VCH GmbH